Study of the forming of the cladded work-pieces by hot forging

Muhammad Rafiq

ParisTech
INSTITUT DES SCIENCES ET TECHNOLOGIES
PARIS INSTITUTE OF TECHNOLOGY

ARTS ET MÉTIERS ParisTech

2011-ENAM-0035

École doctorale n° 432 : SMI- Sciences des Métiers de l'Ingénieur

Doctorat ParisTech

T H È S E

pour obtenir le grade de docteur délivré par

l'École Nationale Supérieure d'Arts et Métiers

Spécialité "Génie Mécanique et procédés de Fabrication"

présentée et soutenue publiquement par

Muhammad RAFIQ

Le 15 Décembre 2011

Etude de mise en forme de pièces rechargées par forgeage à chaud

Directeur de thèse : **M. Régis BIGOT**
Co-encadrement de la thèse : **M. Laurent LANGLOIS**

Jury

M. Bernard ANSELMETTI, Professeur des Universités à l'IUT de génie mécanique de Cachan, France	Président
Mme. Helen ATKINSON, Professor of Engineering, University of Leicester, UK	Rapporteur
M. Guillaume RACINEUX, Professeur des Universités à l'Ecole Centrale de Nantes, France	Rapporteur
M. Saïd ETTAQI, Professeur des Universités à l'ENSAM de Meknès, Maroc	Rapporteur
M. Fabrice SCANDELLA, Docteur à l'Institut de Soudure Yutz, France	Examinateur
M. Régis BIGOT, Professeur des Universités, ARTS ET METIERS ParisTech Metz, France	Examinateur
M. Laurent LANGLOIS, Maitre de conférences**,** ARTS ET METIERS ParisTech Metz, France	Examinateur

T H È S E

Arts et Métiers ParisTech - Centre de Metz
Laboratoire de Conception, Fabrication Commande (LCFC)-EA4495

Remerciement / Acknowledgements

First and foremost, I would like to thank the members of the jury of the thesis for their time, effort and consideration. I would like to thank Professor Helen ATKINSON, Professor Guillaume RACINEUX and Professor Saïd ETTAQI for accepting to be the referees, for their attention and for their detailed review and critique of my thesis. I would like to give special gratitude to Professor Bernard ANSELMETTI for presiding over the thesis jury and for his valuable comments on the thesis. Special thanks to Mr.Fabrice SCANDELLA for his practical advices.

Words fail me to express my appreciation to my PhD supervisor Mr. Laurent LANGLOIS, without whom, this thesis would not have been possible. His guidance, determination and insight provided me with the direction whenever I needed it. I am also thankful for his special tireless efforts during the review of the French and English thesis manuscripts.

I would like to thank my thesis director, Prof. Régis BIGOT, who made sure the relevance of industrial demands and practicalities to improve the quality of my PhD research. His practical expertise in the forging process is matchless.

I am also thankful to all the technicians of the plastic deformation and material section of ENSAM who were important to the successful realization of experimental work of the thesis.

Collective and individual acknowledgments are also owed to my colleagues at ENSAM for wonderful experiences and golden memories. I would like to thank in particular my friends Sadiq and Nejah for their support for the preparation of my PhD defence presentation.

I am forever indebted to my mother and late father. My mother deserves special mention for her inseparable support and prayers.

I owe my deepest gratitude to my loving wife sadia, for being a pillar of support during all the hardships and difficulties that we encountered during the last five years. She was a constant source of motivation, encouragement and help in the times of stress and despair.

I would like to thank everybody who was important to the successful realization of thesis, as well as expressing my apology that I could not mention personally one by one.

Lastly, I gratefully acknowledge the financial support for this research from the higher Education Commission of Pakistan (HEC), Arts et Métiers ParisTech France and the Lorraine Region.

Avant Propos

Ce mémoire de thèse représente une synthèse de mes activités de recherché menées depuis Septembre 2007. Ces activités ont été effectuées sous les ststus d'allocataire d'une bourse « Higher Education Commision (HEC) Pakistan » de Septembre 2007 à Juin 2011.Cette bourse a été obtenue suite à un concours national, pour le développement des ressources humaines.

Ces travaux s'inscrivent dans la problématique de l'étude de mise en forme de pièces rechargées par forgeage à chaud ».

Pour donner l'aspect international de cette thèse selon le règlement des études doctorales (page20) suite au règlement (art. 11 arrêté cotutelle internationale de thèse), la réduction est réalisé en deux langues : anglais et française. De ce fait, ce document serait divisé en deux parties :le mémoire de thèse en anglais et un résumé étendu en français faisant référence aux figures et équations du mémoire en anglais.

Dedicated to my kids Taimoor, Amina and Hafsa.

Contents

List of Figures

List of Tables

Part I

Résumé Étendu Én Français

Chapter 1

Introduction Générale

Fabriquer des pièces multi-matériaux peut être une solution pour répondre à des cahiers des charges fonctionnelles complexes ou obtenir un compromis entre performances et coût de fabrication. La solution multi-matériaux permet de mettre aux différents endroits de la pièce un matériau adapté aux sollicitations locales. La réalisation de pièces de ce type nécessite toutefois d'introduire dans sa gamme de fabrication des procédés permettant "l'assemblage" des différents matériaux. Parmi ces derniers, on retrouve les procédés de soudage. Les procédés de soudage à l'état solide comme le soudage par friction permettent la soudure de matériaux de nature différente (alliage d'aluminium sur acier, alliage de cuivre sur alliage d'aluminium). La pièce finale est obtenue par l'assemblage des différentes parties réalisées séparément dans un matériau. D'autres procédés d'assemblage peuvent également être utilisés comme le brasage ou le collage. Les procédés de soudage à l'état liquide, comme les procédés de soudage à l'arc ou le soudage laser, permettent de faire du rechargement. Ils sont utilisés lorsque les sollicitations superficielles de la pièce conduisent à des choix de matériaux très différents de celui du cœur de la pièce. C'est par exemple le cas des socles de charrues de labour pour lesquels la surface est fortement sollicitée par abrasion alors que le cœur doit résister aux sollicitations mécaniques. Les fonctions de surface et du cœur de la pièce conduisent à des choix de matériaux différents.
Les procédés de soudage par fusion réalisent des revêtements par juxtaposition et superposition de cordons de soudure. Le revêtement est obtenu de proche en proche par solidification d'un mélange de métal d'apport et de métal du substrat.

La qualité du procédé de soudage à produire des rechargements peut être évaluée par le taux de métal de base se retrouvant dans le revêtement que l'on appelle taux de dilution. La maîtrise de la composition chimique du revêtement passe par la maîtrise de ce taux de dilution au travers des paramètres de conduite du procédé de soudage. Le revêtement étant constitué de cordons de soudures juxtaposés, l'état de surface présente souvent un défaut d'ondulation dont la régularité dépend essentiellement de la forme rechargée et du mode de soudage, manuel ou automatisé. Le rechargement de forme gauche, comme par exemple, des outillages de forgeage, est difficile à automatiser. Souvent dans le cas de gravures peu profondes, cela consiste à réaliser une couche d'épaisseur uniforme supérieure à la profondeur de la gravure et dans laquelle toute la surface sera usinée. Le rechargement de surface complexe nécessite la génération de trajectoires permettant d'obtenir un bon recouvrement entre les passes adjacentes avec la régularité nécessaire au maintient d'un taux de dilution le plus uniforme possible. Les procédés de soudage manuels permettent de s'adapter aux surfaces complexes au détriment toutefois de la productivité et souvent de l'homogénéité du revêtement obtenu.

L'idée développée dans ce manuscrit est d'obtenir des pièces multi-matériaux par déformation plastique à chaud d'une préforme rechargée. La gamme de fabrication conventionnelle d'une pièce rechargée consiste à recharger une pièce obtenue préalablement par forgeage et/ou usinage. L'opération de rechargement est l'une des dernières de la gamme de fabrication juste avant les opérations de parachèvement comme l'usinage de la surface pour obtenir la qualité dimensionnelle et d'état de surface minimale requise. Le travail présenté ci-dessous est le fruit d'une première étude de la faisabilité d'inverser globalement la gamme et de recharger une forme simple (lopins cylindriques ou parallélépipédiques, tôle) et de la mettre en forme par déformation plastique.

Les procédés de mise en forme sont parfaitement adaptés à l'obtention de formes complexes. La déformation plastique et la température de mise en forme sont à l'origine de phénomène métallurgique comme l'écrouissage ou la recristallisation dynamique qui vont conférer au matériau des propriétés intéressantes. Les procédés de mise en forme par déformation plastique peuvent mettre en œuvre une grande variété d'alliages métalliques parmi lesquels ceux qu'il est intéressant

de déposer en surface de pièce comme les superalliages ou les aciers inoxydables. Dans la littérature, la mise en forme par forgeage de pièces multi-matériaux est peu développée. La question de l'estimation de la forgeabilité d'un lopin revêtu demeure ouverte. Celle-ci peut toutefois s'exprimer suivant trois aspects que sont:

1. La forgeabilité intrinsèque de chaque matériau
2. La forgeabilité de la structure composée du revêtement et de la partie du substrat proche du revêtement
3. L'aptitude à maîtriser la répartition des matériaux lors de la mise en forme.

La question peut se résumer ainsi : Dans quelle mesure est-on capable de trouver des conditions de mise en œuvre de la mise en forme permettant à partir d'une ébauche rechargée d'obtenir une pièce sans défaut et avec la répartition de matériaux désirée ? La question n'est donc pas uniquement d'évaluer l'aptitude à la mise en forme mais également d'identifier les indicateurs de celle-ci.
Dans un premier temps, une étude bibliographique sur les procédés de rechargement et de traitement de surface est conduite. L'objectif de celle-ci est de classifier les différents procédés en fonction des matériaux qu'ils peuvent déposer, des formes susceptibles d'être traitées. L'étude bibliographique se concentre ensuite sur les procédés de rechargement par soudage par fusion et de proche en proche. Le cas particulier du rechargement des aciers inoxydables est abordé. Le premier chapitre se termine par l'étude des tests de forgeabilité et de ductilité des matériaux.
Dans un deuxième temps, le manuscrit propose une méthodologie pour la maîtrise du procédé de rechargement. Cette étude s'appuie sur le cas du rechargement d'un acier de construction S235 avec un acier inoxydable par le procédé MIG. Cette méthodologie s'appuie d'un côté sur l'étude paramétrique du dépôt d'un cordon et sur des modèles géométriques de recouvrement des cordons. A partir de spécifications sur le revêtement (épaisseur, taux de dilution, énergie nominale) la méthodologie permet de déterminer l'ensemble des paramètres de conduite du procédé de rechargement. Dans une dernière partie de ce chapitre, on s'attache à valider l'utilisation du taux de dilution et de l'énergie nominale comme paramètres caractéristiques de la qualité des revêtements.

La dernière partie est consacré à la forgeabilité des multi-matériaux. L'étude s'appuie toujours sur le rechargement d'un acier de construction avec un acier inoxydable austénitique. Trois tests sont étudiés : le pliage à chaud, le test d'écrasement et le test de bi-poinçonnement. Les deux premiers sont étudiés expérimentalement et par simulation, le dernier n'a fait l'objet que d'une étude numérique. Le travail présenté permet d'estimer l'aptitude de chaque test à évaluer la ductilité du bi-matériau aux différents niveaux décrits ci-dessus.
Le manuscrit de thèse se termine par une conclusion et quelques perspectives. Le travail présenté n'est qu'une première contribution à l'étude du forgeage des multi-matériaux. Il n'a pas la prétention d'apporter des réponses définitives aux questions soulevées ci-dessus. Il permet toutefois d'entrevoir les difficultés et les futurs verrous à soulever. Notamment, le travail aborde peu les aspects métallurgiques. La forgeabilité par exemple est considérée sous son aspect limité de ductilité (apparition de fissure par endommagement) ou sous la forme de déformation de pièce et de répartition de matière. Les transformations métallurgiques, espérées bénéfiques, lors de la mise en forme n'est pas un objet de l'étude.

Chapter 2

Bibliographie

Voir la partie Anglais.

Chapter 3

Opération de Rechargement

3.1 Description de l'opération de rechargement

Ce chapitre est dédié à l'opération de rechargement par procédé GMAW (Gas Metal Arc Welding) robotisé. Les couches rechargées sont obtenues par juxtaposition de cordons de soudure. Pour cela, le profil du cordon seul et le recouvrement des cordons successifs jouent un rôle important sur la qualité géométrique et métallurgique des revêtements obtenus. Cette dernière peut être maîtrisée au travers du contrôle sur les paramètres de soudage comme la vitesse de dévidement du fil, la tension de soudage, la vitesse de soudage, les angles d'inclinaison de la torche, ainsi que le pas de rechargement.

3.2 Principe de la méthodologie pour le choix des paramètres de soudage

L'objectif dans cette partie est de définir la méthodologie permettant le choix des paramètres de rechargement par procédé GMAW. Cette étude se restreint au dépôt d'une seule couche par juxtaposition de cordons. Cette méthodologie s'appuie sur dans un premier temps sur l'étude du dépôt d'un cordon seul établissant le lien entre les paramètres de conduite du procédé et la géométrie et la qualité des cordons obtenus. Dans un deuxième temps, un modèle géométrique de recouvrement est développé pour établir la relation entre le pas de rechargement

et la géométrie du cordon seul. La figure 3.1 illustre la méthodologie suivie pour le choix des paramètres de rechargement.
Dans un premier temps, les paramètres de conduites du procédé de rechargement sont identifiés. La mise en place du modèle de recouvrement et de la qualité des couches revêtues vont permettre d'identifier les paramètres de sortie de l'étude du dépôt du cordon seul. L'étude du dépôt d'un cordon seul sera menée sous la forme de plan d'expérience. Des lois de type statistique sont alors établies reliant les paramètres de conduite du procédé aux paramètres de sortie de l'étude. Dans la figure 3.1, les spéficications "required characteristics", concernent à la fois la géométrie des couches rechargées (épaisseur, défaut d'ondulation), la métallurgie (structure métallurgiques, caractéristiques mécaniques) ou l'opération de rechargement, (temps de soudage). Dans un premier temps, il est nécessaire d'identifier les paramètres de sortie de l'étude du cordon seul qui vont intervenir pour la détermination du pas de rechargement. Pour cela, il est nécessaire de mettre en place le modèle de recouvrement des cordons.

3.3 Modèles de recouvrement de cordon

Comme décrit précédemment, en rechargement par procédé GMAW, le revêtement est obtenu par recouvrement successif de cordons de soudure. Le pas de rechargement doit être choisi afin de minimiser les défauts d'ondulation et éviter les manques de pénétration (défaut de compacité). Une passe de soudage se dépose en refondant une partie du cordon précédent. Cette refonte est nécessaire dans la mesure où elle assure une bonne liaison entre passes. De façon générale, une passe est déposée sur une surface constituée en partie du substrat et en partie de la surface du cordon précédent. Pour obtenir une surface de rechargement la plus plane possible tout en assurant une bonne pénétration des cordons, des critères de recouvrement sont proposés. L'expression de ces critères sera analytique afin de faciliter le calcul inverse des paramètres de conduite du procédé et du pas de rechargement en fonction des spécifications.

3.3.1 Critère de "surface équivalente" et d' "hauteur équivalente"

Deux critères sont considérés dans cette étude. Les deux critères sont basés sur la section du cordon seul et son décalage du pas de rechargement (voir figure 3.2 b). Le critère de surface équivalente considère que le pas de rechargement donnant le défaut d'ondulation le plus faible est tel que la surface de recouvrement est égale à la surface du creux entre les deux cordons. Le principe de ce critère est illustré sur la figure 3.3(a). Le critère de hauteur équivalente considère la somme du profil du cordon et de ce même profil décalé du pas de rechargement. Dans le cas où le décalage est suffisamment faible pour qu'il y ait recouvrement, la somme des profils présent un maximum local entre les cordons. Le pas de rechargement doit être choisi tel que ce maximum soit égal à la hauteur du cordon seul. Ce critère est illustré sur la figure 3.3(b).

3.3.2 Expression générale des critères pour le choix du pas de rechargement

Les deux critères décrits ci-dessus considèrent la section supérieure du cordon de soudure seul. On fait l'hypothèse que la section du cordon est constante tout le long de la soudure. On détermine un repère associé au cordon de soudure comme présenté sur la figure 3.4. Le vecteur "z" est la normale à la surface du substrat recevant le cordon. L'origine du repère est placée au niveau de la surface du substrat à la verticale du point le plus haut du profil. Cette hauteur est appelée "r". Le vecteur "x" est le vecteur perpendiculaire à "z" dans le plan de la section du cordon. On considère la fonction z(x) représentant le profil supérieur du cordon comme illustrée sur la figure 3.4.
Considérons, comme illustré sur la figure 3.5, deux profils identiques décalés de la valeur du pas de rechargement "p". Si "p" est inférieur à la largeur du cordon (voir les équations 3.1 et 3.2), il existe un point d'intersection entre les deux profils dont l'abscisse sera notée x_p définie par l'équation 3.3. Le critère de la surface équivalente est défini de telle sorte que la surface de recouvrement est égale à la section du creux. La surface du creux entre les deux profils est donnée

par la relation 3.5. La surface de recouvrement est donnée par la relation 3.6. Ces surfaces sont données par des intégrales faisant intervenir le pas de rechargement et l'abscisse du point d'intersection x_p.

En considérant la fonction Z(x), une primitive de z(x). L'expression du pas défini par le critère de surface équivalente est donnée par l'équation 3.7. Finalement, le pas de rechargement, donnée par l'équation 3.10 correspond au rapport entre la surface totale de la section du cordon de soudure seul et de la hauteur du cordon. Le critère de la hauteur équivalente est défini pas la relation 3.11. x_p étant défini comme l'abscisse du point d'intersection entre les profils (équation 3.3), le pas de rechargement défini par le critère de la hauteur équivalente est finalement donné par l'équation 3.12. L'expression des deux critères de recouvrement fait intervenir le profil supérieur du cordon de soudure seul z(x). Ce dernier sera approché par une fonction usuelle afin d'obtenir une expression analytique des pas de rechargement donnés par les deux critères.

3.3.3 Représentation du profil des cordons

Dans un premier temps, nous considérerons que le profil du cordon de soudure seul est symétrique par rapport à (O, z) (voir figure 3.4). Quatre fonctions ont été étudiées :

- Un polynôme de degré 2
- Une fonction sinusoïdale centrée sur l'axe des abscisses
- Un polynôme de degré 4 symétrique
- Une fonction arc d'ellipse centrée sur (O,z)

Les deux premières fonctions ne respectent que la hauteur "r" et la largeur "L" du cordon. Les deux autres fonctions feront également intervenir l'angle de mouillage "θ" au pied du cordon (voir figure 3.8). Les expressions des profils approchés par les deux premières fonctions listées ci-dessus sont données par les équations 3.13 and 3.14. L'équation 3.15 donne l'expression générale d'un polynôme de degré 4 symétrique. Le respect de la largeur, de la hauteur du cordon et de son angle de mouillage donne les conditions décrites par les équations 3.16 à 3.18. Les

trois coefficients du polynôme sont des fonctions des paramètres géométriques du cordon (voir équation 3.19 à 3.21). La représentation du profil d'un cordon par un polynôme de degré 4 symétrique contient des limites. En effet, il est nécessaire que le polynôme soit concave, c'est-à-dire que sa dérivée seconde demeure négative sur tout le profil. Ceci impose que la représentation n'est valide que si la valeur de la tangente de l'angle de mouillage reste dans un intervalle défini par l'équation 3.23. Au dessus de l'intervalle, le profil contient deux maximums. En dessous de l'intervalle, le cordon devient convexe au pied du cordon. A ce stade de l'étude, nous pouvons introduire un facteur de forme "Δ", dont l'expression est donnée par l'équation 3.2.3.

L'équation 3.29 donne l'expression générale d'un arc d'ellipse symétrique. Les conditions permettant de déterminer les paramètres de la fonction sont les mêmes que pour le polynôme de degré 4, à savoir, respect de la largeur, de la hauteur et de l'angle de mouillage du cordon. En introduisant le facteur de forme défini précédemment (voir équation 3.2.3), les coefficients sont définis par les relations 3.33 à 3.35.

Sur la figure 3.9, le profil obtenu par les quatre fonctions a été tracé pour différents facteurs de forme et en maintenant une largeur de 10mm et une hauteur de 3mm. Sur cette figure on remarque que le profil obtenu avec le polynôme de degré 2 et la fonction cosinus est indépendant du facteur de forme. On peut remarquer également que pour des facteurs de formes élevés, le profil obtenu en pied de cordon entre les fonctions polynôme à deux paramètres et les fonctions à trois paramètres devient important. L'approche du profil d'un cordon réel par une fonction à deux paramètres risque de ne pas être satisfaisante pour les grands facteurs de forme. L'erreur sur le calcul de l'aire de la section du cordon peut devenir grande. L'erreur sur le calcul de la hauteur du cordon au point d'intersection des deux profils (cas du critère de la hauteur équivalente) peut également devenir importante. Pour les grands facteurs de forme, le modèle polynomial de degré 4 ne donne plus de résultats valides. On obtient un profil à deux extrémums. Par contre le profil en arc d'ellipse permet de représenter des profils avec un grand facteur de forme. La figure 3.10 montre des profils de cordons obtenus par le polynôme de degré 4 et par l'arc d'ellipse. On remarque que la variation de forme obtenue par l'arc d'ellipse est plus faible que celle obtenue par

le polynôme de degré 4.
Dans ce paragraphe, nous avons mis en place quatre modèles analytiques de représentation du profil supérieur d'un cordon de soudure. Il s'agit maintenant d'introduire ce modèle dans l'expression des critères de surface équivalente et de hauteur équivalente.

3.3.4 Pas de rechargement calculé avec les fonctions profil

Dans le cas d'un profil approché par un polynôme de degré 2, l'expression des pas de rechargement donnée par les critères de surface équivalente et de hauteur équivalente est donnée par les équations 3.36 et 3.37 où "L" est la largeur totale du cordon. Il est possible de considérer un taux de recouvrement défini par l'équation 3.38. Il s'exprime comme le rapport entre la largeur théorique de cordon refondue par la passe suivante et la largeur totale du cordon. Dans le cas des deux critères, on obtient les taux de recouvrement donnés par les équations 3.39 et 3.40.
Dans le cas d'un profil approché par une fonction cosinus, les pas de rechargement et les taux de recouvrement obtenus sont donnés respectivement par les équations 3.41 à 3.44. On peut remarquer que les deux critères appliqués aux deux fonctions d'approche du profil donnent des valeurs de recouvrement constantes (indépendantes de la forme du cordon) proches de 30%, valeur communément admise en rechargement par soudage à l'arc. La valeur donnée par le critère de la hauteur équivalente est toutefois légèrement inférieure à celle du critère de surface équivalente.
Dans le cas d'un profil approché par un polynôme de degré 4 symétrique ou un arc d'ellipse, les expressions des pas de rechargement et des taux de recouvrement pour les deux critères sont données par les équations 3.46 et 3.48 à 3.54. On peut remarquer dans un premier temps, que les taux de recouvrement ne dépendent que du facteur de forme. Celui-ci apparaît donc comme un paramètre caractéristique du cordon de soudure vis-à-vis de l'opération de rechargement.
L'expression des pas de rechargement et des taux de recouvrement ci-dessus a été développée dans le cas de cordon de soudure avec un profil supposé symétrique. Ceci n'est pas toujours le cas. En fonction notamment de l'orientation de la torche

ou de la position de soudage, le cordon peut être non symétrique. Dans le cas de cordon non-symétrique, l'idée est de divisé le profil en deux parties, chacune d'entre elles étant approchées par des fonctions du type de celles utilisées pour les profils symétriques. La figure 3.13 présente un profil de cordon non symétrique. Le profil est donc approché par une fonction définie sur deux morceaux, un premier décrivant la partie négative et un second la partie (voir relation 3.56 et 3.57). L'expression du pas de rechargement calculé à partir du critère de surface équivalente est donnée comme le rapport de l'aire de la section du cordon sur la hauteur du cordon(voir équation 3.62). Dans le cas de l'approche du profil non symétrique, l'aire de la section du cordon est la somme des aires des différents morceaux. Dans ce cas, le pas de rechargement devient la moyenne des pas calculé dans le cas d'un cordon symétrique pour les deux fonctions.
Dans le cas du critère d'hauteur équivalente, il est nécessaire dans un premier temps de déterminer l'abscisse du point d'intersection x_p. Ceci n'est pas toujours possible de façon analytique. Dans le cas d'une représentation du cordon par deux polynômes de degré 2 ou deux fonctions cosinus, les expressions du pas de rechargement sont données par les équations 3.67 et 3.68 respectivement.
Sur les figures 3.15 et 3.16 illustre d'évolution des pas de rechargement donnés par les critères de surface équivalente et de hauteur équivalente en fonction du facteur de forme pour les différentes représentations du profil symétrique décrites ci-dessus. On peut noter que la représentation par un polynôme de degré 4 donne la plus grande variation de pas. Ceci peut être relié à la plus grande variété de forme de profil illustrée par la figure 3.10.

3.4 Qualité du rechargement

Dans ce paragraphe, on cherche à identifier les paramètres de soudage qui vont être représentatifs de la qualité métallurgique des revêtements obtenus. De façon générale, la qualité de la couche rechargée va dépendre de sa composition chimique et du cycle thermique qu'elle subit. On va distinguer le cas d'un cordon seul et le cas d'une couche obtenue par juxtaposition de cordons. On considérera les caractéristiques métallurgiques du revêtement et de la zone affectée thermiquement.

3.4.1 Cas d'un cordon seul

La structure métallurgique du cordon dépend de sa composition chimique. En première approximation, cette dernière peut être définie par une loi des mélanges:

$$\%E = \delta\%E_{apport} + (1-\delta)\%E_{base} \tag{3.1}$$

Où %E, $\%E_{apport}$, et $\%E_{base}$ sont les teneurs exprimées en pourcentage de l'élément E, respectivement dans le revêtement, le métal d'apport et le matériau de base. "δ" est le taux de dilution. Cette expression ne tient pas compte des éventuelles pertes d'éléments par projection, évaporation ou réaction chimique. Comme indiqué dans le chapitre *Bibliography*, les phases métallurgiques présentes dans le cordon de soudure dans le cas du rechargement d'un acier inoxydable sur un acier de construction vont dépendre du taux de dilution. Pour des taux de dilution faible, le cordon sera austénitique ferritique avec une teneur en ferrite de l'ordre de quelques pourcents. La structure de solidification sera soit de la forme Ferrite Austénite ou Austénite Ferrite. Pour des taux de dilution plus importants, la structure métallurgique peut présenter les trois phases Austénite, Ferrite et Martensite ou Austénite Martensite. Le cordon possède une structure de solidification. La nature de la structure de solidification pour une composition donnée va pouvoir évoluer en fonction de la vitesse d'avance. En effet, comme présenté dans le chapitre I, la vitesse de solidification du bain de fusion est directement liée à la vitesse d'avance. La vitesse de refroidissement de la zone fondue et de la Zone affectée thermiquement, pour une épaisseur de substrat donnée et un procédé de soudage donné, va dépendre de l'énergie nominale et de la température initiale du substrat. L'énergie nominale est donnée par la relation ci-dessous :

$$E_n = \frac{IU}{V_a} \tag{3.2}$$

La tension et la vitesse d'avance sont deux paramètres du procédé. Par contre l'intensité va dépendre de la vitesse de fil et de la hauteur de l'arc. Cette dernière va dépendre essentiellement de la tension. Dans les générateurs, l'intensité est reliée à la vitesse de fil au travers de la courbe de fusion. La courbe de fusion pour un fil d'acier inoxydable de diamètre 1,2mm sous un gaz (96% d'argon, 3% de CO_2

et 1% d'hydrogène) et une longueur de sortie de fil de 10 mm est présentée sur la figure suivante. Pour connaître la structure métallurgique du cordon de soudure seul, l'étude paramétrique du dépôt d'un cordon seul devra avoir comme sortie le taux de dilution et l'intensité de soudage. La vitesse d'avance est un paramètre d'entrée de l'étude. La structure métallurgique obtenue dans la zone affectée thermiquement du substrat va dépendre essentiellement de l'énergie nominale et de la température initiale du substrat. L'étendue de la ZAT dépend également de ces deux paramètres. Dans les aciers de construction, la ZAT peut se décomposer en trois sous-zones que sont :

- La zone "trempée" où la température maximale atteinte dépasse la température de transformation austénitique AC3. Le matériau est totalement transformé en austénite. Proche de la zone de fusion, la température atteinte est proche de la température de fusion ce qui génère de gros grains (taille 0-1) austénitiques.
- La zone de "recuit" totalement ou partiellement recristallisée. Cette zone peut subir une transformation austénitique partielle (entre AC3 et AC1) ou subir une recristallisation statique à des températures inférieures à AC1.
- Une deuxième zone de "recuit" où le matériau en fonction de sont état initial peut subir un adoucissement. Les aciers de constructions laminés à froid subissent dans cette zone un recuit d'annihilation conduisant à une baisse de dureté.

Les structures métallurgiques de zone affectée thermiquement pourront, en première approximation, être caractérisées au travers de l'énergie nominale de soudage et de la température initiale du substrat.

3.4.2 Cas d'une couche

Composition chimique et taux de dilution Du fait de l'élaboration du revêtement par juxtaposition et recouvrement partiel de cordons, la composition chimique du revêtement sera hétérogène. Le taux de dilution va évoluer d'un cordon de soudure à l'autre. Le taux de dilution d'un cordon seul peut être

approché à partir de la mesure de surface sur une macrographie transversale comme illustrée sur la figure suivante. Le taux de dilution est alors donné par l'expression suivante :

$$\delta = \frac{S_{apport}}{S_{totale}}$$

Où S_{apport} est la section de la zone fondue située au dessus de la surface initiale du substrat et S_{totale} est la section totale de la zone fondue de la soudure. Cette approximation du taux de dilution est basée sur l'hypothèse que le cordon de soudure est un cylindre ayant comme base le contour de la section transversale du cordon et une génératrice orientée par le vecteur vitesse d'avance. Dans le cas du recouvrement du cordon "n-1" par le cordon "n", le taux de dilution est donné par la relation suivante :

$$\delta_n = \frac{(S_{apport,n} + \delta_{n-1} S_{r,nn-1})}{S_{totale,n}}$$

Où δ_n, δ_{n-1} sont les taux de dilution des cordons n et n-1 et $S_{r,nn-1}$ est la surface du cordon n-1 refondu par le cordon n (voir figure 3.17). On fait l'hypothèse d'un "régime géométrique établi", c'est-à-dire, de l'existence d'un nombre n_{lim} de cordons au-delà duquel les surfaces intervenant dans l'expression du taux de dilution n'évoluent plus.

$$\forall i, j > n_{lim} S_{totale,i} = S_{total,j}, S_{r,ii-1} = S_{r,jj-1}, S_{apport,i} = S_{apport,j} \tag{3.3}$$

La dernière relation est vraie même en dehors du régime géométrique établie. La surface d'apport est reliée au débit de fil et à la vitesse d'avance. Dans le cas où la relation (5) est vérifiée, le taux de dilution tend vers une valeur limite donnée part:

$$\lim_{n \to \infty} (\delta_n) = \frac{S_{apport}}{S_{base}}$$

Où S_{base} est la section de métal de base fondue par la passe et est définie par la relation:

$$S_{totale} = S_{apport} + S_r + S_{base}$$

La surface d'apport reste constante quelle que soit la passe. La surface de base de la première passe est plus grande que celle des passes suivantes par l'effet de recouvrement. Le rapport entre l'aire de la surface de base du premier cordon et celle du deuxième cordon peut être mis en relation avec le taux de recouvrement et donc le pas de rechargement. Il ne s'agit toutefois pas d'une fonction linéaire du taux de recouvrement dans la mesure où une grande partie de la surface de base est occupée par le lobe (dû à l'effet Marangoni), la position de ce dernier étant difficile à anticiper.

Cycle Thermique Pour obtenir la forme du cycle thermique subi lors de la réalisation d'une couche, un essai de rechargement a été mené. Les paramètres de soudage et le taux de recouvrement sont donnés dans le tableau suivant. Il s'agit comme dans le cas de l'étude du rechargement d'un acier inoxydable 316L sur un substrat en acier doux S235 d'épaisseur 30 mm. Le rechargement est constitué de 10 cordons. La plaque substrat est instrumentée avec 10 thermocouples de diamètre 1,5mm. Les trous de positions de ces thermocouples arrivent à deux mm de la surface du substrat et sont décalés par rapport à l'axe de la torche lors de la réalisation des cordons. Ceci permet d'éviter que les thermocouples se retrouvent dans le lobe de la soudure. La position des trous des thermocouples est fixée en considérant la géométrie du cordon seul translatée de la valeur du pas de rechargement p (voir le figure 3.18). La numérotation des thermocouples est telle que le n° i est situé entre les cordons "i-1" et "i". La figure 3.19 présente une photographie de la plaque substrat avant rechargement, vue 3D issue de la CAO de la plaque substrat rechargée et une photo de la plaque substrat après rechargement. Sur la figure 3.20 est présentée la courbe de température correspondant aux mesures des thermocouples 1, 6 et 10. Le thermocouple "n" étant placés entre les cordons "n-1" et "n" (à l'exception du n°1), on peut noter sur chaque courbe deux pics d'intensité équivalente correspondant au passage de la source de

chaleur lors du dépôt des cordons "n-1" et "n". Pour les cordons plus éloignés, la courbe de température peut présenter un pic d'amplitude moindre avec un retard correspondant au temps nécessaire à la chaleur de diffuser jusqu'au point de mesure. La température moyenne de la plaque, donnée notamment par le thermocouple 1 lors de la réalisation des derniers cordons, monte progressivement jusqu'à atteindre une température limite. Si on regarde les pics de température, on trouve une vitesse de refroidissement plus importante pour le thermocouple 1 lors de la réalisation du premier cordon que pour les pics des thermocouples suivants. Ceci illustre la baisse de la vitesse de refroidissement au fur et à mesure de la réalisation des cordons par un effet d'échauffement de la pièce de base. Les essais réalisés permettent d'illustrer le fait que d'un point de vue thermique, en l'absence de préchauffage, le premier cordon est le plus contraignant, étant celui présentant la plus grande vitesse de refroidissement. Ceci n'est toutefois pas toujours vérifié. Dans le cas de rechargement de pièces ayant des épaisseurs variables, il se peut que par un effet géométrique (évacuation de la chaleur de la zone de soudage par conduction) la vitesse de refroidissement puisse varier de façon importante. En première approximation, on peut estimer la température de préchauffage limite atteint par la pièce au cours du soudage. On suppose pour cela que la température du substrat est uniforme. On suppose négligeable les temps d'arrêt de l'arc. On suppose également que le temps de soudage est suffisamment long pour atteindre le régime thermique établi. L'équilibre thermique est atteint lorsque l'apport d'énergie par l'arc électrique est compensé par les échanges avec l'extérieur. Ces derniers se résument aux échanges avec le montage et ceux avec le milieu extérieur par convexion et rayonnement. Si on néglige le flux de chaleur échangé par rayonnement, on obtient une température d'équilibre donnée par la relation suivante :

$$T_{lim} = \frac{Puissance}{H_{change}}$$

Où T_{lim} est la température limite moyenne atteinte par la pièce, Puissance est la partie de la puissance de l'arc effectivement transmise à la pièce et H_{change} le coefficient d'échange thermique global en supposant que l'échange de chaleur entre la pièce et son environnement est proportionnel à la température moyenne de la

plaque. La température limite ainsi que la montée en température dépendent de la puissance de soudage. Le cycle thermique limite est donc celui obtenu pour une température de préchauffage définie par la puissance de soudage. Pour une même énergie nominale, une puissance et une vitesse d'avance faibles conduiront à une température limite plus faible qu'une forte puissance et une vitesse d'avance importante.

Conclusion La composition chimique du revêtement est hétérogène. Le taux de dilution du métal d'apport varie d'une passe à l'autre. Toutefois, dû à l'effet de recouvrement, celui-ci est minimum pour la première passe. La vitesse de refroidissement est également la plus forte pour le premier cordon. L'effet de préchauffage de la pièce par l'énergie des passes précédentes tend à baisser la vitesse de refroidissement au fur et à mesure de la réalisation des cordons. Les critères utilisés pour caractériser la qualité du revêtement seront donc le taux de dilution et l'énergie nominale. Pour obtenir cette dernière, il est nécessaire d'ajouter aux grandeurs de sortie de l'étude l'Intensité de soudage.

3.4.2.1 Cas d'une couche, l'étude experimentale

Dans cette partie, l'influence des paramètres de soudage sur les paramètres géométriques et la qualité des cordons est étudiée. Dans cette étude on se restreint à l'étude de l'influence de la vitesse d'avance, de la vitesse de fil et de la tension de soudage. Il est possible d'étendre la démarche à d'autres paramètres comme les angles d'inclinaison de la torche ou la distance tube-contact pièce. La méthode suivie consiste dans un premier temps à déterminer l'intervalle de variation de chaque paramètre de soudage. Le plan d'expérience suivi est complet et comporte trois niveaux par paramètre. L'ensemble des valeurs testées est donné dans le tableau 3.2.

Les essais sont réalisés dans une cellule de soudage robotisée dotée d'un robot polyarticulé 6 axes et d'un générateur CY385 MPR. Les opérations de rechargement consistent à déposer un acier inoxydable 316L sur une tôle en acier doux S235 d'épaisseur 30mm. Le diamètre du fil d'apport est de 1.2mm et le gaz de protection est un mélange ternaire à base d'argon (96%Ar, 3%CO_2, 1%H_2). La composition chimique des matériaux mis en œuvre est donnée dans le tableau 3.3. Chaque

essai est répété trois fois pour obtenir une première estimation de la répétabilité des résultats. Les résultats obtenus permettent d'obtenir des lois statistiques (voir équation 3.85 à 3.89) donnant les caractéristiques du cordon seul (largeur, hauteur, angle de mouillage, le taux de dilution et l'intensité de soudage). On remarque que les dispersions sur la valeur des paramètres géométriques du cordon peuvent atteindre 20% de la valeur moyenne. Celle-ci est la plus forte pour les cordons obtenus avec un mode de transfert par grosses gouttes ou transitoire entre grosses gouttes et pulvérisation axiale.

3.4.3 Validation des fonctions représentant le profil des cordons.

Lors de l'étude paramétrique expérimentale, nous avons obtenu des cordons avec des facteurs de forme allant de la limite inférieure à la limite supérieure de la représentation par un polynôme de degré 4. On remarque le excepté pour deux cordons à fort facteur de forme, le modèle de représentation par un polynôme de degré 4 est satisfaisant sur toute la gamme des cordons obtenus.

3.4.4 Etude du rechargement d'une couche

Parmi les essais de l'étude du dépôt d'un cordon, trois jeux de paramètres ont été retenus donnant un taux de dilution autour de 25%. L'étude paramétrique porte uniquement sur le pas de rechargement. Afin de suivre ces paramètres d'une passe à l'autre, la surface rechargée est composée de cordons de longueur différente comme présenté sur la figure 3.31. Le calcul du taux de dilution et des paramètres géométriques de chaque cordon est effectué à partir de coupe macrographique successive et après une attaque au réactif de FRY de plusieurs minutes. Le calcul du taux de dilution de la passe n est calculé en superposant les profils de la passe n-1 comme illustré sur la figure 3.17. L'attaque chimique permet de révéler la limite de la zone fondue du deuxième cordon. En superposant le profil de la passe précédente, on peut déterminer une section, appelée $S_{n,n-1}$, correspondant à la section de la passe n-1 refondue par la passe n. Le taux de dilution de la passe n s'exprime alors à partir des surfaces et du taux de dilution

de la passe n-1 par l'équation 3.78. où $S_{total,n}$ est la surface totale de la zone fondue de la passe n. Si on suppose que le taux de dilution et la géométrie des passes se stabilisent à partir de quelques passes, on obtient un taux de dilution limite donné par :

$$\lim_{n\to\infty}(\delta_n) \quad = \quad \frac{S_{apport}}{S_{base}}$$

où S_{apport} et S_{base} sont les surfaces d'apport et de pénétration du substrat lorsque la géométrie des passes s'est stabilisée. La section de la passe correspondant au métal d'apport est déterminée par le diamètre du fil d'apport et le rapport entre la vitesse de fil et la vitesse d'avance. Celle-ci est constante quelle que soit la passe. On peut introduire un rendement tenant compte de la perte de matière due aux projections et à l'évaporation dans l'arc de certains éléments. Les résultats ont été obtenus avec les paramètres de rechargement du tableau 3.30. Dans ce dernier, les dimensions du cordon et le facteur de forme sont celles prédites par le modèle statistique issu de l'étude paramétrique.

Avec les paramètres de soudage de la ligne A du tableau 3.7, des rechargements ont été réalisés avec des valeurs de recouvrement de 60%, 40%, 30%, 22% et 17%. Les deux dernières valeurs correspondent aux valeurs nominales du pas calculées par les deux critères (équations 3.49 et 3.50). La figure 3.37 présente les macrographies des rechargements testés suivant une section constituées de cinq passes.

Identification des phénomènes limites Les observations macrographiques montrent que pour les valeurs fortes de recouvrement (60%) il apparaît un manque de pénétration ou collage dès la troisième passe. Ceci provient de la fermeture de l'angle de mouillage au fur et à mesure des passes. Sur la macrographie de la figure 3.36 for 60% overlapping, on observe un angle de mouillage superieur à 90° rendant inaccessible le pied de cordon par la passe suivante. Pour les valeurs faibles de recouvrement certaines passes sont disjointes. Ceci provient de la combinaison de deux facteurs. Sur la figure 3.35 sont présentées trois macrographies du rechargement avec le recouvrement de 17% correspondant aux sections avec

1, 2 et 3 passes. Dans un premier temps, le pas de rechargement et donc le recouvrement est calculé à partir de la valeur moyenne des dimensions du cordon seul estimé à partir des lois statistiques. Les dispersions de ces dimensions associées à l'erreur du modèle statistique font que, dans notre cas, le cordon à une largeur plus faible que celle estimée. Le taux de recouvrement réel est de 14% et non 17%. Dans un deuxième temps, la deuxième passe est décalée vers le premier cordon contrairement à l'hypothèse à la base du modèle de recouvrement. Ces deux phénomènes font que le troisième cordon se dépose avec un recouvrement nul. Ceci est dû à la forte valeur du facteur de forme du cordon rendant la valeur du taux de recouvrement très sensible aux variations géométriques du cordon.
La figure 3.37 présente les macrographies obtenues avec les deux autres jeux de paramètres (B et C du tableau 3.7) pour les recouvrements calculés à partir des deux critères. On constate que dans tous les cas, la couche est compacte avec une épaisseur de revêtement variant très faiblement depuis le premier cordon. Le défaut d'ondulation de la surface supérieure du revêtement est du même ordre de grandeur quel que soit le recouvrement choisi.
La figure 3.42 donne l'évolution du taux de dilution en fonction du cordon pour un rechargement réalisés avec les paramètres A et trois taux de recouvrement différents (40%, 30% et 22%). Ces résultats montrent que le premier cordon est celui avec le plus fort taux de dilution. Le taux de dilution des passes suivantes sont plus faibles du fait du recouvrement mais fluctuent en fonction de la variation de la surface de la passe précédente qui est refondue. Cette surface varie sensiblement notamment pour les taux de recouvrement les plus faibles. Le pas de rechargement p_A semble satisfaisant quels que soient les paramètres de soudage et la géométrie du cordon associée. Ce pas permet donc d'obtenir des revêtements compacts avec un défaut d'ondulation faible. Le pas de rechargement p_H présente une trop forte sensibilité aux variations géométriques du cordon et peut dans le cas d'un facteur de forme important conduire à des défauts de recouvrement des cordons.

3.4.5 Qualité métallurgiques des cordons obtenus

Pour étudier la qualité métallurgique des cordons obtenus, neuf jeux de paramètres ont été déterminés. Parmi ces jeux :

- Trois permettent suivant les lois statistiques identifiées d'obtenir la même énergie nominale et le même taux de dilution
- Trois permettent d'obtenir le même taux de dilution mais des énergies nominales différentes
- Trois permettent d'obtenir une même énergie nominale mais des taux de dilution différents

Avec l'ensemble des cordons, on doit être en mesure d'isoler l'effet séparé de l'énergie nominale et du taux de dilution et de vérifier pour un cas que ces deux grandeurs suffisent à caractériser la qualité métallurgique d'un cordon seul. La caractérisation des cordons réalisés a consisté à réaliser :

- Des micrographies à différentes échelles et à différents endroits des cordons
- Des mesures de dureté également dans différents lieux du cordon
- Des dosages de phases par RX sur quatre des neuf cordons étudiés

Les observations micrographiques ont montré que la structure dans les cordons est identique pour les trois cordons réalisés à même taux de dilution et même énergie nominale. La structure est cellulaire dans les trois cas, la taille et la forme de ces cellules étant identique pour les trois cordons. Le taux de dilution est de 25% environ. La structure obtenue devrait être austénitique avec présence d'une faible quantité de ferrite ou de martensite. Dans le cordon avec le plus fort taux de dilution, 38%, on obtient une structure cellulaire avec une présence très nette de martensite dans les cellules. Dans le cordon à plus faible taux de dilution, la structure n'est plus cellulaire et est constituée d'une matrice martensitique avec la présence de quelques zones fines de ségrégation. Les cordons obtenus avec différentes énergies nominales ne présentent pas de différences marquées. Il semblerait que la variation de celle-ci, et donc du cycle thermique du cordon, ne

modifie pas de façon significative la structure obtenues. Les dosages de phase par RX ont confirmé les résultats observés par micrographie. Le cordon à plus fort taux de dilution présente 69% d'austénite alors que tous les autres présentent entre 96 et 100% d'austénite. Le dosage par RX ne permet pas de différencier la ferrite de la martensite. Dans le cas du cordon à 69% d'austénite, on sait donc qu'il reste 31% d'un ensemble martensite + ferrite. Le diagramme de Schaeffler ainsi que les observations métallographiques tendent à démontrer la présence de martensite. Le dosage exact entre cette martensite et la ferrite n'est toutefois pas établi. Les mesures de dureté réalisées sur différents cordons ont montré que la présence de martensite avérée était associée à une dureté plus élevée. Pour les autres cordons, les duretés sont très proches. Si on considère les erreurs de mesure, on obtient un ensemble du dureté homogène d'un cordon à l'autre.

3.5 Conclusion

Dans ce chapitre, une méthodologie de choix des paramètres de rechargement a été proposée. Cette méthodologie s'appuie un modèle de recouvrement des cordons successifs formant la couche rechargée utilisant les paramètres géométriques décrivant le cordon seul. Le modèle permet de déterminer le pas de rechargement donnant le minimum de défaut d'ondulation en surface de couche. Une étude expérimentale de type plan d'expériences permet de relier les paramètres géométriques intervenant dans le modèle de recouvrement aux paramètres de soudage. La méthodologie a été mise en place et testée dans le cas du rechargement d'un acier inoxydable sur un acier doux par le procédé MIG. Le pas de rechargement obtenu permet d'obtenir des couches compactes avec un défaut d'ondulation minimum, ceci depuis le premier cordon. L'étude de la qualité métallurgique des cordons réalisés a montré dans le cas du rechargement d'un acier inoxydable sur un acier la prépondérance du taux de dilution sur l'énergie nominale.

Chapter 4

Forgeabilité de piece rechargé

Ce chapitre est dédié à la mise en forme des pièces rechargées. Ce domaine est très peu abordé dans la littérature, les cas de mise en forme multi-matériaux traités ne concernant pas au rechargement par soudage. Le problème essentiel vient de plusieurs aspects:

- On ignore le comportement en déformation à chaud du matériau du revêtement. Ceci vient du fait que sa composition ne correspond pas à celle d'une nuance connue de matériau. De plus, sa microstructure ne correspond à celle des métaux habituellement mis en forme à chaud (structure de solidification évolutive d'un cordon à l'autre).
- La différence de comportement à chaud du matériau du substrat et du revêtement peut être à l'origine de problème de maîtrise de la répartition des matériaux dans la pièce finie.

Les différents niveaux de forgeabilité Trois niveaux ou échelles ont été identifiées pour définir la forgeabilité d'une pièce rechargée (voir figure3.7):

1. La forgeabilité intrinsèque du matériau du revêtement. Elle concerne l'aptitude à la mise en forme du matériau dont la composition chimique est celle issue de la dilution des métaux d'apport et de base avec une structure hétérogène de solidification.

2. La forgeabilité de la structure composée du revêtement et de la zone proche du substrat. La structure concernée est celle proche de la surface de la pièce rechargée et revêt à la fois un aspect métallurgique et géométrique. On peut noter, par exemple, le caractère périodique de la forme de l'interface entre le substrat et le revêtement et de la surface libre du revêtement à l'origine de variation d'épaisseurs.

3. La forgeabilité de la pièce. Cette dernière correspond à l'aptitude à forger la pièce tout en maîtrisant la répartition et la structure des matériaux. Par exemple, si la contrainte d'écoulement du revêtement est très supérieure à celle du substrat, il sera difficile de maîtriser la déformation du revêtement. Pour évaluer l'aptitude à la mise en forme d'un bi-matériaux suivant les trois niveaux présentés ci-dessus, on propose d'étudier différents tests expérimentaux. Ces essais sont des essais de mise en forme de pièces de forme simple.

Dans le premier cas, on estimera la forgeabilité aux échelles 1 et 2 alors que le deuxième type d'essai pourra évaluer la forgeabilité aux trois échelles moyennant certaines conditions. En effet, le problème des essais de mise en forme provient de la difficulté dans certains cas de maîtriser la déformation et la vitesse de déformation que l'on fait subir au revêtement. En fonction de la géométrie de la pièce forgée, il se peut que la sollicitation en déformation du revêtement varie fortement avec la différence de consistance des matériaux du revêtement et du substrat. Dans ce cas, le pilotage de l'essai devrait dépendre de la consistance du revêtement qu'on ne connaît pas. De même, pour estimer la forgeabilité à l'échelle 3, l'essai doit présenter des grandeurs de sortie fortement dépendante de la variation de consistance entre le substrat et le revêtement. Ces grandeurs de sortie doivent être des grandeurs macroscopiques comme l'effort de mise en forme en fonction de la course ou la déformée finale de la pièce. Dans le travail de thèse, trois essais sont considérés:

- L'essai de pliage à chaud
- L'essai d'écrasement

- L'essai de bi-poinçonnement

Pour les deux premiers essais, un modèle analytique et une modèle par éléments finis ont été mis en place. Des essais expérimentaux ont ensuite été conduits pour valider les modèles et évaluer la forgeabilité du bi-matériau constitué d'un acier inoxydable déposé sur un acier doux par MIG robotisé. Le dernier essai n'a été étudié que de façon analytique.

4.1 Pliage à chaud de tôles revêtues

Le principe de l'essai de pliage à chaud est donné par la figure 4.3. Il consiste en un pliage trois points d'une tôle revêtue dont le revêtement a été placé à l'envers du pliage. De cette façon, le revêtement se trouve en contrainte de traction ce qui favorise l'apparition de fissure et permettra d'évaluer la limite de ductilité du revêtement aux échelles 1 et 2. Les paramètres d'entrée de l'étude sont le matériau du revêtement, la température de mise en forme et le comportement thermique et tribologique de l'interface outil/matière et l'épaisseur du revêtement. Pour que l'essai puisse évaluer le niveau 1 et 2 de la forgeabilité, il est nécessaire d'évaluer dans quelle mesure la déformation subie par le revêtement n'est fonction que de la course de pliage et non des autres paramètres d'entrée. Dans le cas où cette dépendance est importante, l'obtention du comportement du revêtement dont sa limite de ductilité devra se faire par méthode inverse depuis, par exemple, la courbe de l'effort de pliage en fonction du déplacement.

4.1.1 Modèle analytique

Pour obtenir une première approximation de l'influence des matériaux sur la déformation obtenue en surface de tôle et l'effort de pliage, un modèle analytique a été mis en place. Les principales hypothèses à la base de ce modèle sont:

- La tôle est considérée homogène, Le calcul est donc effectué sans revêtement. Il s'agit donc dans un premier d'estimer cette influence en monomatériau.

- On fait un calcul en petite déformation avec des sections droites de la tôle restant droites au cours de la déformation de forgeage. L'état de contrainte correspond à de la traction plane
- On suppose que la transformation est isotherme
- On adoptera un comportement thermoplastique de type Norton-Hoff

A partir de ces hypothèses, on obtient une déformée de poutre définie par les équations 4.5, 4.15 et 4.17. La dernière équation définit le mode de déformation. La déformée de la poutre est proportionnelle à la déformée de ce mode. Le mode de déformation est une fonction exclusive de la longueur de pliage et de la somme q des coefficients de sensibilité de la loi de Norton-Hoff à la déformation plastique et à la vitesse de déformation plastique. La déformation plastique équivalente obtenue en surface de tôle est maximum au droit de l'appui central de pliage et est donnée par l'équation 4.23. Cette dernière permet de constater que le comportement du matériau a une influence sur la sollicitation en déformation de la tôle. Cette influence est tracée en fonction du paramètre q sur la figure 4.6. Pour le comportement des aciers, le paramètre q prend une valeur généralement comprise entre 0.25 et 0.35. Cet intervalle de variation correspond en termes de déformation à une variation de 20% environ. La figure 4.7 donne l'évolution de l'effort de pliage obtenue à partir de l'équation 4.19. Cette courbe servira de base de comparaison avec les résultats expérimentaux.

4.1.2 Modèle par éléments finis

Les paramètres d'entrée de l'étude sont :

- Les coefficients de la loi de comportement du revêtement sont des paramètres d'entrées de l'étude.
- Le comportement thermique et tribologique de l'interface entre les outils et la matière
- L'épaisseur du revêtement
- La température de pliage

Le modèle par éléments finis a été mis en place en adoptant pour les lois de comportement des deux matériaux une loi de type Hansel-Spittel. A l'interface entre le substrat et le revêtement les conditions de continuité du champ de température et de déplacement ont été modélisées en adoptant un coefficient d'échange thermique très grand ($10^8 W m^{-2} K^{-1}$) et une condition de collage bilatéral (aucun glissement ni décollement à l'interface).
Afin d'améliorer la gestion du contact entre le substrat et le revêtement, une "boîte de maillage" a été introduite. Celle-ci permet de définir dans le substrat proche de l'interface une taille de maille égale à celle dans le revêtement. Enfin, vue les symétries du problème, on a opté pour une modélisation 2D. Une première simulation a été réalisée en adoptant pour le revêtement le comportement d'un acier inoxydable 316L. La température initiale de la tôle revêtue est de 900°C. Les premiers résultats montrent que l'évolution de la déformation dans le revêtement en fonction de la course de pliage s'approche d'une évolution linéaire. La plus forte valeur est obtenue en surface de revêtement. La courbe de l'effort en fonction du déplacement présente la même forme que celle obtenue avec le modèle analytique. L'étude paramétrique a porté sur l'épaisseur de revêtement, le comportement thermomécanique du revêtement, la température initiale et les conditions d'échange thermique et tribologiques à l'interface outil/pièce.

Influence de l'épaisseur du revêtement Avec l'augmentation de l'épaisseur du revêtement, on obtient un effort de pliage plus important. Ceci est d'autant plus sensible que le revêtement est placé loin de la fibre neutre de la tôle par nature. Une augmentation faible de l'épaisseur du revêtement peut donc avoir une incidence importante sur l'effort de pliage. La déformation obtenue en surface de revêtement est peu influencée par l'épaisseur. Ceci vient de ce que la variation d'épaisseur est faible devant l'épaisseur totale du la tôle revêtue. De plus, lorsqu'on dépose un matériau de revêtement avec une consistance plus forte, la fibre neutre est décalée vers le revêtement ce qui contribue à en réduire la déformation. L'augmentation de déformation par l'augmentation d'épaisseur est donc contrariée par le décalage de la fibre neutre.

La figure 4.22 montre que le comportement du matériau peut avoir une influence très importante sur la déformation dans le revêtement. Cette différence provient d'un effet direct du matériau (du type de celui mis en évidence avec le modèle analytique), d'une variation de la profondeur de l'empreinte du poinçon dans la dans tôle ainsi que de la déformation de la partie non revêtue de la tôle. Pour limiter ce dernier effet, on peut prévoir le pliage d'une tôle entièrement revêtue.
Les grandes différences de déformation sont obtenues avec un revêtement ayant le comportement d'un superalliage à base de nickel, ce qui est très éloigné de notre cas d'étude. Si on reste dans le domaine des aciers, on constate que la déformation dans le revêtement varie de l'ordre de 20% de la valeur moyenne. Sur la figure 4.26 sont tracées l'évolution de la déformation avec la course de pliage dans le cas d'un revêtement avec un 316L pour quatre températures différentes. La déformation obtenue dans le revêtement varie peu avec la température.

Conclusion La conclusion de cette étude est que, si on se restreint à des comportements du type de ceux des aciers, la déformation obtenue dans le revêtement semble peu varier avec les paramètres d'entrée de l'étude que sont le matériau, l'épaisseur ou la température. La course de pliage est la principale grandeur pilote de la déformation dans le revêtement. Le comportement thermomécanique du revêtement n'est pas observée au travers de la déformée de la tôle. Par contre, elle a une influence notable sur l'effort de pliage au même titre que l'épaisseur du revêtement.

4.1.3 Essais expérimentaux

Des essais de pliage ont été réalisés sous une presse hydraulique sur des tôles revêtues. Deux types de rechargement ont été testés.

- Rechargement avec 40% de recouvrement à partir d'un cordon seul avec un taux de dilution de 18%. L'épaisseur global du revêtement obtenu est de 5mm
- Rechargement avec 40% de recouvrement à partir d'un cordon seul avec un taux de dilution de 38%. L'épaisseur global du revêtement est de 3 mm.

Les rechargements ont été réalisés avec la même cellule robotisée avec les mêmes matériaux d'apport et de base que pour l'étude de rechargement du chapitre 3. Pour les deux types de tôles rechargées, les cordons juxtaposés sont parallèles au pli. Le chauffage de la tôle avant pliage est réalisé dans un four électrique avec atmosphère protectrice. Le transfert du four vers la presse est manuel. L'instrumentation de la presse hydraulique permet la mesure de la pression dans le vérin principal et du déplacement du coulisseau. Les essais ont été conduits à trois températures 750˚C, 950˚C et 1050˚C. Pour être plus représentatif des conditions de forgeage à chaud, il serait nécessaire de tester une température proche de 1250˚C. Celle-ci n'est malheureusement pas envisageable avec les moyens disponibles dans le laboratoire.
Les figures 4.29 and 4.30 et tableau 4.4 décrivent et résument les principaux résultats obtenus. On constate l'apparition de fissure lors du pliage des deux tôles à 750˚C. A 900˚C, aucune fissure débouchante ou non débouchante n'est observée. A 1050˚C, des fissures apparaissent au cours du refroidissement de la tôle après pliage. Toutes les fissures observées sont parallèles aux cordons et prennent naissance au défaut de pénétration au pied des cordons. Il semblerait donc qu'à 750˚C, le matériau du revêtement n'est pas suffisamment ductile pour accommoder la déformation autour du défaut de compacité à l'interface entre le substrat et le revêtement. A plus haute température (950˚C) la ductilité est suffisante pour accommoder la déformation autour des défauts. A 1050˚C, la fissuration pourrait être causée par des déformations supplémentaires liées aux différences de dilatations thermiques entre le substrat et le revêtement. Lors du passage du revêtement dans l'intervalle de température où sa ductilité est faible, la déformation et la contrainte associées aux dilatations thermiques provoquent la fissuration. Il est à noter que les deux types de rechargement se fissurent de la même façon aux mêmes températures.
Une première comparaison entre les efforts de pliage obtenus expérimentalement et avec la simulation par éléments finis est présentée sur la figure 4.32. Les allures et la position relative de courbes correspondent, toutefois le niveau d'effort obtenu par la simulation n'est pas correct. Cela peut provenir, d'une part, du fait que la simulation a été menée avec comme matériau du revêtement l'acier inoxydable 316L. Il faudrait, par analyse inverse, rechercher les paramètres de la

loi de comportement pour faire correspondre les deux courbes. D'autre part, cela peut provenir également des erreurs de mesures des efforts de la presse. La presse hydraulique à une capacité maximum de 600 tonnes, l'effort mesuré est faible (environ 5%) et peut donc être non négligeable par rapport aux incertitudes de mesure. Pour compléter l'étude, il serait nécessaire de:

- Réaliser les mêmes rechargements avec des cordons perpendiculaires au pli. Ceci permettrait d'orienter la traction plane parallèlement au cordon et donc parallèlement à la direction principale des défauts de pénétration
- Réaliser les mêmes rechargements mais sans produire de défauts de pénétration par exemple en inclinant la torche GMAW. Cela permettrait de vérifier ou non que la fissuration constatée dans les essais ci-dessus sont bien dues à un problème d'accommodation de la déformation autour des défauts.
- Réaliser des essais de chauffe refroidissement sans pliage pour vérifier si la fissuration à 1050°C est produite par l'action combinée du pliage à chaud et du refroidissement.

4.1.4 Conclusions

L'essai de pliage à chaud permet de tester la forgeabilité des pièces rechargées aux échelles 1 et 2. Il est possible de piloter dans une certaine mesure la déformation imposée dans le revêtement à partir de la course de pliage. Par contre, la forme de la pièce pliée varie peu avec le comportement du matériau. La forgeabilité au niveau 3 ne pourra être atteinte qu'au travers de l'exploitation de la courbe donnant l'effort en fonction du déplacement.

4.2 L'essai d'écrasement

Le principe de l'essai d'écrasement est donné dans la figure 4.33. Cet essai est utilisé dans le cas de mono matériau pour obtenir la limité de ductilité. Dans notre cas, comme dans le cas du pliage à chaud, il s'agit de déterminer les niveaux de forgeabilité que cet essai est capable d'évaluer. Les paramètres d'entrée de l'étude sont le matériau du revêtement, la température de mise en forme, le

comportement thermique et tribologique de l'interface outil/matière et l'épaisseur du revêtement. Pour que l'essai puisse évaluer le niveau 1 et 2 de la forgeabilité, il est nécessaire d'évaluer dans quelle mesure la déformation subie par le revêtement n'est fonction que de la course de pliage et non des autres paramètres d'entrée. Dans le cas où cette dépendance est importante, le comportement du revêtement, dont sa limite de ductilité, sera obtenue par méthode inverse depuis, par exemple, la courbe donnant l'effort d'écrasement en fonction du déplacement.

4.2.1 Modèle analytique

Pour obtenir une expression analytique de l'influence des paramètres d'entrée de l'étude sur la sollicitation du revêtement et l'effort d'écrasement, un modèle basé sr la méthode des tranches a été développé.

- L'hypothèse forte de ce modèle est que la symétrie cylindrique de la pièce demeure au cours de l'écrasement. La déformation en " tonneau " constaté expérimentalement lors de ce type de mise en forme n'est pas prise en compte.

- La déformation est considérée isotherme. On néglige donc l'effet de refroidissement du lopin au contact outil/pièce.

Le champ de déformation dans le cylindre est défini par l'équation 4.36. On constate que les hypothèses cinématiques à la base du modèle imposent un champ de déformation uniforme dans la pièce. Après application du principe fondamental de la statique, en considérant un critère de plasticité de type Von Mises et en considérant les conditions limites en contrainte (la surface extérieure de pièce est libre, continuité de la contrainte radiale à l'interface revêtement substrat), on obtient l'expression de la contrainte axiale donnée par les équations 4.52 et 4.53 complétées de 4.59 et 4.60. L'effort d'écrasement est donné comme l'intégrale de la contrainte axiale sur la surface supérieure du lopin. Ceci donne l'expression 4.62 dans laquelle les paramètres géométriques de la pièce sont donnés par les équations 4.63 et 4.64. Le champ de déformation étant uniforme dans la pièce, on peut introduire dans l'expression de la force la loi de comportement thermo-visco-plastique que l'on veut. On a choisi la loi de Spittel pour faciliter

les comparaisons avec les simulations pas éléments finis. La figure 4.36 illustre l'effort de mise en forme obtenu en fonction de la course d'écrasement. La courbe obtenue contient trois stades :

1. Une montée brutale de l'effort au début de l'écrasement. Ce stade est dû à la forme de la loi de comportement pour les faibles déformations plastiques

2. Une montée importante de l'effort en fin d'écrasement. Ce stade est dû à l'action des contraintes tangentielles de frottement entre l'outil et la pièce ainsi qu'à la montée de la vitesse d'écrasement

3. Entre les deux stades, autour d'un point d'inflexion, on trouve un troisième stade correspondant à la partie de la courbe ayant la pente la plus faible

La frontière entre les stades n'est pas définie de façon précise. Il s'agit simplement de décrire la réponse en effort de l'écrasement d'un lopin rechargé. Les figures 4.37, 4.38, 4.39 et 4.40 donnent l'évolution des courbes efforts déplacement en fonction respectivement de la température, de l'épaisseur du revêtement, du frottement et du matériau. On remarque que la température, l'épaisseur et le matériau ont un effet sensible sur l'effort dès le stade 2. Par contre, l'effet du frottement ne se fait sentir qu'en fin d'écrasement lorsque le taux d'écrasement est important. En conclusion, le modèle développé permet de mettre en évidence l'effet du matériau sur la réponse en effort de l'écrasement d'un lopin revêtu et de le distinguer de celui du frottement. La forgeabilité au stage trois pourra être estimée à partir de l'étude du stade 2. L'hypothèse cinématique forte à la base du modèle ne permet pas de conclure quant à la maîtrise de la déformation dans le revêtement à partir de la hauteur d'écrasement.

4.2.2 Modèle par éléments finis

Les paramètres de l'étude numérique de l'essai d'écrasement sont :

- Les coefficients de la loi de comportement du revêtement sont des paramètres d'entrées de l'étude.

- Le comportement thermique et tribologique de l'interface entre les outils et la matière

- L'épaisseur du revêtement
- La température de mise en forme

Le modèle par éléments finis a été mis en place en adoptant pour les lois de comportement des deux matériaux une loi de type Hansel-Spittel. A l'interface entre le substrat et le revêtement les conditions de continuité du champ de température et de déplacement ont été modélisées en adoptant un coefficient d'échange thermique très grand ($10^8 W m^{-2} K^{-1}$) et une condition de collage bilatéral (aucun glissement ni décollement à l'interface). Afin d'améliorer la gestion du contact entre le substrat et le revêtement, une "boîte de maillage" a été introduite. Celle-ci permet de définir dans le substrat proche de l'interface une taille de maille égale à celle dans le revêtement. Enfin, vue les symétries du problème, on a opté pour une modélisation 2D. Une première simulation a été réalisée en adoptant pour le revêtement le comportement d'un acier inoxydable 316L. Un premier essai à été réalisé avec une température initiale de 900°C, un revêtement ayant le comportement de l'acier inoxydable 316L et une condition de collage bilatéral entre l'outil et la pièce. La figure 4.43 illustre la répartition de matière obtenue ainsi que le champ de déformation plastique équivalente obtenu dans la pièce. On remarque un volume à faible déformation en contact avec l'outil. La faible déformation de ce volume est due à la condition de collage et au refroidissement de la matière par conduction de la chaleur dans les outils. Une partie du substrat a flué et est venu " gonfler " le revêtement. L'épaisseur de ce dernier n'est pas uniforme. On note un amincissement du revêtement proche du point A sous l'outil. Les figures 4.44 et 4.45 montrent l'évolution de la déformation plastique équivalente dans l'épaisseur du revêtement au point B et l'évolution de l'effort d'écrasement. On note que la déformation dans le revêtement est quasi uniforme et évolue de façon presque linéaire avec la course d'écrasement. La courbe donnant l'effort en fonction de la course d'écrasement possède les trois stades présentés précédemment. Pour estimer la position des fissures éventuelles, la figure 4.50 donne la répartition de la valeur donnée par le critère de Latan. On remarque deux zones dans le revêtement ayant des valeurs importantes du critère. La première zone correspond à celle d'un écrasement d'un lopin mono-matériau. La deuxième zone est spécifique aux lopins rechargés. Quand on regarde l'état de contrainte dans

le revêtement au droit de cette deuxième zone, on se rend compte que le revêtement est sollicité en cisaillement entre l'outil et l'écoulement du substrat et est également en "tiré" par la partie du revêtement située en périphérie de lopin. L'étude paramétrique a porté sur l'influence du matériau du revêtement, de la température de mise en forme La figure 4.52 montre l'influence de l'épaisseur du revêtement sur l'effort de forgeage. On note la même tendance que celle obtenue avec la méthode des tranches, c'est-à-dire une influence dès le stade 3.
La figure 4.54 présente la répartition de matière obtenue pour trois revêtements différents. On ne note pas de différence majeure entre le revêtement en 316L et en C35 (lopin homogène). Par contre on note la présence d'un repli pour le revêtement en superalliage à base nickel. Ce repli est dû à l'effet du refroidissement du superalliage en contact avec l'outil. Le comportement de ce matériau est très sensible aux variations de température au voisinage de 900°C notamment. Le matériau en contact avec l'outil voit donc sa limite d'écoulement augmenter de façon significative. Le gradient de limite d'écoulement provoque la formation du repli. La figure 4.56 montre l'effet combiné du frottement et des échanges thermiques. On remarque que dans le cas d'un frottement nul et d'un comportement adiabatique, le lopin conserve sa symétrie cylindrique. Avec un frottement nul et un échange thermique faible avec les outils, on observe une déformation en "tonneau". Celui-ci est dû à l'effet de gradient de limite d'écoulement associé au gradient thermique dans la pièce au contact avec l'outil. Avec l'accroissement de la valeur du frottement, on obtient un revêtement de plus en plus déformé et étendu sur la surface du substrat. La figure 4.57 présente les courbes obtenues dans le cas d'un frottement nul et adiabatique et dans le cas d'une interface outil/matière collante avec transfert thermique. On remarque que l'effort dans le stade 2 est plus élevé dans le cas d'un frottement nul adiabatique. Ceci provient probablement d'un effet de l'épaisseur du revêtement. Dans le cas glissant, le revêtement ne cesse d'augmenter en épaisseur au fur et à mesure de l'écrasement. Dans le cas d'un contact collant, le revêtement est aminci. En fin d'écrasement, au cours du stade 3, l'accumulation de contrainte tangentielle due au frottement provoque une montée importante de l'effort de mise en forme qui atteint des valeurs plus importantes que pour un contact glissant et adiabatique. La figure

4.62 donne l'évolution de l'effort d'écrasement pour trois températures de mise en forme. On remarque que l'effet de la température est notable dès le stade 2.

Conclusions L'étude de l'opération d'écrasement par simulation par éléments finis à mis en évidence comme le modèle analytique trois stades de déformation visible sur la courbe donnant l'effort en fonction de la course d'écrasement. L'étude paramétrique de sensibilité a montré que le frottement et les échanges thermiques sont à l'origine de la déformation en " tonneau " de la pièce. La courbe effort déplacement est sensible à la valeur du frottement et des échanges surtout dans le stade 3. L'épaisseur du revêtement, son comportement et la température de mise en forme ont un effet dès le stade 2. La répartition de la matière dans la pièce est surtout sensible aux comportements thermique et tribologique de l'interface outil/matière.

4.2.3 Essais expérimentaux

Des essais d'écrasement ont été menés sur des lopins cylindriques rechargés. Les cordons de soudure sont déposés de façon circonférentielle. Les lopins sont réalisés avec la même cellule robotisée que pour les essais de rechargement sur tôle. Les lopins sont chauffés dans un four électrique, leur transfert jusqu'à la presse est manuel. L'instrumentation de la presse permet la mesure de l'effort de forgeage au travers de la pression dans le vérin principal et la mesure du déplacement du coulisseau. Des essais d'écrasement ont été conduits à trois températures différentes (750°C, 900°C et 1050°C) sur un seul type de rechargement. Trois niveaux de frottement ont été testés : outil tas plan strié, outil tas plan lisse sans lubrification et outil tas plan avec lubrification (eau+graphite) Les principaux résultats sont les suivants :

- On observe les deux types de fissuration prédits par la simulation. A 750°C et 900°C on obtient une fissuration longitudinale pour un taux d'écrasement entre 60% et 65%. A 1050°C on obtient une fissuration circonférentielle sur la partie inférieure ou supérieure du lopin écrasée. Les deux types de fissuration sont observables sur la figure 4.70.

- L'effort de mise en forme mesuré possède les trois stades mis en évidence par les simulations. Les niveaux d'effort ne sont toutefois pas reproduits. La mesure de l'effort est toujours dans la limite basse des capacités de la presse.

La figure 4.68 donnent les courbes effort en fonction du déplacement obtenues pour les trois conditions tribologiques décrites en début de cette partie. On note un effort au stage 3 plus important dans le cas de l'outil strié. On ne note pas de différence notable entre l'outil lisse lubrifié et non lubrifié. Ceci peut provenir de ce que le frottement plus faible dans le cas lubrifié est compensé par des échanges thermiques plus forts du fait de la présence du lubrifiant.

4.2.4 Conclusion concernant l'essai d'écrasement

L'essai d'écrasement permet d'évaluer la forgeabilité aux échelles 1 er 2 dans la mesure où on maîtrise les échanges thermiques et les frottements à l'interface outil/matière. C'est la raison pour laquelle on a choisi de réaliser les écrasements avec un outil strié. Dans ces conditions tribologiques, l'influence des échanges thermiques est considérablement limités.
L'essai d'écrasement sur des lopins rechargés est susceptible de générer deux types de fissuration. Un premier axial du type de celle obtenue par écrasement d'un lopin monomatériau. Le deuxième ortho radial est spécifique aux lopins rechargés. Lors des essais expérimentaux, ce deuxième type de fissuration est celui qui est apparu aux plus hautes températures (1050°C).

4.3 Conclusions

Pour caractériser l'aptitude à la mise en forme d'un lopin multi-matériau, nous avons identifié trois échelles. Une première échelle correspondant au comportement intrinsèque du matériau du revêtement. La deuxième échelle prend en compte le revêtement et le substrat proche et tient compte de la géométrie de la surface libre de revêtement et de celle de l'interface. La troisième échelle est celle de la pièce et prend en considération les aspects géométriques globaux comme la répartition des matériaux. L'essai de pliage et d'écrasement à chaud

ont permis d'estimer la ductilité à l'échelle 1 et 2. L'essai de pliage permet de solliciter ne traction plane le revêtement, la déformation plastique obtenue étant presque exclusivement corrélée à la course de pliage. L'essai d'écrasement entre tas plans striés permet également de solliciter l'interface au travers de la course d'écrasement. Pour cet essai deux types de fissuration sont observés. Le revêtement n'est pas sollicité de façon homogène. Ces deux essais mettent en évidence le rôle important joué par la forme de l'interface. La variation d'épaisseur de revêtement peut sans doute être à l'origine de concentration de contrainte contribuant à réduire la ductilité du revêtement. Pour le niveau 3 de forgeabilité. L'essai de bi-poinçonnement a été testé par simulation numérique. La forme finale de la pièce poinçonnée est fortement dépendante de la différence de consistance entre le substrat et le revêtement. Ce type d'essai pour lequel la forme de la pièce finale, ou la distribution des matériaux sont très dépendantes de la consistance relative du substrat et du revêtement permet d'estimer la forgeabilité à l'échelle 3.

Chapter 5

Conclusions et perspective

Le travail de thèse présenté est dédié à la mise en forme des pièces rechargées. L'idée initiale est d'inverser la gamme de fabrication "conventionnelle" consistant à recharger une pièce pré-ébauchée en faisant la mise en forme d'un "lopin" préalablement rechargé. Les avantages escomptés de cette gamme vient dans un premier temps de ce qu'on recharge une forme simple. Ceci devrait notamment faciliter l'automatisation du rechargement. Le deuxième avantage vient de ce que le revêtement obtenu à été déformé à chaud après son dépôt par le procédé de rechargement ce qui devrait contribuer à améliorer les structures métallurgiques de solidification issues du soudage.

L'étude bibliographique a montré qu'il existe un très grand nombre de procédés de rechargement. La variété de matériaux qu'il est possible de déposer va des métaux aux céramiques en passant par les polymères. Les géométries de surface et les épaisseurs accessibles peuvent être très variables d'un procédé à l'autre. Les procédés de dépôt comme le PVD ne permettent le dépôt que de couches minces sur des formes qui peuvent être complexes. A l'opposé le procédé de placage par explosion ne permet le dépôt que de tôle métallique d'épaisseur minimum de l'ordre du millimètre sur des plans ou des cylindres de grands diamètres. Les procédés de rechargement par soudage par fusion de proche en proche permettent le dépôt sur des surfaces complexes d'alliages métalliques aux propriétés superficielles intéressantes comme les aciers inoxydables ou les superalliages. Le souci de ces procédés provient souvent de leur manque de productivité et de reproductibilité de la qualité des revêtements obtenus. Ces deux inconvénients peuvent être

partiellement résolus par l'automatisation de l'opération de rechargement.
Les travaux de thèse présentés concernent dans un premier temps la mise en place d'une méthodologie pour la maîtrise de l'opération de rechargement sur des formes simples. Cette méthodologie est appliquée dans le cas du rechargement d'une tôle en acier S235 avec un acier inoxydable 316L par le procédé MIG par juxtaposition de cordons linéaires. La méthodologie s'appuie sur deux axes:

- L'étude expérimentale statistique du dépôt d'un cordon
- La détermination du pas de rechargement par l'intermédiaire d'un modèle de recouvrement

Le pas de rechargement est calculé à partir du critère de "Surface équivalente" basé sur la géométrie du cordon déposé seul. Les paramètres d'entrée de la méthode sont les caractéristiques de la couche rechargée à obtenir. Ces paramètres peuvent concerner la géométrie de la couche, les propriétés métallurgiques de la couche (taux de dilution, énergie nominale, vitesse d'avance et température initiale), la durée de l'opération (vitesse d'avance). La méthodologie mise en place a été éprouvée. Les pas de rechargement obtenus par la méthode sont satisfaisants en termes de compacité du revêtement et de défaut d'ondulation. Une première étude à permis également de mettre en place le lien entre le taux de dilution, l'énergie nominale de soudage et la qualité métallurgique des revêtements obtenus dans le cas du rechargement d'un acier inoxydable sur un acier doux. La méthodologie mise en place devra être éprouvée également dans le cas d'autres types de rechargement (matériaux différents, procédés de soudage de proche en proche différents).
Dans un deuxième temps, le travail s'est concentré sur l'étude du comportement en mise en forme des pièces rechargées. La difficulté provient du fait que le comportement du revêtement n'est pas connu. Sa composition peut être approchée par le calcul du taux de dilution et sa structure est issue de la solidification de soudage. Les compositions obtenues ne correspondent pas à des matériaux connus et la structure métallurgique initiale ne correspond pas à ce qui est habituel en forgeage. Il est donc nécessaire de mettre en place des essais de caractérisation de la forgeabilité des pièces rechargées. Trois échelles de forgeabilité ont été définies:

- L'échelle du revêtement : elle correspond au comportement rhéologique du matériau du revêtement obtenu par rechargement incluant notamment sa limite de ductilité à chaud.

- L'échelle du revêtement incluant le revêtement et la partie proche du substrat. Cette échelle tient compte de la géométrie de l'interface entre le revêtement et le substrat ainsi que des éventuels défauts de cohésion.

- L'échelle de la pièce. Cette partie tient compte de l'aptitude du multi matériaux à être mis en forme pour obtenir la répartition de matière voulue dans la pièce finale.

Les tests de forgeabilité classique de la littérature sont développés uniquement dans le cadre de pièce mono matériau. Leur application à des pièces revêtues n'est pas abordée. Dans le travail de thèse deux essais de caractérisation possibles ont été étudiés, le pliage à chaud et l'essai d'écrasement. Cette étude a consisté à estimer leur aptitude à évaluer la forgeabilité d'un multi matériaux donné aux trois niveaux décrits ci-dessus. Les simulations à partir de modèle analytique ou numérique par éléments finis ont montré que ces deux essais permettent d'évaluer la forgeabilité du matériau du revêtement aux deux premiers niveaux.
Dans le cas du pliage à chaud, la déformation plastique maximale dans le revêtement peut être maîtrisée au travers de la course du poinçon. Pour une même course, la déformation obtenue varie peu suivant le matériau ou l'épaisseur du revêtement ou les conditions de frottement ou d'échange thermique entre la pièce et l'outil. Le pendant de cette propriété est que la déformée finale de la pièce est peu sensible aux différences de comportement entre le substrat et le revêtement ce qui rend difficile l'évaluation de la forgeabilité à l'échelle 3. Il est possible d'envisager de l'évaluer au travers de l'effort de pliage en fonction de la course et d'une analyse inverse pour remonter au comportement du revêtement. Ceci n'a toutefois pas été validé dans le travail de thèse. Les essais expérimentaux ont montré le rôle important joué par l'interface substrat/revêtement notamment sa forme et ses défauts de cohésion. Le pliage à chaud sollicite le revêtement et l'interface en traction plane. L'orientation des cordons de soudure et donc de ses défauts et de l'ondulation de l'interface avec le substrat joue un rôle prépondérant

sur la ductilité du revêtement. Ceci confère une forme d'anisotropie à l'échelle du revêtement et de son interface entre termes de limite de ductilité à chaud et probablement de comportement en déformation. Les résultats expérimentaux obtenus dans le cas du rechargement d'un acier S235 par un acier inoxydable 316L ont montré également le rôle important pouvant être jouée par le refroidissement de la pièce après mise en forme. La différence de coefficient de dilatation thermique entre le revêtement et le substrat pouvant être à l'origine d'apparition de fissure dans le revêtement au cours de son refroidissement. Des essais expérimentaux ont été effectués pour deux épaisseurs et taux de dilution du revêtement différents. Les résultats en termes de ductilité sont identiques, les essais effectués à 750°C présentent des fissures, ceux menés à 900°C ne présentent pas de fissure et les essais à 1050°C présentent des fissures apparaissant au cours du refroidissement. Dans le cas de l'essai d'écrasement, pour maîtriser l'effet des frottements, l'outil utilisé est constitué de tas plans striés. En maîtrisant ainsi les glissements outil/matière, on retrouve comme dans le cas du pliage à chaud une bonne corrélation entre la déformation obtenue dans le revêtement et le course d'écrasement, ceci, indépendamment du matériau du revêtement ou de l'épaisseur du revêtement. Les simulations par éléments finis ainsi que les essais expérimentaux ont mis en évidence deux formes de fissurations possibles. La première correspond à ce qui est communément rencontré dans le cadre de l'écrasement de lopins mono matériau. La seconde, en revanche, est une forme spécifique aux lopins rechargés et correspond à une fissuration circonférentielle proche ou sous le contact outil/pièce. Les deux essais permis de montrer le rôle important que peut jouer la forme de l'interface entre le substrat et le revêtement. Son ondulation, due à la juxtaposition des cordons réalisant le revêtement, confère un comportement "anisotrope" à une échelle incluant le revêtement dans son épaisseur et la partie proche du substrat. Cet aspect là n'est pas encore pris en compte dans les simulations mais devra faire l'objet d'un développement prochain.
Le problème de l'évaluation de la ductilité à l'échelle globale n'a pas été abordé puisque les deux essais étudiés s'y prêtaient mal. Des premières simulations ont montré que l'essai de bi-poinçonnement permet au travers de la forme de la pièce mise en forme de remonter aux différences de comportement entre le revêtement et le substrat. Cet essai fera l'objet d'une étude comme le pliage à

chaud et l'écrasement pour estimer dans quelle mesure il est capable de caractériser la forgeabilité globale du bi-matériaux. Un des avantages escomptés au fait de forger le bi-matériaux est l'amélioration de la microstructure du revêtement par la déformation à chaud. Ceci n'a pas été abordé dans les travaux présentés ici. Les tests de forgeabilité devront également caractériser les transformations métallurgiques se produisant dans le revêtement et le substrat pour qualifier et quantifier le gain potentiel.

Part II

English Version

Chapter 1

Introduction

Fabrication of the multi-material parts can be a solution for the complex functional requirements by attaining a compromise between performances and manufacturing cost. This multi-material solution enables us to deposit the suitable material according to the local demands by using a suitable joining technique. For example in engine exhaust valve, high-temperature strength and wear resistance are required in the head and to meet functional requirements, alloys containing nickel may be used. On contrary, the valve stem experiences comparatively lower temperatures and the necessary strength and wear resistance can be achieved by using a less costly alloy. In this case, the optimum solution may be to use a "bi-metal" alloy to minimize material cost and fulfill the necessary design requirements. The selection of the coating deposition techniques depends on many parameters such as size, geometry and metallurgy of the substrate, adaptability of the coating material to the selected technique as well as the availability and cost of the equipment.

1.1 Placement and importance of the weld cladding process

Among the coating techniques, weld cladding is a process of depositing a thick layer of a material with specific properties over a substrate. They are used when the surface properties of a component lead us the selection of materials very dif-

ferent from that of the substrate. There are solid state welding processes such as friction welding or brazing that allow the welding of different types of materials for example, aluminum alloy on steel and copper alloy on aluminum alloy etc. During the liquid welding processes, such as arc welding or laser welding, a part of the substrate melts and mixes with the cladding due to the convection and diffusion in the melt pool and the cladding is achieved gradually by solidifying a mixture of filler metal and substrate metal. In this way the composition of the layer becomes different from the nominal composition of the used cladding alloy. Normally, the cladding quality is measured by dilution rate which defines the composition of the cladded layer and by bead wetting angle. The composition of the cladded surface determines the physical properties like corrosion resistance, hardness, thermal expansion etc., which ultimately are determined by cladding parameters and thermal cycle of the process. The fusion weld cladding is done by side by side deposition of weld beads. For multi bead deposition, bead overlapping is an important parameter which affects largely the dilution rate or cladding thickness. The cladding consisting of juxtaposed weld beads, often exhibits a lack of corrugation and ripples in the surface which depends mainly on the form to be cladded and method of welding, manual or automated. Any how the wavy profile of the top cladding surface can be controlled by welding parameters, overlapping distance and torch orientation. Excessive bead overlapping may produce voids between successive beads acting as internal pores, reducing the adhesion of cladded surface while less overlapping may cause wavy top surface profile. Cladding the complex shape, for example, forging tools, is difficult to automate. Often in the case of shallow engravings, a layer of uniform thickness greater than the depth of engraving is deposited and then machined up to required limits. Cladding complex surface requires the generation of trajectories to obtain a good overlap between adjacent beads with the required regularity to maintain a dilution rate as uniform as possible. Manual welding processes can be adapted to complex surfaces, however, at the expense of productivity. The main advantage for the weld cladding is the lower cost although it may reveal some weaker mechanical properties due to a wide variety of flaws and their low ductility have always been a matter of concern.

1.2 Positioning of Work

The idea developed in this manuscript is to obtain multi-material parts by hot plastic deformation of a weld cladded preform. The conventional manufacturing layout of a component consists of cladding the part previously obtained by forging and/or machining. The cladding operation is one of the last step in the production layout just before the finishing operations such as machining the surface to obtain the dimensional quality. The reason to reverse the conventional fabrication layout is that the forging process may improve the material properties by the reduction in as-cast grain size, breaking of segregation, minimizing porosity and enhancing homogenization and enhancing the fibrous grain structure that improves mechanical properties parallel to the grain flow. The forging process tends to reduce surface porosity and discontinuities (may close up small internal cavities) of weld cladded layer. To refine the work piece properties, hot forging of the cladded product is proposed. As the forged component achieved by a single piece of monolithic bar stock cannot be tailored to satisfy all the design requirements at different locations of the part. Presently, a little work is available on the hot forging of bi-metal performs. The work presented here is the result of an initial study of the feasibility of reversing the overall layout and clad a simple shape (cylindrical or rectangular billet, sheet metal) and get in shape by hot forging which are considered ideal for obtaining complex shapes. During hot forging process, the plastic deformation and forming temperature are the source of metallurgical phenomena such as hardening or dynamic recrystallization that will give the material properties of interest. The forming processes by plastic deformation can implement a wide variety of metal alloys. The question of estimating the forgeability a cladded workpiece remains open. This may, however, follow the following three aspects:

1. The intrinsic forgeability of each material
2. The forgeability of the structure composed of the cladding and the substrate portion near the interface
3. The ability to control the overall material distribution during the forming.

The question can be summarized as: To what extent are we able to find conditions for implementation of the forming that allows from a rough cladding to get a fault free part with the desired distribution of materials? The issue is not only to assess the forgeability, but to identify its indicators as well.

1.3 Layout of the Thesis

In order to present the research carried out, the thesis divided five distinct chapters. The chapter no.1 provides an introduction to the research work under the scope of this thesis. Chapter no.2 is dedicated to a detailed state of the art related to the main areas in the research work. The chapter is divided into two main parts. The first part provides an overview different cladding process and surface treatment followed by a discussion related to geometrical and material limitations of each process. The purpose of this is to classify the different processes depending on the materials and the forms that can be treated. The concentration on the cladding processes by fusion welding and the special case of stainless steels cladding is made. The second part of the chapter is dedicated to the state of the art dealing with hot forgeability of bi-material. The first chapter ends with study tests forgeability and ductility of materials.
Chapter no.3, provides a methodology for the control of the cladding process. This study uses the case of cladding a structural steel S235 with a stainless steel by Gas metal arc welding (GMAW). This methodology is based on one side of the parametric study of the deposit of a bead and geometric models related to the single bead. From specifications of the cladding (thickness, dilution rate, nominal energy etc.) the methodology used to determine all the driving parameters of the cladding process. In the last section of this chapter, we try to validate the use of dilution rate and the nominal energy as characteristic parameters of the quality of cladding.
The Chapter no.4 is devoted to the forgeability of the multi-materials. The study is related to the cladding of mild steel substrate by stainless steel. The hot ductility and fracture behavior of weld cladded workpiece after forging is under investigation. As compression testing is an accepted procedure for testing forgeability, so upsetting and plane compression test along with hot bending were selected

as the primary means of assessing the cladded work piece workability. The hot bending and upsetting are studied experimentally and by simulation, but the plane compression test(bi-punching)been the subject of a numerical study only. The work is presented to estimate the ability of each test to evaluate the ductility of the bi-material at the various above described levels.
The manuscript of the thesis ends with a conclusion and some perspectives which is chapter no.5. The work presented is only a first contribution to the study of the forging of multi-materials. It does not pretend to provide definitive answers to the questions raised above. However, it allows a glimpse of the future challenges and deadlocks to raise. In particular, the work addresses some metallurgical aspects. The forgeability example is considered in its limited aspect of ductility (appearance of crack damage) or as part of deformation and material distribution. The metallurgical transformations, hoped for benefits during the forming are not an object of the study.

Chapter 2

Bibliography

2.1 Cladding process

Cladability is the formation of a continuous, high density clad deposit with a uniform microstructure, possessing a strong metallurgical bond with the substrate. The cladded layer should have low dilutions with some exceptions, certain clad height, certain deposition efficiency and specific required materials properties. Cladability is primarily determined by the process parameters of the cladding operation and the metallurgical interactions or compatibility of the clad and substrate materials.

Cladding is the deposition of an overlay to allow the surface to perform functions that are distinct from those of the bulk of the material. A cladded part may be considered as a composite, with the base material selected for strength and economy while the cladding material (which may be unsuitable and too costly for use in fabricating the complete part) selected for the specific service conditions to which the critical sections of the part will be subjected. Cladding techniques are being used in almost every area of technology, including automotive, aerospace, missile, power, electronic, biomedical, textile, petroleum, petrochemical, chemical, steel, cement, machine tools and construction industries. Almost all types of materials, including metals, ceramics, polymers and composites can be deposited onto similar or dissimilar materials. The cladding process may develop

a wide range of advanced functional, physical, chemical, electrical and mechanical properties at the required substrate surfaces and some are described below (ASM Handbook, 2001):

- Improved corrosion resistance
- Improved wear resistance
- Improved mechanical properties like enhanced fatigue, toughness or hardness
- Improved thermal insulation
- Improved electronic or electrical properties
- Reduced frictional energy losses
- Improved aesthetic appearance

Classification of Coating / Cladding technologies Cladding technologies can be classified into different categories as in figure 2.1 and each of these methods has its own advantages and limitations.

Globally, the surface cladding methods to improve the surface characteristics of a substrate may be identified by the following two basic approaches :

1. **Providing the substrate a discrete coating**
2. **Surface modification by integral coating**

Integral Coatings have no distinguishable boundary with the substrate and there exists a continuous gradient in concentration from pure substrate material to pure coating material. This continuous variation is associated with strong bonding of the coating to the substrate and is considered to be completely integrated with the substrate. In integral coatings, there may be an alteration in composition, microstructure or residual stress profile to improve the properties of the surface, e.g. hardness and corrosion and wear resistance as compared in figure 2.2.

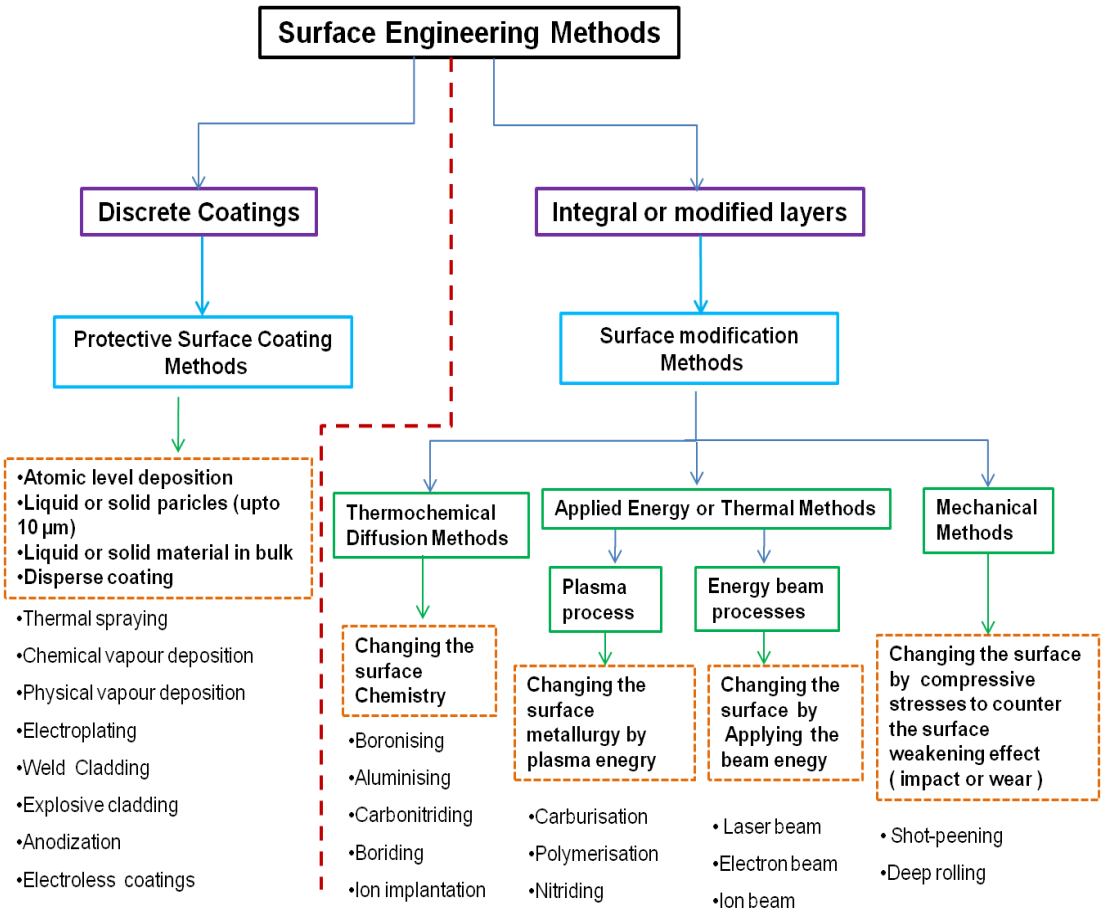

Figure 2.1: Main approaches for surface engineering (ASM Handbook, 2001; Batchelor *et al.*, 2002; Charles *et al.*, 1989; Tillmann & Vogli, 2006)

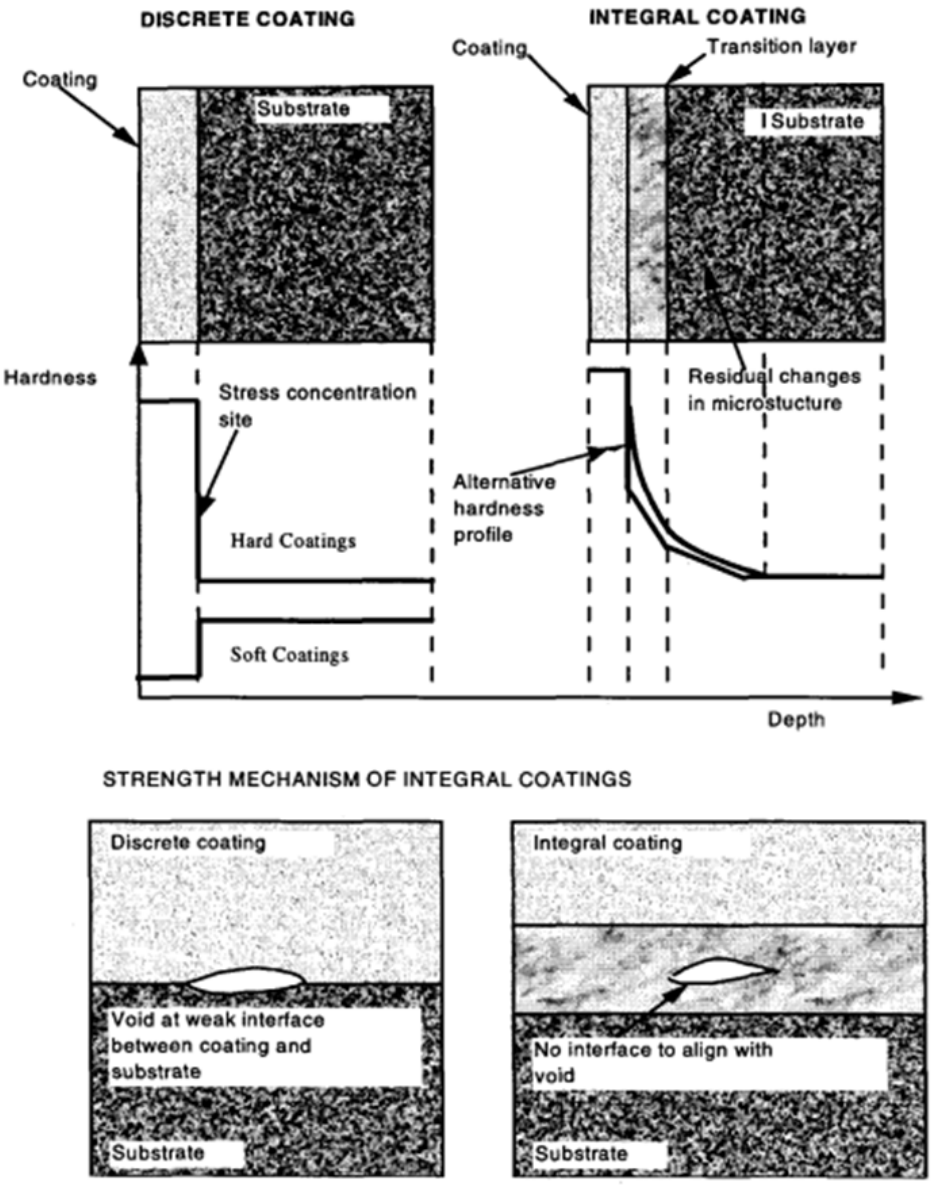

Figure 2.2: Comparison of hardness profiles and failure mechanisms for integral and discrete coatings (Batchelor *et al.*, 2002)

An approach to classification of coating technologies as well as surface modification techniques, including basic advantages and disadvantages is given in tables 2.1 and 2.2 respectively.

Advantages	Technologies	Disadvantages
+ high hardness values + good corrosion resistance + reduces friction in contact with steel	**Electrochemical deposition** (e.g. Cr) up to 0.5 mm coating thickness	– coating of complex geometries is difficult – danger of hydrogen embrittlement – environmental problems
+ low-temperature process + very high corrosion protection + suitable for most metal substrates and many non-conducting materials + uniform coating thickness even on complex geometries	**Chemical (electroless) deposition** from electrolyte solution (e.g. NiB, NiP)	– expensive – additional heat treatment necessary
+ very high hardness values + good adhesion	**CVD, chemical vapour deposition** chemical vapour deposition at high temperatures	– distortion – coating of sharp-edged geometries is difficult – disposal of aggressive gaseous waste
+ dense coatings with high adhesion + low coating process temperature + allows deposition of pure elements, compounds and alloys	**PVD, physical vapour deposition** – evaporation – cathode sputtering	– low growth rate of coating – expensive vacuum process – restrictions in terms of part geometry
+ large variety of materials + good adhesion + properties well controllable by choice of materials and process	**Thermal spray processes**	– residual porosity – deposition efficiency of coating process (overspray)
+ very high adhesion + large parts coatable + inexpensive	**Build-up welding**	– coating materials limited – impact on substrate material
+ very high adhesion + coating of complex geometries	**Build-up brazing** powdery hard material and brazing filler metal with binding agent protective gas process	– coating materials limited

Table 2.1: Selected coating technologies (Tillmann & Vogli, 2006)

Advantages	Process technologies	Disadvantages
+ inexpensive + selective treatment possible + depth 1–10 mm	**Hardening** by means of induction flame laser, electron beam TIG (tungsten-inert gas)	– limited to steel, Co, 3–0.6% – distortion possible
+ applicable to many types of steel + well-controlled coating properties	**Carburisation** • diffusion of C (up to 0.8%) into surface including hardening • variety of different C-carriers	– distortion – cooling cracks
+ less distortion of surface compared to hardening and carburisation	**Carbonitriding** • compare above, additional nitrogen • low-temperature process	– slow process
+ less distortion of surface + high elevated temperature hardness	**Nitriding** • N-diffusion, formation of surface nitrides	– slow process
+ good resistance against adhesive wear + allows oxidising for corrosion protection	**Nitrocarburising** – cf. nitriding	– modifies thin surface zone
+ high hardness	**Boronising** • boron diffusion for boride formation • also applicable for Co-, N-, Ti-alloys	– distortion (high process temperatures) – brittle – low corrosion resistance
+ inexpensive	**Sherardising** • Zn-diffusion with subsequent chromatising	– no wear protection
+ good corrosion protection + less vibration fatigue + increased resistance against stress-corrosion cracking and corrosion fatigue	**Shot peening** for plastic deformation of workpiece surface	– modifies thin surface zone – low increase in hardness
see above	**Deep rolling** comparable with shot peening	– expensive
+ can create high surface hardness values + good wear and corrosion protection	**Plating, metallising** (e.g. Cr, V, Nb, Si-containing diffusion coatings) large variety of processes	– high process temperatures (distortion)

Table 2.2: Selected technologies for surface modification (Tillmann & Vogli, 2006)

Selecting Coating and Surface Technologies Selection of the cladding process for a given job depends on a number of factors like accessibility of the equipment used for cladding, state of repair of worn components, number of similar components to be cladded etc. Based on the given operating conditions, four fundamental aspects are important for systematic approach of cladding process selection (Charles *et al.*, 1989; Pradeep *et al.*, 2010; Toyserkani *et al.*, 2005):

1 Function:

- Size and shape of component
- Metallurgy of the substrate
- Adaptability of the coating material to the selected technique
- Availability and cost of the equipment
- What are the functional characteristics of the part surface ?

2 Purpose:

- What needs to be maximized ?
- What needs to be minimized ?

3 Limitations:

- From technical and economic point of view
- Considering design-to-cost concepts
- Considering design for environment concepts
- Considering life-cycle costs

4 Options:

- What options exist ?

2.2 Details of Different Surface Coating / Cladding Methods

The details of several methods for surface cladding are discussed as under.

2.2.1 Chemical Vapor Deposition (CVD)

CVD is formation of a coating on a heated surface by a chemical reaction. The substrate temperature usually ranges between 500°C and 1500°C (Takadoum, 2008). These relatively high temperatures depict that this process may not be applied to materials having a low melting point. CVD may be categorized into, sputtering, ion plating, plasma-enhanced CVD, laser-enhanced CVD, ion beam and laser evaporation. The coating thickness is in the range of microns.

Geometrical Limitations: CVD technique due to its excellent throwing power can produce coating on substrates of complicated shapes. It is also capable of localized or selective deposition on patterned substrates.

Materials: The most widely deposited coatings metals are W, Ta, Nb, Si and Cr etc. While some compounds and ceramics included are: Cr_7C_3, SiC, Si_3N_4, Al_2O_3, TiC and TiN (gold color). Main categories of deposited materials are shown in table 2.3:

Material	Example
Metals	Al, As, Be, Bi, Co, Cr, Cu, Fe, Ge, Hf, Ir, Mo, Nb, Ni, Os, Pb, P, Re, Rh, Ru, Sb, Si, Sn, Ta, Th, Ti, U, V, W, Zr, also carbon and boron
Compounds	II–Vi and III–V compounds, borides, carbides, nitrides, and silicides of transition metals, as well as sulfides, phosphides aluminides, etc.
Ceramics	Al_2O_3, AIN, B_2O_3, BN, SiC, Si_3N_4, UO_2, Y_2O_3, ZrO_2, etc.

Table 2.3: Typical materials deposited by CVD (Bhat, 2007)

Surface morphology and microstructure Surface morphology and microstructure of CVD materials are controlled by some interrelated factors, like substrate temperature, supersaturation, deposition rate, impurities, temperature gradients and gas flows (Martin, 2010). Blocher (Blocher, 1974) investigated the effect of temperature and supersaturation on microstructure formed during CVD. He observed the epitaxial growth at high temperature/low supersaturation while the formation of platelets, whiskers at low temperature/high supersaturation was resulted as shown in figure 2.3.

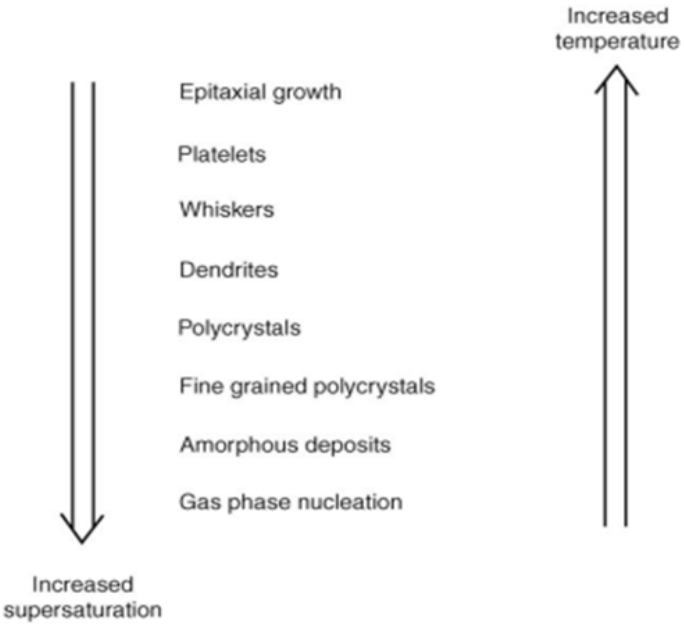

Figure 2.3: Microstructure sequence of CVD materials (Blocher, 1974)

It is important to understand that the driving force for the deposition or supersaturation will decrease with the increase in temperature and consequently, a driving force value, yielding no heterogeneous nucleation, will be reached. From the microstructure sequence diagram, it is clear that the epitaxial growth occurs, at relatively high rates near equilibrium conditions, i.e. at a low driving force and hence, low supersaturation. In a CVD process, surface irregularities have better access to fresh reaction gas, which results in a higher supersaturation and hence

a higher deposition rate. Random surface irregularities are frequently formed in growth processes especially if they extend into higher supersaturation regions. For heterogeneous nucleation, a higher supersaturation is generally required and the conditions of selective growth prevail at supersaturation lower than that required for heterogeneous nucleation.

2.2.2 Physical Vapor Deposition (PVD)

PVD is the formation of a coating on a substrate by physical deposition of atoms, ions or molecules of the coating material. The thickness range of PVD coatings varies from angströms (Å) to millimeters (mm). PVD refers to several types of processes operating under low pressure conditions, ranging from 10^{-4} to 10^{-1} Pa and at low temperatures (between 100 and 500°C) with surface hardness typically around 2500 HV (ASM Handbook, 2002; Takadoum, 2008).
PVD can be categorized into: ***evaporation***, ***ion plating*** and ***sputtering***. The evaporation process is carried out by vapors of a material located in a heat source which may be direct resistance, radiation, eddy currents, electron-beam, laser beam or an arc discharge. Ion plating is a hybrid process while sputtering is the ejection of atoms by the bombardment of a solid or liquid target by energetic particles, mostly ions. A measure of the removal rate of surface atoms is the ratio between the number of sputter-ejected atoms and the number of incident projectiles.

Geometrical Limitations PVD is most suitable for coatings of regular shapes such as sheet, foil and tubing etc.

Materials and surface morphology PVD may be applied to deposit virtually any metal, alloy, refractory or intermetallic compound and their mixtures. Any how it exhibits inability to deposit polymeric materials with some exceptions. PVD has the ability to produce unusual microstructure and new crystallographic modifications, e.g. amorphous deposits. The figure 2.4 shows the columnar to amorphous morphology of crystalline TiAlN.

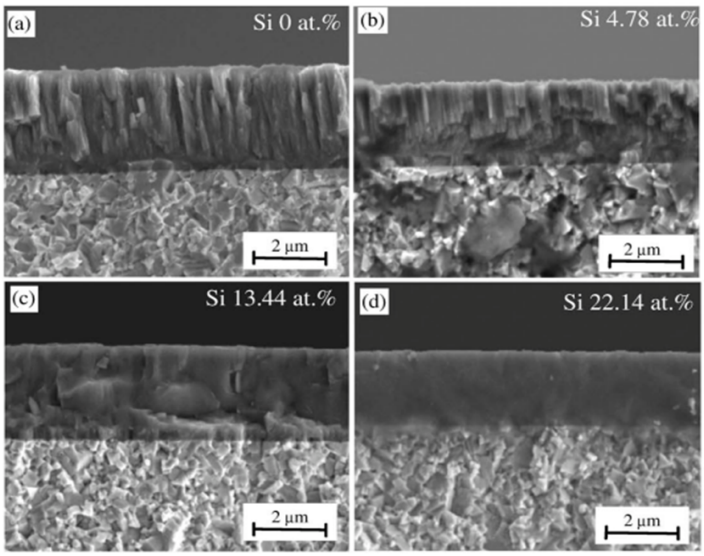

Figure 2.4: Cross sectional morphology of TiAlSiN coatings with different Si content deposited by PVD (Yu *et al.*, 2009)

Duplex treatment: PVD coating produces a thin coating layer of a few micrometers with high micro hardness and only the high micro hardness of coatings is not sufficient for high temperature applications like protection of hot forging tools. One of the possible way to achieve high hardness in combination with high wear, oxidation and fracture resistance and load bearing capacity of hot forging tools is duplex treatment which is combination of plasma nitriding and PVD hard coating (Panjan *et al.*, 2004). The surface roughness is less for duplex treatment than that of plasma nitrided surface only. TiN coating film acts as barrier at the front of subsurface crack and reduces the crack growth toward surface. Some recently developed aluminium or chromium based coating like TiAlN or AlCrN are specially adapted for high temperature applications.

2.2.3 Thermal Spraying

In thermal spraying, the clad material is melted by some flame or arc and then sprayed on the work-piece. The principle of thermal spraying is that the cladding material in the form of wire or powder on a wide variety of substrate materials

including metals, ceramics and plastics, is heated to its melting point by the thermal energy and the molten particles are deposited on the workpiece by a jet of gas. Main advantages are the low heat input into the part, which means there is no heat affected zone and minimal dilution. The biggest drawback of thermal spraying is that the bond between the clad layer and the substrate material is mechanical, not metallurgical in nature which can cause adhesion problems and poor wear resistance. The thermal spray cladding is normally much stronger in compression than in tension and often exhibit some level of porosity (Parker, 2011; Weman, 2003).

Geometrical Limitations: The main limitation is the coating of small and deep cavities into which a torch or gun will not fit. They can coat only the surfaces that are accessible by the torch or gun.

Materials and surface morphology: A very wide variety of materials, virtually any material that melts without decomposing can be used to make a coating (ASM Handbook, 2002) by this process.
The thermal spray can be categorized into three methods, which are:

1. Combustion torch spraying (Flame-spray, High-velocity oxyfuel and Detonation gun spraying)
2. Electric arc spraying
3. Plasma arc spraying

2.2.3.1 Flame Spraying and High-velocity Flame Spraying

The heat source for flame spraying is a flame produced by combustion of acetylene or propane in oxygen and the molten particles are then blown on to the work piece by a jet of compressed air. The cladding material is generally applied in powder form, fed into the nozzle by an inert gas. High velocity oxy-fuel (HVOF) spraying produces a high velocity of the molten particles giving a very strong and dense layer, with less porosity and low oxide inclusion. HVOF produces characteristic shock waves in the flame, which are visible as a diamond pattern. Lidong Zhao

et al. studied plasma spraying and HVOF spraying processes to produce 316L stainless steel coatings and concluded that the oxidation of the spray material could be significantly reduced using HVOF process with suitable parameters. The HVOF coating showed the best corrosion behavior among all the other coatings performed (Zhao & Lugscheider, 2002).

2.2.3.2 Electric Arc Spraying

This method uses an electric arc as the heat source so the cladding material is always electrically conductive. The electrodes are fed continuously into the arc and the molten particles are blown onto the work piece by a jet of compressed air or gas. Compared to other thermal spraying processes, arc spraying is more cost-effective due to its high efficiency and deposition rate it is a potential alternative to weld cladding techniques due to its ability of thick layer deposition (Buchanan, 2009).

2.2.3.3 Plasma spraying

The plasma spraying temperatures are higher than other spray methods which enables ceramics and metal oxides with high melting points to be sprayed. The commonly used plasma gases are: H_2, N_2, Ar or He. The cladding material is supplied in the form of wire, bar or powder and fed into the arc, where it melts and is blown to the workpiece by the plasma jet as shown in figure 2.5.

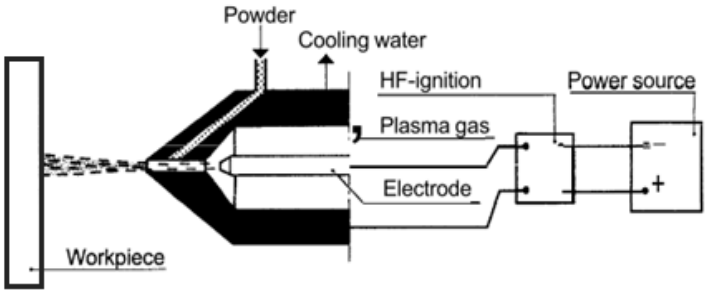

Figure 2.5: Schematic diagram of plasma spraying (Weman, 2003)

2.2.4 Weld Cladding Processes

The welding processes are primarily developed as a method of joining metals for the fabrication industry but these may also be used for surfacing, cladding and hard facing of different parts and products (Deyev & Deyev, 2006). Their use as coating or surfacing may be a secondary purpose and require the adaption and modification of certain features of the processes to suit the needs of cladding process. This is in contrast to the metal spraying and other coating techniques which are originated for the specific purpose of overlaying. Weld deposits can be applied in thicknesses greater than most other cladding techniques, depending on the number of cladded layers. Cladding thickness range for different surfacing techniques is shown in figure 2.6.

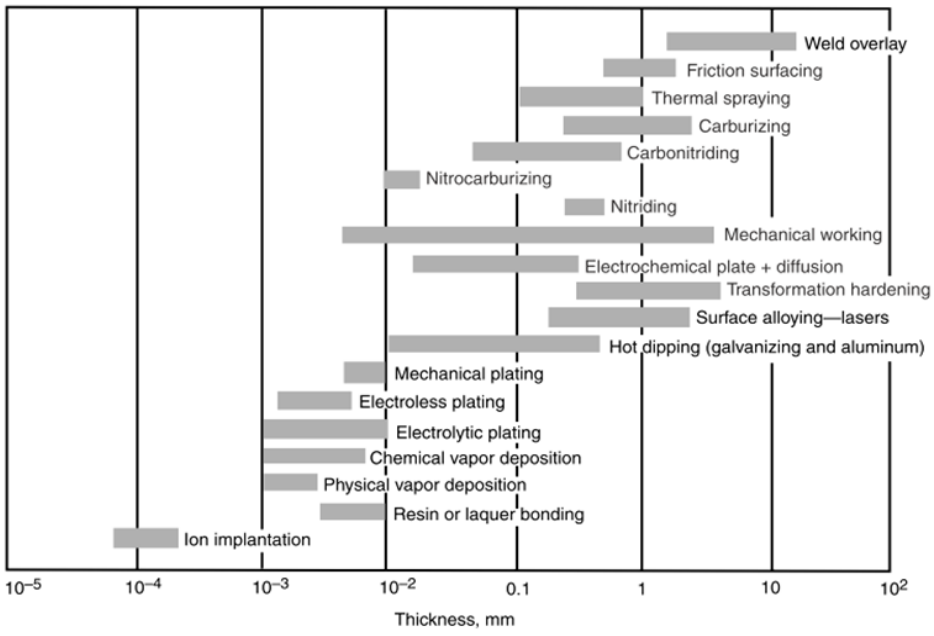

Figure 2.6: Approximate thickness of various surface engineering treatments (ASM Handbook, 2001)

Weld cladding methods offer high deposition rates with relatively low capital cost for the equipment and is being applied in numerous industries such as

chemical, fertilizer, nuclear and steam power plants, food processing, and petrochemical. The biggest difference between welding and cladding is the dilution. The composition and properties of cladding are strongly influenced by the dilution, where typically low dilution is desirable, which means, the final deposit composition is closer to that of the filler metal. Weld cladding is normally performed with fusion welding process, solid state welding or some particular process like brazing and are discussed in the following sections.

2.2.4.1 Brazing and Soldering

Brazing and soldering (for soldering the liquidus temperature of filler metals is below 450°C while for brazing it is above 450°C but lower than the melting temperature of the base metal) create a metallurgical bond below the solidus temperature of the substrate which distinguishes them from other welding based joining and coating technologies. High-temperature brazing techniques also exist where the liquidus temperature of filler metals lies above 900°C. Filler metals used in brazing and high-temperature brazing are shown in the figure 2.7 with the corresponding brazing temperatures (Krappitz, 2006).

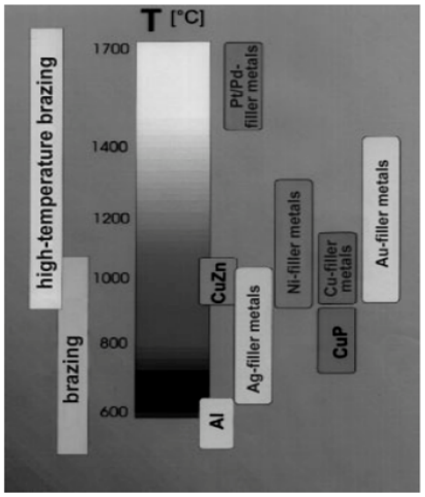

Figure 2.7: Filler metal groups for brazing and high-temperature brazing (Krappitz, 2006)

A direct metallic contact for molten filler metal is an important prerequisite for wetting the substrate material. Initial wetting effect between the alloying of filler metal and substrate material occurs within a few atomic layers of the joining interface, which subsequently by diffusion processes create a metallurgical bond between the filler metal and the substrate.

Heat Sources for Brazing: Several heat sources depending on the specific requirements are used for the brazing process. In ***Torch Brazing,*** heat is supplied by a fuel gas (acetylene, hydrogen or propane) flame, typically to braze copper or silver brazing filler metals. ***Induction Brazing*** normally uses the electric coils designed for specific joint geometries. In ***Retort or Batch Furnace,*** gas, oil or electrically heated system are used. In ***Vacuum Furnace***, electrically heated elements heat the brazing filler metal to the liquidus state until the capillary attraction are achieved. To permit brazing of alloys that are sensitive to oxidation at high temperatures, a pumping system is employed that removes oxygen. Ni, Co, Au, Cu and ceramic based filler metals are successfully vacuum brazed. Different heating methods for the brazing process are shown in figure 2.8.

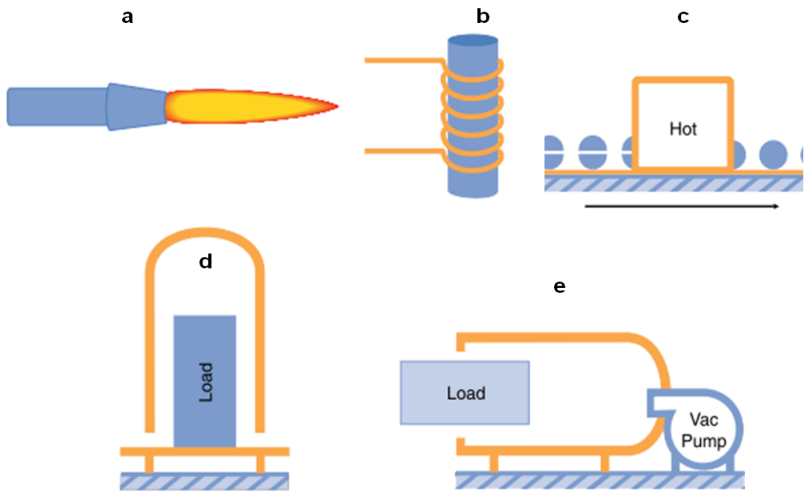

Figure 2.8: Heat Sources for brazing (a) Torch Brazing, (b) Induction Brazing, (c) Continuous Furnace, (d) Retort or Batch Furnace, (e) Vacuum Furnace (Sulzer, March 2009)

Materials and morphology: Main filler metals used are **Ag, Cu, Ti, Ni, Co, Au, Zn** and **their alloys** (Schwartz, 1993). The coatings materials may include metals and the ceramics with, oxides (zirconium oxide, aluminium oxide), nitrides (silicon nitride, aluminium nitride) and carbides (boron carbide). Some possible combinations of braze filler metal and base material are shown in the figure 2.9.

Coating of glass ceramic materials on metals by Ti containing filler metals and

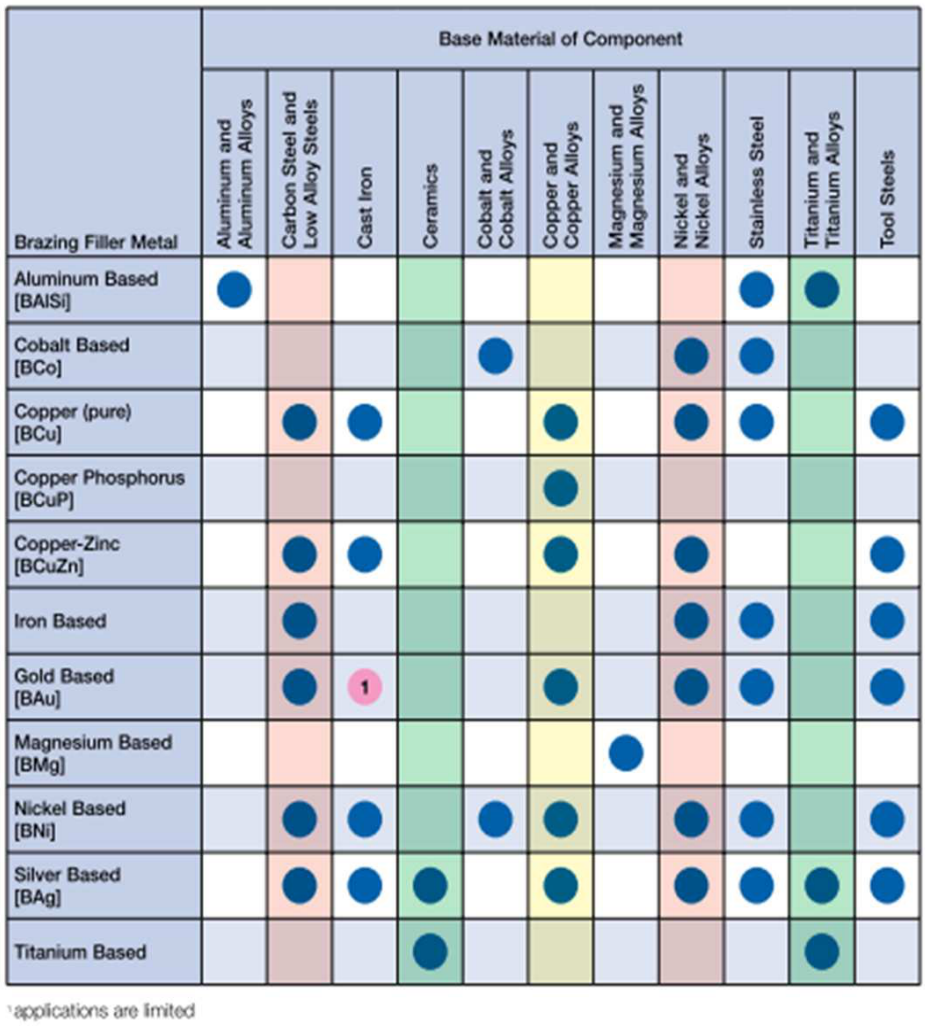

Figure 2.9: Braze Filler Metals and Base Material combinations (Sulzer, March 2009)

brazing for superhard materials (boron nitride) on steel cutting tools are some examples (Naidich *et al.*, 2008). Figure 2.10 shows V-5Cr-5Ti and SS304 brazed by Cu.

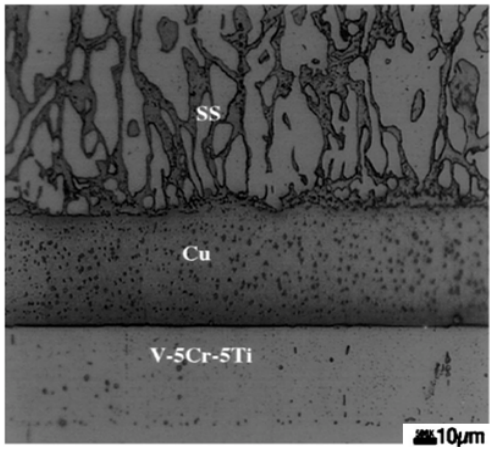

Figure 2.10: Cross section through a braze joint of SS304-Cu–(V 5Cr 5Ti) brazing (Steward *et al.*, 2000)

Geometrical Limitations: This process may be applied on a large variety of geometrical shapes. Size limitation of the parts to be brazed is of major importance. Since the outer area to be brazed must be heated therefore large sections or large heavy plates are normally difficult to braze.

2.2.4.2 Solid state weld cladding processes

Solid state weld cladding processes take place at temperatures below the melting point of the base metal, without the addition of filler metal like brazing or soldering, with or without the applied pressure. ***Friction welding*** is an example of solid-state welding process in which the heat is produced by the relative motion of the two interfaces to be joined. The main idea is the direct conversion of mechanical energy to thermal energy to form the weld, without the application of heat from any other source. ***Friction surfacing*** is an adaptation of friction welding where the consumable rotates and changes the location on the substrate.

After the initial heating period, the consumable continues to rotate while being simultaneously drawn across the substrate to deposit a thick layer of metal on the substrate. The process of friction surfacing is illustrated schematically in figure 2.11.

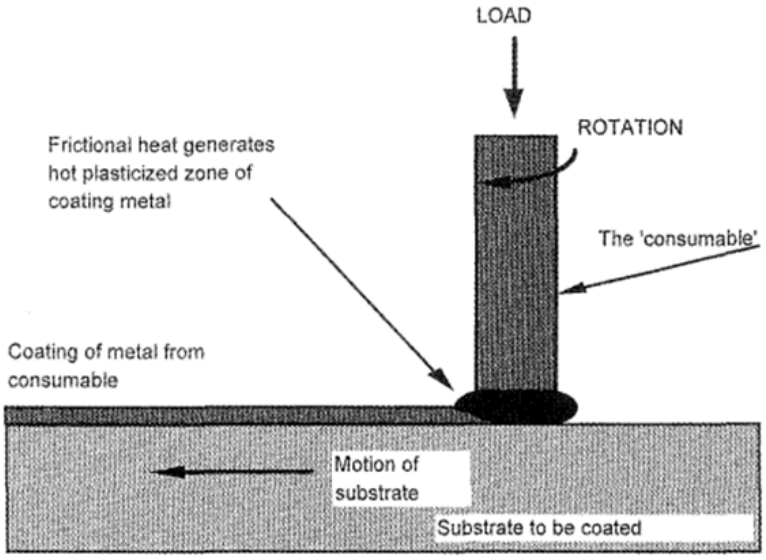

Figure 2.11: Mechanism of friction surfacing (Batchelor *et al.*, 2002)

Friction surfacing occurs at a lower temperature than fusion welding and because of this lower temperature, there is virtually no heat affected zone (HAZ) beneath the coating. Thicker friction surfacing coatings can be produced by multi-layer surfacing i.e. by repeated friction surfacing over the same area.

Geometrical Limitations: Friction surfacing is limited to planar surfaces or surfaces with uniform curvature, e.g. cylinders, plates and discs because more complex surface geometry hinders physical contact between consumable and substrate probably because of the difficulty to have a machine which is capable to press whole trajectory of the work-piece.

Materials and morphology A wide range of similar and dissimilar materials (metals, ceramics, metal-matrix composites (MMC) and polymers)com-

binations that cannot be joined by conventional fusion welding techniques may readily be joined by friction cladding technique. These include alloys based on aluminum, copper (brass, bronze), iron (low-alloy steel, tool steel, stainless steel, maraging steel), nickel, titanium, and tantalum (Welding Handbook, 1991). The microstructure of the friction coating is characteristic of hot forging above the recrystallization temperature of the material and is considered superior to weld overlays having as-cast microstructure and solidification cracks(Batchelor *et al.*, 2002). Typical microstructure of friction surfacing of tool steel grade H13 on low carbon steel plate is shown in figure 2.12.

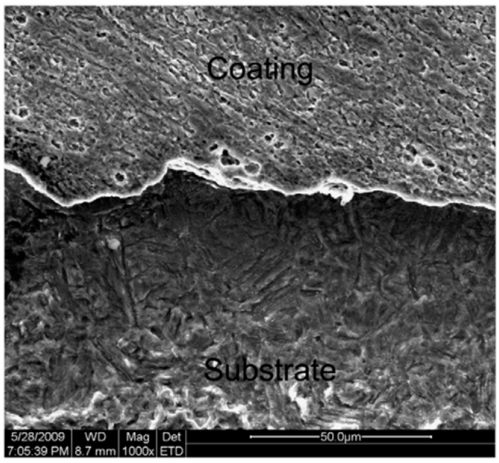

Figure 2.12: SEM microstructure of a coating produced by friction surfacing with substrate traverse speed of 4.4 mm/s (Khalid Rafi *et al.*, 2010)

Explosive Cladding process: Explosive cladding is a solid-state cladding process in which controlled explosive detonations force is applied to clad two or more metals together at high pressures. The energy produced by explosive is used to accelerate a material termed as flyer plate, across a predetermined distance (stand-off distance) in contact with the base material. The process may be described as a cold technique, as there is no external heat used to promote the bonding, rather high-localized temperatures are normally generated at the cladded interface due to the dynamics of the process. The combination of the pressure, heat and plastic

flow on the materials can produce an interface bond. Basic parameters are flyer plate velocity, collision point velocity and collision angle which are influenced by explosive detonation rate, explosive mass and standoff distance.

Geometrical Limitations: The explosive cladding process may be used for angle bonding and parallel-plate bonding. It is limited to geometries like plates or hollow cylindrical substrate.

Materials and morphology: A wide range of similar and dissimilar metals (see table 2.4)that cannot be joined by conventional fusion welding techniques may readily be joined by explosive cladding technique.

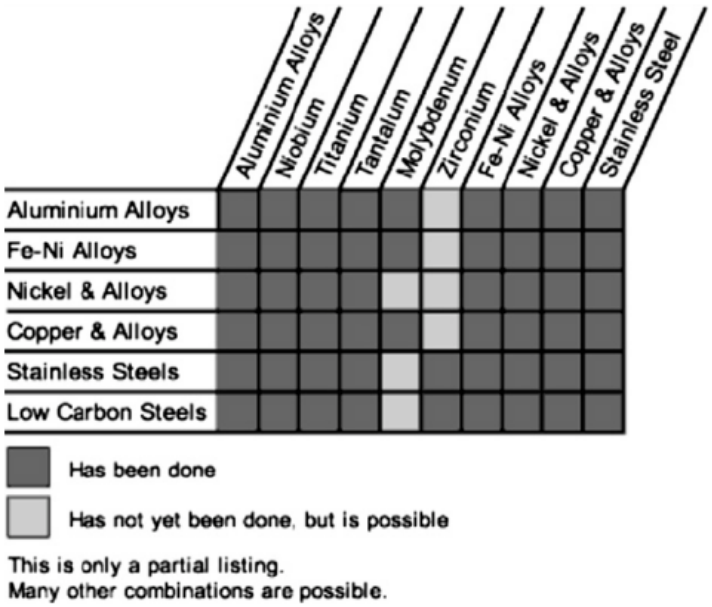

Table 2.4: Common explosive clad material combinations (Howes, 2001)

Figure 2.13 shows the microstructure close to and at the interface of Co-based superalloy/steel cladding by explosive cladding. Due to typical wavy morphology at the interface, the bond has a good tensile strength or shear strength because of the large and wavy contact surface.

The two types of local fusion at the interface are the result of rapid local

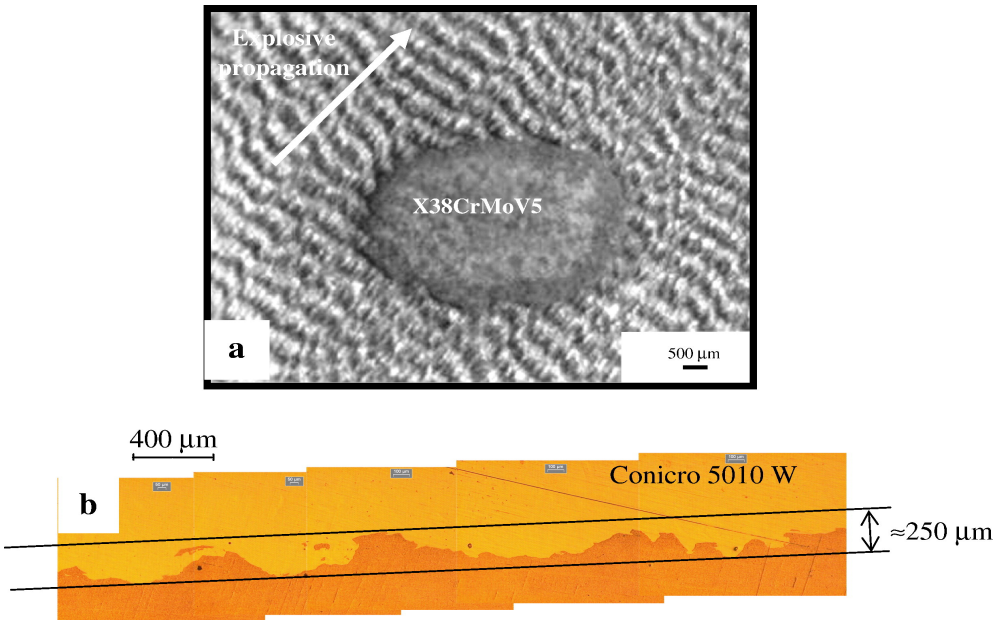

Figure 2.13: Macrographs of the wavy morphology of the interface of the explosive cladding of Co-based super alloy and /steel(X38CrMoV5) a) After removal of the steel. b) Cross section (Ettaqi *et al.*, 2008)

fusion/solidification phenomena and may be the result of the difference of cooling rate or a difference between the thermo mechanical conditions of their formation.

2.2.4.3 Fusion Welding processes

Fusion welding techniques use a heat source that is intense enough to melt the edges as it traverses along a joint. The three most important characteristics of a fusion welding process are **Heat source intensity** , **Heat input rate per unit length** and **shielding of the molten weld pool**. Fusion welding is carried out either by melting of the part edges (auto-genious welding) or by simultaneous melting of the base and filling metal and it subsequently solidifies without the application of external pressure. Depending on the applied heat source, following are some examples of fusion welding processes: **Electric arc, Electron beam, Electroslag, Laser** and **Gas welding** .

Physics of Fusion welding processes: During fusion welding several phenomena like heating, melting, evaporation, solidification and cooling of the solid metal, the phase transition and their interaction are part and parcel. In the weld pool following forces participate in metal transfer and subsequent liquid metal circulation (Norrish & Richardson, 1988):

- Gravitational force.
- Electromagnetic force.
- Surface tension.
- Gas flow induced force.
- Buoyancy forces.

Several complex physical processes take place in a small area normally of the order of a few millimeters during the fusion welding process. The spatial variation of temperature in the weldment is very high and the physics of the weld pool is illustrated in the figure 2.14.

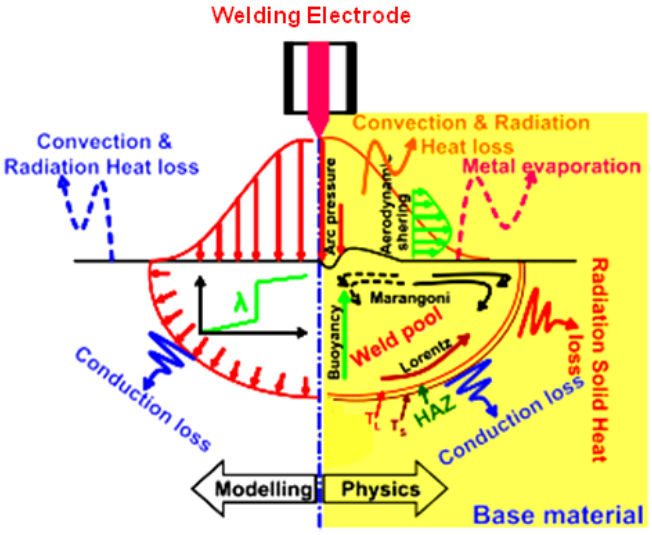

Figure 2.14: Weld pool physics and modelling (Gilles *et al.*, 2009)

Globally, there are three distinct regions in the fusion weldment:

1. The fusion zone(FZ)
2. The heat affected zone(HAZ)
3. The base material.

The FZ undergoes melting and solidification and the convective heat flow affects its geometry and the temperature distribution in the HAZ.

Arc Weld Cladding processes: Arc welding is the most frequently used fusion welding technique which offer high deposition rates and relatively low equipment capital cost. The arc welding processes primarily developed as a method of joining metals for the fabrication industry. These are also used for surfacing, cladding and hard facing of different parts and products. Their use as cladding or surfacing is a secondary purpose, requiring some adaption and modification of certain features of the processes to suit the needs of cladding. Arc weld cladding is normally performed with classical arc welding process such as gas metal arc welding(GMAW), submerged arc welding(SAW), shielded metal arc welding(SMAW) and several others or by some particular process like laser or plasma transfer arc(PTA). In all these processes, an arc is established to melt the surface of the base and filler material, usually in the presence of a shielding gas. The clad material may be deposited using a solid wire, a flux cored wire, twin arc double wire (Tusek & Suban, 2003) or a broad but thin strip electrode (Chiu *et al.*, 2005) which are melted by the arc while forming the clad layer.

Limitation of Arc Weld Cladding processes: High heat input into the substrate and relatively high dilution of the clad material are the major draw backs of arc weld cladding. As high heat input into the base metal can cause distortion which may need for further processing after cladding. So high dilution, distortion and other metallurgical properties are sometimes negatively affected when the arc energy is increased or decreased beyond an optimum level. The details of the main arc weld cladding process is given as under.

Gas Tungsten Arc (GTA) Cladding Process: In GTA cladding process, a non-consumable tungsten electrode shielded by a shielding gas is used to strike an electric arc with the base metal. The heat generated by the electric arc is used to melt the filler and base metal. GTA cladding process involves a number of welding process parameters as shown in figure 2.15.

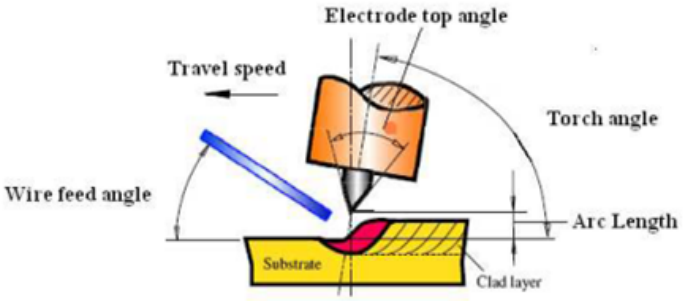

Figure 2.15: Schematic illustration of GTA cladding process ((Xu *et al.*, 2006)-modified)

Filler metal can be added manually in straight length or automatically (Honma & Yasuda, 2004) from a spool or coil in the form of cold or sometimes hot wire for automatic applications.

Materials and microstructural morphology: GTA cladding process may be used for almost all metals, mostly stainless steel, carbon and alloy steels, aluminum, magnesium, nickel alloys, cobalt alloys, copper, titanium and tantalum. The solidification and microstructure of GTA cladding of stellite-6 on the surface of SS 403 is shown in figure 2.16.

Plasma Transferred Arc (PTA) Cladding: In PTA cladding, the deposition of metal powders is carried out by a gas plasma arc which after passing through the orifice to the work piece becomes part of the electrical circuit. Feeding material is carried to the plasma jet by a gas stream, which may be inert, active or a mixture of both. A third gas flow is employed to protect the metal pool

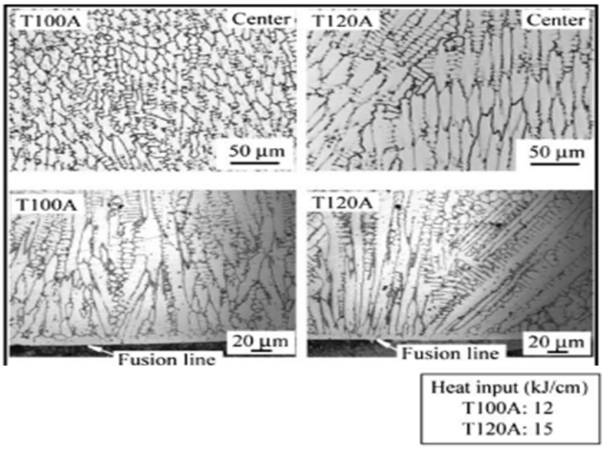

Figure 2.16: Typical solidification and microstructure of stellite-6 clad layer on SS403 by GTA cladding. (Xu *et al.*, 2006)

from atmospheric contamination. Metal powder is fed into the collimated plasma beam as shown in figure 2.17 to ensure high energy-concentration for narrow and deep welds.

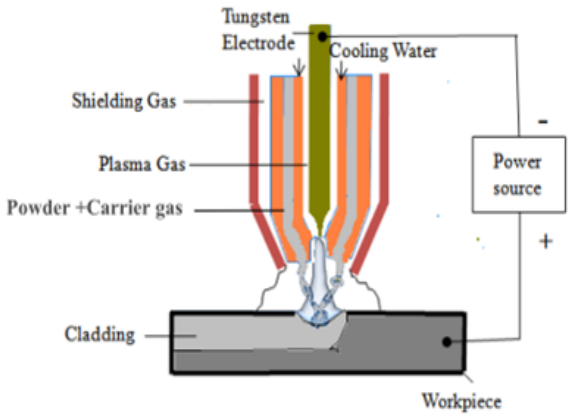

Figure 2.17: Schematic of PTA cladding.

Extremely high temperatures, high welding speeds, excellent arc stability, low thermal distortion of the part, low environmental impact (low oxides emissions) are the main characteristics of PTA process. Among the wide choice of metal

powders for PTA deposition, Ni and Co-base alloys are some choices for high wear and corrosion-resistant coatings (Siva *et al.*, 2009). The Figure 2.18 shows a robotic PTA manipulation.

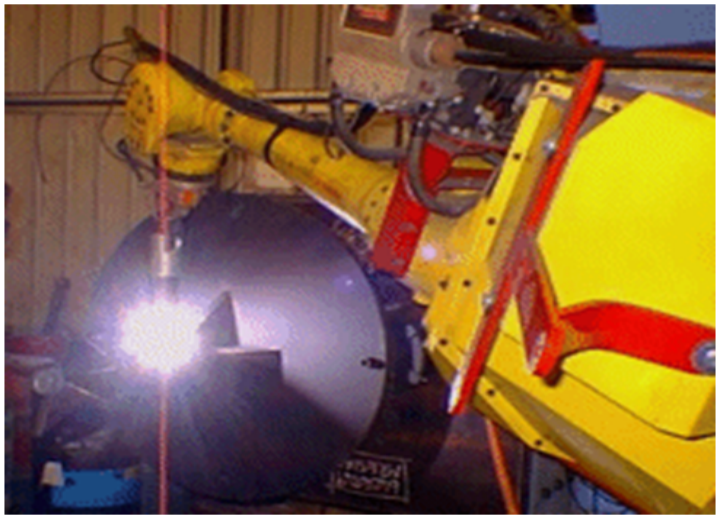

Figure 2.18: Manipulation of robotic PTA cladding (http://bossong.biz)

Geometrical Limitations: A large variety of geometrical shapes can be cladded by PTA process but mainly symmetrical shapes in flat position are more feasible.

Laser cladding Process Laser cladding is conceptually similar to arc welding methods, where the laser energy is used to melt the surface of the substrate and the clad material, which can be in wire, strip or powder form and fuses it to the substrate producing a fusion bond between the clad layer and substrate(Chiu *et al.*, 2005). The important process parameters are laser power, powder mass flow rate, scan rate and a schematic diagram is shown in figure 2.19. When compared to arc welding methods, laser systems offer lower heat distortion, reduced dilution, lower porosity, finer microstructure and better surface uniformity. Both laser and thermal spraying techniques avoid significant heat input into the part and minimize dilution. Guojian Xu et al. (Xu *et al.*, 2006) compared laser cladding

with TIG cladding layer of cobalt based alloy and concluded that laser cladding exhibits small dilution rate, fine microstructure, narrow heat-affected zone (HAZ), narrow alloy elements segregation, high Vickers hardness and excellent wear-resistance.

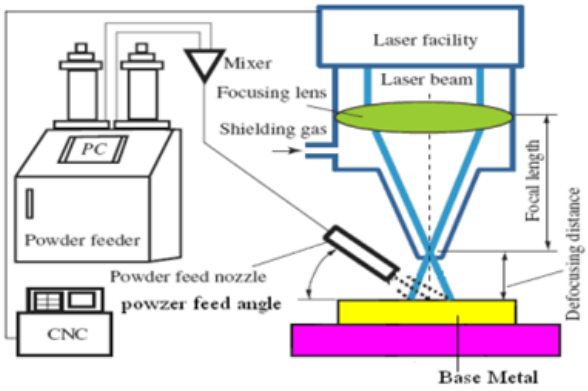

Figure 2.19: Schematic diagram showing the Laser cladding parameters ((Xu *et al.*, 2006)-modified)

Geometrical Limitations: The equipment can make it difficult to integrate into some production settings. Although a large variety of geometrical shapes can be cladded by Laser process yet comparatively symmetrical shapes in flat position are more feasible.

Materials and Microstructural morphology: Co-alloys, Ni-alloys, Al-alloys, titanium, tool steels and many others may be deposited by laser cladding process. Hard surfacing of WC, TiC, SiC and other metallic powders may also be applied. Coatings by laser exhibit a low overlay dilution rate compared to PTA (Deuis *et al.*, 1998). Laser cladding shows typical weld solidification structures, for an example the microstructure of multi-layer deposition of stellite-6 on SS304 plate is shown in figure 2.20 which exhibits a planar, followed by columnar, cellular and dendritic region at the interface with the base metal.

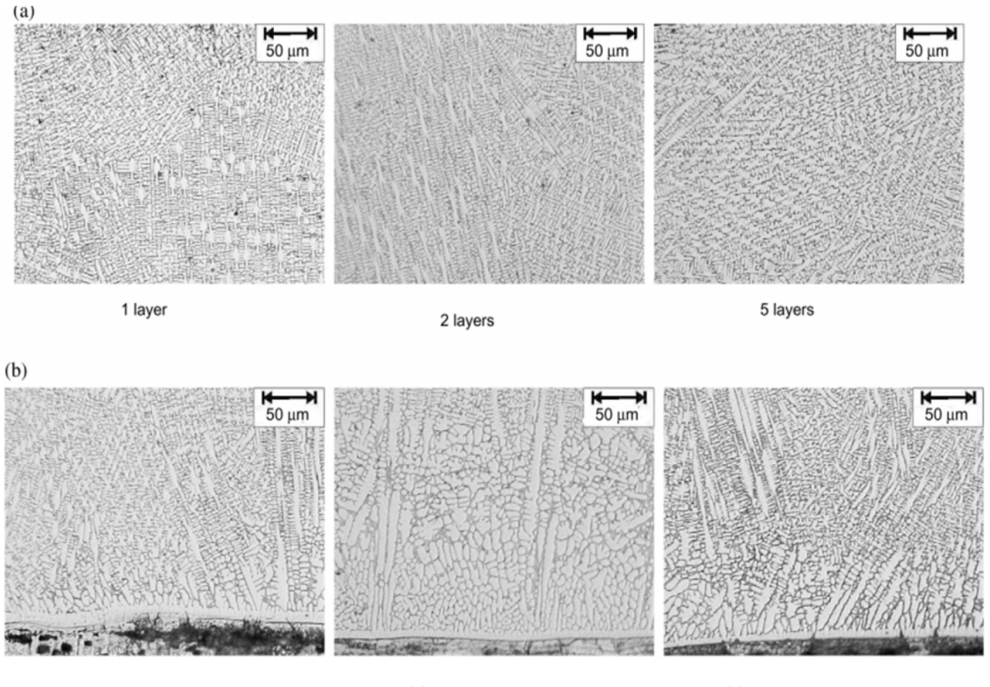

Figure 2.20: Typical solidification structure observed by Stellite-6 laser cladding (a) near the interface with the base metal(SS304) and (b) at the external surface (D'Oliveira *et al.*, 2002)

GMA Cladding Process: In the gas-metal arc welding (GMAW) process an electric arc is established between a consumable electrode, fed continuously to the weld pool. If the weld pool is shielded by an inert gas, it is termed as metal inert gas (MIG) and for active gases such as carbon dioxide or mixtures of inert and active gases the process is called metal-active gas (MAG).

Materials and Microstructural morphology: A large range of similar and dissimilar metals can be deposited by GMA cladding process. Typical microstructure of fusion weld cladding layer of corrosion-resistant SS 347 on high strength low alloy (HSLA) steels with austenitic dendrites of as-cast structure is shown in figure 2.21.

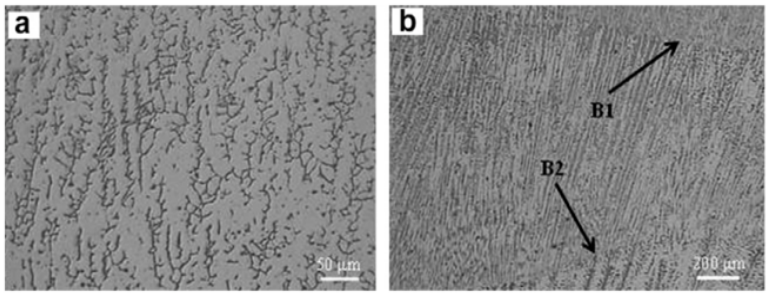

Figure 2.21: Microstructure of the clad layer by GMAW revealing (a) austenite dendrites and (b) inter-layer boundaries B1 and B2 within austenite dendritic structure (Rao *et al.*, 2011)

Metal transfer modes: Dilution rates in GMA cladding process depends upon the type of metal transfer and the welding gun manipulation. An insight to the main GMAW metal transfer modes is described below. In **short-circuiting or dip transfer** mode, the metal melts to form large droplets whose diameter is often greater than the electrode diameter. The arc is so short that the molten globules at the electrode tip 'short-circuit' to the workpiece at rapid and regular intervals and the current during short-circuiting melts off the electrode tip and allows re-establishment of the arc. The surface tension causes a pinching effect which separates the droplet from the electrode. This is ideal for welding on thin gauge materials and out of position working or root runs for butt welds. In **Globular or gravity transfer** the melting occurs in the form of large droplets, which break away when their mass is sufficient to overcome the surface tension and fall freely before coming in contact with the weld pool. **Spray transfer** mode involves the current densities above a certain transition level. In spray transfer the metal is transferred across the arc in free flight droplets in the form of a fine spray and is recommended for thicker materials. Spray transfer gives the greatest dilution while short-circuiting or dip transfer causes the least dilution.

The three metal transfer modes are shown in figure 2.22, where I_{cc} max corresponds to the maximum current for which a short-circuit transfer is possible while the $C\acute{C}$ line indicates the maximum voltage for this type of transfer, the current $I_s min$, corresponds to the minimum current for the axial pulverization or spray mode while the segment $S\acute{S}$ indicates the minimum value of voltage for

this mode of transfer.

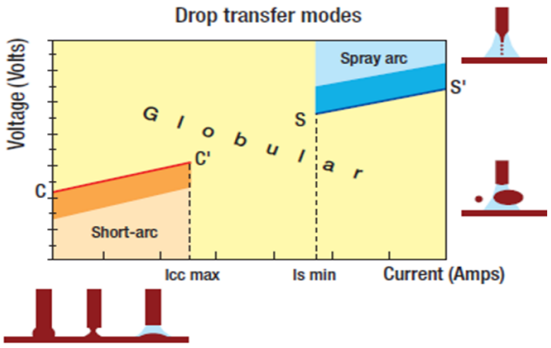

Figure 2.22: Metal transfer modes vs. welding parameter set up in MIG /MAG welding (Leduey *et al.*, May 2007)

Selection of the GMAW as Cladding Process: GMAW process has several advantageous features and is considered a viable long term applications by the industry due to the following advantages:

- High productivity due to ease of automation.
- High deposition rate.
- All position capability.
- High reliability and low cost.
- Ease of out door use with out shielding gas, Flux Core Arc Welding (FCAW).
- Applicable to both ferrous and nonferrous metals.

In the coming text we will discuss in detail all the process parameters involved in the GMA cladding process.

Power supply In GMAW, a constant voltage power supply is used in which a contact tube in the torch energizes the wire, which is fed towards the work piece at a predefined constant speed. Heat generated by the arc, fuses both the filler wire and the work piece. The constant voltage power supply allows the welding current to float by controlling the wire fusion rate and arc length for smooth running of the process as shown in figure 2.23.

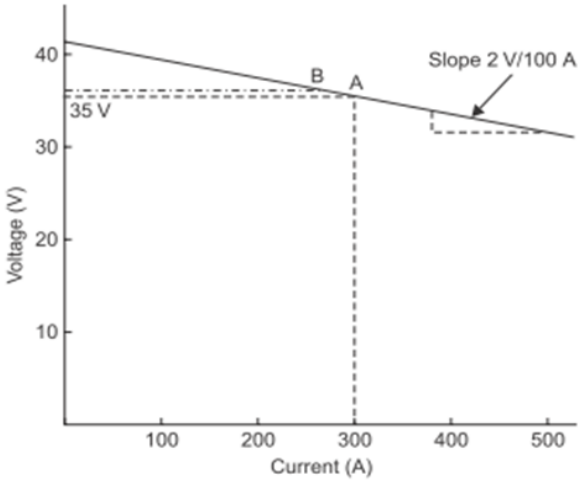

Figure 2.23: Self-regulation of arc voltage (Khan, 2007).

Following are the details of some process variables of the GMA cladding process and shown schematically in figure 2.24:

Geometrical parameters: Geometrical parameters include the orientation and position of the welding torch. Orientation aspect is related to the torch angle relative to the work piece. Position aspect is concerned with the torch height (contact tip to work piece distance) and stick out distance. The offset distance of the torch with respect to the previous bead for necessary overlapping is taken into account for multi-bead cladding process.

Wire Stick-out: Stick-out distance is the length of the unmelted electrode extending beyond the end of the contact tip (see figure 2.25). This is the area

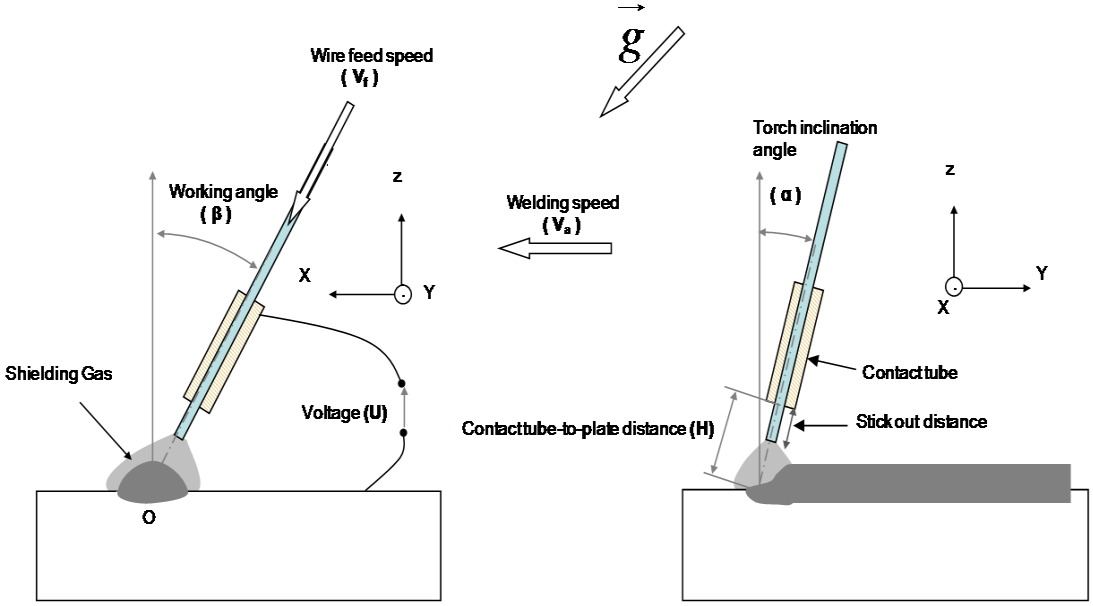

Figure 2.24: Important MIG or MAG cladding process parameters.

where preheating of filler wire occurs. As a rule of thumb a normal wire stick-out distance is 10-15 times the diameter of the filler wire. Excessive stick-out can create a lack of shielding gas effect to the weld zone. For longer electrode extensions, self-shielding electrodes are preferred, while shorter and medium range electrode extensions are used while using additional shielding gases. A long extension may cause too much filler metal to be deposited with low heating by the arc. This may cause spatter and shallow penetration with poor bead shape. It will increase the risk of stubbing especially at the start. The arc length and bead width increases with increase in stick-out. Too small stick-out increases the risk of burn-back and the fusion of the filler wire with the contact tip. The contact tip-to-work distance also has an influence on the current and penetration profile (Weman, 2003).

Contact tip to base metal distance: Contact tip to base metal distance is taken into account to have more accuracy due to variation of stick-out distance during the welding process and the difference in both is shown in figure 2.25.

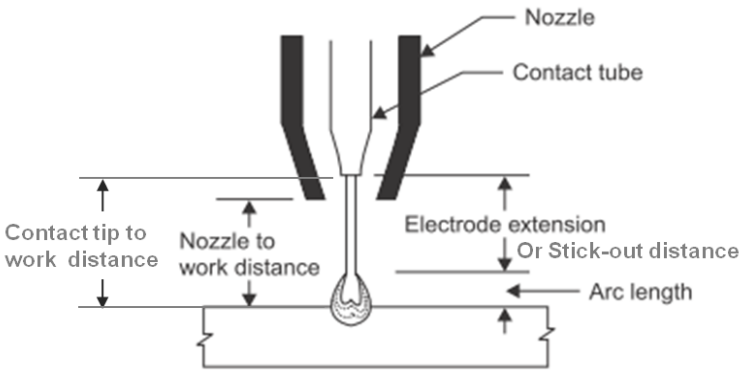

Figure 2.25: Definitions of GMAW terminology (Khan, 2007)

Welding current can be varied by changing the contact tip to work piece distance which consequently affects the penetration.

Torch angles and position: Angles and position of the torch relative to the weld bead (see figure 2.26) are important welding parameters which help in utilizing the natural arc force to push weld metal against vertical surface to provide good bead contour by torch angle manipulation. They influence the risk of lack of fusion and arc forces, acting on the weld-pool metal. An angle of 10 to 20 degrees with the normal is sufficient for a consistent bead with good penetration. Excessive inclination can result in aspiration of air into the shielding gas and cause porous or oxidized welds. For multiple pass welding, gun tilting angle (working angle) may also be taken into account. If the torch is directed away from the finished part of the weld forehand technique, then it is referred as the **push angle** or lead angle. Welding with a push allows to watch the welding pool as it forms with out being blocked by the torch. Due to the direction of forces, heat and shielding gas being focused ahead of the weld towards the surface to be welded, the push angle method offers some distinct welding advantages such as:

1. Broad/flat bead appearance.
2. Shallow penetration.
3. Better gas shielding that helps cleaning the surface to be welded.

4. Slight preheating to the welding surface before welding.

5. Slower bead cooling.

As the direction of forces is forward, any spatter generated will be forced into the atmosphere rather than back into the weld pool, creating more visible spatter.

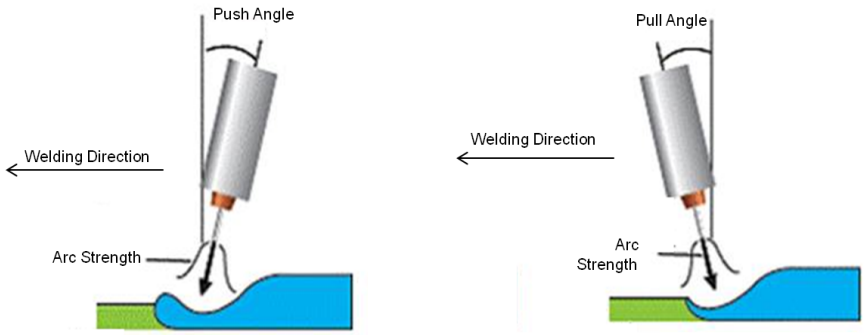

Figure 2.26: Torch angles and welding technique (Brooks, 2008)

The Pull angle: Pulling, dragging or a lag angle, refers if the torch is directed towards the finished part of the weld **Backhand technique**. Since the puddle is behind the weld, it is difficult to see the arc's sudden adjustments. Most of the advantages of using a pull angle are simply opposite of the push angle and include:

1. Deeper penetration.

2. Slightly cooler welds.

3. Narrow bead width.

4. Better spatter control.

When welding with a pull angle, the weld bead tends to hump more and may cause overlap if not properly fused at the weld toes. In some cases, such as downhill welding or welding with galvanized materials, pull angles offer much greater control and are often the only method recommended.

The Venturi Effect: The Venturi effect is a phenomenon that occurs when the welding torch is tilted too much. This can occur with both push and pull angles. Due to this effect air from the atmosphere is sucked in the welding zone. The mixture of shielding gases and active atmosphere gases cause contamination and porosity. "The venture Effect" is common for torch angles greater than 45° as shown in figure 2.27.

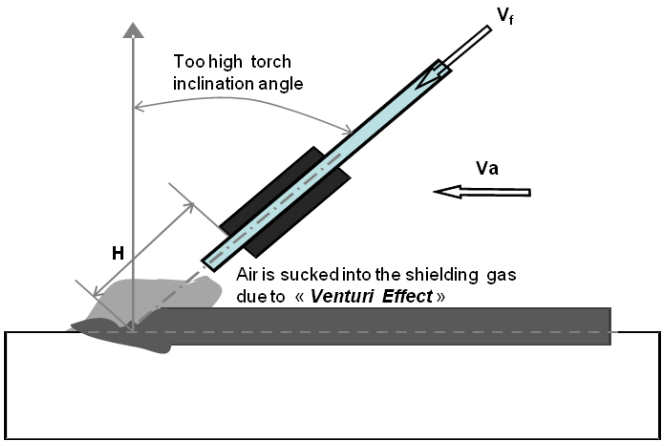

Figure 2.27: Air contamination of the shielding gases by the "Venturi Effect"

Work Angle: The work angle refers to the angle relative to the base materials, tilted in transverse or lateral direction relative to bead length as shown in figure 2.28, also affect bead appearance and is more significant for multibead deposits.

Environmental parameters

Shielding Gas: The shielding gas protects the weld pool and molten droplets. Density of the shielding gas has influence on the efficiency of the protection of the arc and the weld pool against the ambient atmosphere. Argon and carbon dioxide are gases having higher density and form an efficient gas shielding around the arc. Carbon dioxide ($C0_2$) is suitable for arc shielding when welding low carbon and

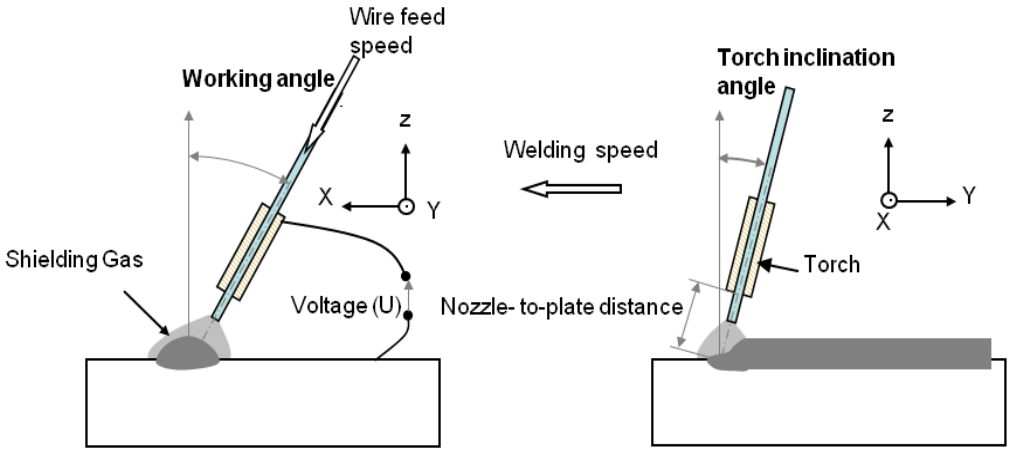

Figure 2.28: GMAW torch angles

low-alloy steel. Pure inert gas (pure argon or argon helium mixtures) shielding is used for welding alloys of aluminium, magnesium, copper, titanium, stainless steel, nickel alloys and highly alloyed steel. Mixtures of argon with carbon dioxide are most popular for the welding of mild and low alloyed steels. For spray and pulsed arc welding, a low content of $C0_2$ can be an advantage. Pure $C0_2$ is an alternative for short arc welding that gives good penetration and safety against lack of fusion but increases the amount of spatter. The physical and chemical properties of shielding gases, such as thermal conductivity, ionization energy and chemical activity affect the arc behavior and the weld bead profiles.

The diagram 2.29 shows that thermal conductivity of hydrogen in the temperature range between 3000 K and 4500 K (welding arc temperature range), is almost ten times higher than that of argon. The argon-hydrogen mixture is used in practice mostly as a plasma gas in plasma welding and plasma cutting. Helium increases the heat input, which will compensate for the large heat conduction in thick walled aluminium or copper. The gas flow must be adapted to the arc. At low current it can be enough with 10 liters per minute while at higher welding data up to 22 liters per minute may be required. Hydrogen addition to argon

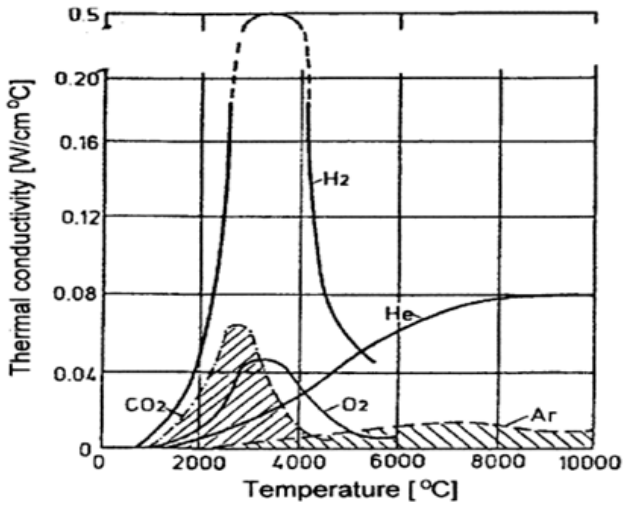

Figure 2.29: Thermal conductivity of gases as a function of temperature (Tusek & Suban, 2000)

increases voltage drop in the arc, and consequently arc power. Due to high thermal conductivity of hydrogen, the arc gets narrower and energy concentration in it increases, which causes a deeper penetration. Hydrogen as a reducing gas hinders oxide formation on the surface of the weld and weld appearance is nicer. Hydrogen addition to a shielding atmosphere may produce gas bubbles and cracks (Tusek & Suban, 2000). The quality, efficiency and overall operating acceptance of the GMAW process are strongly dependent on the shielding gas composition. NOXALIC 12 is a mixture of Ar, $C0_2$ and H_2. It assures good penetration, very good weld appearance (good wetting) and greatly reduced emission of fumes (up to 25% less).

Preheating and postheating: **Preheating** reduces the post weld cooling speed which minimizes the cold cracking in some materials by reducing the magnitude of shrinkage stresses. At lower temperature gradients, the thermal conduction is reduced which lowers the cooling rate resulting a favorable metallurgical structure and restricts the martensite formation in HAZ. When two dissimilar metals of significantly different thermal conductivities are welded together, the welding heat source must be directed at the metal having the higher

thermal conductivity to obtain the proper heat balance. Preheating the base metal of higher thermal conductivity reduces the cooling rate of the weld metal and the HAZ. The net effect of preheating is to reduce the heat needed to melt that base metal (AWS, 1982). **Post weld heat** treatment is done below the critical range holding at this temperature for a predetermined period of time to undo the effect of uneven cooling.

Energy parameters

Heat Input: Heat input can affect chemical compositions and microstructure of the weld. Heat input is related directly to three factors:

- Welding current
- Arc voltage
- Travel speed

The heat input H (J/mm) that enters bead with a welding speed (mm/s) for arc welding process is given by:

$$H = \frac{UI}{V_a} \tag{2.1}$$

If we take in account the heat transfer efficiency (see figure 2.30) from filler metal tip to deposited bead f_1 and melting efficiency f_2, then the heat actually used for melting is:

$$H = f_1 \frac{f_2 UI}{V_a} \tag{2.2}$$

The bead cross-section and heat energy can be related by$A = \frac{H}{Q}$, where Q=heat required for melting

$$A = f_1 \frac{f_2 UI}{V_a Q} \tag{2.3}$$

Heat Source	Heat transfer efficiency from filler metal tip to bead
SMAW/GMA	0.8-0.66
SAW	0.9-0.99
GTAW	0.21-0.48

Figure 2.30: Heat transfer efficiency from filler metal tip to bead for different arc welding processes (Khan, 2007)

Welding Current: The current significantly affects the deposition rate and finished clad characteristics. An increase in current will increase penetration, bead width, reinforcement and dilution rate. Excessive current can cause a lack of slag coverage, excessive spatter and increase cracking susceptibility. With increase in welding current the weight of wire fused per time increases, the arc becomes stiffer and hotter which penetrates deeply by melting more metal. With all other variables held constant, an increase in welding current (electrode feed speed) will result in the following:

- An increase in the depth and width of the weld penetration
- An increase in the deposition rate
- An increase in the size of the weld bead

Arc Voltage: Increased voltage increases the arc length and gives a wider weld bead. High voltage levels increase the possibility of contamination from the atmosphere. Undercut and weld spatter also increase with higher voltage. Too low voltage will increase the risk for stubbing and bad start performance. The total voltage drop is sum of drop across cable, contact tube to wire, in the wire extension and in arc. Constant voltage welding machine used for gas metal arc welding provides for self-adjustment of arc length by automatic increase or decrease of burn off rate of filler wire. At a given current, arc voltage depends upon nature and diameter of wire, shielding gas, arc length and stick-out distance.

Movement related parameters

Travel speed: Weld travel speed has a major effect on heat input, cooling rate, penetration and dilution. At a given current level, faster travel speeds reduce heat input. The amount of weld metal deposited in a given length of bead is increased with slower travel speed. At low welding speed, the arc is almost vertical and weld pool cushions the arc and prevents deeper penetration although the evolution of the bead penetration with the welding speed is a complex phenomenon. With all variable keeping constant, a certain intermediate travel speed gives the maximum penetration.

Wire feeding speed: The actual amperage in GMAW is controlled by the wire feed speed.The faster the speed the higher the amperage draw. The current depends on the rate at which the wire is fed into the arc. Good arc stability is achieved under good metal transfer conditions, especially when the wire feed rate is exactly matched by the wire melting rate. Low wire feed rate causes melt back, and a high feed rate can cause the arc to extinguish through short-circuiting. While adjusting the wire feed speed, the feed roll pressure is an important factor to be considered. Too high pressure will deform the wire and cause poor current pick-up, too little pressure will misfeed the wire.

GMAW wire melting characteristics The GMAW process has two basic requirements to be filled (Modenesi, 1990):

1. The wire feed speed must be balanced with the burn-off rate / wire melting speed, to maintain a constant arc length

2. There must be a stable transfer of metal from the electrode wire to the weld pool

Melting rate during the process, is controlled by factors like electrode diameter, electrode extension (Arc length), current magnitude and shielding gas etc. Electrode melting rate for reverse polarity (electrode positive) can be expressed as in

equation 2.4 (Khan, 2007):

$$\text{Melting Rate} \quad = \quad aI + bLI^2 \tag{2.4}$$

where, a = Constant of proportionality for heating, depending upon the composition of electrode, b = Constant of proportionality for electrical resistance heating and includes the electrode resistivity, L = Electode Stick out distance and I = Welding Current. The first term of the equation becomes more significant at low currents and short stick out distances. The first term may be important for Aluminium due its low resistivity. The significance of second term of the equation increases at reduced electrode diameter and increased stick out (resistivity) and current.

In GMAW generators, the intensity is related to the wire feed speed through the fusion curve. The fusion curve for a stainless steel wire of different diameters under a shielding gas Noxalic 12, (96% Ar, 3%CO_2 and 1%H_2) and a stickout distance from 10 to 20mm is shown the Figure 2.31.

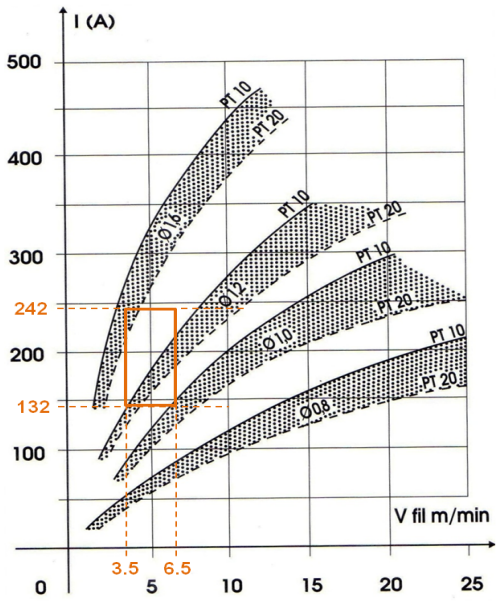

Figure 2.31: Typical fusion curve for the stainless steel ER 308 LSi and 316 LSi using NOXALIC 12 as shielding gas (SAF manual, 1996)

Parameters related to single layer cladding process In case of multi-beads deposition for a complete cladding layer, the potential voids between the successive weld beads, reduce the bead adhesion, strength and endurance of the part in service. These voids between the successive beads largely depend upon the bead wetting angle and is most probable when the bead wetting angle is obtuse. The wettability and bonding force of liquid and solid phase is improved with the lower wetting angle (Liu & Qi, 2009). The wetting angle also affects significantly on the fatigue strength and higher wetting angle can likely increase the fatigue cracks probability due to notching effect and results in larger stress concentration factor and local stresses (Kannan & Yoganandh, 2010; Maurice *et al.*, 1996).

Bead Overlapping for layer cladding The single layer cladding is done by multi-pass deposition of beads at a certain offset or bead center to center distance which adds to the complexity of cladding process due to partial remelting of the existing bead while depositing the next bead. The quantity of material deposited varies from the center of the bead to the edges. To achieve a uniform surface, two beads are deposited close enough so that the deficit of material along the edges gets compensated by an overlap between the beads. The melting of the beads during the deposition process causes extra smoothness along the surfaces. Figure 2.32 shows the cross section of the overlap of two beads with bead width L_{180}, separated by a suitable offset distance L_ϕ (bead center to center distance)(Rajeev & Radovan, 2004).

The macrographic study shows that the cross-sectional profile of the cladded bead shows a sinusoidal behavior. The resultant bead profile (P) of two adjacent beads for the smooth deposition is given by the following formula 2.5:

$$P = \sin\theta + \sin(\theta + \phi) \tag{2.5}$$

where (ϕ) is the equivalent phase difference maintained between two adjacent beads. The (ϕ) can be determined using the formula.

$$\phi = \frac{L_\phi}{L_{180}} \times 180 \tag{2.6}$$

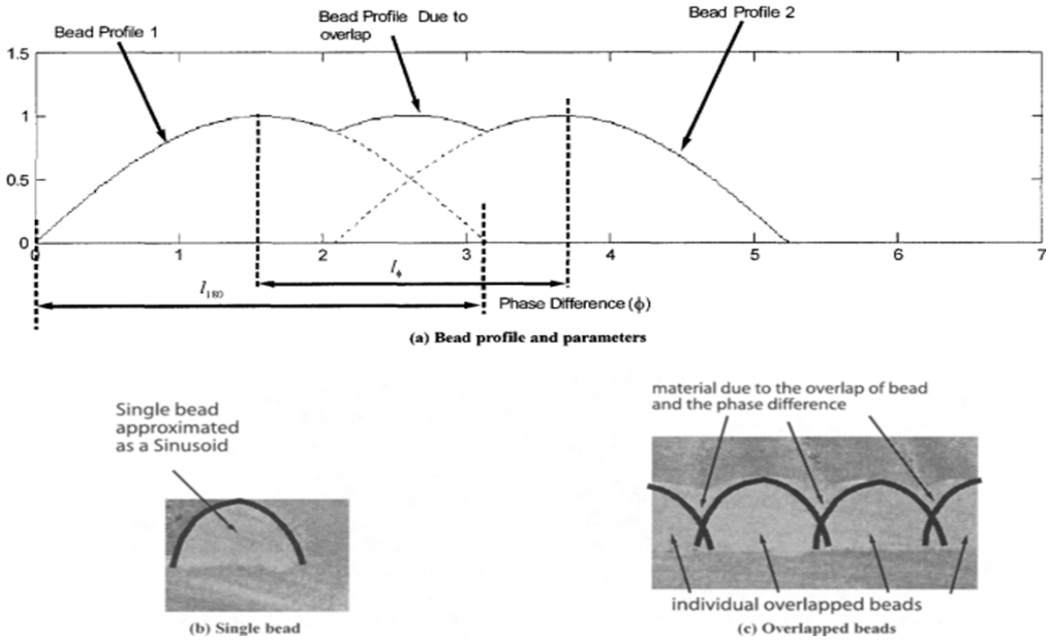

Figure 2.32: Approximation of Beads as Sinusoidal Curves and Overlap Profile of Beads(Rajeev & Radovan, 2004)

The experimental results have shown that an equivalent phase difference of 120 degrees or about 34% bead overlapping of the total bead width (Cao *et al.*, 2011) , provides the best surface quality. X. Cao et al. proposed that if the weld bead is assumed to have an approximately semicircular section, surface defects for multi layer weld cladding can appear if (Cao *et al.*, 2008):

$$p \leqslant \frac{L+D}{2} \tag{2.7}$$

where, L=Bead width, D=diameter of the filler wire, and p=central spacing between the first and second bead. In this case, the critical value for central spacing between the first and second bead is an important factor. At higher bead spacing the two clad beads may become disconnected or separate or two single beads are formed. The smaller bead spacing forms more flat surface while larger spacing may create a groove between the two adjacent beads which may have a positive impact on the shape of the weld beads for the second layer. For multi-layered cladding, larger bead spacing is better in the lower clad layer.

Residual stresses at the surface build-up as multi-layers are deposited, due to the solidification and results in non-uniform hardness across the coating and the structures show alternate regions of fine and coarse dendrites (D'Oliveira *et al.*, 2002). The mechanical strength of the clad metal is influenced by the composition of the metal and the clad bead shape (Harris & Priebe, 1993b). The small variations in bead dimensions is due to the inherent arc instabilities in GMAW process (Doumanidis & Kwak, 2002). Hard alloys are not recommended for multi-layer cladding, as their poor coefficients of thermal conductivity can result in the clad cracking or separating from the underlying material. To avoid this a foundation layer (buttering) of less hard alloys is often applied, with the fully hard surface layer applied on top of it.

2.3 Weld Cladding Materials

The weld cladding improve the properties like corrosion, erosion or wear-resistance and many others at the surface and is used due to economic and technical reasons.

Economic point of view : From an economic point of view, it makes a sense to use relatively expensive wear and corrosion-resistant alloys only on the specific area where these properties are required.

Technical point of view : From a technical point of view, as wear-resistant alloys, normally brittle in nature, are unsuitable for use in bulk. For the wear improvement, different highly alloyed steels may be used to resist abrasion under non-corrosive conditions and at moderate temperatures. For wear under corrosive conditions and at high temperatures, several cobalt and nickel-based compositions and a few special stainless steels are available. A weld deposit of stainless steel on the surface of a low alloy steel is done to improve corrosion resistance.

Nickel, cobalt, iron-based and refractory alloys are the usual choices for cladding and hard facing processes and a brief description of these super alloys is given below.

2.3.1 Cobalt-based alloys

These alloys have high resistance to corrosion and oxidation, possess a suitable combination of ductility and wear resistance at high temperatures. Due to low coefficients of friction, that are suitable for applications involving metal-to-metal wear. The cobalt-base alloys retain much of their original hardness at red heat (800°C) (Pradeep *et al.*, 2010). These are normally alloyed with nickel in order to stabilize the face-centered cubic (FCC) matrix. Stellite group of cobalt alloys have low wear rate at high temperatures in the range of 850 to 1000 °C. These are readily joined and cladded by GMAW or GTAW techniques. Appropriate preheat techniques are needed in GMAW and GTAW to eliminate tendencies for hot cracking.

2.3.2 Nickel-based alloys

Nickel-based materials can withstand temperatures up to 1100°C and have high resistance to creep and oxidation. Addition of Al and Ti evoke precipitation hardening due to coherent intermetallic precipitates in the FCC, Ni matrix. Iron, chromium, boron and carbon are main constituents in nickel based alloys. Iron content is largely incidental, allowing the use of ferrocompounds during manufacture. Chromium increases the alloy's resistance to hot corrosion. Boron is added to increase the high-temperature strength and ductility as well as to improve the creep resistance. Together with nickel, the other three elements determine the level and type of hard phase within the structure upon solidification, with boron being the primary hard-phase forming element. Because of the boride and carbide dispersions within their microstructure of the nickel-base (boride-type alloys, ERNiCr-C, ERNiCr-B) exhibit excellent resistance to abrasion (ASM Handbook, 2002).

2.3.3 Refractory metal alloys

The refractory metals and their alloys have high melting points(well above the melting points of the common alloying bases, iron, cobalt, and nickel), good elevated-temperature strength and good resistance to softening. The refractory

metals include molybdenum, tungsten, niobium, tantalum and rhenium. With the exception of rhenium, which has a hexagonal close-packed (hcp) crystal structure, the refractory metals have body-centered cubic (bcc) crystal structures. The refractory metals can be cladded by electron beam welding, GTAW or resistance welding.

2.3.4 Iron-Based alloys

Iron-base alloys offer low cost and a broad range of desirable properties including the excellent wear resistance, cavitation erosion resistance and corrosion resistance. It is being substituted for an expensive cobalt-based stellite alloy, which has been used for the hard facing of a nuclear power plant valve, eliminating the formation of radioactive isotopes of cobalt (Kim *et al.*, 2005). Due to the great number of alloys involved, iron-base hard facing alloys are classified by their suitability for different types of wear and their general micro structures rather than by chemical composition (ASM Handbook, 2002). These include, Pearlitic Steels, Austenitic (manganese) steels, Martensitic steels, High-alloy irons and Austenitic stainless steels.

2.3.4.1 Stainless steels types

Stainless steels according to their matrix structure, are classified as austenitic, ferritic, martensitic, precipitation hardened and duplex stainless steels. ***Ferritic stainless steels*** have body-centered cubic(bcc) atomic structures and possess mechanical properties close to carbon steel, but less ductile. They are magnetic, can be hardened moderately by cold working but not by heat treatment. ***Martensite stainless steels*** are hardenable because of the phase transformation from body-centered cubic(fcc) to body-centered tetragonal and are ferromagnetic. ***Austenitic stainless steels*** are the most widely used family of stainless alloys in process industry, have fcc structure, are nonmagnetic and non-hardenable by heat treatment, but can be strain hardened by cold work without embrittlement which also induces a small amount of ferromagnetism. Fully austenitic structures are sensitive to hot cracking during solidification. In ***Precipitation Hardenable Stainless Steels*** a thermal treatment is utilized to

intentionally precipitate phases causing a strengthening of the alloy by the addition of one or more element like titanium, niobium, molybdenum, copper or aluminum to generates the precipitating phase. There are three types of precipitation hardenable (PH) stainless steels: Martensitic, Austenitic and Semi-austenitic. An elevated temperature exposure precipitates the desired phases to cause an increase in mechanical properties. ***The duplex stainless steels*** have roughly 50% austenite and 50% ferrite and contain molybdenum to improve the corrosion resistance and to reduces the susceptibility to chloride pitting, crevice corrosion, and stress corrosion cracking. The general corrosion resistance of the duplex stainless steels is slightly greater than that of 316 stainless steels in most media but these offer higher strengths than austenitic steels. Welding requires more care than with the austenitic alloys due to a greater tendency to compositional segregation and sensitivity to weld heat input (Schweitzer, 2003).

2.3.4.2 Welding features of stainless steel

Important weld related features of stainless steel are as under (Khan, 2007):

- They have low thermal conductivity (about half of the mild steel).
- Thermal expansion about 50% percent more than mild steel, requiring less heat input and less current for melting due to the chances of warping and buckling .
- They require 20-30% less heat input than carbon steels due to low thermal conductivity and high electrical resistance which cause overheating in the electrodes.
- The austenitic stainless steels do not air harden and therefore do not require post weld heat treatment but may be stress relieved or postweld heat treated to reduce residual stresses to improve their resistance to stress corrosion cracking.
- These stainless steels have a FCC structure from far below zero up to near melting temperatures as a result of the alloy additions of nickel and manganese.

Stainless Steel cladding on carbon steels: The structure of stainless steel weld deposits on carbon steel or low-alloy steel may vary from full martensitic to full austenitic or mixture of martensite, austenite and ferrite. This variation in structure depends on local compositional gradients and diffusion effects (John & Damian, 2005). Weld structures properties are dependent on the microstructure which are determined by the welding process and parameters used. During arc welding processes of a moving heat source, the weld bead solidifies at a cooling rate of order ranging from 1 to 10^2 K/s. The cooling rates in laser and electron-beam welding processes may attain the values as high as 10^6 K/s. This wide range of cooling rates during the solidification of steel welds can cause a phase different from that is expected under equilibrium conditions as also found in the literature. Babu et al. (Babu *et al.*, 2002) studied the phase transitions and microstructure evolution of low alloy steel under rapid weld heating and cooling. During rapid cooling and solidification, formation of non-equilibrium austenite and under normal weld cooling the formation of equilibrium δ-ferrite is observed. According to ASM handbook (Harris & Priebe, 1993b), fully austenitic cladding is more susceptible to hot cracking, especially during solidification or reheating and the tendency for hot cracking is greatly reduced by the presence of a small amount of δ-ferrite in the structure. So a small amount of ferrite with stable austenite is desirable to avoid solidification cracking and to increase ductility.
The amount of ferrite required to eliminate hot cracking varies from material to material, but it is generally admitted that a 4 or 5 ferrite number (FN) in the as-clad structure is sufficient for most austenitic stainless steel cladding alloys. Excessive ferrite in the deposited layer can cause poor ductility, toughness, and corrosion resistance while insufficient ferrite can result in poor mechanical properties. FN increases with a decrease in heat input. The welding current, welding speed and voltage directly contribute to the heat input. T. Kannan et al. (Kannan & Murugan, 2006) carried out a study relating the effect of some primary welding parameters, like welding current, voltage and welding speed and secondary process parameters like contact tip-to-workpiece distance and welding gun angle on the FN. During austenitic stainless steel cladding on carbon steel, the amount of ferrite in the deposit is a function of chemical composition of the filler and base metals, welding process and procedure, nature of shielding

gas, and heat input during cladding. While cladding stainless steel on carbon steel, the higher carbon content of base metal will migrate from HAZ to fusion zone during welding or PWHT which can result a narrow martensitic region at the fusion boundary with high micro hardness. The higher Cr content of the depositing metal than base metal may increase the carbon migration tendency during PWHT. The base metal higher carbon content and its affinity for higher Cr, causes carbon migration from carbon steels. This migration may cause local microstructural changes in HAZ and transition zone due to carbon depletion and results in soft ferrite zone which lead to premature creep failure (Deyev & Deyev, 2006; Klueh & King, 1982).

Weld-metal microstructure prediction diagrams: Dissimilar metal welds between carbon steel and stainless steel can exhibit a number of cracking mechanisms like solidification cracking, clad disbonding, reheat or PWHT cracking and creep failure in HAZ (John & Damian, 2005). For stainless steel cladding, it is vital to understand how the dilution of the filler metal with the base metal affects the composition and metallurgical balance, such as the ferrite level to minimize hot cracking, absence of martensite at the interface for bond integrity and a low carbon level to ensure corrosion resistance etc. The prediction of the microstructure and properties (such as hot cracking and corrosion resistance) for the austenitic stainless steels has been the topic of many studies (Olson, 1985). During the last two decades, four microstructure prediction diagrams have found the widest application. These include the **Schaeffler diagram**, the **DeLong diagram** and the **Welding Research Council (WRC) diagrams** (WRC-1988 and WRC-1992).

The **Schaeffler diagram** provides approximate microstructure for dissimilar metal welds. The structure obtained in austenitic chromium-nickel steel weld metal varies with composition and cooling rate. Chromium, molybdenum, silicon, niobium and aluminium are the common ferrite-forming elements, while nickel, carbon, nitrogen and manganese favor the formation of austenite. The combined effects of ferrite and austenite formers on the constitution of weld metal are summarized in Schaeffler diagram. The effect of austenite formers and ferrite formers is accounted for by numerical factors in the chromium equivalent

and nickel equivalent. These are the Schaeffler equivalents and are commonly used for predicting room-temperature ferrite content. The Figure 2.33 shows the positioning of stainless steel 316 L cladding on S 235 having 25% dilution rate.

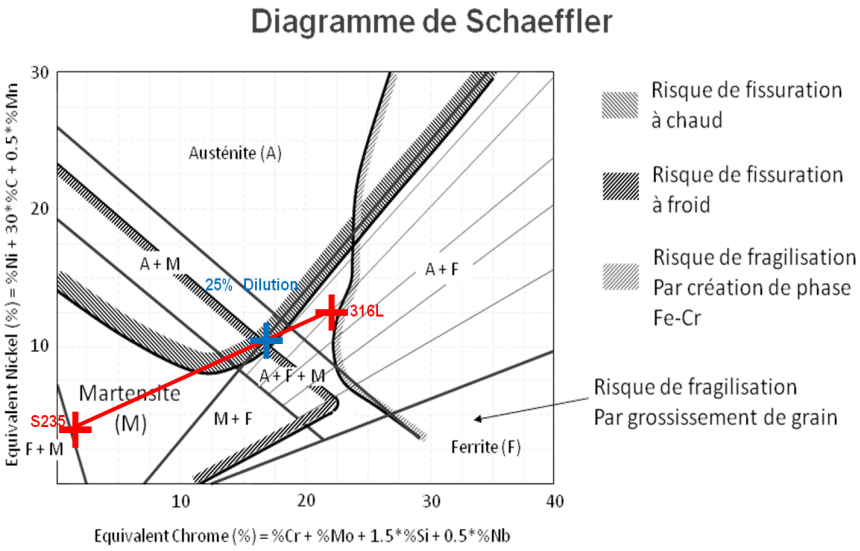

Figure 2.33: Positioning of cladding elements on Schaeffler diagram

Chromium (ferrite formers) and nickel (austenite formers) equivalents may also be calculated from the **DeLong diagram** as shown in Figure 2.34.

Factors affecting the cladding integrity of dissimilar metals: The cladding processes usually involve a combination of materials with different chemical, mechanical and physical properties. These materials must be selected keeping in mind that they should be capable to be mixed during welding without causing cracks and the resulting weldment must perform well in the intended service. The main factors to be considered for dissimilar metal cladding are discussed below.

Thermal Conductivity: When two dissimilar metals of significantly different thermal conductivities are cladded together, the heat source must be directed at the metal having the higher thermal conductivity for the sake of proper heat balance (Harris & Priebe, 1993b). Preheating the base metal of higher thermal conductivity also reduces the cooling rate and the HAZ of the substrate. The net

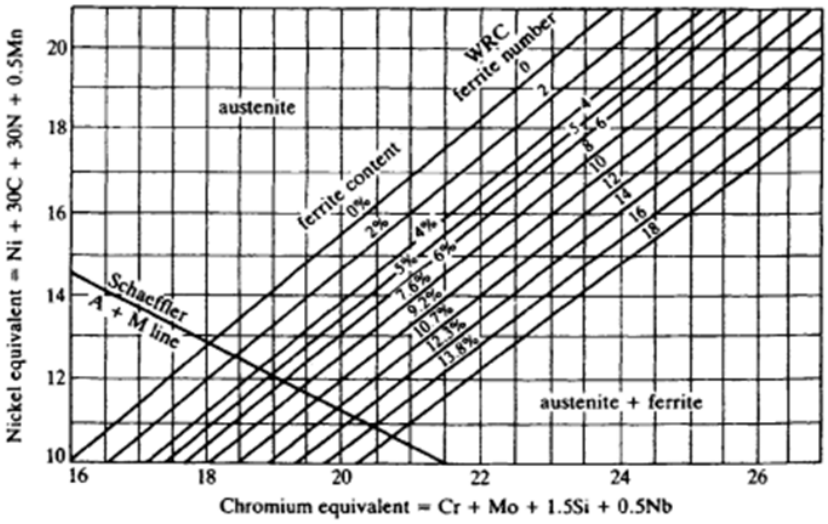

Figure 2.34: DeLong diagram showing Chromium and nickel equivalents

effect of preheating is to reduce the heat needed to melt that base metal. The thermal conductivity of typical austenitic stainless steels is lower than ferritic and martensitic stainless steel. Therefore, the molten weld pool of the austenitic stainless steels tends to be more viscous or "sluggish" than ferritic and martensitic grades.

Coefficient of Thermal expansion: Large differences in thermal expansion coefficients will induce tensile stress in one metal and compressive stress in the other during cooling. The metal subjected to tensile stress may hot crack during the cladding process or it may cold crack in while in service unless the stresses are relieved thermally or mechanically. This factor is particularly important for high temperature or cyclic heating service mode (AWS, 1982).

Summary of clad quality parameters for different cladding techniques: Clad quality parameters by different cladding techniques are summarized in the Table 2.5 (Deuis *et al.*, 1998; Gabriel, 2004; Gebert & Bouaifi, 2006; Illiberi *et al.*, 2011; Springer, 1992; Vill, 1962).

Cladding process	Coating Material (Consumable)	Coating Thickness	HAZ	Repeata-bility	Controll-ability	Cost	Dilution (%)	Deposition rate	Important Process parameters
Laser	Metals, Ceramics (powder efficiency 60%-70%)	50 µm to 3 mm	Low	Moderate to high	Moderate to high	High	1-5	0.25-1.8 Kg/h	Feed rate, Laser beam spot size, Carrier and shielding gas nature
TIG	Metals (Wire)	1 to 5 mm	High	Moderate	Low to Moderate	Low	10-20	2-2.5 Kg/h	Current , voltage, welding speed, Shielding gas and its flow rate, Filler wire angle and feed rate, Torch angle
MIG/ MAG	Metals (Wire)	3 to 8 mm	High	Moderate	Moderate	Moderate	10-40	3.-8 Kg/h	Current, Voltage, Welding speed, Shielding gas and its flow rate, wire feed speed, Torch angle, Nozzle to work piece distance
PTA	Metals, Ceramics (powder efficiency 80%-90%)	0.8 to 6 mm	High	Moderate	Moderate	Moderate to high	5-20	0.5-15 Kg/h	Current, Torch stand off distance, Flow rates of powder and process gases
Submerged welding	Metals (Wire)	5 to 8 mm	Very high	Moderate	Moderate	Moderate	13-40	10-40 Kg/h	Current, Welding speed, Voltage,
Manual Welding	Metals (Wire)	2 to 4 mm	Very high	low	low	low	15-30	1 Kg/h	Current, Voltage, Electrode position
Beam Welding	Metals	0.1 to 2 mm	Low	Moderate	Moderate	High	1-5 LOW	1-2 Kg/h	Beam energy and power, Accelerating voltage,Focus current , Welding speed, Beam deflection,
Friction welding	Metals	4 to 5 mm	High	Moderate	Moderate	Moderate	10-15	18 Kg/h	Relative speed, Applied pressure, Duration of the force and surface temperature, rotational speed of the consumable rod,
Brazing	Metals	≈ 50µm to 2mm	high	Moderate	Moderate	Moderate	10-15	-	Brazing Temperature ,
Thermal spray	Metals, Ceramics (powder efficiency 40%-50%)	≈ 50 µm to several mm	Low	Moderate	Moderate	Moderate	NIL	0.5-3 Kg/h	Thermal and kinetic energy of spray particles, gas velocity and temperature. Feed rate
CVD	Metals, Ceramics	≈ 0.05 µm to 20 µm	Very low	High	Moderate to high	High	NIL	8400 A°/ min	Temperature, Pressure
PVD	Metals, Ceramics	≈ 0.05 µm to 10 µm	Very low	High	Moderate to high	High	NIL	25-250000 A°/ min	Particle energies and trajectories, Temperature, base pressure, pumping speed, substrate and surface cleanliness

Table 2.5: Summary of the characteristics of main cladding techniques

2.4 Hot forging process

Forging is a group of fabrication processes which use compressive forces to carry out plastic deformation of the work-pieces of wide range of sizes and shapes from a variety of metals. Forging process, carried out at room temperature is referred as cold working and at elevated temperatures, are called warm and hot forging, depending on the temperature. Hot forging is used for enlarging and reshaping of a given product to form a required shape. The rearrangement of the metal during hot forging does not affect so much the hardness and strength of the steel and it puts the strength where it is required most. Forging improves the impact resistance, fatigue resistance, ductility, creep-rupture life and other mechanical properties due to following reasons (ASM Handbook, 1993; Schweitzer, 2003):

- Breaks up segregation, heals porosity, and aids homogenization to form solid, nonporous and uniform metallurgical structure.
- Produces a fibrous grain structure that enhances mechanical properties parallel to the grain flow.
- Reduces as-cast grain size through grain refinement and flow.

2.4.1 Forgeability Tests

The forgeability of a metal is its capability to undergo deformation by forging without cracking. So a material that can be shaped with low forces without cracking is said to have good forgeability. General forgeability of different metals and their alloys is classified in the Figure (2.35 a), which are normally applicable to open die forging. But for closed die forging, the overall forgeability depends upon combination of inherent forgeability and flow stress/forging pressure as illustrated in the Figure (2.35 b).

A number of tests, to establish the forgeability of a material are given below, but none of them is universally accepted and measure only the specific behavior of the material under test.

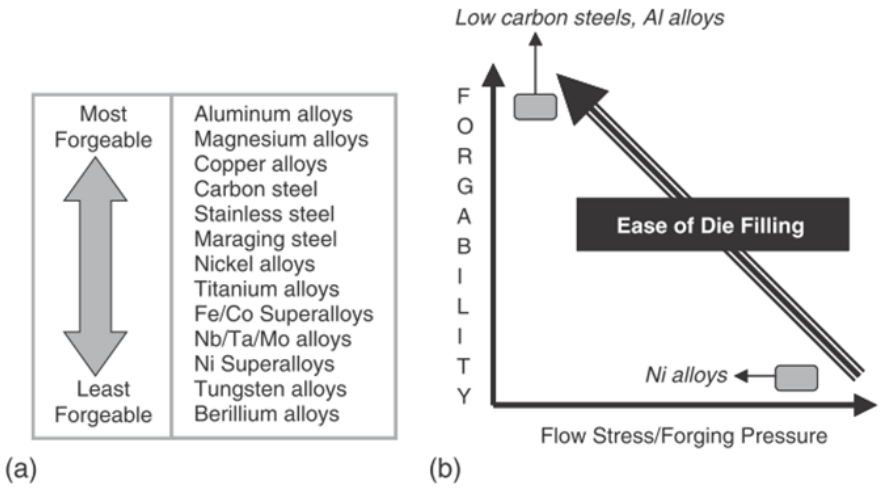

Figure 2.35: (a) Relative forgeability for different metals and alloys – applicable to open die forging. (b) Ease of die filling as a function of relative forgeability and flow stress/forging pressure – applicable to closed die forging. (Verlinden *et al.*, 2007)

The upset test, in which a cylinder is compressed between flat dies up to fracture and the surface strains at the equator of the cylinder are measured. This test allows to determine the flow stress data (true stress/true strain relationships) of metals at various temperatures and strain rates. Figure (2.36) shows the deformation of a cylindrical ring under low and high friction conditions.

Due to constant volume, any decrease in height results an increase in the di-

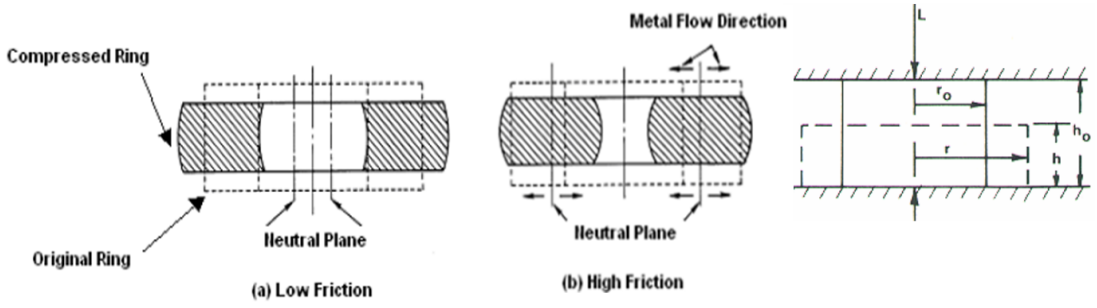

Figure 2.36: (a) Low friction deformation in upsetting for a cylindrical ring compressed between flat frictionless dies. (b) Deformation in upsetting with high friction at the die work piece interfaces.

ameter of the cylinder. A commonly encountered problem in the upsetting tests is "barrelling" (see Figure 2.36 (b)) which occurs in upsetting of hot work pieces between cool dies due to frictional forces at the die-work piece interfaces opposing the outward flow of the material at the interfaces. This test is effective to characterize flow localizations through die chilling. This test is often used to simulate forging deformation.

The Plane strain compression, in which the aim is to compress along one direction and elongate by the same quantity along a perpendicular direction so that by volume conservation the deformation along the third axis is zero.This approximately simulates rolling deformation. This test is performed by pressing a rectangular die into a strip of sheet or slab termed as strip PSC (plane strain compression) while, the test performed by compressing a near-cube sample in a channel die is termed as channel-die compression as shown in figure 2.37 (a) and (b)respectively.

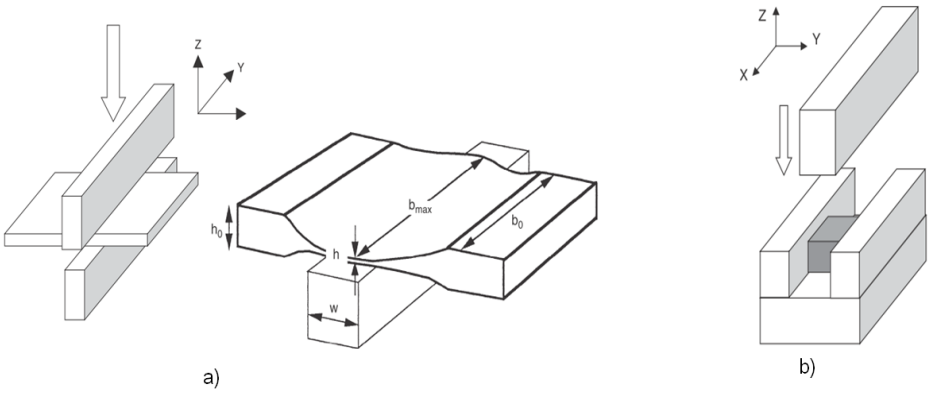

Figure 2.37: (a) Schematic strip plane strain compression (PSC) arrangement and as deformed strip PSC sample, (b) Schematic channel-die plane strain compression set-up (Verlinden *et al.*, 2007)

The Hot-twist testing is a common means of measuring the forgeability in which a heated bar specimens is twisted up to fracture at different temperatures

to cover the possible hot working temperature range of the material under test. The number of twists to fracture and the torque required to maintain twisting at a constant rate are noted by an initially vertical line winds round the sample. The temperature at which the number of twists is the highest, is assumed to be the optimal hot working temperature of the test material. By applying this test we can study the high strains and strain rates, achieved in the near-surface zones of the sample.

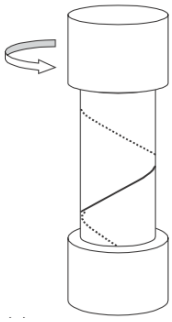

Figure 2.38: Schematic of torsion test (Verlinden *et al.*, 2007)

The wedge-forging test, in which a wedge-shape specimen is forged between flat dies and the vertical deformation upto cracking is attained. Wedge–forging test establish forgeability at different reductions and forging conditions (Verlinden *et al.*, 2007).

The side-pressing test, in which a cylindrical bar with unconstrained ends is compressed upto cracking between flat, parallel dies having the axis of the cylinder parallel to the dies. This test is effective to study surface related cracking. Schematic of the wedge forming and side stepping tests are shown in figure 2.39.

The hot tensile test, in which a special test apparatus is applied to vary both strain rates and temperatures over a wide range.

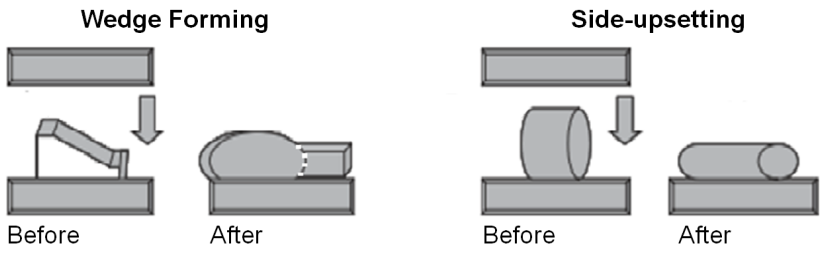

Figure 2.39: Schematic of the wedge forming and side stepping tests.

2.4.2 Hot forging of Austenitic Stainless steel

The austenitic stainless steels can be forged at a wide range of temperatures above 930°C and do not under go major phase transformation on contrary to martensitic types. There are some exceptions, when the composition of the austenitic stainless steel promotes the formation of δ-ferrite depending on the composition, which adversely affects the forgeability at elevated temperature of about 1100°C. Stainless steel cladding materials are susceptible to sensitization (precipitation of chromium carbides in grain boundaries that leaves chromium-depleted adjacent areas). Sensitization can occur when unstabilized stainless steels are heated in the range of 430 to 820°C either during stress relief or in service. The stabilized or extra low-carbon austenitic stainless steels are less susceptible to sensitization and are strain hardened by small reductions at temperatures well below the forging temperature in the range of 535 to 650°C. For non stabilized austenitic stainless steel forging, rapid cooling from about 1065°C is advised in order to retain the chromium carbides in solid solution. The highly alloyed grades like 309, 310 and 314 may be influenced by finishing temperature, because of their susceptibility at lower temperatures to hot tearing. The best way to inhibit these problems is to use low-carbon grades (such as type 308L, 309L or 316L) or stabilized grades (such as type 347) of austenitic stainless steels that are not readily sensitized. Also, finer micro structures produced by the lower heat-input processes improve corrosion resistance for all grades. Type 316L stainless steel is the low carbon version of type 316 and offers the additional feature of preventing excessive intergranular precipitation of chromium during welding and stress relieving. It contains 2-3% molybdenum which substantially increases resistance to

pitting and crevice corrosion in systems containing chlorides (Schweitzer, 2003). Hot forging temperature for SS 316L is reported as 925-1260°C and a forgeability comparison in terms of dynamic hot hardness for various ferrous alloys is shown in the figure 2.40 (Harris & Priebe, 1993a).

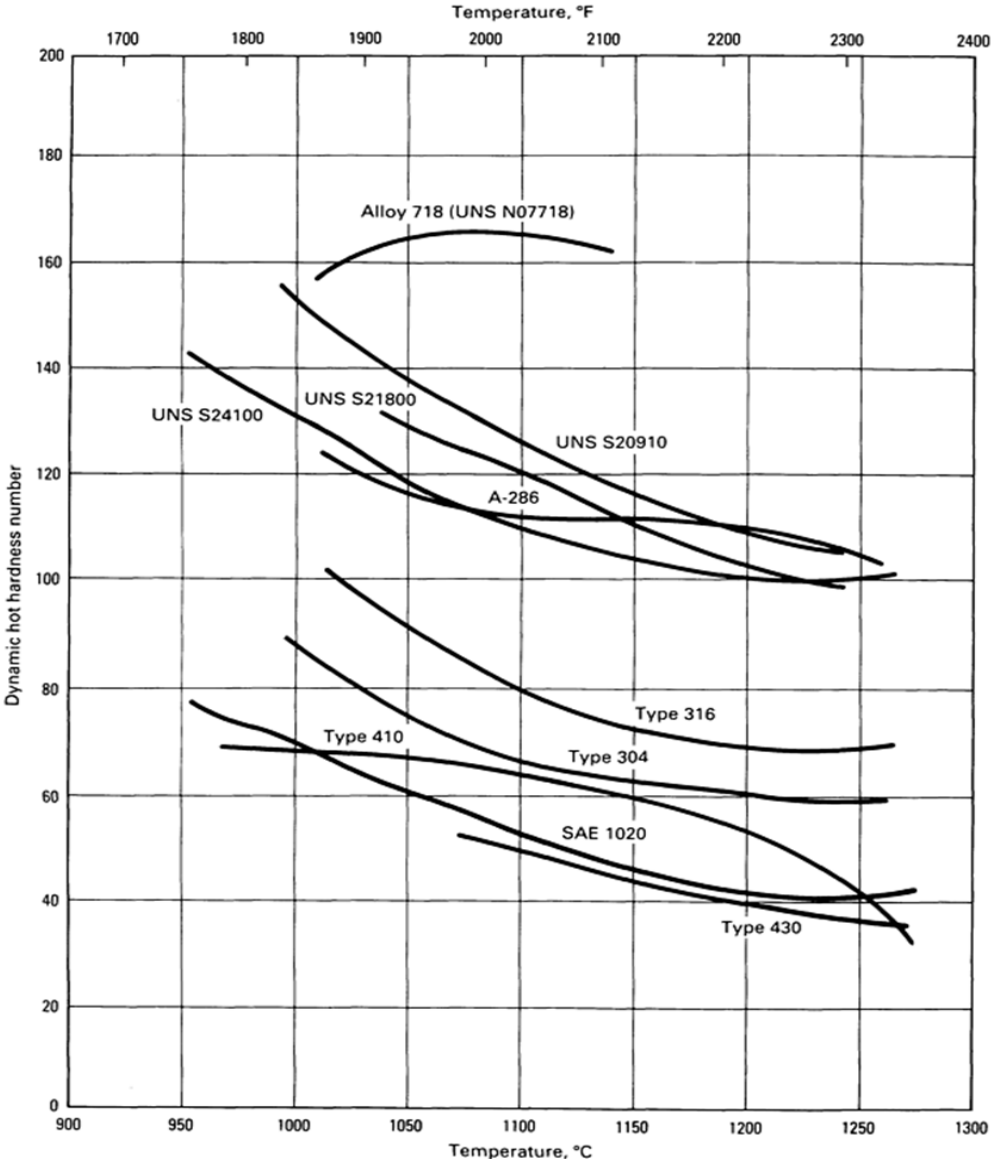

Figure 2.40: Comparative dynamic hot hardness versus temperature (forgeability) for various ferrous alloys (Harris & Priebe, 1993a)

The susceptibility of an austenitic steel to solidification cracking depends on the solidification mode as well as on the sulphur and phosphorus content. The mechanism of cracking is not well understood but cracking starts in high-temperature regions, where there is micrographic evidence of the liquation, the brittle temperature range (BTR) of low-melting constituents, but may propagate through regions of substantially lower temperature, where there is no liquation. However, the correlation between nil-ductility range and cracking tendency does suggest that a grain-boundary segregation or liquation mechanism is involved.

Hot ductility characterization of stainless steel: Austenitic alloys with FCC structure experience a ductility reduction during high temperature processing in the temperatures range between 0.5 and 0.8 of their melting temperature. Fully austenitic multi-layer weld metals and HAZ are more vulnerable to cracking by ductility-dip cracking (DDC) and solid state intergranular cracking (Ramirez & Lippold, 2004). The presence of ferrite reduces the risk of DDC by forming tortuous and crack resistant grain boundary paths. A schematic diagram of the ductility curve for both normal elevated temperature ductility and a material that exhibits a ductility-dip (gray area) is shown in fig 2.41.

DDC is well distinguished from the brittle temperature range(BTR) and are separated by a temperature of about 200°C. DDC is observed in HAZ and weld metal of austenitic stainless steels. In weld metals it occurs along migration grain boundaries (MGBs) (John & Damian, 2005).

2.4.3 Bi-material hot forging

The forged component achieved by a single piece of monolithic bar stock cannot be tailored to satisfy all the design requirements at different locations of a specific part. To resolve this issue, bi-metal forging is performed which has a substantial impact on efficient operation of the parts. For example, the "bi-metal" valves are being produced by friction welding of dissimilar metals and by subsequent forming. As in engine exhaust valve, high-temperature strength and wear resistance are required in the head and therefore to meet functional requirements alloys

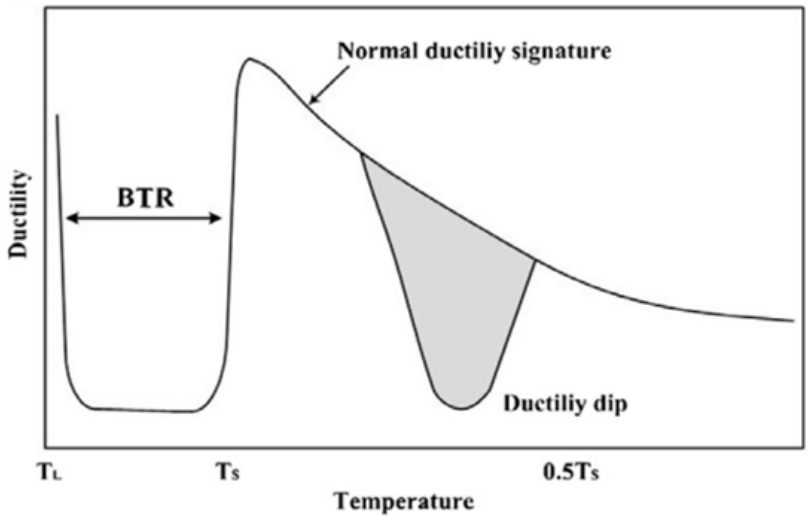

Figure 2.41: Elevated temperature ductility including the brittle temperature range (BTR) during solidification, T_L = Liquidus temperature, T_S = Solidus temperature (John & Damian, 2005)

containing nickel may be used. On contrary, the valve stem experience comparatively lower temperatures and the necessary strength and wear resistance can be achieved using a less costly alloy. In this case, the optimum solution may be to use a "bi-metal" alloy to minimize material cost and fulfill the necessary design requirements.

Presently, a little work is carried out on the hot forging of bi-metal. The feasibility of the welded preform concept was previously used by Domblesky and Kraft (Domblesky *et al.*, 2006) and they investigated the hot forging behavior of different materials like, copper, aluminum, steel and 304 stainless steel (see figure 2.42). They performed ***the upset test*** and ***the side-pressing test*** on same and dissimilar metal pre-forms, to assess workability and the resulting mechanical properties. A hybrid process with both solid-state welding and forging is used to generate an optimum forged shape and composition .

Domblesky et al. (Domblesky & Kraft, 2007) investigated the results of bulk

Figure 2.42: Dissimilar metal preforms after hot compression to 50% reduction showing the effect of (a) small difference (Cu–Al), b) intermediate difference (stainlesssteel-steel)and,(c)large difference(steel-Cu) in flow stress between the base metals. (Domblesky & Kraft, 2007)

forming of same metal and bi-metal friction-welded pre-forms. The mechanical properties, fracture behavior and the microstructural integrity along with the effect of tensile deformation in the weld vicinity of welded preforms after forging were also investigated.

2.5 Proposed Idea of Research

We have tried an experimental study to understand the hot forging behavior of dissimilar weldments from a basic point of view. Investigation about hot forging behavior of different welded metals have already been carried out by using friction welding as joining technique (Domblesky *et al.*, 2006). In our study we have applied GMA cladding process to deposit SS 316L clad layer on S 235 substrate. In order to understand the overall behavior during GMA cladding and then hot forging of the cladded plate, work is initiated with the study of GMAW process parameters for single bead and single layer cladding systems. The proposed idea of research is based on reversing the classical fabrication sequence of a simple cladded preform by performing the hot forging process after the weld cladding. The expected benefits are structural refinement of fusion welding solidification by hot forging structure. Moreover due to ease of automation of GMA cladding on simple preforms like plates, disc or cylinder, good control on clad quality parameters (metallurgical and geometric) can be achieved.

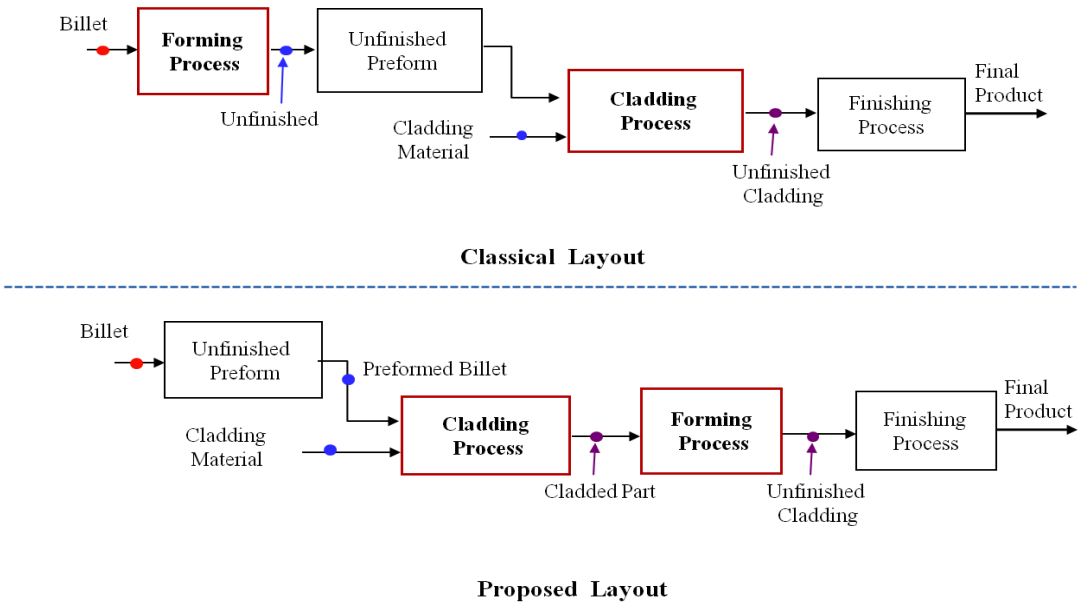

Figure 2.43: Schematic representation of classical and proposed fabrication layout.

If successful, the proposed concept can have a great technological relevance in manufacturing industry.

Chapter 3

The Weld Cladding Process

3.1 Description of Cladding process

This chapter is related to the cladding process performed by robotic Gas Metal Arc Welding (GMAW) process. During the robotic GMAW cladding process, the sectional geometry of single bead and the overlapping of the adjacent beads have remarkable effects on the cladding thickness, dilution rate and hence the clad quality. The wavy profile of the top cladding surface can be controlled by main process parameters like wire feed speed, welding speed and voltage as well as by bead overlapping and torch orientation. A single bead clad study study is carried out to determine the single layer cladding parameters.

3.1.1 Global Principle of Cladding Methodology

The main objective of the present section is to define a methodology for characterizing a single bead and consequently a multi-bead single layer cladding by robotic GMAW process. It is important to consider that the single bead clad study, leads us to determine the cladding parameters along with the adjacent beads overlapping for the subsequent single layer cladding. Keeping in mind, that in the GMA cladding process, the weld beads are deposited in side by side manner, the single bead quality parameters are investigated. The global view of the proposed methodology is shown in figure 3.1. Single bead cladding is performed according to a predefined experimental plan with a given input material

and source. The analytical study of the single bead cladding enables us to proceed for the single layer cladding related models. The method consists on establishing relation between the chosen input process parameters and the output clad quality parameters (bead geometry and dilution rate etc.), obtained from the single bead. From the analytical study of single bead, the input cladding parameters are determined for the required single layer cladding characteristics. The dilution rate and nominal energy of the clad bead are important factors to be considered while defining the cladding metallurgical quality. The former determines the cladding composition while the latter determines the thermal cycle of the weld bead and heat affected zone. Multi-bead overlapping reduces the cooling rate due to the gradual heating of the substrate and lowers the dilution rate with the effect of overlapping.

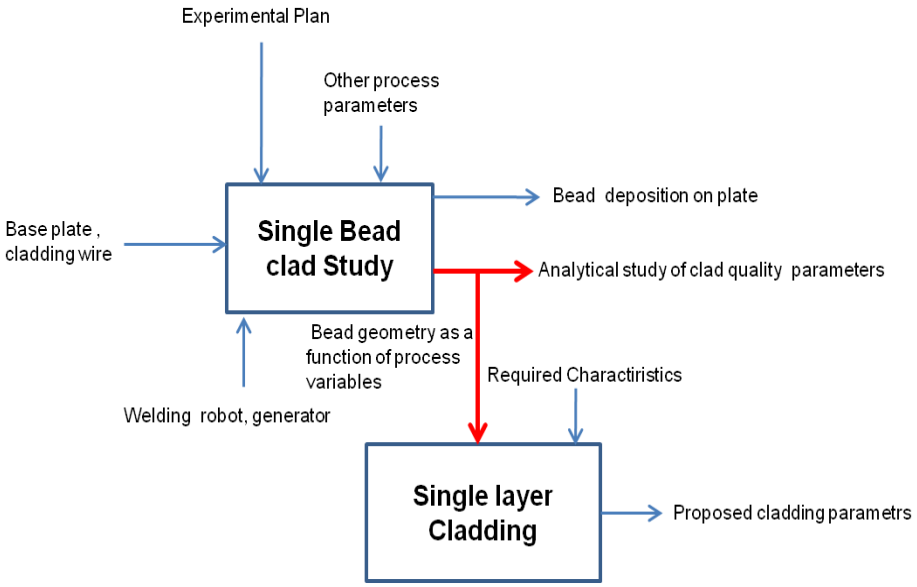

Figure 3.1: Global layout of the proposed cladding process methodology.

From the geometrical study of single bead cladding, statistical laws are established relating the chosen input process variable and the clad quality parameters. The results obtained are applied for determining the input parameters for required single layer cladding.

3.1.2 Bead Overlapping Models

As discussed in the previous chapter that, in GMAW cladding process, each weld bead is overlapped by the next one to obtain a maximum plane surface. So, layer cladding is done by multi-beads deposition at a certain offset or bead center to center distance which adds to the complexity of cladding process due to partial remelting of the existing bead while depositing the next bead. The quantity of material deposited varies from the center of the bead to its edges. To achieve a uniform surface, two beads are deposited close enough so that the deficit of material along the edges gets compensated by an overlap between them. To minimize the corrugation of the top cladded surface and to assure the complete fusion between the adjacent beads, some bead overlapping criteria are proposed here as illustrated in figure 3.2.

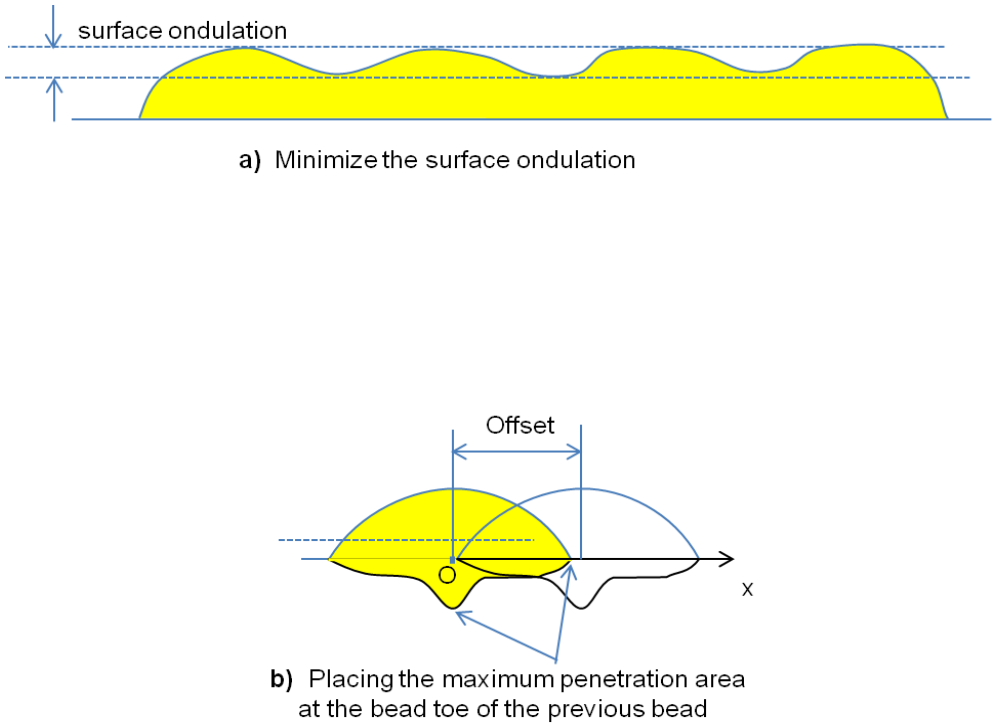

Figure 3.2: Important approaches for the implemented criteria

The analytical expressions of the proposed models to get the maximum smooth

top surface are also worked out and are discussed in the following section.

3.1.2.1 "Equivalent Area" and "Equivalent Height" criteria

In the present study, the offset distance corresponding to a maximum plane surface for multi-bead cladding is determined based on the following assumptions:

- The crater between adjacent beads is filled during the overlapping of beads by the "Superfluous liquid".
- The effects of interfacial force of liquid metal and arc pressure are not taken into account.

Two overlapping criteria, to get the maximum plane top cladding surface, are proposed and discussed below.

Equivalent area criterion In the equivalent area criterion, the concept of ideal surfacing of equivalent area (equal overlapping and crater filling area) is applied as shown in figure 3.3(a) (Cao *et al.*, 2011).

Equivalent Height Criterion While, in the equivalent height criterion, it is assumed that the two beads starts intercepting at the mid-point (in case of the symmetrical bead profiles) of bead center to center distance (P_H). The maximum height of two overlapped beads is assumed to be equal to the maximum height of the single bead as shown in figure 3.3(b). This criterion is applicable for symmetric bead profiles.

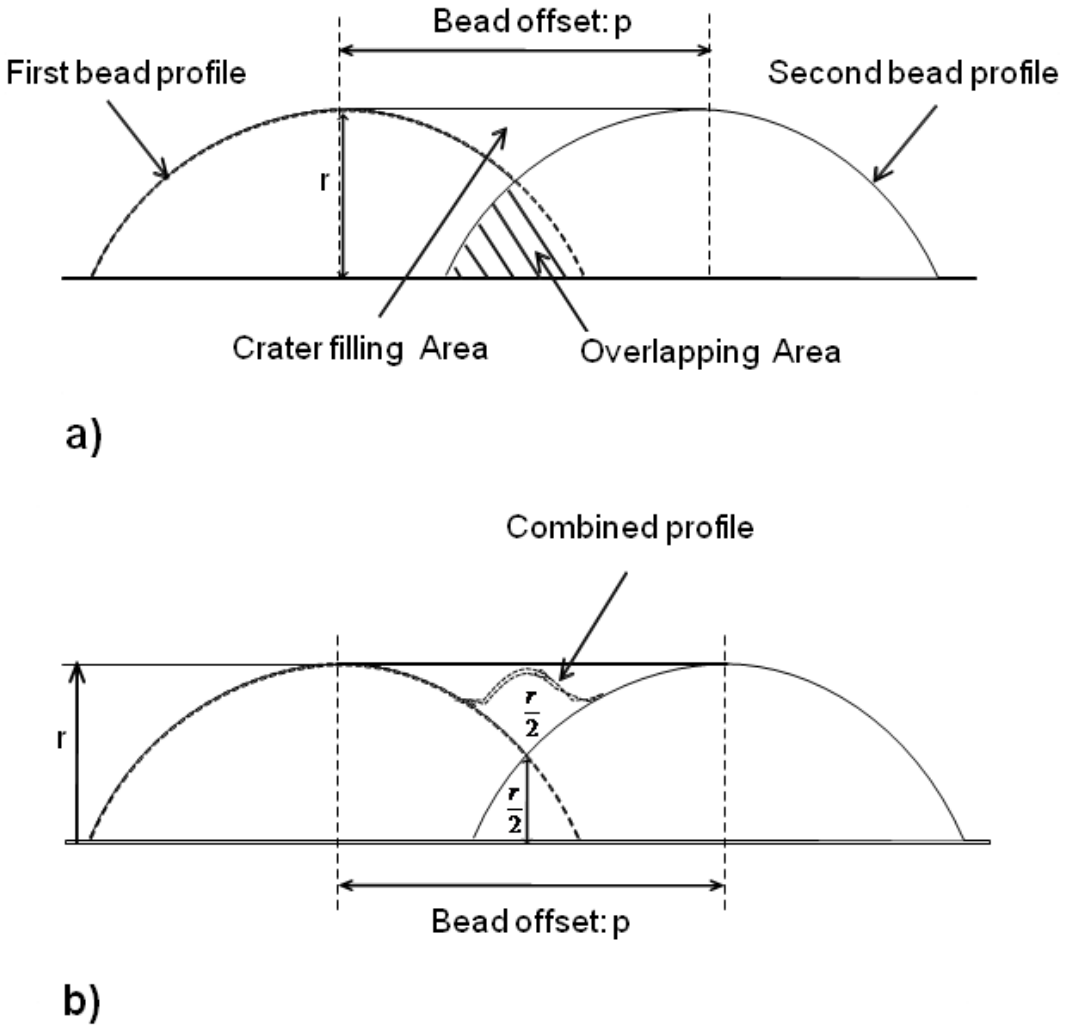

Figure 3.3: Overlapping criteria (a) "Equivalent area" and (b) "Equivalent height".

3.1.2.2 General representation of overlapping models

The above two criteria are applied to develop models for determining the bead center to center distance for single layer cladding. These models are based primarily on the upper section of the weld bead obtained by cutting the weld bead and represented by the plane (O, x, z). Consider the function z(x) representing the profile (See Figure 3.4).

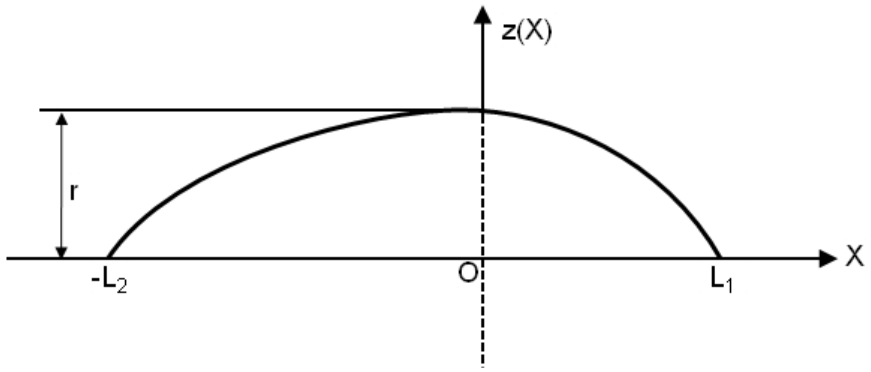

Figure 3.4: Schematic diagram representing a general clad bead top profile.

Assume that the profile of two beads are juxtaposed with an offset distance or bead center to center distance, p (see Figure 3.5).

where x_p is the intersection point of two bead profiles along the abscissa under

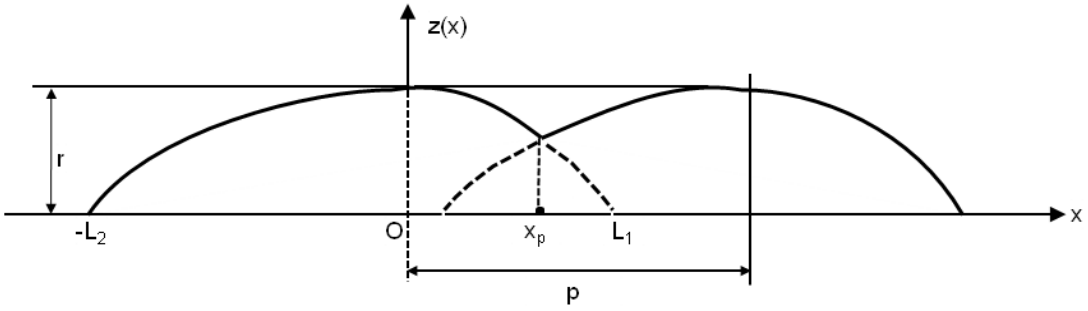

Figure 3.5: Schematic diagram representing the overlapping of bead top profiles.

the following condition.

$$2p > L_1 + L_2 \Longrightarrow \text{no intersection} \tag{3.1}$$

$$2p < L_1 + L_2 \Longrightarrow x_p \text{ as intersection} \tag{3.2}$$

and

$$z(x_p) = z(x_p - p) \tag{3.3}$$

Equivalent area criterion This criterion is based preliminary on the assumption that two consecutive beads are deposited in such a way that the crater area and overlapping area between them are equal as shown in Equation 3.4. Assume that the profile of two beads are juxtaposed with an offset distance or bead center to center distance, p_A as shown in the Figure 3.6).

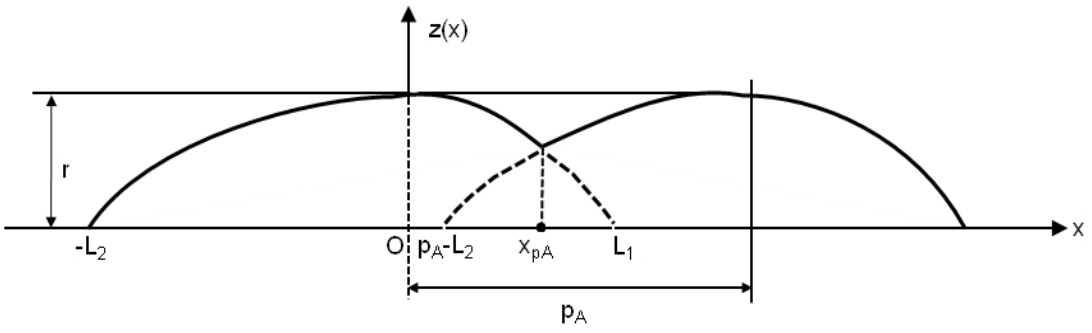

Figure 3.6: Schematic diagram representing the overlapping of bead top profiles for Equivalent area criterion.

$$\text{Crater filling Area} = \text{Overlapping Area} \tag{3.4}$$

$$\text{Crater filling Area} = \int_0^{x_{p_A}} (r - z(x))dx + \int_{x_{p_A}}^{p_A} (r - z(x-p))dx \tag{3.5}$$

$$\text{Overlapping Area} = \int_{p_A - L_2}^{x_{p_A}} z(x - p_A)dx + \int_{x_{p_A}}^{L_1} z(x)dx \tag{3.6}$$

by putting these values of Crater filling area and Overlapping area from the above equations, in the Equation (3.4) we can derive a relation for bead center to center distance p_A as given in the following steps.

$$p_A = \frac{Z(L_1) - Z(-L_2)}{r} \tag{3.7}$$

as we know for the two overlapped beads:

$$Z(L_1) = \int_0^{L_1} Z(x)dx \tag{3.8}$$

$$\begin{aligned} Z(-L_2) &= \int_0^{-L_2} ((x)dx \\ -Z(-L_2) &= \int_{-L_2}^{0} Z(x)dx \end{aligned} \tag{3.9}$$

where Z(x) is primitive of z(x) and by putting these from equations 3.8 and 3.9 in equation 3.7 we got the following general relation.

$$r.p_A = \int_{-L_2}^{L_1} (z(x))dx = \mathcal{A} \tag{3.10}$$

where $\mathcal{A}$ is the total surface area of the top bead section.

Equivalent Height Criterion This criterion is illustrated by the diagram 3.7 and is applicable when the given condition is satisfied.

$$z(x_p) + z(x_p - p) = r \tag{3.11}$$

if we put the value of $z(x_p)$ from equation 3.3 we got the following relation for equivalent height criterion.

$$\Rightarrow z(x_p) = r/2 \tag{3.12}$$

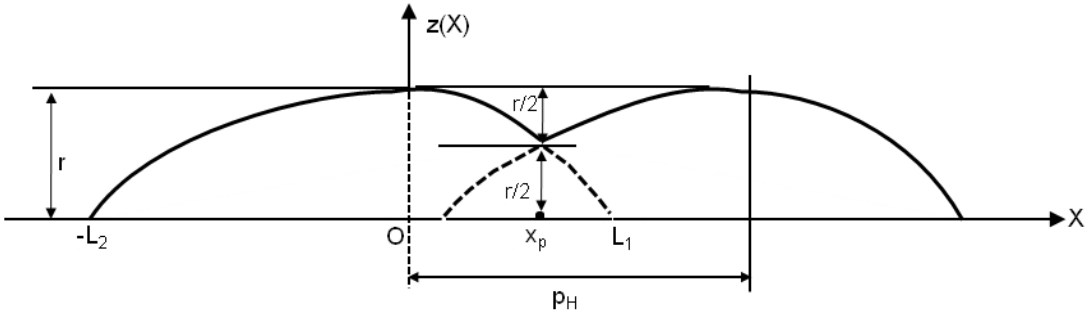

Figure 3.7: Schematic diagram representing the overlapping of bead top profiles for Equivalent Height Criterion.

3.1.2.3 Representation of bead profiles

The bead top profile may be represented by different functions with respect to its geometrical parameters to facilitate the reverse analysis with the help of analytical expressions. Initially, the analytical study is done by assuming a symmetrical bead profile as discussed below.

Second degree equation The analytical expression for bead profile represented by a second degree equation are given as under.

$$z(x) \quad = \quad r(1 - \frac{x^2}{L^2}) \tag{3.13}$$

where L is the total bead width.

Cosine function equation The analytical expression for the bead profile represented by cosine function may be given as under:

$$z(x) \quad = \quad r\cos(\frac{\pi}{2}.\frac{x}{L}) \tag{3.14}$$

It is obvious from the above expressions that, the second degree polynomial equation and cosine functions take into account only the bead width (L) and bead reinforcement (r) for simplicity purpose. For more refined bead profile, symmetrical four degree polynomial and ellipse arc function by taking in account

its geometrical parameters like bead width (L), bead reinforcement (r) along with the bead wetting angle, θ (see the Figure 3.8) may be applied.

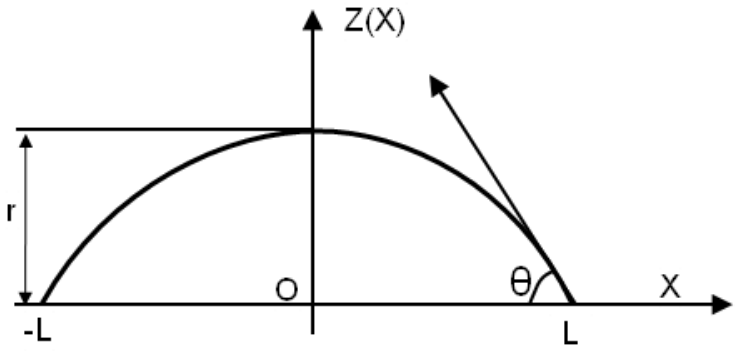

Figure 3.8: The bead reinforcement profile showing the bead width, reinforcement and wetting angle

Symmetrical four degree polynomial The (top) profile represented by a symmetrical four degree polynomial equation (see the Figure 3.8), may be shown mathematically by equation 3.15 along with the applied conditions given below.

$$z = ax^4 + bx^2 + c \tag{3.15}$$

given that:

$$z(0) = r \tag{3.16}$$

$$z(\frac{L}{2}) = 0 \tag{3.17}$$

$$z'(\frac{L}{2}) = -\tan\theta \tag{3.18}$$

and by applying the above given boundary conditions the relation for co-efficient a, b and c are derived as given below.

$$a = \frac{16}{L^4}(r - \frac{L\tan\theta}{4}) \tag{3.19}$$

$$b = \frac{\tan\theta}{L} - \frac{8r}{L^2} \tag{3.20}$$

$$c = r \tag{3.21}$$

Model limitations The applicable ranges are determined from the bead profile study as shown mathematically by the condition given below.

$$\frac{\partial^2 z}{\partial x^2} < 0 \tag{3.22}$$

By using the above condition, the model limitations and range of application are given below by the equation 3.23.

$$\tan\theta \ \epsilon \ ]\frac{16r}{5L}; \frac{8r}{L}[\tag{3.23}$$

If we define the **"form factor"**, Δ (involving the bead width, height and the wetting angle) by the following relation:

$$\Delta = \frac{L\tan\theta}{r} \tag{3.24}$$

then the range of the application and coefficients of the proposed model in terms of the **"form factor"**, Δ are given by the following relations:

$$\Delta \ \epsilon \ ]\frac{16}{5}; 8[\tag{3.25}$$

$$a = \frac{4r}{L^4}(4-\Delta) \tag{3.26}$$

$$b = \frac{r}{L^2}(\Delta - 8) \tag{3.27}$$

$$c = r \tag{3.28}$$

Ellipse arc function equation The analytical expression for the two criteria for simple and symmetric bead profile represented by ellipse arc function may be given as under:

$$z = b\sqrt{1 - \frac{x^2}{a^2}} - z_o \tag{3.29}$$

where a, b and z_o are half major-axes (along x), half minor-axes (along z) and transformation along z-axis respectively. Following conditions are supposed to be satisfied for the while deriving the analytical expressions for an ellipse profile.

$$z(0) = r \tag{3.30}$$

$$z(L) = 0 \tag{3.31}$$

$$z'(L) = -\tan\theta \tag{3.32}$$

where,

$$a = \frac{L}{2}\sqrt{\frac{(\Delta-1)^2}{\Delta(\Delta-2)}} \tag{3.33}$$

$$b = r\frac{(\Delta-1)}{(\Delta-2)} \tag{3.34}$$

$$z_o = r\frac{1}{(\Delta-2)} \tag{3.35}$$

Comparison of the proposed bead profile functions The bead profiles obtained by different proposed functions with different form factor values are compared in the Figure 3.9.

While, the Figure 3.10 shows the superposition of different bead form factors for symmetrical four degree polynomial and ellipse functions. This figure also demonstrate the model limitations and range of application for the bead profile represented by a symmetrical four degree polynomial showing that for the form factor less than 3.2, the profile curvature at the weld bead toe becomes positive. While, for the form factor values greater than 8, the profile shows two maxima with a large deviation from any real bead profile. When the value of the form factor is 2, the bead profile of the 2nd degree polynomial and arc of ellipse function coincides.

The 4 degree polynomial function shows large variation in the bead profile as compared to the ellipse arc function with the variation of form factor. For the form factor values less than 3.2, the bead toe positive curvature can also be achieved while using the 4 degree polynomial function.

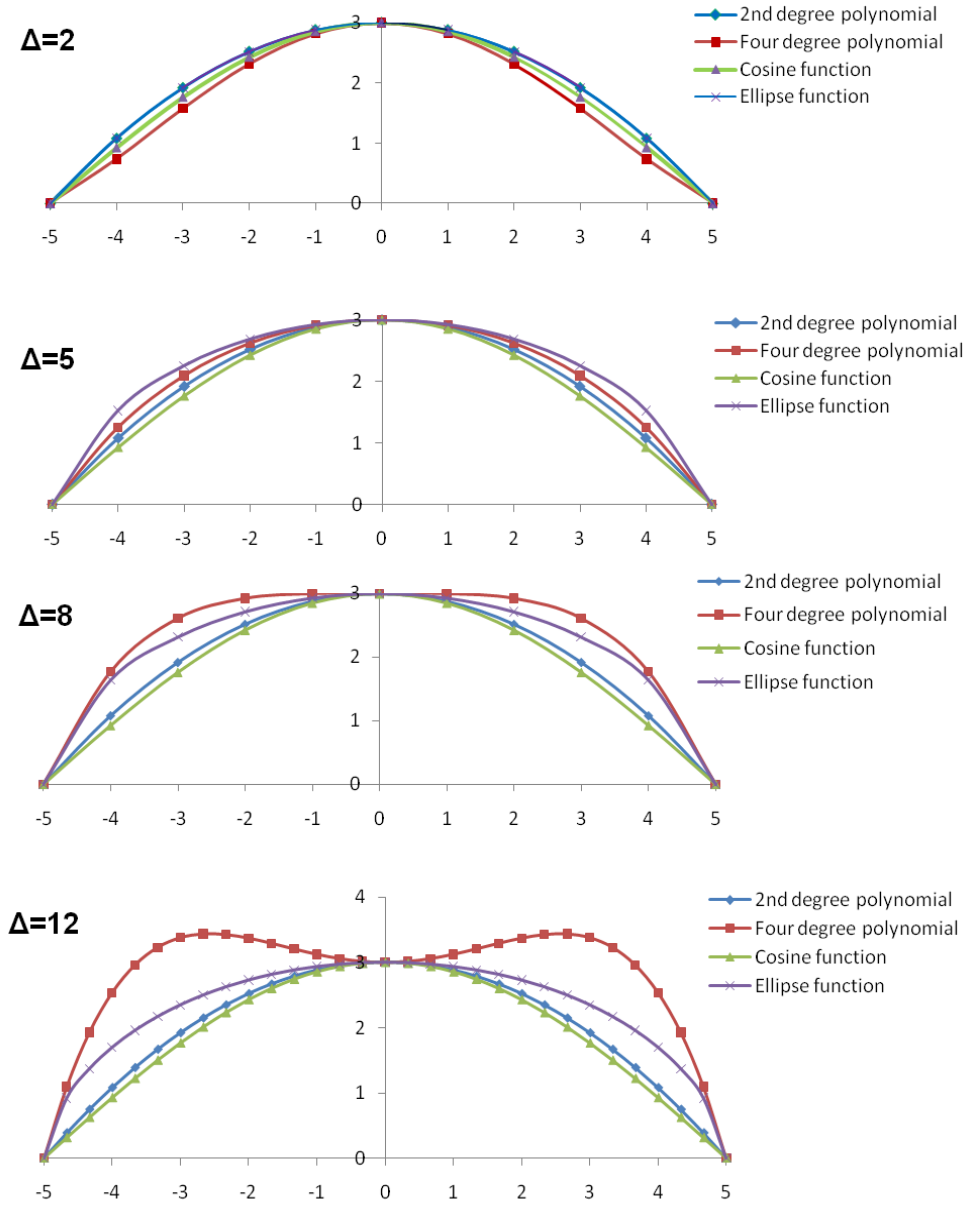

Figure 3.9: Superposition of different bead profile functions with different form factor values with L=10mm(x-axis) & r=3mm(y-axis)

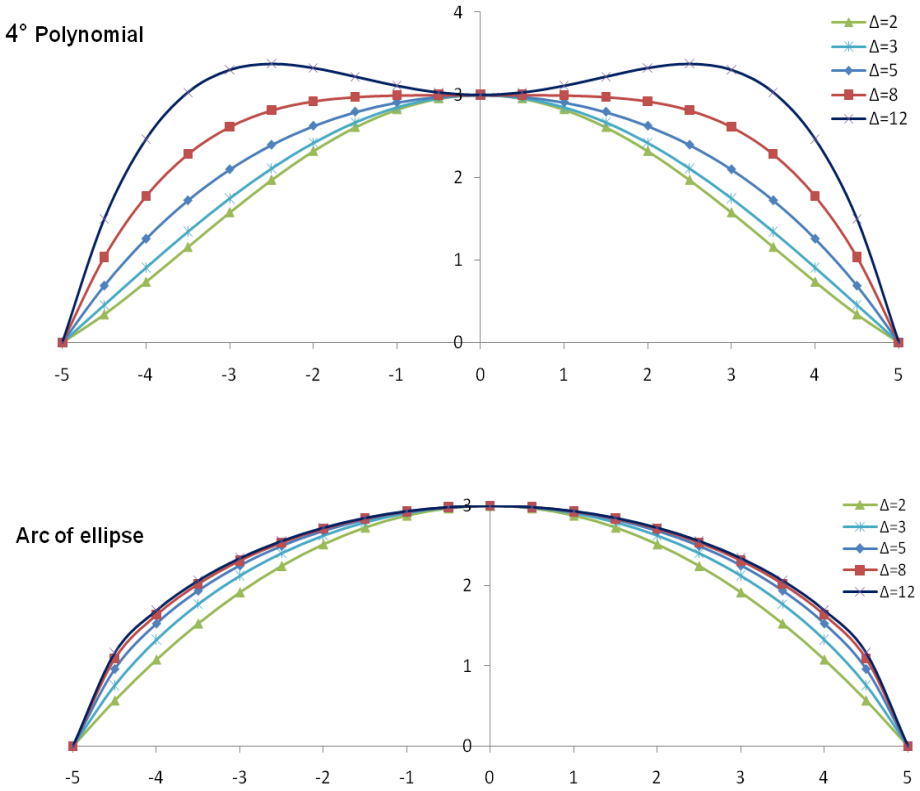

Figure 3.10: Representation of the weld profile for different values of the form factor for symmetrical four degree polynomial and ellipse functions with L=10mm & r=3mm

The Figure 3.11 shows the sensitivity of bead reinforcement (height) on the overall bead profile and its wetting angle for the ellipse arc and symmetrical 4 degree polynomial function while keeping the form factor at a constant value of 5.

The above comparison shows that the ellipse arc profile is more convex or crowned as compared to the profile obtained by 4 degree polynomial for all values of bead profile height while keeping the form factor value at 5 for an example.

3.1.2.4 Overlapping Models for the proposed bead profile functions

Some of the analytical relations obtained by the different symmetric profile functions by the applications overlapping model are discussed below.

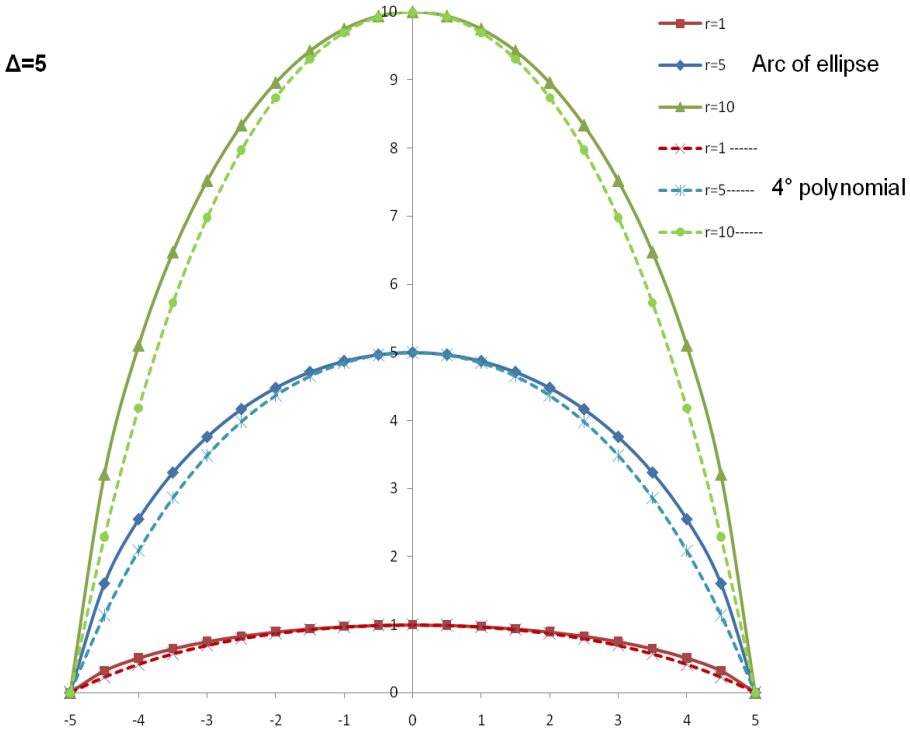

Figure 3.11: Bead profile sensitivity to bead reinforcement (r in mm) for ellipse and symmetrical four degree polynomial at constant form factor=5

Optimum bead overlapping by the 2nd degree polynomial The relation for the optimum bead center to center distance for the two discussed criteria for 2 degree polynomial bead profile may be given as under:

$$p_A = \frac{4}{3}L \tag{3.36}$$

$$p_H = \sqrt{2}L \tag{3.37}$$

where L is the total bead width. If we define the overlapping rate as the ratio of overlapping width to the total bead width, given by:

$$\acute{\delta} = \frac{L-p}{L} \tag{3.38}$$

then the optimum bead overlapping for 2 degree polynomial bead profile is:

$$\acute{\delta}_A = \frac{1}{3} \tag{3.39}$$

$$\acute{\delta}_H = 1 - \frac{\sqrt{2}}{2} \tag{3.40}$$

Optimum bead overlapping by the cosine function In case of cosine function, the relation for the optimum bead center to center distance for the both criteria may is given in the following relation:

$$p_A = \frac{4}{\pi}L \tag{3.41}$$

$$p_H = \frac{4}{3}(L) \tag{3.42}$$

where L is the total bead width. The optimum bead overlapping given by cosine function is:

$$\acute{\delta}_A = \frac{1}{\pi} \tag{3.43}$$

$$\acute{\delta}_H = \frac{1}{3} \tag{3.44}$$

Here we can see that we got the pre-recognized classical overlapping values for the cosine and 2 degree polynomial functions for the both criteria. These functions gives always fix and near enough values, independent of the bead profiles form factors.

Optimum bead overlapping by the symmetrical four degree polynomial For the equivalent area criterion optimum bead offset for 4 degree symmetrical polynomial in terms of form factor is given in equation 3.45, while the derived relation for the bead center to center distance is shown in equation 3.46.

$$\int_{\frac{p_A}{2}}^{\frac{L}{2}} Z(x)dx = \int_{0}^{\frac{p_A}{2}} (r - Z(x))dx \tag{3.45}$$

$$p_A = \frac{L}{30}(16 + \Delta) \tag{3.46}$$

The calculated bead center to center distance p_H for 4 degree symmetrical polynomial is shown in equation 3.48.

$$Z(\frac{p_H}{2}) = \frac{r}{2} \tag{3.47}$$

$$p_H = L\sqrt{\frac{8-\Delta-\sqrt{(\Delta-4)^2+16}}{2(4-\Delta)}} \tag{3.48}$$

The equations 3.46 and 3.48 show that the form factor is an important parameter which will characterize the single weld bead vis-à-vis the layer cladding. In case of the above two criteria, we notice that the overlapping rate is only a function of the form factor when represented by 4 degree symmetrical polynomial, as shown by the following equations.

$$\acute{\delta}_H = 1-\sqrt{\frac{8-\Delta-\sqrt{(\Delta-4)^2+16}}{2(4-\Delta)}} \tag{3.49}$$

$$\acute{\delta}_A = \frac{(14-\Delta)}{30} \tag{3.50}$$

Optimum bead overlapping by the ellipse arc function While considering the ellipse arc function, the relation for the optimum bead center to center distance for the two discussed criteria may be given as under:

$$p_H = \mathbb{L}.\sqrt{\frac{3\Delta-2}{\Delta}} \tag{3.51}$$

$$p_A = \frac{\mathbb{L}}{\Delta-2}(-1+\frac{(\Delta-1)^2}{\sqrt{\Delta(\Delta-2)}}\arcsin\sqrt{\frac{\Delta(\Delta-2)}{(\Delta-1)^2}}) \tag{3.52}$$

For the above both criteria, we notice that the overlapping rate for the ellipse arc function are also only a function of the form factor as shown by the following equations.

$$\acute{\delta}_H = 1-\sqrt{\frac{3\Delta-2}{\Delta}} \tag{3.53}$$

$$\acute{\delta}_A = 1-\frac{1}{\Delta-2}(-1+\frac{(\Delta-1)^2}{\sqrt{\Delta(\Delta-2)}}\arcsin\sqrt{\frac{\Delta(\Delta-2)}{(\Delta-1)^2}}) \tag{3.54}$$

Symmetric bead profile The bead profile represented by different functions in order to find the analytical expressions for the above mentioned criteria were considered as symmetrical. For a symmetrical top profile (see the Figure 3.12) the intersection point is the mid-point of the offset distance as shown mathematically in the following equation.

$$x_p = p/2 \tag{3.55}$$

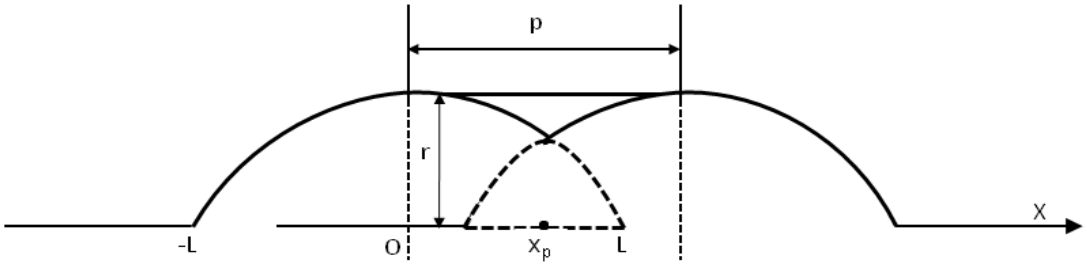

Figure 3.12: Schematic diagram representing the overlapping of symmetrical bead top profiles.

But in fact, the bead profile may be symmetric or non-symmetric depending on the torch orientation and other cladding parameters. The analytical relations for a non-symmetric bead profile may be obtained by dividing the whole profile in different segments of some regular profile as discussed below.

Non-symmetric bead profile The Figure 3.13 shows a typical non-symmetric bead profile with origin O where bead height is maximum. This origin may not necessarily the intersection of the torch axis and the substrate initial surface. The analytical relations for a non-symmetric bead profile may be obtained by dividing the whole profile in different segments of some regular profile.

$$z(x) = z_1(x) = a_1x^4 + b_1x^2 + c_1 \Longrightarrow x\epsilon[0, L_1] \tag{3.56}$$

$$z(x) = z_2(x) = a_2x^4 + b_2x^2 + c_2 \Longrightarrow x\epsilon[-L_2, 0] \tag{3.57}$$

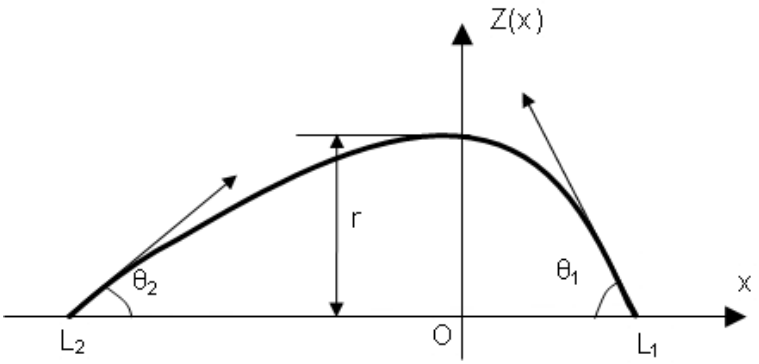

Figure 3.13: Schematic diagram representing the non-symmetrical bead top profiles.

with

$$z_1(0) = z_2(0) \quad = \quad r \tag{3.58}$$

and

$$\frac{d(z_1(0))}{dx} = \frac{d(z_2(0))}{dx} = \quad 0 \tag{3.59}$$

By applying the above boundary conditions in the two segments of the non-symmetric profile by the two 2nd degree polynomials, we got the following relations.

$$z(x) \quad = \quad r(1 - \frac{x^2}{{L_2}^2}) \Rightarrow \text{if}, x\epsilon[-L_2, 0] \tag{3.60}$$

$$z(x) \quad = \quad r(1 - \frac{x^2}{{L_1}^2}) \Rightarrow \text{if}, x\epsilon[0, L_1] \tag{3.61}$$

As we know for the equivalent area criterion, optimum bead offset distance for a symmetric bead profile is given by the following equation.

$$p_A \quad = \quad \frac{\mathbf{A}}{r} \tag{3.62}$$

where A, is the total surface area of the top bead section. For a non-symmetric profile, the optimum bead offset distance may be given by the following equation.

$$p_A = \frac{\mathbf{A}_1 + \mathbf{A}_2}{2r} \tag{3.63}$$

where $\mathbf{A}_1$ is symmetrical section of the positive part of a non-symmetric profile and $\mathbf{A}_2$ is the equivalent in the negative part of the non-symmetric profile. The overall offset distance may be given by the following relation.

$$p_A = \frac{1}{2}(p_{A_1} + p_{A_2}) \tag{3.64}$$

where p_{A1} and p_{A2} are the offset distances calculated from two half profiles if as the bead has symmetrical section with respect to each half profile. For the equivalent height criterion, optimum bead offset for non-symmetric bead profile is dependent on the following condition.

$$z_1(x_p) + z_2(x_p - p) = r \tag{3.65}$$

if we put the value of $z(x_p)$ from equation 3.3 we got the following relation for equivalent height criterion.

$$z_1(x_p) = z_2(x_p - p_H) = r/2 \tag{3.66}$$

For 2nd degree polynomial the optimum bead offset is calculated as follow

$$p_H = \frac{L_1 + L_2}{\sqrt{2}} \tag{3.67}$$

and for cosine function it is calculated by the following formula.

$$p_H = \frac{2}{3}(L_1 + L_2) \tag{3.68}$$

For the arc of ellipse and four degree polynomial the analytical expression of x_p in terms of p is not solved and can be found numerically.

Non-symmetrical Bead optimum offset distance represented by four degree polynomial For equivalent criterion, the optimum bead offset may be calculated analytically as follows. Assume that the profile of two beads are juxtaposed with a certain offset distance or bead center to center distance, p (see Figure 3.14) and their top bead profile is represented by the following equations.

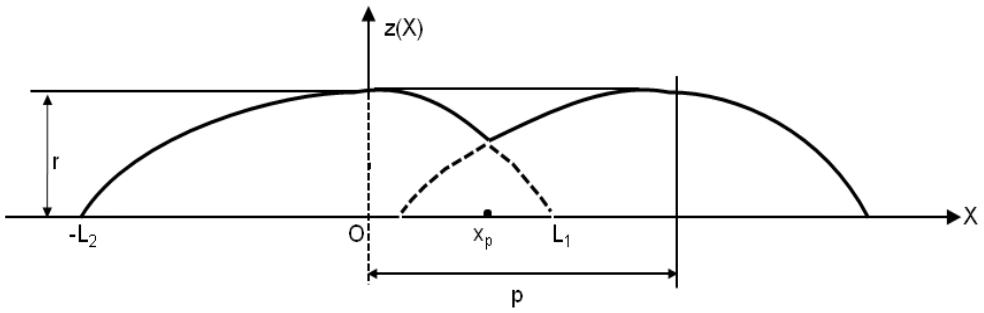

Figure 3.14: Schematic diagram representing the overlapping of non-symmetric bead top profiles.

$$z = \quad a_1x^4 + b_1x^2 + c_1 \Rightarrow x\epsilon[0, L_1] \tag{3.69}$$

$$z = \quad a_2x^4 + b_2x^2 + c_2 \Rightarrow x\epsilon[-L_2, 0] \tag{3.70}$$

where a_1, b_1, c_1 and a_2, b_2, c_2 are functions of Δ_1 and Δ_2 (form factors at both ends of the bead) respectively. By applying the above boundary conditions given in equations 3.16, 3.17 and 3.18, the relation for co-efficients a_1, b_1, c_1 and a_2, b_2, c_2 are driven as given below.

$$a_1 = \frac{r}{L_1^4}(1 - \frac{1}{8}\Delta_1) \tag{3.71}$$

$$b_1 = \frac{2r}{L_1^2}(\frac{1}{4}\Delta_1 - 1) \tag{3.72}$$

$$c_1 = r \tag{3.73}$$

and

$$\begin{aligned} a_2 &= \frac{r}{L_2^4}(1-\frac{1}{8}\Delta_2) \\ b_2 &= \frac{2r}{L_2^2}(\frac{1}{4}\Delta_2 - 1) \\ c_2 &= r \end{aligned}$$

As discussed above, in the **Equivalent Area Criterion** , the concept of ideal surfacing of equivalent area (equal overlapping and crater filling area) is applied. For the equivalent area criterion optimum bead offset for non-symmetric bead profile in terms of form factor is given in equation 3.74.

$$p_A = \frac{8}{15}(L_1+L_2)+\frac{17}{120}(L_1\Delta_1+L_2\Delta_2) \tag{3.74}$$

3.1.2.5 Conclusion related to bead profile

The proposed "equivalent area" and "equivalent height" criteria are applied to calculate the optimum bead overlapping by representing the bead profile by different functions to get the analytical expressions. For the beads represented by two degree of freedom functions (2nd degree polynomial, cosine function) taking into account the bead height and width, we got a fix value of the optimum bead overlapping for the both criteria. On the other hand, when bead profile is represented by four degree of freedom functions (four degree polynomial and arc of ellipse function) the optimum bead overlapping in case of symmetrical profile, depend on the form factor which takes into account the profile wetting angle along with the bead height and width. The non-symmetric profile are represented by parts by two different suitable functions and the final expression of bead overlapping take in account the form factor of each segment.

3.1.2.6 Bead overlapping as a function of bead profile

The bead optimum overlapping is affected largely by the bead profile representation function. The figure 3.15 shows the evolution of the overlapping rate with the form factor while using different bead profiles functions by applying the equivalent area criterion. While,the figure 3.16 shows the evolution of the overlapping rate

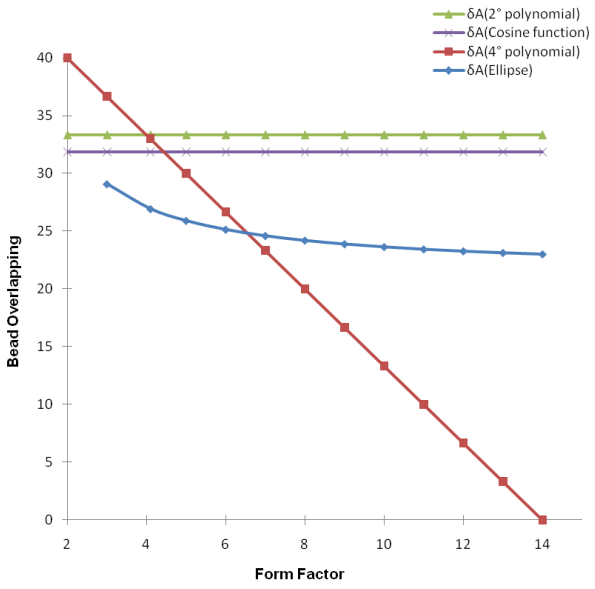

Figure 3.15: Evolution of the overlapping rate with form factor for different bead profile functions for equivalent area criteria

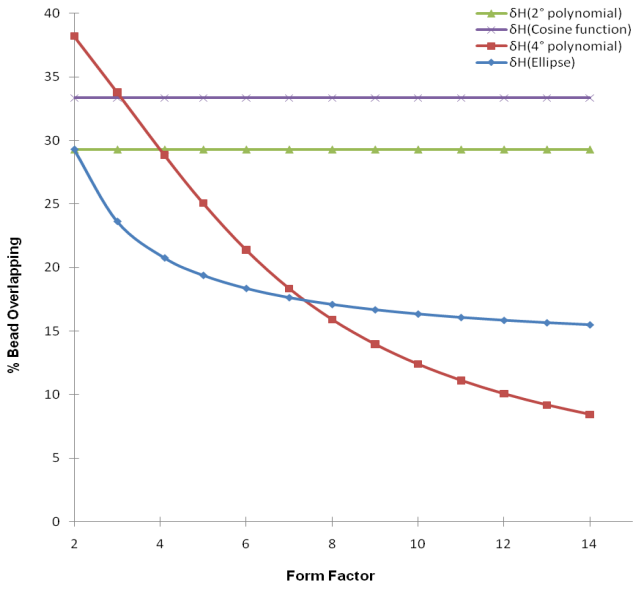

Figure 3.16: Evolution of the overlapping rate with form factor for different bead profile functions for equivalent height criteria

with the form factor while using different bead profiles functions by applying the equivalent height criterion. For 2nd degree polynomial and cosine function, bead overlapping is independent of the form factor and remains constant for the both criteria but the overlapping rate is an inverse function of the form factor in the case of the both proposed criteria for 4 degree polynomial profile and equivalent height criterion of the ellipse arc function. For the equivalent area criterion the ellipse function shows approximately fixed overlapping ratio especially at higher form factors as shown in the Figure 3.15. To implement the method for determining the parameters of cladding described in the Figure 3.1 the bead width, bead height and the wetting angle at the weld bead toe (All of them determine the bead form factor) should be output parameters of the experimental parametric study.

3.1.3 Conclusion

The approach proposed in this section to determine the GMAW cladding layer parameters, is based on the parametric study of a single bead. For layer cladding, two overlapping models to determine the optimum bead overlapping are introduced by representing the bead profiles by different functions. The proposed method makes it possible to determine welding parameters and bead overlapping for the required characteristics of single layer cladding. The analysis shows that for the high value of form factor, the bead profiles represented by a 2nd degree polynomial and cosine function do not show a good approximation because they do not take into account the bead wetting angle. These functions give always fixed value of the optimum overlapping rate for the both proposed criteria. To refine and optimize the results, symmetrical polynomial of degree 4 and arc of ellipse functions which take into account the bead profile form factor and hence the bead wetting angle are introduced and the overlapping rate becomes function of the bead form factor. The ellipse function shows good approximation for higher form factor values only. The symmetrical polynomial of degree 4 shows a form factor ranging from 3.2 to 8 which determine the ability of the weld bead to form a smooth layer cladding by using this bead representation for the proposed overlapping models. For the values of the form factor less than 3.2, the profile

curvature at the weld bead toe becomes positive. For values greater than 8, the profile shows two maxima. For the weld beads having lower values of wetting angles for a constant value of form factor (Δ), the combined effect of dispersion in the overlapping rate is lower for the both proposed criteria. In all the analyzed cases, the calculated bead overlapping distances by the equivalent area criterion gives good results but do not necessarily represent an optimum. The criterion based on the equivalent height, can lead to cladding disjoint in the case of large values of the form factor.

3.1.4 Quality of Cladding

In this section, we will try to seek out the parameters that will be representative of the metallurgical quality of the cladding. In general, the quality of the cladded layer will depend on its chemical composition and thermal cycle during its deposition. We may distinguish the case of single bead as well as the single layer obtained by juxtaposition of beads, considering the metallurgical characteristics of the cladding and the heat affected zone.

3.1.4.1 Chemical composition and solidification rate

The metallurgical structure of the bead depends on its chemical composition and approximately latter may be defined by a law of mixtures given below:

$$\%E = \delta\%E_{filler} + (1-\delta)\%E_{base} \tag{3.75}$$

Where $\%E$, $\%E_{filler}$ and $\%E_{base}$ are the amounts expressed as percentage of element E, in the cladding layer, filler metal and base material respectively and "δ" is the dilution rate. This term does not include the potential losses of elements by spatter, evaporation or chemical reaction.
As discussed in the previous chapter, the metallurgical phases present in the stainless steel cladding on structural steel will depend on the dilution rate. For low dilution rate, the cladding structure may be austenitic ferrite with a few percent of ferrite content. The solidification structure will either in the form of ferritic-austenite or Austenitic-ferrite. For larger dilution rates metallurgical structure

can have the phases austenite, ferrite and martensite or austenite-martensite. The cladded bead has a solidification structure. The nature of the solidification structure for a given composition will be able to evolve according to the welding speed. Indeed, as presented in Chapter I, the solidification rate of weld puddle is directly related to the welding speed. The cooling rate of the melted zone and heat affected zone, for a given substrate thickness and a given welding process, will depend on the nominal energy and the initial temperature of the substrate. The nominal energy is given by the equation below:

$$E_n = \frac{IU}{V_a} \tag{3.76}$$

Voltage and welding speed are two primary process parameters but the current intensity will depend on the wire feed speed and the arc height. The latter will depend mainly on the voltage. To investigate the single bead clad metal structure, the parametric study will have the dilution rate and current intensity as output parameters while the welding speed is an input parameter. The metallurgical structure obtained in the heat affected zone of the substrate will depend essentially on the nominal energy and the initial temperature of the substrate. The extent of the HAZ also depends on these two parameters. In steels, the HAZ can be further divided into three sub-zones as under:

Quenched Zone, in which the maximum temperature exceeds the austenitic transformation temperature AC3. The material is completely transformed into austenite. Near the fusion zone, the temperature approaches to the melting temperature which generates large grains (size 0-1) austenitic.

Annealing Zone, totally or partially recrystallized. This zone may undergo a partial austenitic transformation (between AC1 and AC3) or may undergo static recrystallization at temperatures lower than AC1.

A "Secondary Annealing Zone", where the material depending on its initial state may undergo a thermal softening. Cold rolled structure steel face annealing annihilation in this zone leading to a decrease in hardness.

3.1.4.2 Cladding Quality, case of a single layer

As the weld cladding is the result of the juxtaposition and partial overlapping of beads, therefore, the chemical composition of the cladding will be uneven. High dilution means the percentage of base metal in the weld metal deposit is high and the surface properties are not enhanced to the expected level because of the presence of a higher amount of base metal. At a lower percentage of dilution level, the surface properties are much better compared to the base metal. The dilution rate will evolve from one bead to another. The dilution rate of a single bead can be accessed by measuring the surface areas from the cross-section of the macrographs. The dilution rate is then given by the following expression:

$$\delta = \frac{S_{filler}}{S_{total}} \tag{3.77}$$

where S_{filler} is the cross-section area of the molten zone above the original surface of the substrate and S_{total} is the total fused cross-section area of the bead. This approximation of the dilution rate is based on the assumption that the weld bead has a cylindrical outline of the traversal cross section of the bead. In the case of overlapping of *'n-1'* bead by bead *'n'*, the dilution rate is given by the following equation:

$$\delta_n = \frac{(S_{filler,n} + \delta_{n-1} S_{r,nn-1})}{S_{total,n}} \tag{3.78}$$

Where δ_n, δ_{n-1} are the dilution rate of n and n-1 beads and $S_{r,n.n-1}$, is the surface of the bead "n-1" remelted by the bead "n" (see figure 3.17).

3.1.4.3 Cladding pattern evolution for a single layer

Single layer cladding is the result of the juxtaposition and partial overlapping of beads which may cause some unevenness in the successive beads. So a "geometrical equilibrium state" is assumed that beyond a certain number of beads, n_{lim}, the surfaces involved in the expression of the dilution rate remain constant.

$$\forall i, j > n_{lim} S_{total,i} = S_{total,j}, S_{r,ii-1} = S_{r,jj-1}, S_{filler,i} = S_{filler,j} \tag{3.79}$$

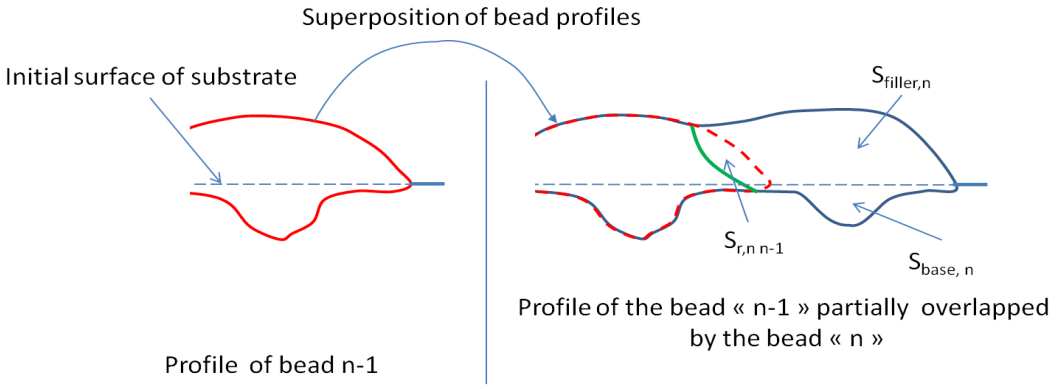

Figure 3.17: Schematic representation of beads overlapping for layer cladding

One can note that last relation is valid even outside the geometrical equilibrium state. The area of the cladded bead is related to the wire feed and the welding speed. In the case where the above relation holds, the dilution rate tends to a limiting value given by:

$$\lim_{n\to\infty}(\delta_n) = \frac{S_{filler}}{S_{base}} \tag{3.80}$$

Where, S_{base} is the section of base metal melted by the clad bead and is defined by the equation:

$$S_{total} = S_{filler} + S_r + S_{base} \tag{3.81}$$

The clad surface area is constant regardless of the clad bead number. The base area of the first bead is greater than that of next one due to the overlapping effect. The ratio between the base surface area of the first bead and the second bead may be related with the overlapping and hence the bead center to center distance or offset distance. However, this is not a linear function of the overlapping rate as much of the base surface is occupied by the lobe (due to the Marangoni effect), the position of the latter being difficult to anticipate.

Thermal cycle To obtain the behavior of the thermal cycle during the layer cladding, a test by placing the thermocouple was conducted. The cladding pa-

rameters and the overlapping rate are given in the following table (3.1).

The cladding of 316L stainless steel on a mild steel substrate S 235 on a 30mm

Parameters of Cladding
➢ Welding Speed (V_a) = 2.5 mm/s
➢ Wire feed Speed (V_f) = 5 m/min
➢ Voltage (U) = 24 V
➢ Offset distance (p) = 8.1mm
➢ Over lapping = 40%

Table 3.1: Process parameters used for the performed layer cladding

thick plate is carried out. The cladding consists of 10 beads and the substrate plate is instrumented with 10 thermocouples of diameter 1.5mm. The positions of these holes having thermocouple are 2mm below the surface of the substrate and are offset from the axis of the torch during the deposition of beads. This ensures that the thermocouple are prevented to be in the lobe of the weld bead. Hole positions of the thermocouples is fixed by considering the geometry of the single bead vis a vis the bead overlapping distance p (see figure 3.18).

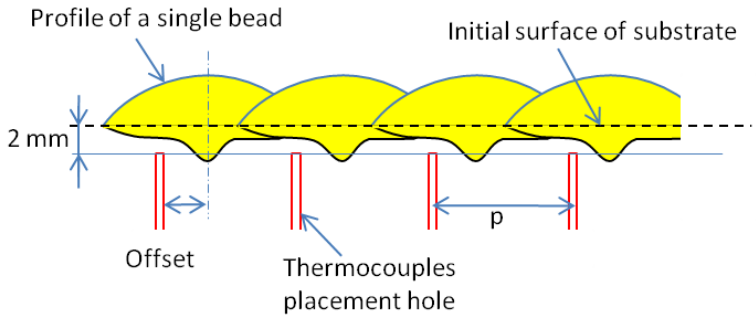

Figure 3.18: Schematic representation of the thermocouple positioning

The numbering of the thermocouple is such that # *i*, is located between the beads *i* and *i-1*. A 3D-CAD design of the cladded substrate plate and a photo

of the substrate before and after cladding showing the thermocouple positioning are shown in the Figure 3.19.

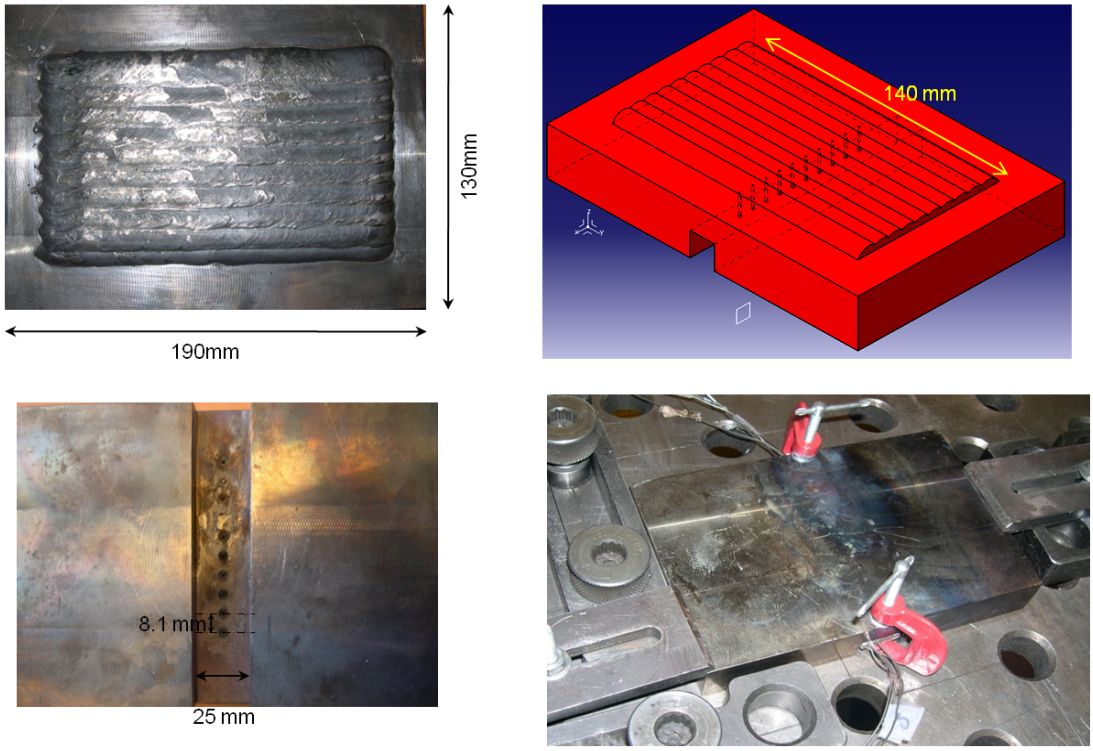

Figure 3.19: Schematic representation of the cladded plate illustrating the thermocouples positioning

The thermal cycle at any point of the cladded beads depends on its distance from the moving heat source. As the distance from the heat source increases, the peak temperature decreases and the temperature further lags behind the source. The Figure 3.20 shows the variation of temperature with time at different distances from the heat source corresponding to measurements of thermocouple locations 1, 6 and 10. The thermocouple "n" is placed between the beads "n" and "n-1" (except for thermocouple No.1), we can see two peaks of equivalent intensity on each curve corresponding to the passage of the heat source during the deposition of beads "n-1" and "n". For more remote beads, the temperature curve may have a lower amplitude peak with a delay corresponding to the time required for heat distribution to the point of measurement as shown in the Figure

3.20. The average temperature of the plate, given in particular by a thermocouple during the deposition of the last bead, gradually rises until it reaches a limiting temperature.

If we look at the temperature peaks, there is a cooling rate higher for the thermocouple 1 at the completion of the first bead for the following thermocouple peaks. This illustrates the decrease in cooling rate due to progressive heating effect of base plate. The tests illustrate that by thermal point of view, in the absence of preheating, the first bead has probably the highest cooling rate. In the case of cladded parts with varying thicknesses, there may be a geometric effect (Heat removal from the welding zone by conduction) the cooling rate can vary significantly. As a first approximation, we can estimate the preheating temperature limit reached by the workpiece during welding. We suppose that the substrate temperature is uniform and negligible downtime of the arc. It is also assumed that the welding time is long enough to reach the thermal equilibrium state. The thermal equilibrium is reached when the energy input from the arc is compensated by the exchanges with the environment. If we neglect the heat flow exchanged by radiation, we obtain an equilibrium temperature given by the following equation:

$$T_{lim} = \frac{Power}{H_{exchange}} \tag{3.82}$$

where T_{lim} is the maximum average temperature attained by the work piece, while the power is the part of the arc power actually transmitted to the work piece and $H_{exchange}$ the overall heat transfer coefficient assuming that the heat exchange between the workpiece and its environment is proportional to the average temperature of the plate. The temperature limits as well as the temperature rise depend on the welding power. The thermal cycle limit is obtained from a preheat temperature defined by the welding power. For the same nominal energy, lower power and welding speed will lead to a low limiting temperature than high power and high welding speed.

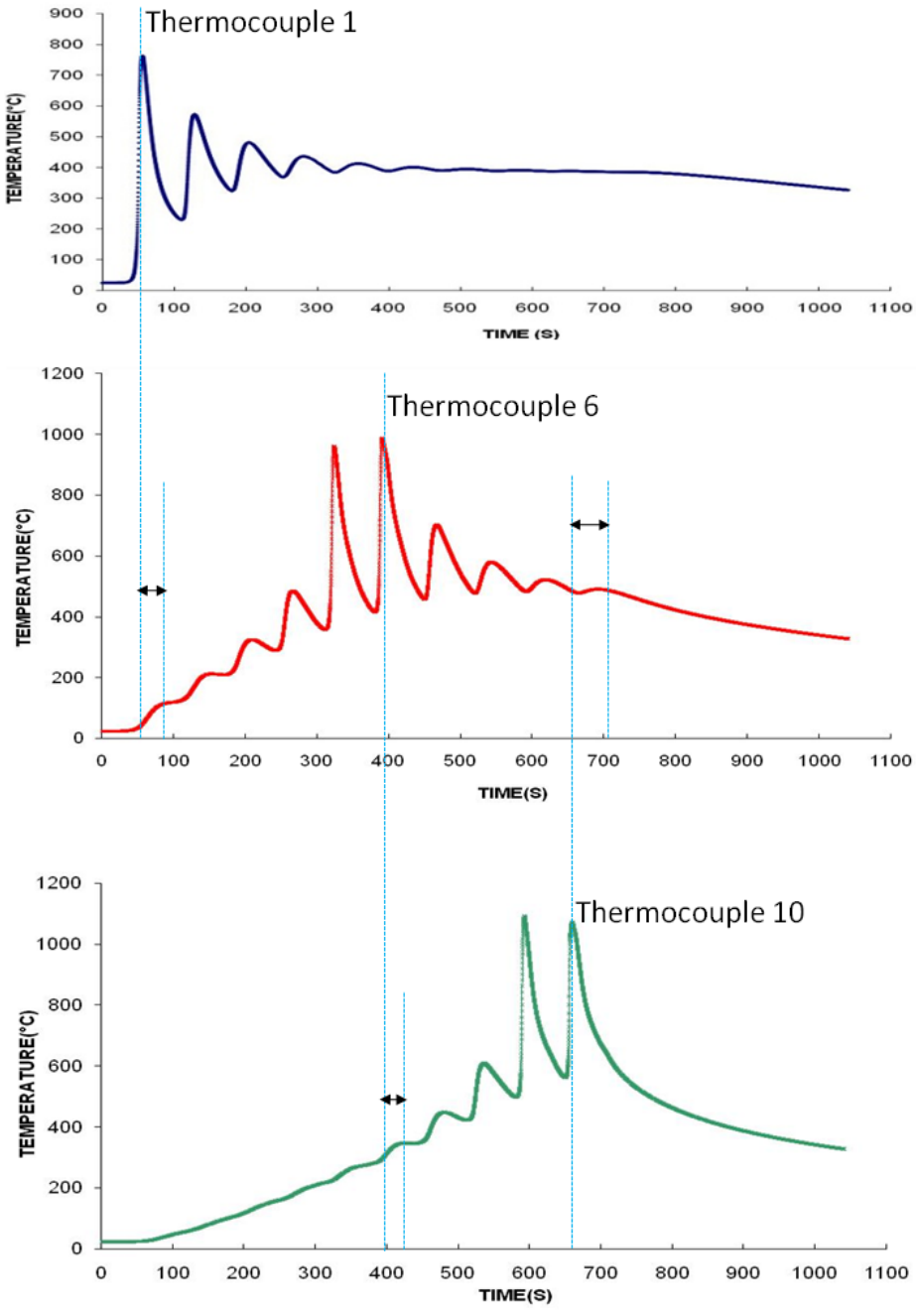

Figure 3.20: Temperature variations with measured at various distances from the heat source

3.2 Single bead clad experimental study

The cladding quality is function of the geometry and metallurgical structure of the deposited layer and heat affected zone of the base metal. The geometrical parameters like bead width, reinforcement, penetration and wetting angle affects the fatigue strength and cladding layer defects. The metallurgical structure largely depends on the dilution rate and nominal energy of the cladded beads. Nominal energy is the indicator of the weld bead cooling rate. The chemical composition of the cladded surface is defined by the dilution rate which affects directly the physical properties like corrosion resistance, hardness and thermal expansion etc. of the deposit which are function of the cladding process variables and thermo-mechanical cycle of the process. Following section is related to the experimental analysis of single bead cladding.

3.2.1 Parametric study of important process parameters

GMA cladding process variables may be classified as **the primary parameters** like wire feed speed (current), arc voltage and welding speed and **the secondary variables** like torch angle, stick-out distance, nozzle to work piece distance, welding direction and position as well as the flow rate of shielding gases. There are some **fixed parameters**, like wire diameter and its composition, type of protective gas which are defined before starting the welding process and cannot be changed during the process. All these parameters must be matched to each other for optimum welding performance. Main variables of the GMA cladding process are shown schematically in figure 3.21.

The parametric study of single bead cladding is restricted to three primary process variables i.e. voltage, wire feed speed and welding speed. In the literature (Kannan & Yoganandh, 2010; Palani & Murugan, 2006; Rao *et al.*, 2009), there are several articles providing examples of parametric study of integrating other welding parameters such as welding angles or contact tip to work piece distance. It is therefore possible to apply the approach presented here by incorporating other welding parameters. The experiments are performed with a robotic GMAW device consisting of a 6 axis poly-articulated robot and a generator CY385 MPR.

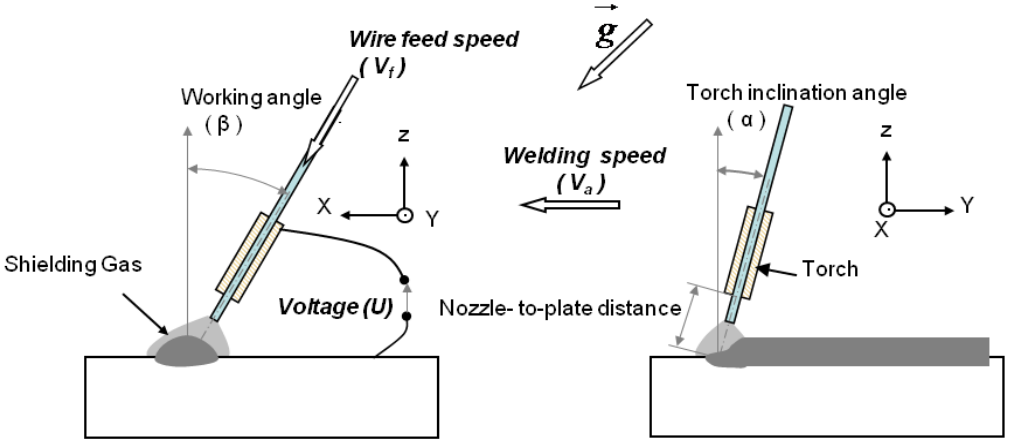

Figure 3.21: Important GMA cladding process parameters.

Determining the Process parameters range The working range of all selected parameters was fixed by conducting trial runs and was decided by inspecting the weld bead for a smooth appearance and the absence of visible defects such as surface porosity, undercut and for the stable cladding process. It was noted that too small stick-out distance, increases the risk of burn-back and the fusion of the filler wire with the contact tip while the too high value caused the difficulty of the bead starting. The chosen set of process variable exhibits the three metals transfer modes depending on the selected current intensity and voltage range.

Implementing the investigation plan According to the proposed methodology, chosen input process parameters are wire feed speed V_{fil}), welding speed V_a), and arc voltage (U). The chosen responses were weld bead width (L), depth of penetration (d), height of reinforcement (r), bead wetting angle (θ) and dilution rate (δ) as shown in figure 3.22. All the input and out cladding parameters are illustrated in the Figure 3.23.

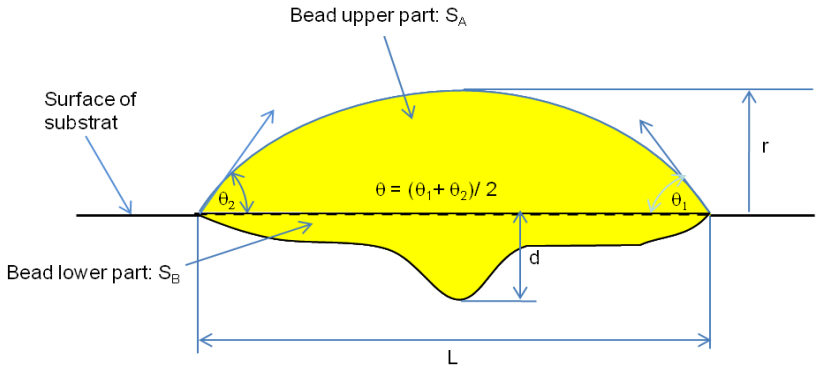

Figure 3.22: Important clad quality parameters.

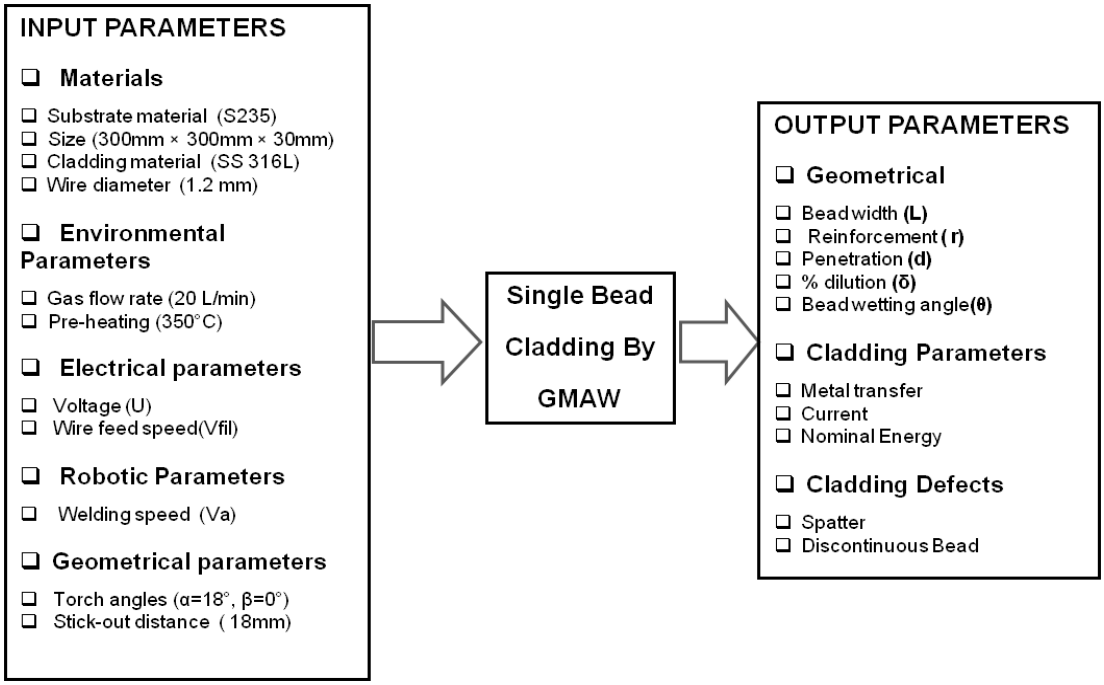

Figure 3.23: Schematic representation of input and out put cladding parameters for GMAW process

Process parameters levels The experimental plan is carried out in three levels of each parameter. This allows us to take into account the variations in the metal transfer mode that can be a potential factor for the discontinuities in the weld bead geometrical evolution laws as a function of welding parameters. The upper limit of the parameter was coded as +1 and the lower limit was coded as -1 while 0 was assigned for intermediate value. The coded values for intermediate values can be calculated using the following expression.

$$X_i = \frac{2X - (X_{max} + X_{min})}{(X_{max} - X_{min})} \tag{3.83}$$

Where X_i is the required coded value of a parameter X. X is any value of the parameter from X_{min} to X_{max}, X_{min} is the lower limit of the parameter and X_{max} is the upper limit of the parameter. Levels of selected process parameters are shown in table 3.2.

level	Wire feed speed (m/min)	Welding speed (mm/s)	Voltage (Volts)
1 (low)	3.5	2.5	20
2 (medium)	5	4.5	24
3 (high)	6.5	6.5	28

Table 3.2: Levels of selected process parameters

Robot programming The robot is programmed to weld from one point to the next for a required bead length in flat position on the substrate plate. The coordinates of the positions are saved in the robot's memory along with the associated instructions by using software ROBONUM 800. For single bead cladding, the position, bead length, torch angles and welding speed are programmed on robot and other welding data such as wire feed speed and voltage are controlled by the welding machine generator.

Materials The substrate used is low alloy steel S235 plate of size $300mm \times 300mm \times 30mm$ and its surface was sand blasted to remove oxide scale and dirt before cladding. SS 316 LSi wire of 1.2 mm diameter was used for depositing the clad beads. Chemical composition of the base metal and cladding wire and cladding metal are given in table 3.3.

	C	Si	P	S	Cr	Mn	Fe	Ni	Cu	Mo	N
Cladding Metal	0.03	.65-1	≤0.02	≤0.03	18-20	1-2.5	Bal.	11-14	-	2-3	-
Substrat	0.1	0.9	0.04	0.04	-	0.9	Bal.	-	0.55	-	0.012

Table 3.3: chemical composition of substrate and cladding metal.

A total of 27 beads were performed (see the Figure 3.24) by varying one parameter and keeping the rest constant.

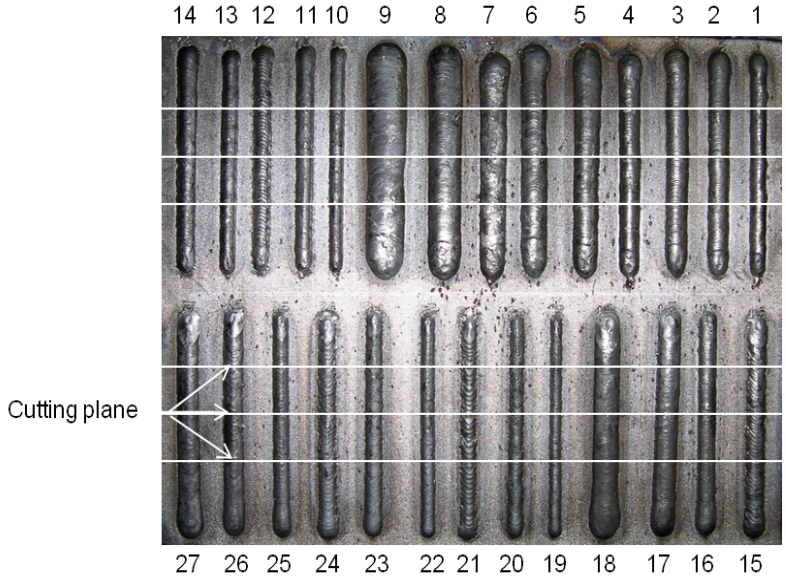

Figure 3.24: Single bead deposition according to investigation plan

Each set of parameters is performed three times to obtain a reliable estimate of of result's repeatability. After each bead, the temperature of the plate is measured

with a contact thermocouple. The maximum temperature allowed is kept at 50°C and waiting time is introduced when necessary lowering the temperature to avoid the effect of preheating on the intermediate weld bead. The affect of selected process parameters on clad quality parameters was studied and results are shown in Table 3.4 showing the mean values of each output parameter of the all performed experiments.

3.2.2 Single bead characterizing results and statistical laws

As discussed above, the clad quality parameters for single bead cladding were determined by repeating the experiment three times. To ensure the robustness of the statistical laws, each bead was analyzed at three different sections as shown by the cutting planes in the Figure 3.24.

Dilution rate calculation Dilution rate, which is the percentage of base metal in the weld metal deposit is calculated geometrically. The geometric parameters of the weld beads are measured on three sections but in statistical studies, average of all the measured values is used. The dilution rate is estimated by calculating the ratio between the surface of the weld bead located above the original surface of the substrate and the total area of the weld bead (see Figure 3.22).

3.2.2.1 Dispersion of clad quality parameters in three experimental sets

The variation in clad quality parameters was observed while repeating the experiments (see Table 3.5) as well as in the same experiment when the bead was cut at different sections as shown in figure 3.24. In the table 3.5, $\%\Delta L$, $\%\Delta r$, $\%\Delta\theta$ are the percentage variations for different experimental sets for bead width, height and wetting angles respectively.

We notice in general that the dispersion of geometrical parameters is most important for the largest voltage and the lowest wire speed values. These parameters correspond to a transfer mode with big drops and are more remarkable in beads with streaks of solidification.

Welding speed	wire feed speed	voltage	Current	Bead Width (ave,)	Reinforcement (ave,)	Penetration (ave,)	dilution	wetting angle	Transfer mode
Va	Vf	U	I	L	r	d	б	Φave	
(mm/s)	(m/min)	Volts	A	mm	mm	mm	%	◦	
2,5	3,5	20	135	9,30	4,21	0,74	8	80	globular
2,5	3,5	24	139	11,36	3,55	1,17	18	61	globular
2,5	3,5	28	158	11,43	3,44	1,81	22	63	globular
2,5	5,0	20	166	10,95	4,37	1,52	15	80	transition
2,5	5,0	24	171	13,52	3,86	2,56	25	66	transition
2,5	5,0	28	193	13,77	3,92	2,90	28	65	transition
2,5	6,5	20	203	12,89	5,11	1,40	13	89	transition
2,5	6,5	24	210	16,49	4,25	2,06	21	65	transition
2,5	6,5	28	242	19,17	3,79	2,80	27	60	spray
4,5	3,5	20	132	7,53	2,70	1,32	25	60	transition
4,5	3,5	24	140	8,85	2,45	1,23	27	54	globular
4,5	3,5	28	143	9,41	2,30	1,55	30	50	transition
4,5	5,0	20	167	9,09	3,04	1,64	25	60	transition
4,5	5,0	24	172	10,78	2,68	1,99	31	57	globalar
4,5	5,0	28	193	11,11	2,89	2,19	26	54	transition
4,5	6,5	20	201	10,30	3,82	1,51	17	65	transition
4,5	6,5	24	205	12,56	3,26	1,96	27	54	transition
4,5	6,5	28	233	13,99	2,95	2,83	35	55	spray
6,5	3,5	20	133	6,83	2,29	1,16	27	55	transition
6,5	3,5	24	142	7,70	1,98	1,07	29	44	globulat
6,5	3,5	28	150	8,25	1,96	1,06	25	42	globular
6,5	5,0	20	158	7,84	2,63	1,37	26	55	transition
6,5	5,0	24	172	9,31	2,37	1,54	30	53	transition
6,5	5,0	28	192	9,45	2,29	1,81	31	50	globular
6,5	6,5	20	202	9,16	3,22	1,51	23	60	transition
6,5	6,5	24	207	11,07	2,67	1,85	32	45	transition
6,5	6,5	28	235	11,99	2,53	2,90	38	45	spray

Table 3.4: Single bead output parameters

No. of bead	V_a (mm/s)	V_f (m/min)	U Volts	%ΔL %	%Δr %	%Δθ %
1	*2,5*	*3,5*	*20*	12	10	29
2	2,5	3,5	24	7	9	17
3	2,5	3,5	28	2	8	8
4	2,5	5,0	20	11	14	21
5	2,5	5,0	24	8	8	5
6	2,5	5,0	28	21	16	11
7	2,5	6,5	20	5	13	13
8	2,5	6,5	24	4	13	7
9	2,5	6,5	28	2	21	4
10	4,5	3,5	20	6	7	3
11	4,5	3,5	24	7	15	7
12	4,5	3,5	28	16	9	14
13	4,5	5,0	20	6	3	5
14	4,5	5,0	24	9	5	5
15	4,5	5,0	28	27	31	17
16	4,5	6,5	20	9	5	3
17	4,5	6,5	24	7	5	5
18	4,5	6,5	28	11	7	10
19	6,5	3,5	20	16	5	9
20	6,5	3,5	24	17	14	23
21	6,5	3,5	28	12	7	4
22	6,5	5,0	20	9	9	6
23	6,5	5,0	24	21	8	9
24	6,5	5,0	28	27	2	20
25	6,5	6,5	20	17	15	0
26	6,5	6,5	24	5	3	1
27	6,5	6,5	28	3	3	2

Table 3.5: Variations in the clad quality parameters for three experimental sets

3.2.2.2 Single bead clad quality statistical laws

From the results of the Table 3.4, statistical laws related to the geometrical parameters of the weld bead, the dilution rate and the current intensity as a function of welding parameters have been identified.

$$Y = X_o + aV_a + bV_f + cU + eV_aV_f + fV_fU + gUV_a \tag{3.84}$$

The value of constants (a,b,c,d,e,f and g) was calculated by the technique of least square method. Although the statistical laws are multi-linear functions of dimensionless cladding parameters derived from the relation 3.83. These are obtained by a linear transformation of the actual welding parameter such as the minimum and maximum welding parameter is dimensionless real value of -1 and 1 as discussed above yet the laws with the real values of the process variables are also derived. The output parameter equations applicable in the applied range of process parameters derived from the real values are given as:

$$r = 4.29 - .58V_a + .62V_f - .03U - .005V_aV_f + .01V_fU - .02UV_a \tag{3.85}$$
$$L = 1.69 - .88V_a + .09V_f + .15U - .16V_aV_f - .05V_fU + .08UV_a \tag{3.86}$$
$$\theta = 146.5 - 13.8V_a + 2.28V_f - 2.3U + 0.46V_aV_f + .24V_fU - .2UV_a \tag{3.87}$$
$$\delta = 38.69 + 3.86V_a - 12.03V_f - 1.02U + .1V_aV_f - .08V_fU + .5UV_a \tag{3.88}$$
$$I = 55.64 + 8.60V_f + 0.655U \tag{3.89}$$

3.2.2.3 Sensitivity of the clad bead form

The effect of cladding parameters (dilution rate and weld bead geometry) on the single bead geometry and dilution rate is shown globally in table 3.6.

Several studies correlating bead dimensions with process parameters are reported for different welding processes (Kannan & Yoganandh, 2010; Palani & Murugan, 2006; Rao *et al.*, 2009) for predicting bead geometry for different welding processes which shows the same tendencies globally, as shown by the results in the Table 3.6.

	Current	Reinforcement	Bead Width	Wetting angle	Dilution rate
Voltage ↗	≈	↘	↗	↘	↗
Wire feed speed ↗		↗	↗	≈	↗
Welding speed ↗	≈	↘	↘	↘	↗

Table 3.6: Global effect of the cladding parameters on the geometry and dilution rate of single bead

Bead profile irregularity defect We notice in general that the dispersion of geometrical parameters is most important for the larger voltage and the lower wire feed speeds values. These parameters correspond to an intermittent metal transfer mode with big drops. The bead profile irregularity defect becomes more remarkable in beads with streaks of solidification due to this metal transfer mode as shown in Figure 3.25.

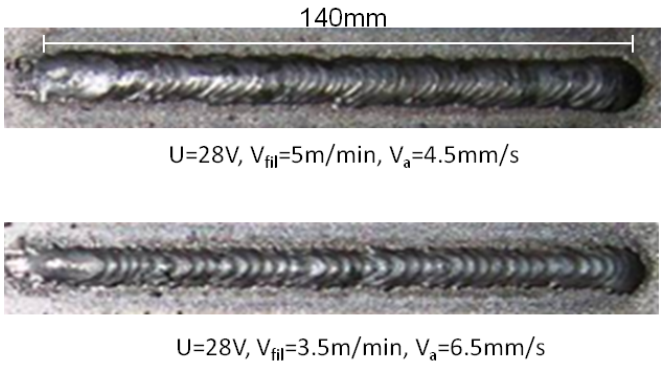

Figure 3.25: Bead irregularities for selected parameters

3.2.2.4 Effect of torch inclination

The torch inclination angles help in utilizing the natural arc force to push weld metal against vertical surface to provide good bead contour by torch angle ma-

nipulation and improve the penetration in the precedent bead toe in case of multi-bead deposition. They influence the bead fusion and arc forces, acting on the weld-pool metal. The welding torch inclination angle (working angle) may transform the bead's maximum penetration area position caused by the "Marangoni effect". It was observed experimentally that the bead profile becomes non-symmetric with increase of torch inclination angle (β) from 0° and 30° while keeping α constant at 18°. The macrographs are shown in the Figure 3.26.

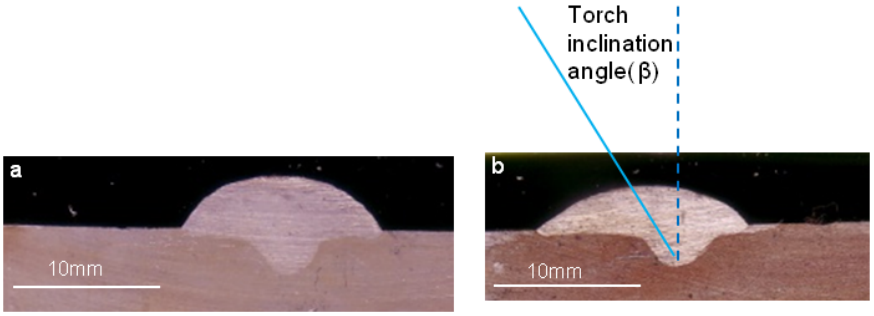

Figure 3.26: The effect of torch inclination on bead profile at the torch working angle = 0° (a) and inclined at 30° (b)

3.2.3 Validation of the bead profile representing functions

In this section, real bead profiles are compared with the profiles achieved by different proposed functions.

Validation of beads having limiting Form Factors The Figure 3.27 shows the comparison of different proposed bead profile models with the real bead profile (deposited at high voltage of 28 V, highest welding speed of 6.5 mm/s and a wire feed speed of 3.5 m/min) having a low form factor (3.4). In this case the bead profile model represented by the arc of ellipse function gives the worst approximation of the real bead profile. Although the form factor is near the lower limit range as described by 4 degree symmetric polynomial functions yet it shows good approximation.

The figure 3.27 also demonstrates the profile curvature at the weld bead toe

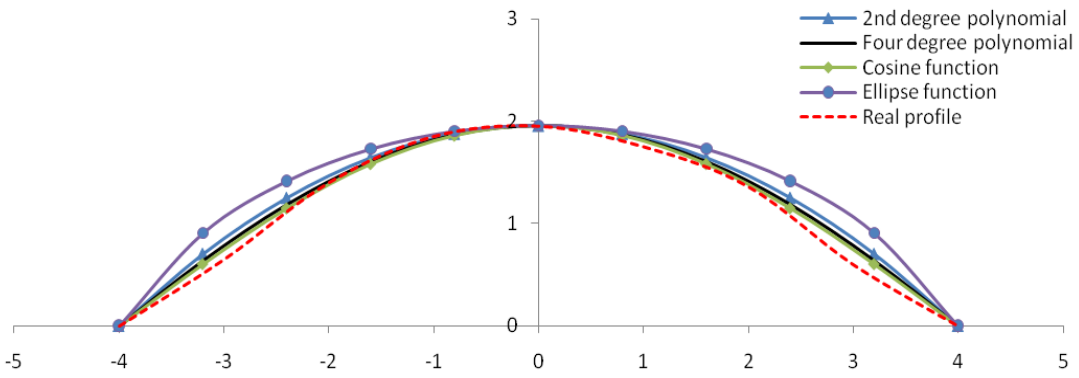

Figure 3.27: Superposition of different bead profile functions on real bead profile(values along x and y-axis in mm) with low form factor=3.4

becomes positive with low form factor. This type of bead profile may be seen experimentally with cladding parameters of high voltage and welding speed and low wire feed speed.

The Figure 3.28 shows the comparison of different proposed bead profile models with the real bead profile (deposited at lowest voltage of 20 V, lowest welding speed of 2.5 mm/s and highest wire feed speed of 6.5 m/min) with a high form factor (12.5). In this case the bead profile model represented by the ellipse function gives best approximation of the real bead profile which means for high form factor values, the ellipse function shows better approximation compared to the other proposed functions. As for the form factor (see the equation ()), values greater than 8, the symmetrical four degree polynomial profile shows two maxima with a large deviation from any real bead profile and we can say the form factor of this bead is out of range of the "true limit".

Comparison of different selected bead profile The Figure 3.29 shows the comparison of different proposed bead profile models with the real bead profile of some selected beads with the form factor within the applicable range of the model considering 4 degree symmetric polynomial. It is obvious that the bead profile represented by the 4 degree symmetric polynomial is good approximation of the

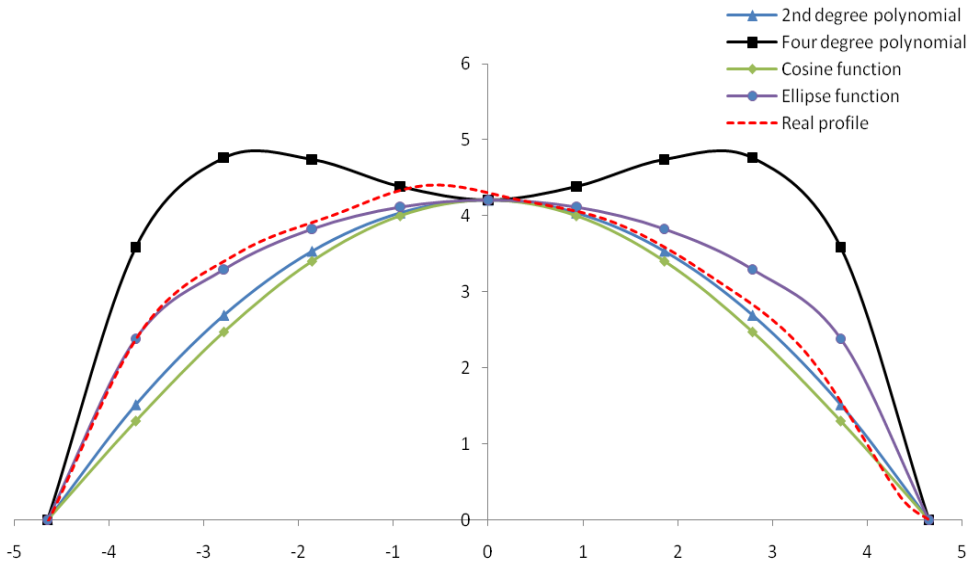

Figure 3.28: Superposition of different bead profile functions on real bead profile (values along x and y-axis in mm) with high form factor=12.5

real bead profile for all the selected beads. The analysis shows that ellipse arc function is not suitable to represent the beads with small form factors while for high form factor the functions with two degree of freedom are not applicable. The bead profile represented by a polynomial of 4 degree gives a good approximation for a large variety of form factors (from 3.2 to 8).

3.2.4 Conclusion

This section is related to the experimental analysis to determine the clad quality parameters for single bead cladding. The results show that the geometrical parameters like bead width, reinforcement and wetting angle largely depend on the input cladding parameters. The chemical composition of the cladded surface is determined by the dilution rate which is determined geometrically here. The experimental plan allows us to take into account the variations in the metal transfer mode that can be a potential factor for the discontinuities in the weld bead geometrical evolution laws as a function of welding parameters.
The statistical laws are derived by the technique of least square method. We

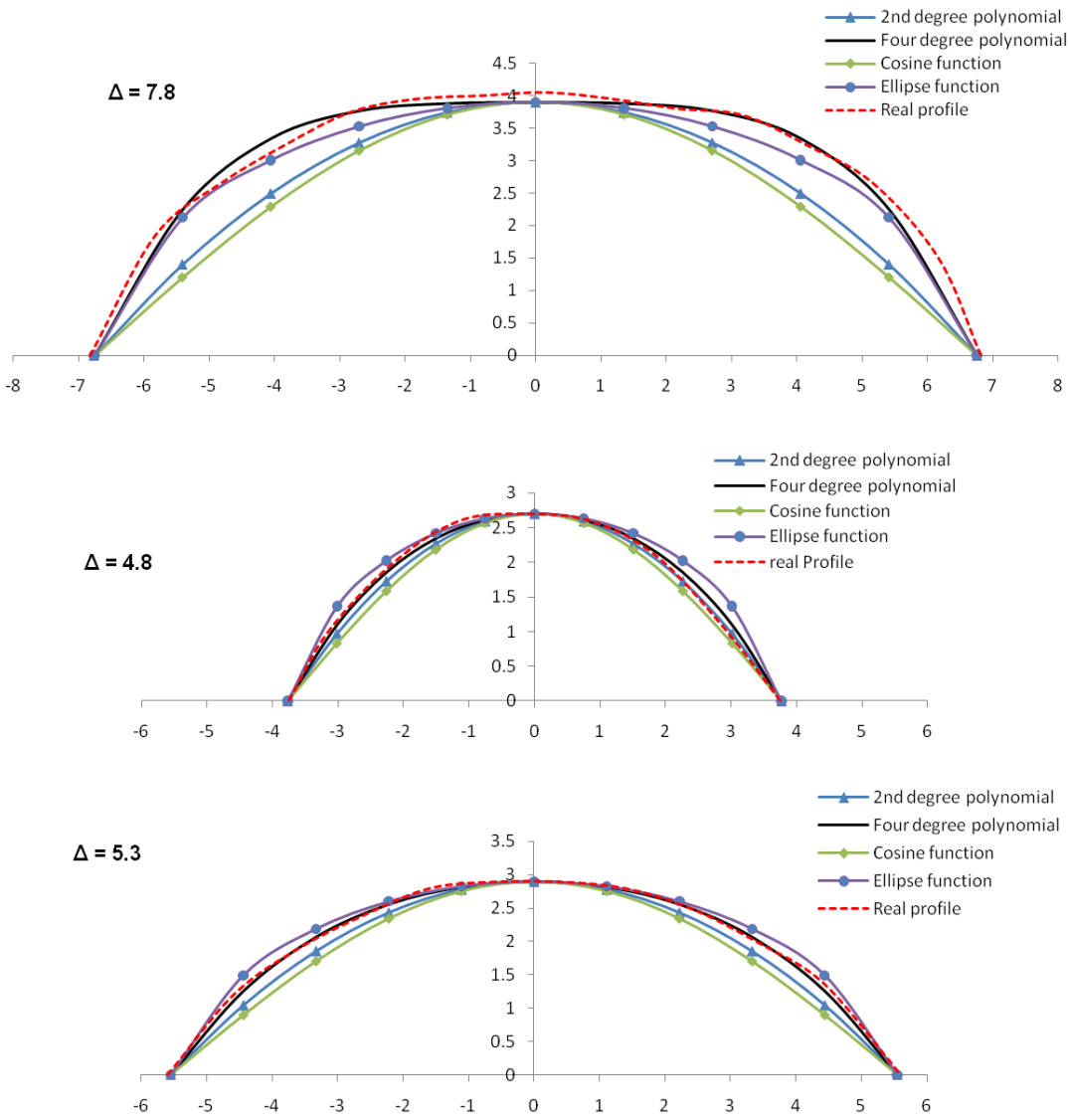

Figure 3.29: Comparison of different proposed bead profile models with real bead profile(both axis in mm)

notice in general that the dispersion of geometrical parameters is most important for the larger voltage and the lower wire feed speeds values. These parameters correspond to an intermittent metal transfer mode with big drops. The bead profile irregularity defect becomes more remarkable in beads with streaks of solidification due to this metal transfer mode. The torch inclination angle "(β)" was varied from 0° and 30° while keeping the "α" constant. It was observed that the bead profile becomes non-symmetric with increase of torch inclination angle (β).

The results of the comparison of bead profiles represented by different functions with the real bead profile show that the bead profile represented by the ellipse arc function gives best approximation of the real bead profile for high form factor values while for low form factor values, cosine and 2nd degree polynomial profile shows good approximation. 4 degree polynomial profile shows satisfactory approximation for a large range of form factors while the arc of the ellipse may be considered more suitable for high form factor profiles. At the end, we have obtained the statistical laws relating the geometrical parameters of the bead with the welding input parameters and the bead profile representation is validated by a polynomial of 4 degree. In the coming part we will apply and validate the proposed overlapping models for the layer cladding process.

3.3 Single layer cladding study

In this section, we will study the layer cladding process by varying the bead center to center distance (offset distance) according to the already proposed two criteria as well as the limiting values (upper and lower) of the bead center to center distance, to identify the cladding phenomena defects. For layer cladding, automatic GMAW process was applied to deposit clad beads on the substrate by a programmed sequence of single bead deposition at a certain offset distance which adds to the complexity of cladding process and partial remelting occurs while depositing the next bead.

3.3.1 Parametric study related to the offset distance for single layer cladding

To achieve a uniform top surface along the single layer cladding, two beads are deposited close enough so that the deficit of material along the edges gets compensated for by an overlap between the beads. The melting of the beads during the deposition process causes extra smoothness along the surfaces which may lead to a uniform top surface. The effect of bead offset is studied here to get a smooth layer cladding.

3.3.1.1 Input and Output parameters for single layer cladding

The main input and output parameters for single layer cladding are shown in the Figure 3.30.

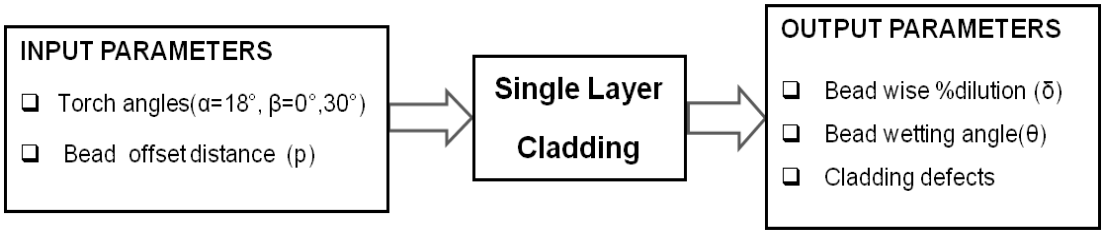

Figure 3.30: Single layer cladding selected parameters

Robot programming The robot was programmed as described for the single bead cladding. Single layer cladding was performed by selected beads with dilution rate of 25% . The beads were deposited in such a way that each bead length is shorter than the precedent one so as the separate effect of each bead on the next can be analyzed. The Figure 3.31 shows the proposed single layer clad strategy.

The Figure 3.32 shows the implementation of the selected parameters according to the above discussed strategy at an overlapping of 40% of the total single

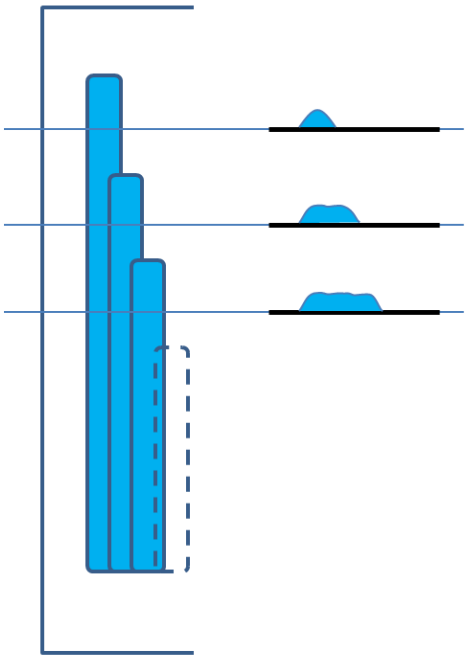

Figure 3.31: Single layer clad strategy for selected parameters

	V_a	V_{fil}	U	L	r	θ	Δ
A	2,5	5	24	13,5	3,9	66	7,8
B	4,5	5	28	11,1	2,9	54	5,3
C	4,5	3,5	20	7,5	2,7	60	4,8

Table 3.7: Selected parameters for single layer cladding

bead width. The input process parameters applied along with some clad quality parameters are also shown in the table 3.7.

3.3.1.2 Trials performed for single layer cladding

In this section, we will study the layer cladding process by varying the bead center to center distance according to the proposed two criteria. The limiting values (upto 75%) of the bead overlappings are also tried to identify the cladding limiting defects phenomena as shown in figure 3.33.

Figure 3.32: Single layer clad strategy for selected parameters at 40% overlapping

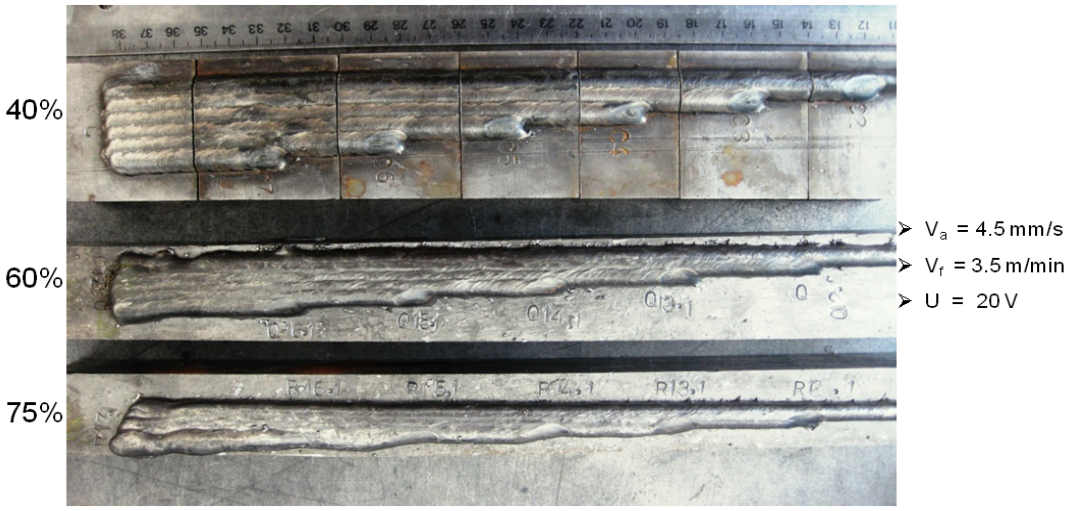

Figure 3.33: Single layer clad overlapping trials by using the parameters A of the table 3.7

3.3.1.3 Single layer cladding limiting phenomena

To identify the cladding limiting phenomena all the selected parameters were deposited at different overlapping rates. To highlight the stainless steel 316L clad overlapping of one bead on the other, etching with Fry's reagent (90g CuCl,

120ml HCl, 100ml H_2O) for a few seconds was performed. The macrographic observations (see the Figure 3.34) show that for high values of overlapping, there appears a lack of penetration or sticking with the progressive deposition of beads due to the increase of the wetting angle of higher beads. We can see that the wetting angle values greater than 90° make it inaccessible for the weld bead toe of the precedent bead.

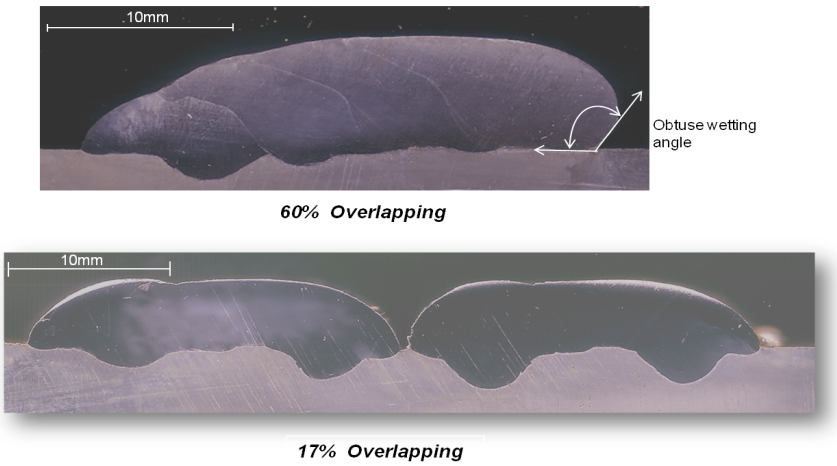

Figure 3.34: Macrographs of the single layer clad overlapping trials by using the parameters A of the table 3.7

One the other hand, lower overlapping values, cause a lack of superposition defects after each pair of cladded beads (for 17% overlapping). For low values of overlapping some beads are disjoint. This may be due to the combination of two factors as explanied in the Figure 3.35 with three beads macrographs are presented with the overlapping of 17 % for the sections of first three beads. The deviation from the proposed height criteria may be explained by the following reasons. Firstly, the bead offset distance or the overlapping width is calculated from the average values of its geometrical parameters and estimated by the statistical laws. The reason of dispersions in these values associated with the statistical model error is that, in our case, the bead width used is lower than the value estimated by the statistical laws. In practical, the actual overlapping is 14 % of the total bead width rather than 17 %. Second reason may be the occurrence of some contradiction in the overlapping model assumptions and arc deviation due to the

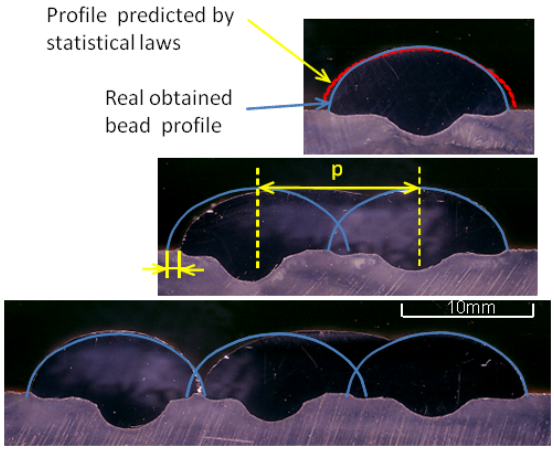

Figure 3.35: Macrographs of the first, second and third bead for 17 % overlapping by using the parameters A of the table 3.7

presence of the precedent bead. Due to the above two phenomena the third bead is deposited with a zero overlap. This is due to the high value of the form factor of the weld bead which makes the value of the overlapping rate very sensitive to geometric variations of the weld bead.

3.3.1.4 Cladded layer overlapping effect

Lower overlapping values, cause a lack of superposition defect after each pair of cladded beads (see Figure 3.36 for 17% overlapping). The reason may be the deviation of the electric arc due to the precedent bead and the next pair of beads is separated due to insufficient overlapping. On the other hand, higher overlapping values and too much superposition of consecutive beads cause high wetting angles values, reaching even higher than 90°(see Figure 3.36 for 60% overlapping), the bead toe of the precedent bead due to excess of material make it inaccessible for the current bead to attain the required penetration.

3.3.2 Validation of overlapping models

The clad overlapping distance, p_A shows satisfactory results for all cladding parameters and bead geometries. This criterion of optimum overlapping distance,

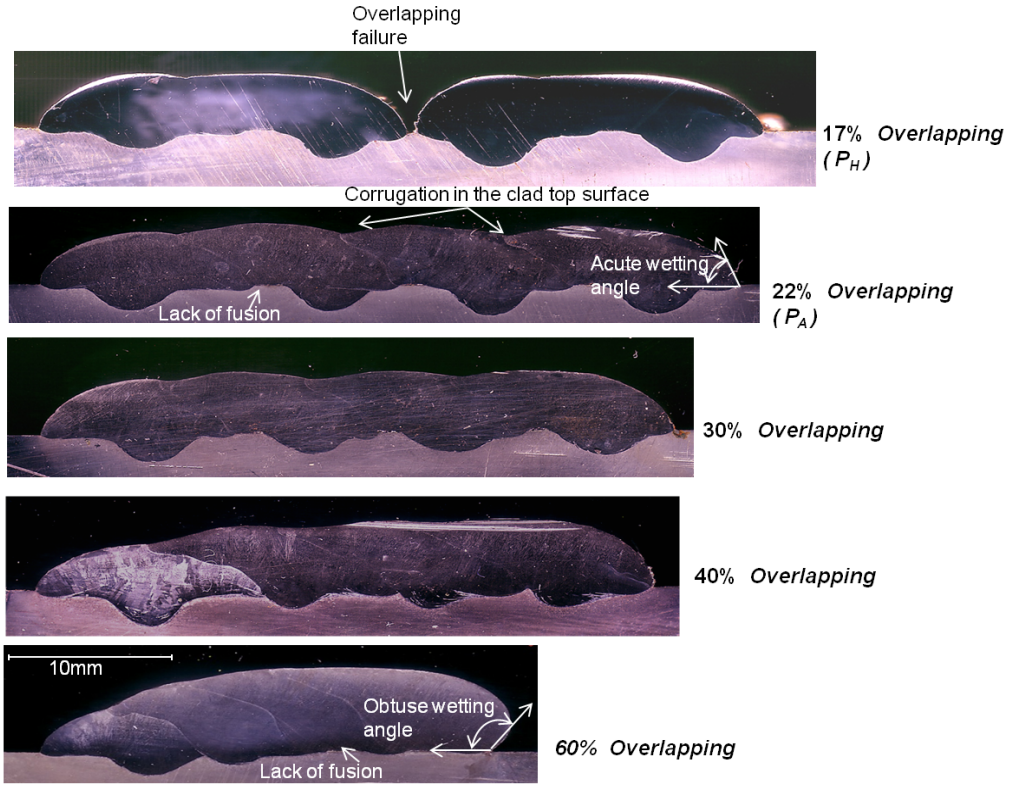

Figure 3.36: Effect of bead overlapping on single layer clad quality by using the parameters A of the table 3.7.

can possibly obtain a compact coatings with a less corrugation defect at the surface of the cladding. On the other hand, cladding overlapping distance p_H shows a high sensitivity to geometric variations of the weld bead and becomes significant for the overlapping defects of weld beads for high values of the form factor.

The Figure 3.37 shows macrographs obtained with the last two sets of parameters (B and C of Figure 3.32) for the overlapping calculated by using the two proposed criteria. We observe that in all cases, the layer is compact with a very slight variation in the coating thickness compared to the first weld bead. The corrugation defect in top surface is of the same order of magnitude for both criteria.

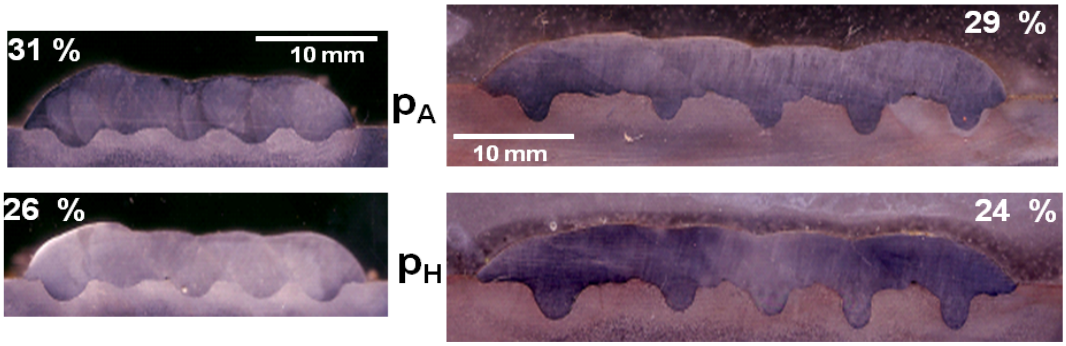

Figure 3.37: Single layer clad overlapping models implementation by using the parameters B and C of the table 3.7

3.3.3 Single layer cladding analysis

Single layer cladding is the result of the juxtaposition and partial overlapping of beads which may cause some unevenness in the successive beads. It is observed that a "geometrical equilibrium state" in the overlapping geometry is established beyond a certain number of beads which plays an important role for the clad layers analysis.

3.3.3.1 Torch inclination angle setting for single layer cladding

The bead wetting angle "θ" increases with the increasing number of beads but this effect is decreased remarkably when deposited with β=30°. The Figure 3.38 shows that the bead wetting angles decrease with increase of torch inclination angle (β) when changed from 0° and 30° while keeping α constant as 18°(see the figure 3.21) and performed at different overlapping rates. The analysis was also performed for 60% overlapping of the adjacent beads and same trend was observed.

The inclination of the torch, decreases the bead wetting angle making the precedent bead toe more accessible by virtue of the arc force direction. The Figure 3.39 shows the effect of torch inclination angle on the bead wetting angles (θ) which are deposited at different torch working or torch inclination angles (β) while fixing all the other parameters.

Single layer cladding was performed by selected beads with a calculated dilution

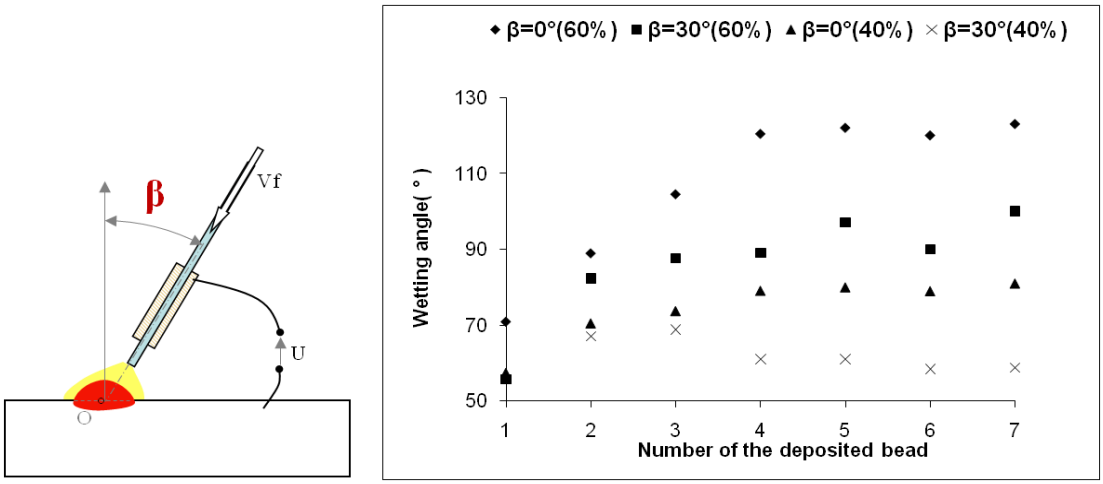

Figure 3.38: Effect of working angle (β) and overlapping rate on the bead wetting angle

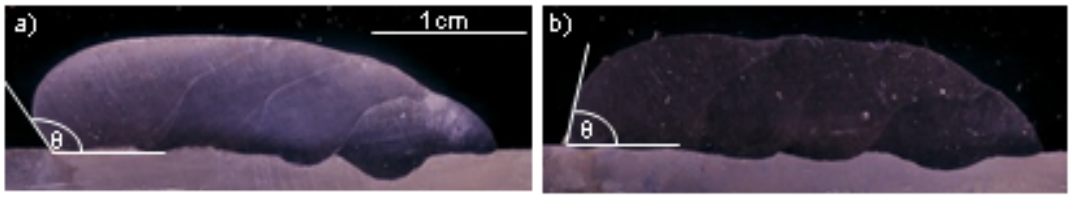

Figure 3.39: Effect of torch inclination angle (β=0°(a) and β=30°(b)) on the wetting angle

rate of 25%. The beads were deposited in such a way that each bead length is shorter than the precedent one so that the separate effect of each bead on the next can be analyzed. The Figures 3.40 and 3.41 shows the single layer cladding of 7 beads deposited at an overlapping of 40% with torch inclination angle β of 0° and 30° respectively. We may observe from the macrographs that the bead wetting angle for β =30° is smaller than for the beads deposited at β =0°.

3.3.3.2 Evolution of dilution rate

The Figure 3.42 shows variation in the dilution rate as a function of the weld bead number for cladding performed with the parameter A (of the Figure 3.32) and with three different overlapping distances (40%, 30% and 22%). The first bead has the highest dilution rate. The dilution rates of the beads deposited after first bead are lower due to the overlap but fluctuate due the variations in the remelted area of the previous bead. This surface varies significantly especially for the lowest overlapping rate due to higher sensitivity of the lower overlapping to the arc deviation and the periodic variation in the dilution rate of the 22% overlapping layer second this phenomenon. The figure 3.42 shows that even number beads exhibit lower dilution rate than the odd number beads and this effect can be found in the geometry especially beads height of the figure 3.43.

3.4 Quality of the cladding

This section provides some primary elements to characterize the properties of the cladding taking in account the dilution rate and nominal energy. The cladding hardness and microstructure are determined at different locations for single bead cladding.

3.4.1 Cladding hardness

The hardness analysis of a single bead near interface and top is performed to see the effect of dilution and dissimilar material mixing during the process.

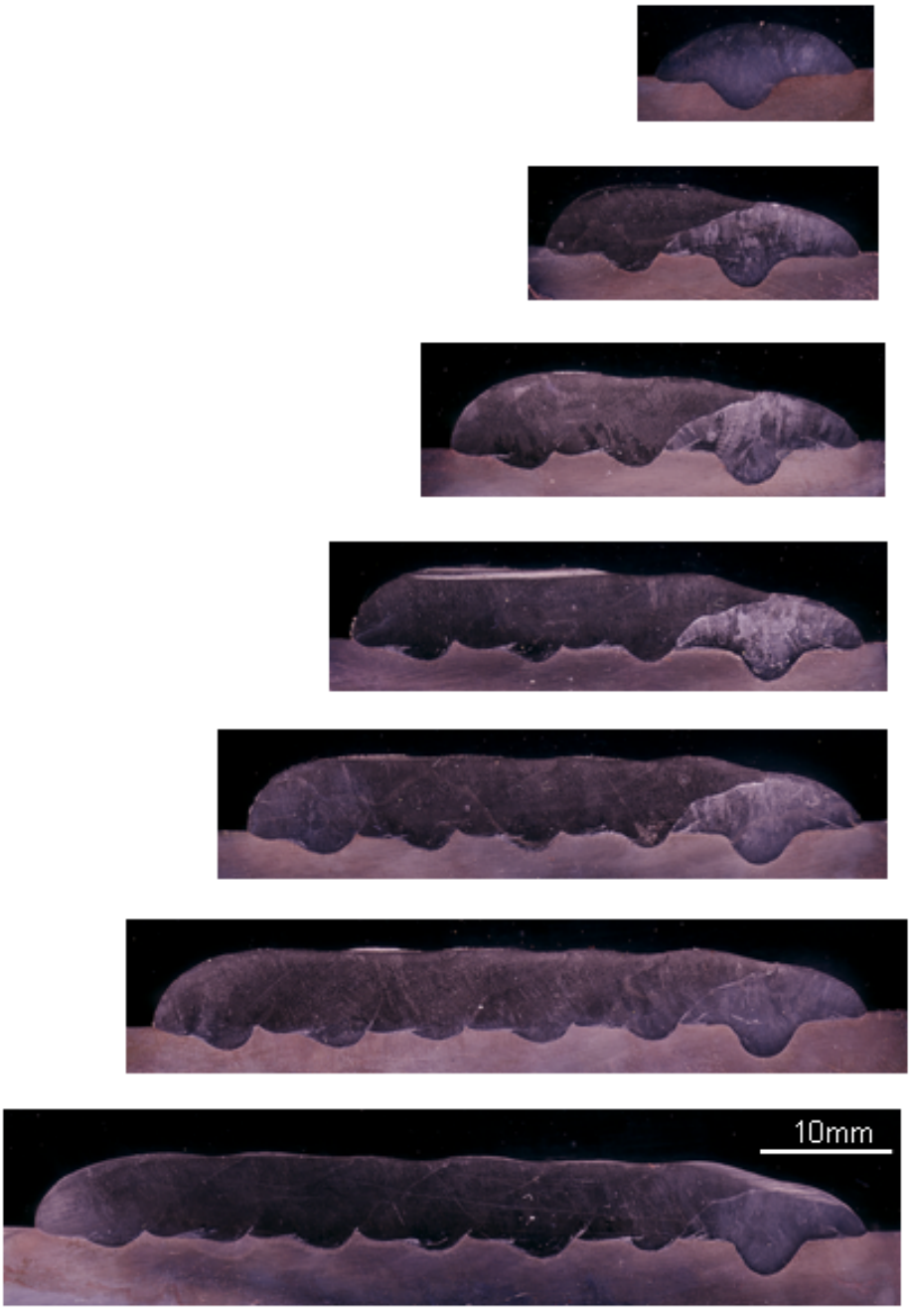

Figure 3.40: Macrographs of 7 beads layer cladding with 40% overlapping deposited with β=0°

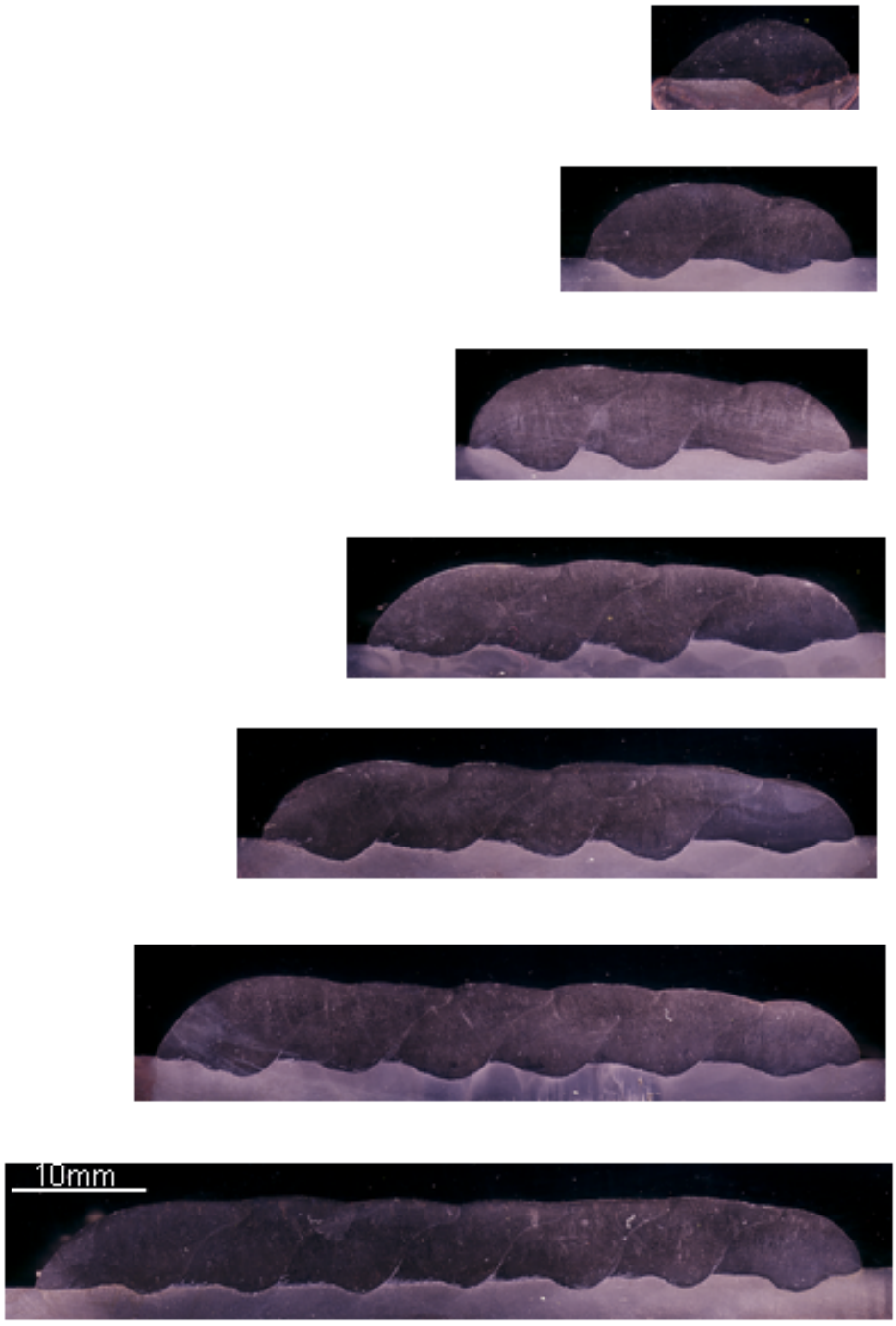

Figure 3.41: Macrographs of 7 beads layer cladding with 40% overlapping deposited with β=30°

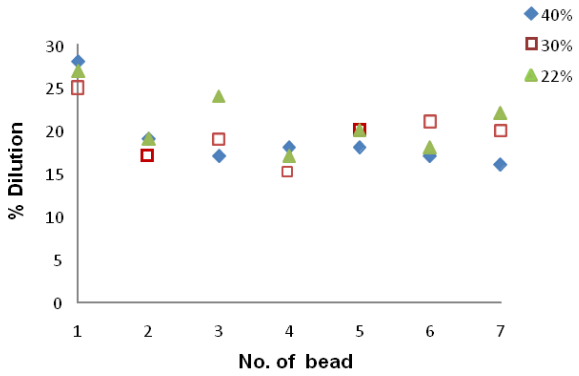

Figure 3.42: Effect of bead overlapping on dilution rate

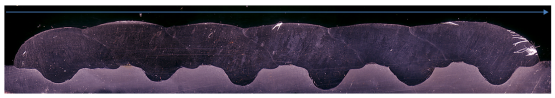

Figure 3.43: The phenomenon of the dilution rate variation for 22% bead overlapping

3.4.1.1 Single bead deposition considering nominal energy and dilution rate

The effect of nominal energy and dilution rate on the clad quality was studied by choosing three sets of experiments with constant values of both for the first set, while changing them alternatively for the next two sets. The process parameters and the values of the nominal energy and dilution rate were calculated statistically. Total 9 macrographs (see the figure 3.44) of the deposited beads according to the experimental plan are determined. The Table 3.8 shows the process parameters and the austenite percentages determined by the X-ray diffraction of the beads deposited at the same and different values of nominal energy and dilution rate calculated statistically.

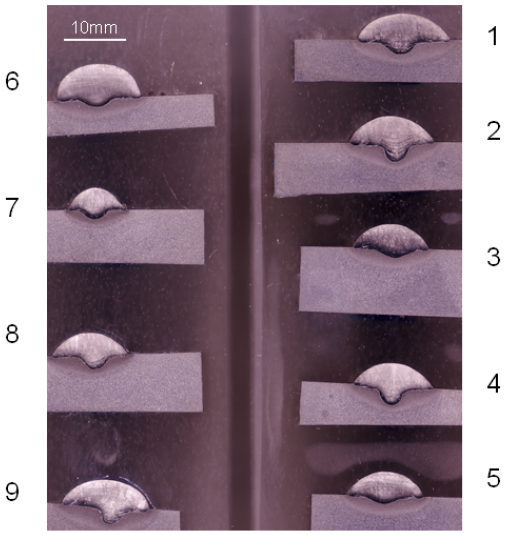

Figure 3.44: Macrographs of the 9 beads deposited considering the Nominal energy and Dilution rate calculated statistically

V_a	V_f	U	Code	En (stat.)	En (real)	I ave	(stat.)	(real)	% Austenite
mm/s	*m/min*	*V*		*J/mm*	*J/mm*	*A*	*%*	*%*	*Rx*
3.7	6.5	24.4	1	1400	1335	202.5	25	22	
3.4	5.5	25	2	1400	1397	190	25	24	
3.1	4	27	3	1400	1394	160	25	24	
4.17	**5.7**	**28**	**4**	**1400**	**1360**	**202.5**	**30**	**28**	**69%**
2.7	3.6	26	5	1400	1420	147.5	23	21	
2.65	**6**	**20**	**6**	**1400**	**1453**	**192.5**	**15**	**13**	**100%**
5.54	**4.8**	**20**	**7**	**575**	**594**	**164.5**	**25**	**22**	**96%**
4.3	5.1	24	8	1000	963	172.5	25	27	
2.93	**4.9**	**26**	**9**	**1600**	**1615**	**182**	**25**	**24**	**100%**

Table 3.8: Table showing the process parameters and austenite percentage calculated by X-ray diffraction of the selected beads

3.4.1.2 Cladded beads hardness

The hardness analysis of a single bead near interface and surface top is performed to see the effect of dilution and nominal energy of the cladding process. The micro hardness at the top and bottom of the beads, deposited at the same and different statistical values of nominal energy and dilution rate are determined.

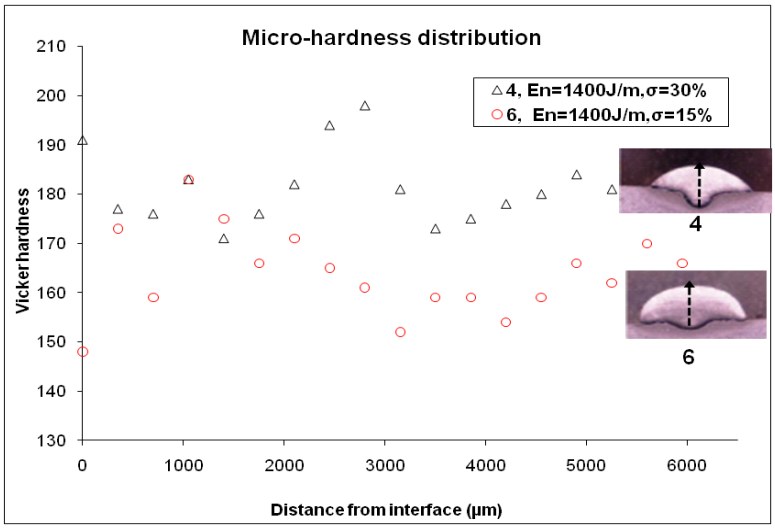

Figure 3.45: Micro hardness (HV 0.3) measured from bead bottom to top having same nominal energy but different dilution rate calculated statistically

It may be observed in the Figure 3.45 that at the same nominal energy, the micro hardness decreases with decrease of the dilution rate. While the figure3.46 shows that there is also a decreasing trend in micro hardness with the decrease of the nominal energy of the deposited bead.

The Figure 3.47 shows the positioning of stainless steel 316 L cladding on S 235 having 25% dilution rate. The ***Schaeffler diagram*** provides approximate microstructure for dissimilar metal welds. The structure obtained may be bi-phase with some percentage of martensite. We can see the beads with higher dilution rate shows higher hardness.

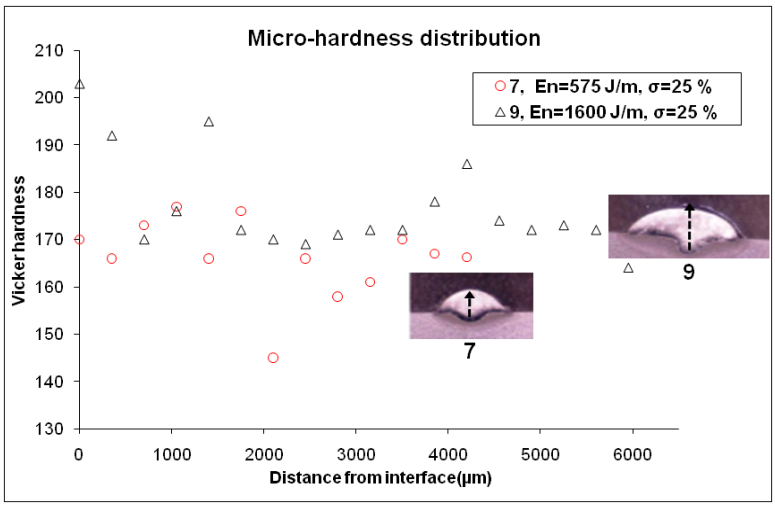

Figure 3.46: Micro hardness (HV 0.3) measured from bead bottom to top having different nominal energy but same dilution rate calculated statistically

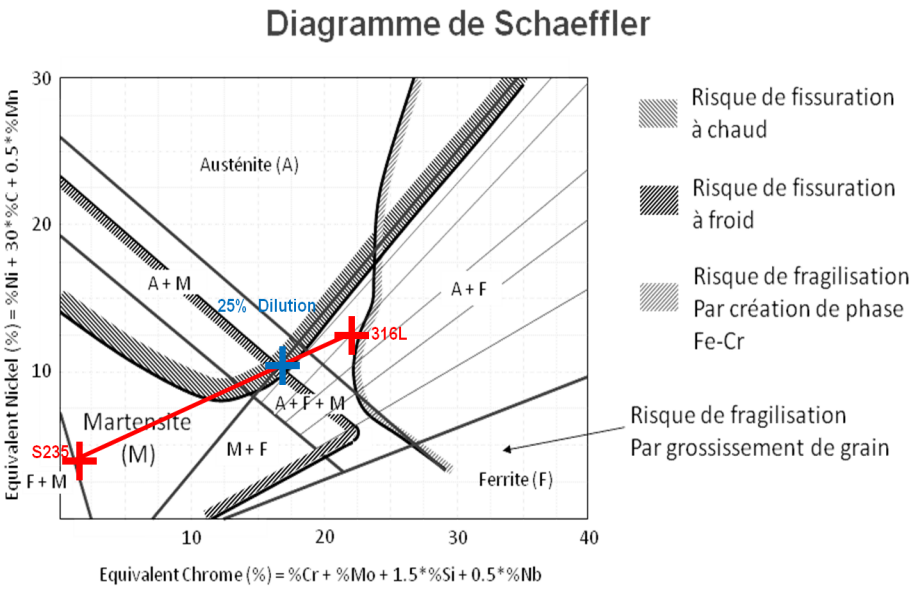

Figure 3.47: Positioning of cladding elements on Schaeffler diagram

3.4.2 Cladded beads metallurgical structure

During GMAW cladding process, the weld pool solidifies on the surrounded solid metal providing a liquid-solid interface at the fusion boundary and highly directional heat flow towards the cold metal. This causes a columnar structure with long grains parallel to the direction of heat flow depending on the heat input as shown in the figure 3.48. The dendrites are more closely spaced for rapid cooling and solidification and grow in the opposite direction to the heat flow, leading to a highly textured material with anisotropic material properties (Pratihar *et al.*, 2009).

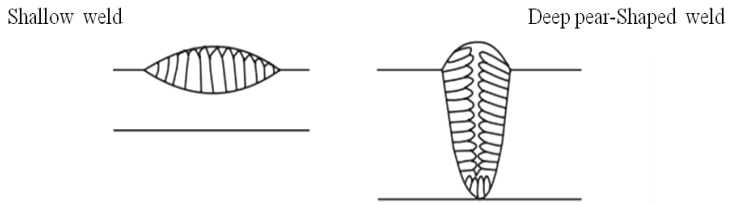

Figure 3.48: Columnar Structure of Welds (Khan, 2007)

3.4.2.1 Micrographic analysis

The microstructure at the different bead locations, deposited at the same and different statistical values of nominal energy and dilution rate is observed by optical microscope after etching with Fry's reagent (90g CuCl, 120ml HCl, 100ml H_2O) for a few seconds.

The Figure 3.49 shows the microstructure of the beads having the same nominal energy and giving the same dilution rate (beads Number 1,2, and 3 in the Figure 3.44) show nearly the same type of microstructure structure. At the bead center (a), same lacy type of microstructure with liquid martix was observed and the bottom (b) shows the same cellular dendritic structure with intergranular liquid phase.

The Figure 3.50 shows the microstructure of the beads having the same % of the austenite and different dilution rate of 15% and 25% respectively (see the

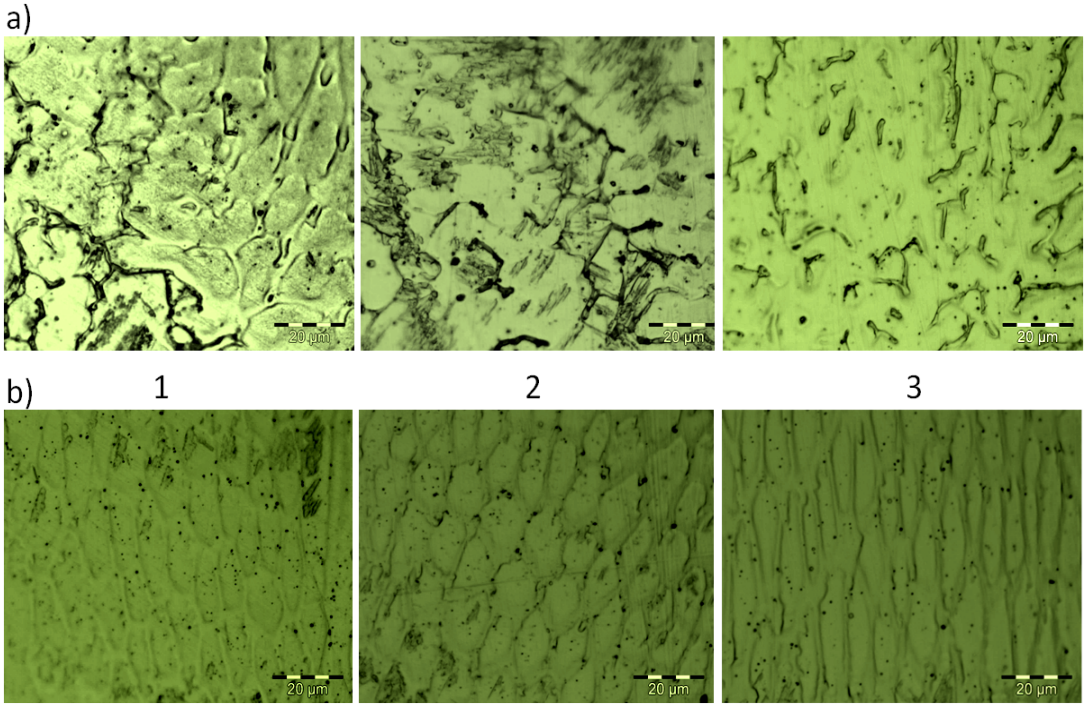

Figure 3.49: Typical microstructure at the bead center (a) and at the bead bottom (b) with same nominal energy and dilution rate calculated statistically (see first three beads of the figure (3.44))

number 6 and 9 of the Table 3.8).

The Figure 3.51 shows the magnified images of the microstructure of the beads

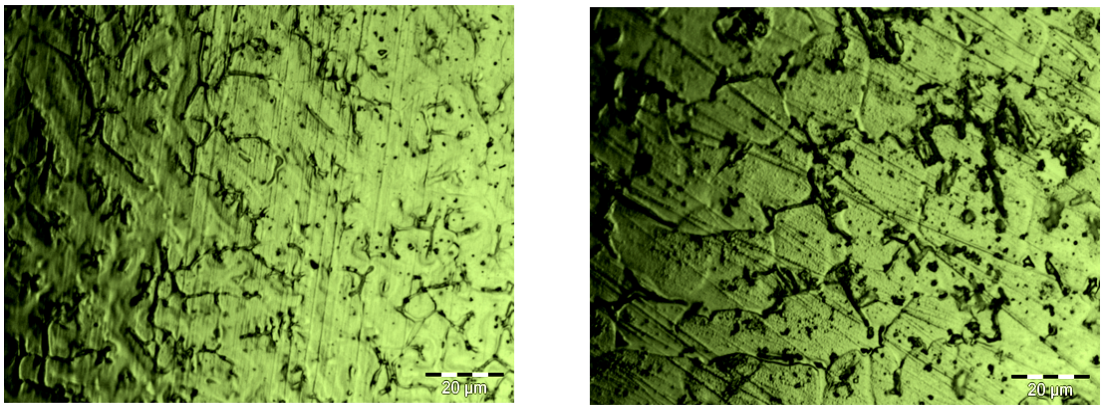

Figure 3.50: Typical microstructure at the bead top with same austenite % and different dilution rate calculated statistically(see bead 6 and 9 of the figure (3.44))

having the different % of the austenite (69% and 96%) and different dilution rate of 30% and 25% respectively (see the number 4 and 7 of the Table 3.8).

Here the cell size and shape seems to be similar. However, the internal struc-

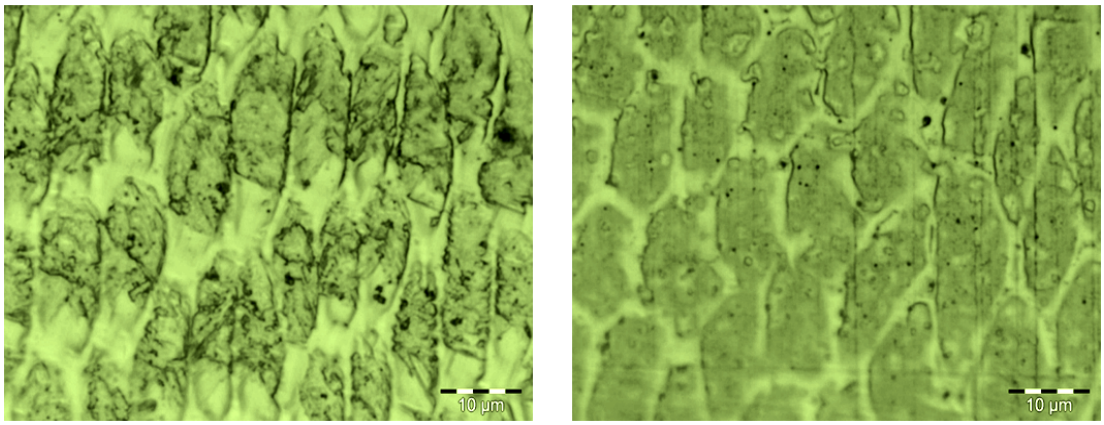

Figure 3.51: Magnified microstructure at the bead bottom with different nominal energy and austenite phase percentage at dilution rate of 30% & 25% calculated statistically

ture of the cell for 69% of the austenite is different may be due to presence of martensite.

3.4.2.2 Segregation and distribution of alloying elements

The Figure 3.52 shows the microstructure morphology of the top of beads (number 4 and 6 of the Table 3.8) having the different % of the austenite (**a**- 69% and **b**- 100%) and different dilution rate of 30% and 15% respectively.

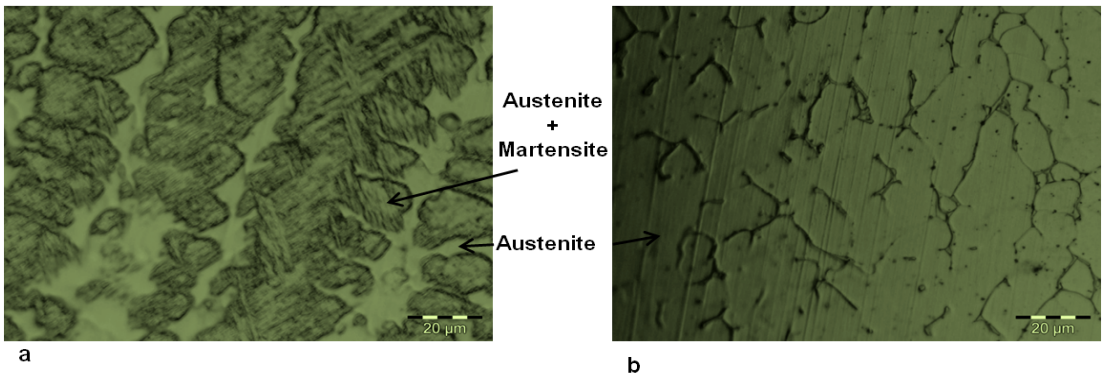

Figure 3.52: Typical microstructure at the bead top at different dilution rate calculated statistically

The microstructure of the bead with 69% austenite reveals the presence of martensitic structure in the cell for 69% of the austenite. The bead with 100% of the austenite shows a matrix form with the traces of segregation.

3.4.2.3 Cladded Layer Hardness

In this section the cladding layer hardness (micro and macro) at different locations of layer cladding are determined as described under. The macro hardness for the single layer 10 bead cladding in the horizontal direction is shown in figure 3.53. The macro hardness near the interface is higher compared with the top of the cladding. There is also a decreasing trend of hardness with the increasing number of beads. The reason may be the decrease of dilution rate with the increasing number of beads due to successive overlapping of beads. This may also be due to the decrease of cooling rate with increasing number of beads.

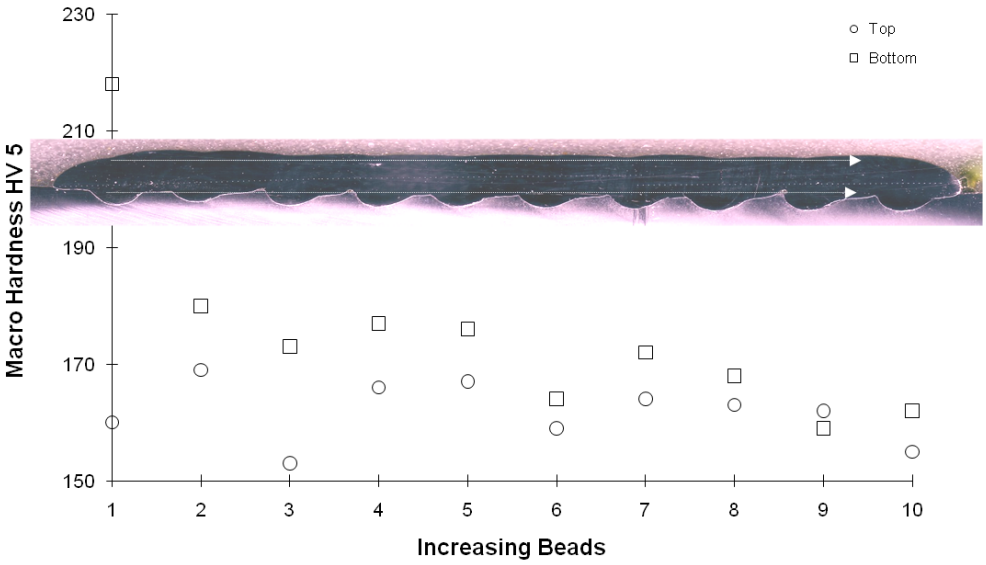

Figure 3.53: Macro-hardness (HV-5) measured at bead bottom and top of the cladded layer by using the parameters A of the table 3.7 at an overlapping of 40%

3.4.3 Cladding quality conclusion

In this section the cladding quality is characterized by using the dilution rate and the nominal energy as major input parameters. The chemical composition of the weld cladding exhibits heterogeneous behavior. The reason may be as the dilution rate of the clad metal varies from one bead to another due to the effect of overlapping. It is minimum for the first bead while the cooling rate is also higher for the first bead. Due to the preheating effect of the work piece by the heat energy of the previous bead, the cooling rate tends to lower for the forthcoming beads. Due to the above mentioned phenomena the cladding micro and macro harness is higher for the initial beads. The beads with higher dilution rate shows a austenitic-martensitic micro structure in accordance with the Schaeffler diagram. The sensitivity of the nominal energy can not be clearly established for the performed SS316L cladding on C35 substrate.

3.5 Conclusion

In the first part of this chapter a methodology is identified to derive statistical laws related to the geometrical parameters of the weld bead, the dilution rate and the current intensity as a function of process parameters and then applied to determine the nominal energy of a single bead. The approach proposed to determine the cladding layer parameters, is based on the parametric study of a single bead. The results obtained from the single bead study, were applied for onward single layer cladding process. It was observed that the dilution rate of the clad metal varies from one bead to another due to the effect of overlapping. Due to the preheating effect of the work piece by the heat energy of the previous bead, the cooling rate tends to lower for the forthcoming beads. The criteria used to characterize the cladding quality are therefore be the dilution rate and the nominal energy.

For layer cladding, two overlapping models for the determination of the optimum bead overlapping are introduced and the bead profile is represented by different functions. The results of the comparison of bead profiles represented by different function with the real bead profile shows that the bead profile represented by the ellipse arc function gives best approximation of the real bead profile for high form factor values. 4 degree polynomial profile shows satisfactory approximation for a large range of form factors. So, we have applied the overlapping models on a bead profile representation by a polynomial of degree 4. It was observed that, for the weld beads having lower values of wetting angles for a constant value of form factor, the combined effect of dispersion in the overlapping rate is lower for the both proposed criteria. For the single layer cladding, the deviation in the bead overlapping value by analytical expressions may be because the penetration of a GMAW bead is not uniform due to the Marangoni effect. The higher overlapping values of consecutive beads cause obtuse wetting angles. The inclination of the torch, reduced the bead wetting angle making the precedent bead toe more accessible by virtue of the arc force direction. However, the proposed methodology should be validated for other cladding processes and materials. In the coming chapter we will investigate the hot forgeability of a cladded work-piece.

Chapter 4

Hot forging behavior of a cladded plate

4.1 Objective

The objective of this study is to analyze the ability of a cladded workpiece under hot forging to obtain a desired defect free material distribution and structure. For this purpose a set of hot forging tests are carried experimentally and numerically to evaluate the feasibility of the proposed idea of weld cladded bi-material forgeability.

Why Hot forging a cladded plate Various mechanical and metallurgical properties are the main driving forces for the selection of the manufacturing processes. Because hot working refines grain pattern and imparts high strength, forged products have comparatively lower possibility of internal defects. The main advantage of the forging process is that, the crystalline grains, any non uniformities in alloy chemistry, inclusions and second phase particles are aligned in the directions of the greatest metal flow known as the grain-flow pattern. So, the directional characteristics in properties like strength, ductility and impact resistance are improved. By virtue of the forging process, the grains could be oriented in the direction where maximum strength is needed. The grain size of forged product is remarkably finer than that of casted or weld cladded product, as the coarser solidification structure is destroyed and refined by the hot forging

process. It is reported (van Bennekom & Wilke, 2003) that finer grain sizes resulted in a substantial increase in the fatigue strength of the stainless steel due to grain orientation effects. However, tensile strength, elongation and impact properties in forged products decrease in the transverse direction(s). Thus forging products are anisotropic and the directional strength, that could be a favorable property if used properly.

4.2 Forgeability levels

It is obvious that the cladded layer has no known chemical composition and is mixture of the base metal and cladding metal depending on the dilution rate. As the forgeability is an intrinsic characteristic of any material therefore due to the difference in rheological properties at different positions of the workpiece, three levels of the hot forging characterization may be considered.

- The intrinsic forgeability of the cladding layer consisting of the cladding material diluted with the base metal. At this level, we come across with the ductility limit and thermo-visco-plastic behavior of the material.
- The hot deformation behavior of the structure consisting of the cladding layer and substrate interface along with the heat affected zone during cladding. The interface geometry is important to be considered due to its periodic nature which is the function of the consecutive bead overlapping.
- The level 3 corresponds to the ability of a cladded workpiece under hot forging to obtain a desired defect free material distribution and structure.

These levels are described by cladding layer material only, cladding layer and substrate interface along with the heat affected zone and the complete cladded work piece as a whole. Bi-material forgeability trials may be conducted in two possible ways, either on isolated cladded layer (forgeability and thermoplastic laws of the material at the level 1)or on bi-material cladding. Due to the unavailability of the sources for detailed testing due to sample dimension limits and exact cladding location, trials on bi-material cladding are performed which may depict the bi-material forging aptitude during transformation to a final forging product

at the described levels. The characterization approach for cladded bi-material hot forged product is shown in the Figure 4.1.

The forgeability of a material is also dependent on the metallurgical structure

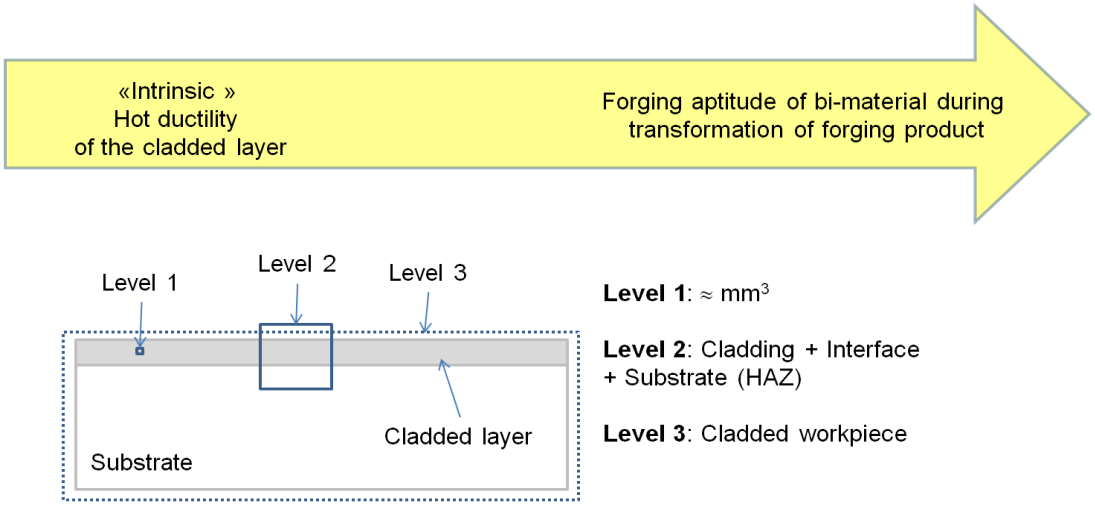

Figure 4.1: Characterization approach for bi-material cladded hot forged product

and is a complex function of temperature and strain rate. A large number of tests may be used to evaluate the forgeability of a material.

4.2.1 Forgeability Tests

As discussed in the Chapter 1, a variety of forgeability tests to measure the specific behavior of a material are in use, but none of them is universally accepted and only determine a specific approximation as discussed below:

- The upset test applied normally to a cylinder is used to measure the surface strains at the equator of the cylinder. This test allows to determine the flow stress data (true stress/true strain relationships) of metals at various temperatures and strain rates and is often used to simulate forging deformation.
- The side-pressing test is effective to study surface related cracking.

- The wedge-forging test estimates the forgeability at different reductions and forging conditions.
- The Hot-twist testing is a common means of measuring the forgeability for the high strains and strain rates in the near-surface zones of the sample.
- The plane strain compression test is applied for approximation of rolling deformation.

4.2.2 Conclusion

Due to the potential difference in rheological properties at different positions of a cladded workpiece, three levels of the hot forging characterization are considered. Bi-material forgeability trials on bi-material cladding to see the overall bi-material forging aptitude during transformation to a final forging product. A large number of tests may be used to evaluate the forgeability of a material to understand the fundamentals of material flow, fracture and workability limits. The main aim of the hot forging simulation and experimental tests is to guess the cladded layer material behavior, ductility limits, geometrical effects and thermal behavior at the interface and heat affected zone.

4.3 Bi-material Forgeability Tests

The bi-material simulation and experimental forgeability trials are performed to understand the fundamentals of material flow, fracture mechanism and workability limits. The objective of the numerical simulation tests is to study the influence of forging parameters on the distribution of matter along with the required forging effort and related equivalent strain on the identified critical points. The simulation is carried out by using the software FORGE-2009 TRANSVALOR. A birds eye view of the material distribution behavior and their effects on forging effort as well as the study of the interface tribological and thermal behavior is carried out. A substrate of mild steel C35 and a cladding material SS316L are applied experimentally but for the simulation purpose, hot forgeability trials are performed by selecting the combination of the following materials:

1. Mono material (Mild steel cladding on Mild steel)
2. Bi-material (SS 316L cladding on Mild steel) « Dilution Neglected »
3. Bi-material (Ni-based alloy cladding on Mild steel) « Hard on soft »
4. Bi-material (Cu based alloy cladding on Mild steel) « soft on hard »

The behavior of the cladding constituted by SS316L and mild steel substrate is different from the individual behavior of its constituents due to dilution. Two materials with extreme properties (Cu based alloy and Ni-based alloy) are also simulated to analyze their behavior. It is important to understand that a single forgeability test can not describe all scales of forging behavior. Therefore a set of different forgeability tests are proposed to evaluate different aspects of forgeability at different levels. The following tests were performed to evaluate the forgeability of a cladded workpiece:

1. Hot bending
2. Upset-testing
3. Plane strain Compression test

A global view of the input and out put hot forging parameters is shown in the figure 4.2.

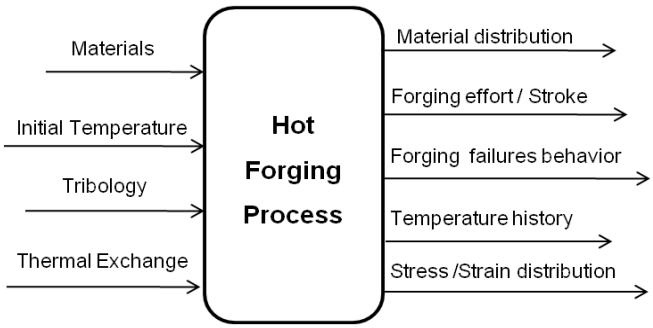

Figure 4.2: Global view of In-put and out-put parameters for hot forging process

4.3.1 Hot Bending Test

As discussed above, concepts involved in bi-material forgeability trials are to understand the fundamentals of material flow, fracture and workability. The hot bending test is applied for assessing the hot ductility of the cladded layer and substrate material at three different temperatures (750°C, 900°C and 1050°C) to asses the behavior of SS 316L cladding on a substrate of C35. The higher chosen temperature, 1050°C corresponds to hot forging process temperature for the chosen material (although the real hot forging temperature is in the range of 1250°C and we were restricted to 1050°C due to some experimental restrictions) and lower temperature is near the range of semi-hot forging process.

The principal input parameter for our analysis is material of the cladding due

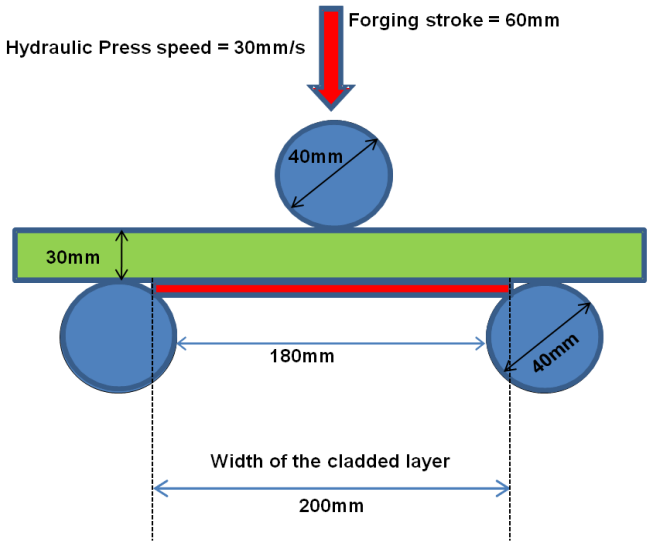

Figure 4.3: The principle of the Hot bending test

to its unknown thermo-mechanical behavior including hot ductility limit. The tribological conditions and thermal exchange values are function of the material under test and is not so easy to control during the forging process. So their effect should me minimized. To access the hot ductility limit the stress and strain distribution in the cladding should be derived through the global input process parameters like ram displacement and velocity. Moreover, we will estimate the

test ability to determine the forgeability at Level-3 through the material distribution in the forged part. From the above setup used for the hot bending test, shown in the figure 4.3, a mild steel substrate having a thickness of 30mm is cladded by a SS316L upto 200mm wide (cladding thickness ≈ 3-5mm for two different experimental tests). The hot bending test is performed by putting the cladded side on the bottom side to analyze the deformation in the cladded layer. The hot bending test is studied analytically, numerically and experimentally as discussed below.

4.3.1.1 Hot Bending Analytical analysis

An analytical study is carried out by modeling of a mono material beam in viscoplastic domain. The purpose is to observe the influence of the material behavior on the hot bending forging effort and plastic deformation on the bottom surface of the beam. The main objective is to estimate the extent of the control of strain through the main input parameters which are ram displacement and velocity.
For this purpose a hypothesis considering a homogeneous and isotropic simply supported straight beam with a concentrated load at the center having a rectangular cross-section is assumed. The aim is to analyze globally the hot bending test analytically.

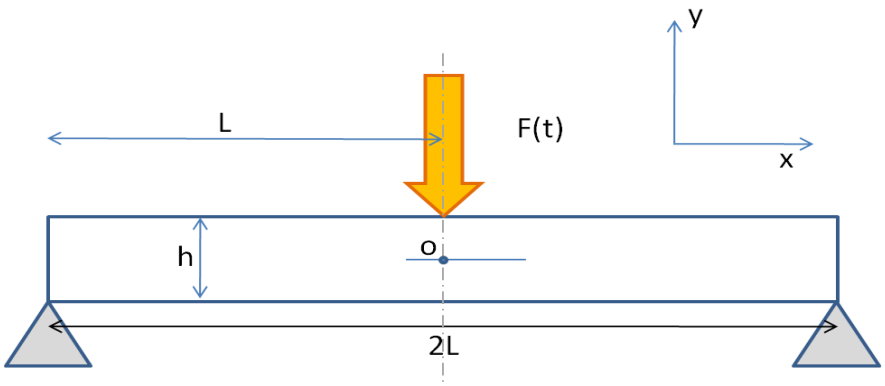

Figure 4.4: The illustration of the Hot bending analytical test

In the figure 4.4, h and b (not visible) are beam cross-section height and width respectively. Initially a hypothesis for small perturbations is applied.

Bending Moment in the beam : Due to symmetry of the system, we will only consider the positive abscissa of the symmetrical beam.

$$M_f(x,t) = \frac{F(t)}{2}(L-x), \Rightarrow x\epsilon[0,L] \tag{4.1}$$

The bending moment in a section of the beam can be represented as a function of the stress distribution as follows:

$$M_f(x,t) = b\int_{-\frac{h}{2}}^{\frac{h}{2}} \sigma_{xx}(x,y,t).y.dy \tag{4.2}$$

Material distribution and strain in the beam : We assume that the straight sections remain straight during the bending. The strains in the beam may be given as under:

$$\varepsilon(x,y,t) = -\frac{\partial^2 Y}{\partial x^2}(x,t).y \tag{4.3}$$

where Y(x,t) is the deflection on the beam along abscissa at any time instant "t". The strain rate may be given by the following equation:

$$\dot{\varepsilon}(x,y,t) = -\frac{\partial}{\partial t}\left(\ \frac{\partial^2 Y}{\partial x^2}(x,t)\ \right).y \tag{4.4}$$

The deformation profile of the beam is assumed in the following form:

$$Y(x,t) = f(t).g(x) \tag{4.5}$$

So, the beam strain and strain rate can be written in the following form:

$$\varepsilon(x,y,t) = -\frac{\partial^2 g}{\partial x^2}(x).f(t).y = -g''(x).f(t).y \tag{4.6}$$

$$\dot{\varepsilon}(x,y,t) = -\frac{\partial^2 g}{\partial x^2}(x).\frac{\partial f}{\partial t}(t).y = -g''(x).\dot{f}(t).y \tag{4.7}$$

The visco-plastic behavior of the material : We can represent the beam material behavior by the Norton-Hoff law by the following relation:

$$\sigma_0 = K_N.\varepsilon_{eq}^m.\dot{\varepsilon}_{eq}^n \tag{4.8}$$

where σ_0 is the flow stress, K_N is the material consistency, ε_{eq} and $\dot{\varepsilon}_{eq}$ are the equivalent strain and strain rate while, m and n are the sensitivities of the strain and strain rate respectively. By putting their values from equations 4.6 and 4.7 in the equation 4.8 and considering the plane strain condition, we get the following relation:

$$\sigma = K.g''(x)^{m+n}.f(t)^m.\dot{f}(t)^n.y^{m+n} \tag{4.9}$$

where K=$K_N * (\frac{2}{\sqrt{3}})^{m+n+1}$

Bending Effort, Deflection, stress and strain in the beam : By putting the equation 4.9 in the equation 4.2 and considering the symmetry of the strain distribution in the section along Y axis, we get the relation as follows:

$$M_f(x,t) = 2b\int_0^{\frac{h}{2}} K.g''(x)^{m+n}.f(t)^m.\dot{f}(t)^n.y^{m+n+1}.dy \tag{4.10}$$

$$M_f(x,t) = K.g''(x)^{m+n}.f(t)^m.\dot{f}(t)^n.\int_0^{\frac{h}{2}} 2b.y^{m+n+1}.dy \tag{4.11}$$

$$M_f(x,t) = K.g''(x)^{m+n}.f(t)^m.\dot{f}(t)^n.I_{vp} \tag{4.12}$$

The equilibrium equation of the beam 4.1 can be written as:

$$F(t)(L-x) = K.g''(x)^{m+n}.f(t)^m.\dot{f}(t)^n.I_{vp} \tag{4.13}$$

The beam bending is controlled by the speed of the point of application of the force/effort:

$$Y(0,t) = \int_0^t V(t)dt = -V.t \tag{4.14}$$

Consequently, the equation 4.5 becomes:

$$f(t) \;=\; -\frac{V.t}{g(0)} \tag{4.15}$$

By putting the equation 4.15 in the equation 4.13 and taking g(0) = -1, the equilibrium equation of the beam can be written as:

$$F(t)(L-x) \;=\; K.g''(x)^{m+n}.V^{m+n}.t^m.I_{vp} \tag{4.16}$$

By using the conditions $g(0) = -1$, $\acute{g}^{(0)} = 0$ and $g(L) = 0$, we can get the following relation:

$$g(x) \;=\; \frac{2m+2n+1}{m+n+1}\left(\frac{x}{L} - 1 + \frac{m+n}{1+2m+2n}(1-\frac{x}{L})^{\frac{1+2m+2n}{m+n}} \right) \tag{4.17}$$

We chose

$$f(t) = \mathbf{V}.t = \mathbf{U} \tag{4.18}$$

and finally we got:

$$\mathbf{F}(t) \;=\; -\mathbf{U}^m.\mathbf{V}^n.I_{vp}\frac{2m+2n+1}{(m+n)L^{\frac{2m+2n+1}{m+n}}}.K.2 \tag{4.19}$$

where U is the die displacement.
The deformation of the beam appears as the function g(x) of the equation 4.17 multiplied by f (t), the value of the displacement U in the center of the beam (x = 0). It may be noted that the coefficients of sensitivity of the flow stress to strain and strain rate appear only in the form of their sum in the expression of the deformation of the beam. If we denote this sum as q, we obtain for g(x)

$$g(x) = \frac{2q+1}{q+1}\left(\frac{x}{L} - 1 + \frac{q}{1+2q}(1-\frac{x}{L})^{\frac{1+2q}{q}} \right) \tag{4.20}$$

Considering equation 4.20, we see that the deflection of the beam tends to a straight line when "q" tends to 0. This produces the phenomenon of plastic hinge.

$$\lim_{q\to 0} g(x) = \frac{x}{L} - 1 \tag{4.21}$$

When the value of "q" approaches to ∞, we get a parabolic deformation profile, therefore a constant curvature.

$$\lim_{p\to \infty} g(x) = \frac{x^2}{L^2} - 1 \tag{4.22}$$

The graph 4.5 shows the deformation profile g(x) for different values of the "q". The above discussed two extreme cases show the deformation profile for q=0.1 (approximately straight line) and q=100 (a parabolic profile).

The deformation obtained at x=0 for the surface opposite of the punch is given by the following equation:

$$\varepsilon^p = U.g''(0).\frac{h}{2} = \frac{2q+1}{q}\frac{h}{L^2}.U \tag{4.23}$$

The equation show that the equation 4.13 shows that the equivalent strain is maximum at the surface x=0 for y=-h/2 or h/2. From the above hypothesis we can see a linear relation between the plastic deformation and ram displacement. The graph (4.6) shows the strain $g''(x)$ as a function of values of the "q".

It may be noted that the deformation on the surface during bending will depend partially on material behavior. The coefficients 'm' and 'n' in the material behavior law (Norton-Hoff) will have a role in the relationship between the ram displacement and undergone bending deformation in the surface of the cladded layer of the sheet. For the steels alloys the value of "q" is in the range of 0.25 to 0.35. This corresponds to a difference of deformation of about 20%. The figure

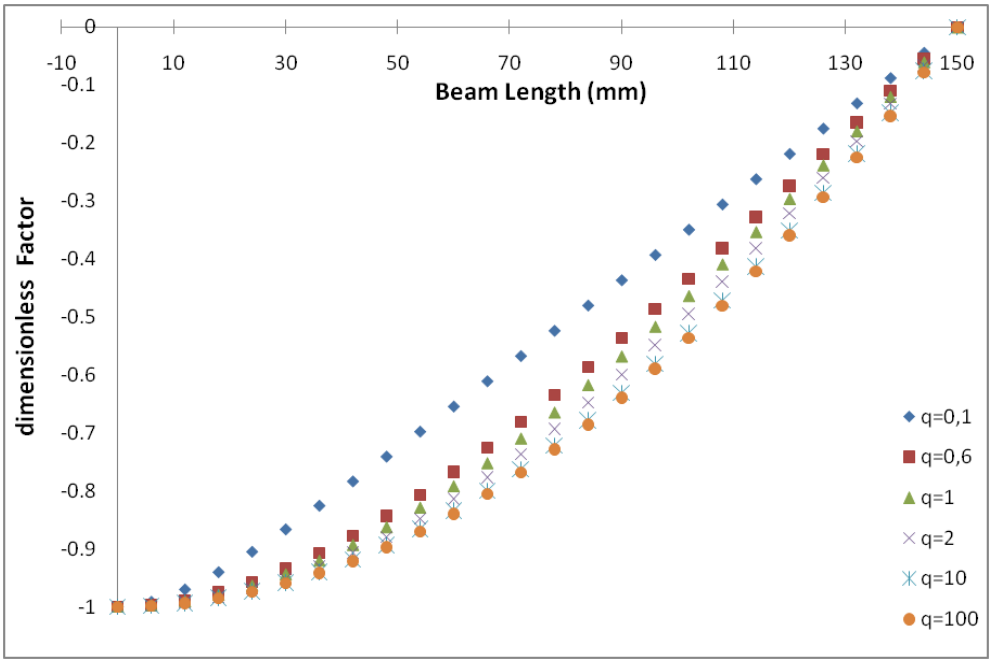

Figure 4.5: Analytical results of the deformation profile

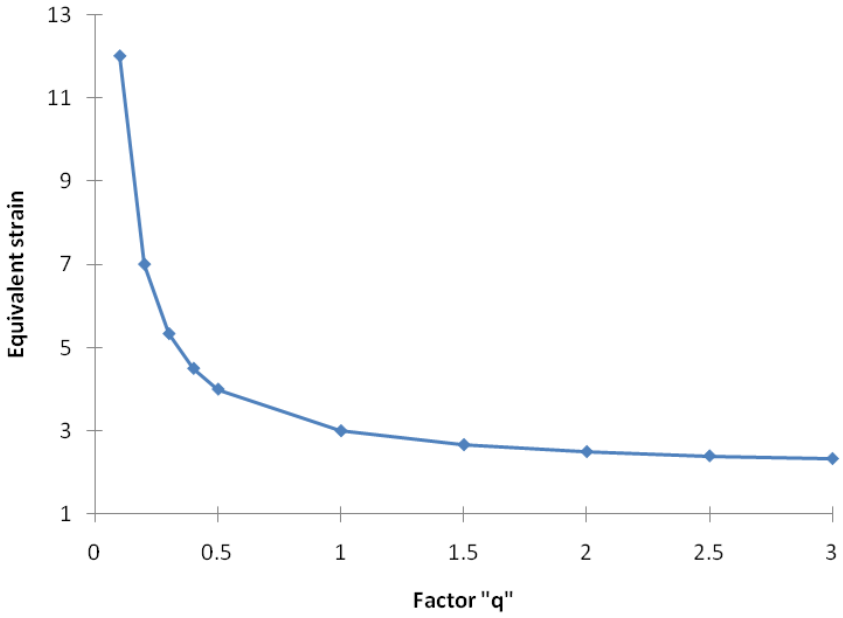

Figure 4.6: Analytical results of the equivalent strain

4.7 for "m=0.23" (related to strain hardening) and "n=0.153" (factor showing the strain rate). The factor "m" is responsible for the initial rapid rise in the forging effort by putting K=59.04. The results obtained by the analytical study

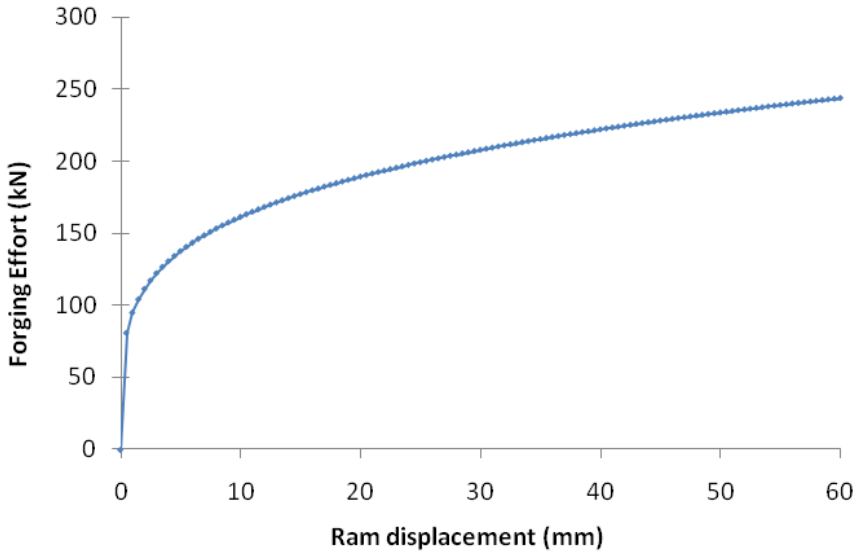

Figure 4.7: Analytical results of the hot bending effort for "m=0.23 and n=0.153" at temperature 900°C

show only the overall tendencies. The study is limited only for the mono-material and does not take into account the evolution of the cross section of the beam and the re-orientation effect of the lower die with the deformation. To refine the analytical results, will start with the numerical simulation of the hot bending test in the coming section.

4.3.1.2 Hot Bending Numerical simulation

The figure 4.8 shows the input and out put parameters for the hot bending forgeability simulation tests.

Material behavior laws: The base metal and cladded material layer are defined from the database of the software describing the rheological and thermal properties of known material grades. The rheological law used for the simulation

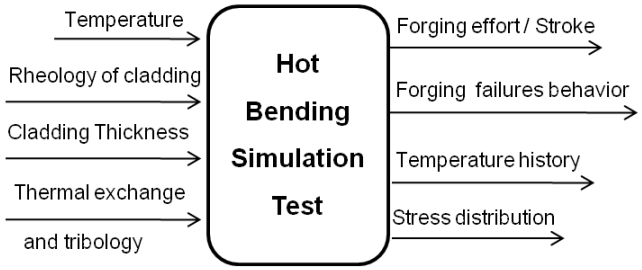

Figure 4.8: In-put and out-put parameters for simulation of the hot bending test

is the Hansel-Spittel law describing a visco-plastic thermal coupling. This law is well suited to represent the behavior of metals when they are hot formed. The general law of Hansel-Spittel is given below:

$$\sigma_f = Ae^{m_1 T} T^{m_9} \epsilon^{m_2} e^{\frac{m_4}{\epsilon}} (1+\epsilon)^{m_5 T} e^{m_7 \epsilon} \dot{\epsilon}^{m_3} \dot{\epsilon}^{m_8 T} \tag{4.24}$$

where σ_f is the flow stress, T is the temperature of the material, ϵ is the equivalent plastic strain and $\dot{\epsilon}$ is the equivalent strain rate (the total strain rate). Here m_i (i = 1,2,3,4,5,7,8,9) are the regression coefficients of the law whose values are dependent on the material. In most cases, we use a simplified law where $m_i = 0$ for i = 5,7,8,9, and Hansel-Spittel law becomes simplified as below:

$$\sigma_f = Ae^{m_1 T} \epsilon^{m_2} e^{\frac{m_4}{\epsilon}} \dot{\epsilon}^{m_3} \tag{4.25}$$

This law and the coefficients are only valid for given range of temperatures, strain and strain rate data for each material. The values of the constants for the materials used are given in the table 4.1 which are available in the data base of the simulation software Forge 2009. It is important to be noted that in the simulation software used, we only apply the pre-selected material behavior governing laws and the actual cladding material is unknown.

Thermal behavior: The database also has information on the thermal behavior of each material including density, heat capacity (specific heat), conductivity, emissivity and the coefficient of thermal expansion. When the thermal computation is activated, the simulation takes into account the thermal exchanges

	A	m_1	m_2	m_3	m_4
C35	1498.8708	-0.00269	-0.12651	0.14542	-0.05957
SS316L	8905.34	-0.00383	0.01246	0.09912	-0.02413
Ni-based alloy	356229.03	-0.00647	0.02892	0.15357	$1.2Xe^{-5}$
Cu-based alloy	11582.76	-0.00686	0.03602	0.24482	-0.00017

Table 4.1: The values of the constants for the materials used

between the deformable objects and the ambient(air), by conduction and radiation. The emissivity of the materials used, is defined to compute the heat loss due to radiation. The convection with the air is low while the air temperature is kept at 20°C. The heat exchange with the rigid dies is computed by defining the heat transfer coefficient with the rigid die, die temperature and die effusivity. The heat exchange between the deformable objects is defined by the heat transfer coefficients only.

Tribological and Interfacial conditions: The friction condition between the substrate and the cladding layer interface is supposed to be bilateral contact(no release from contact) and the velocity field is continuous across the interface. The friction modeling between the deformable object and rigid dies or another deformable object is also defined by different laws. We have applied Visco-plastic and coloumb friction laws for the simulation studies. The viscoplastic friction law is given by the following relation.

$$\tau = -\alpha * K(T, \bar{\varepsilon}) * \Delta V^{p-1} * \Delta \mathbf{V} \tag{4.26}$$

Here, α is the friction coefficient, p is the sensitivity to the sliding velocity, Δ V, the difference in velocity between the two solids, $K(T, \bar{\varepsilon})$ is the consistency of the material depending on the thermo-mechanical conditions. The Coulomb friction law is written as under in the general form:

$$\tau = -\mu\sigma_n \frac{\Delta \mathbf{V}}{\Delta V} \tag{4.27}$$

if

$$\mu\sigma_n < \bar{m}\frac{\sigma_o}{\sqrt{3}}$$

and

$$\tau = \bar{m}\frac{\sigma_o}{\sqrt{3}}\frac{\Delta \mathbf{V}}{\Delta V} \tag{4.28}$$

if

$$\mu\sigma_n > \bar{m}\frac{\sigma_o}{\sqrt{3}}$$

where τ is the friction shear stress, μ is friction co-efficient, σ_n the normal stress, σ_o is the flow stress and $\bar{m}$ is the Tresca coefficient.
The selected simulation criterion for hot bending test is shown in the figure 4.9.

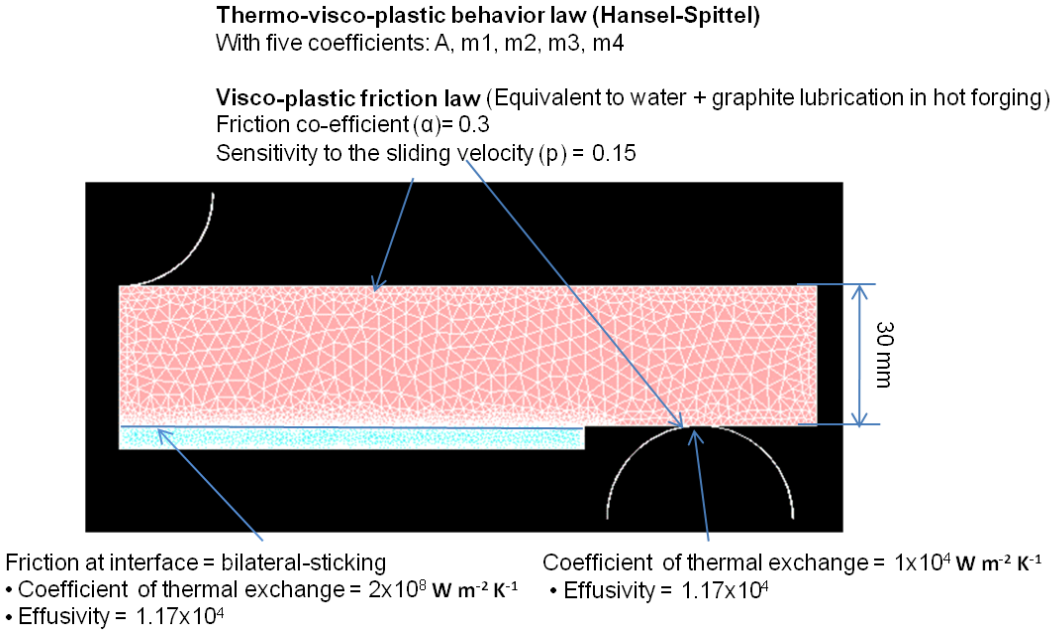

Figure 4.9: Simulation criterion for hot bending test

A re-meshing box with a suitable mesh size (to ease the contact continuity) is

generated around the clad and substrate interface for the continuation of the mesh size. Hypothesis of the plane deformation (2-D) is applied and by considering the symmetry conditions, half part of the cladded plate is under study.

Hot bending simulation Results The figure 4.11 shows the equivalent strain at different clad and billet positions for SS 316L cladding on C-35 substrate (see the figure 4.10).

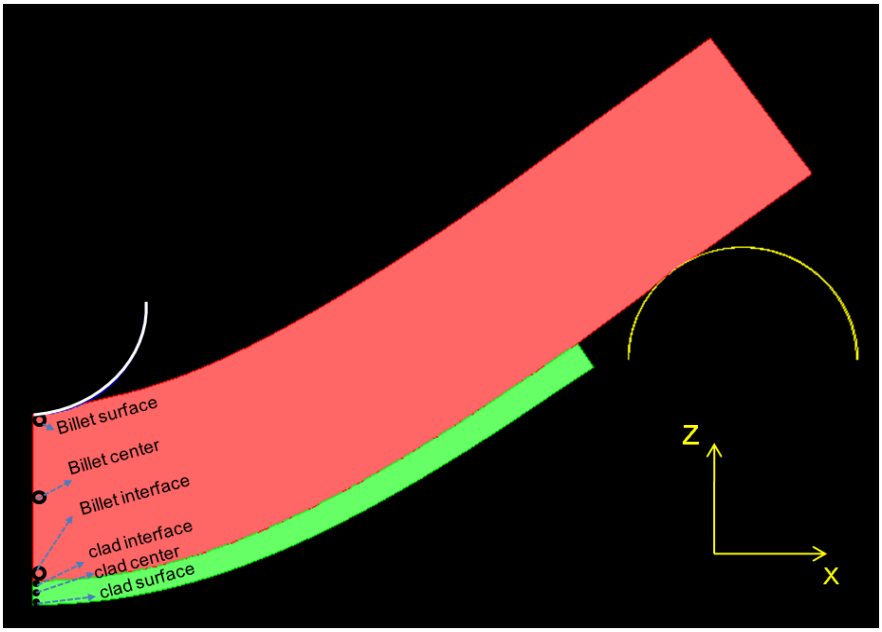

Figure 4.10: Clad and billet positioning for hot bending test

The strain curve for the billet surface shows a rapid increase in deformation due to upper die direct contact and penetration at this point. The maximum equivalent strain is at the clad surface. For a clad thickness of 5mm a difference of 0.04 and on the average an equivalent strain of 0.2 in the center is obtained.
If ε^p_{xx} and ε^p_{zz} are the strains along xx and zz-axis, the equivalent strain may be given as:

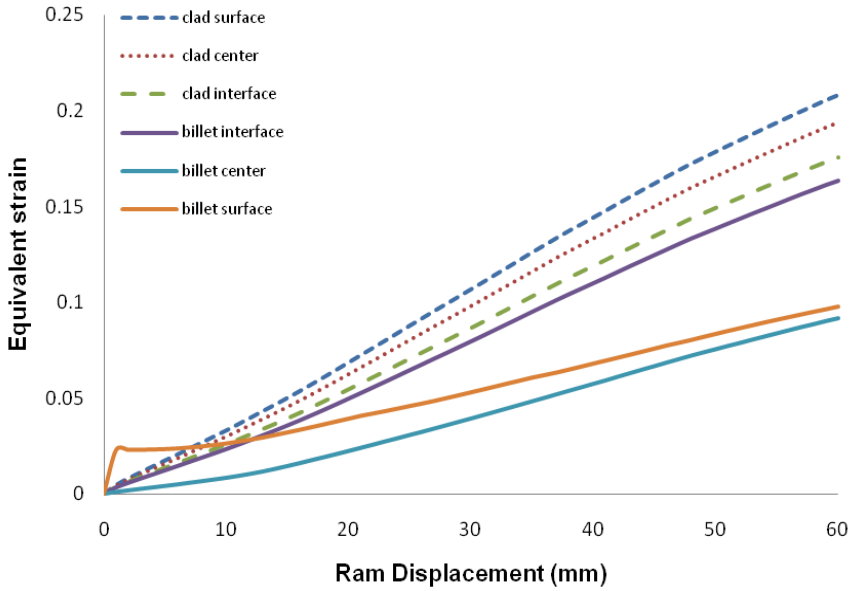

Figure 4.11: Simulation results of the equivalent strain at different clad and billet thickness for SS316L cladding on C35 substrate

$$\varepsilon_{eq} = \sqrt{\frac{4}{3}}\varepsilon_{xx} \tag{4.29}$$

$$\varepsilon_{xx} = \frac{\sqrt{3}}{2}\varepsilon_{eq} \tag{4.30}$$

In fact the cladding layer is in the plane strain state and during the hot bending test decrease in the cladding layer thickness is observed. The effect id due to the 2-D simulation. This should be verified by the 3-D simulation test although it is more time consuming. The cladding surface and interface deformation profiles for SS316L cladding on C35 substrate at 900˚C is shown in the figure 4.12 which shows that the clad thickness (5mm) after the deformation is about 4.22 mm which is close to the value calculated analytically. From the relation 4.30 by putting the equivalent strain as 0.2 we calculate the deformation along zz-direction is 0.17

and the initial clad thickness of 5mm after the deformation becomes about 4.15.

$$\text{clad thickness} \quad = \quad (1 - 0.17) * \text{Initial clad thickness}$$

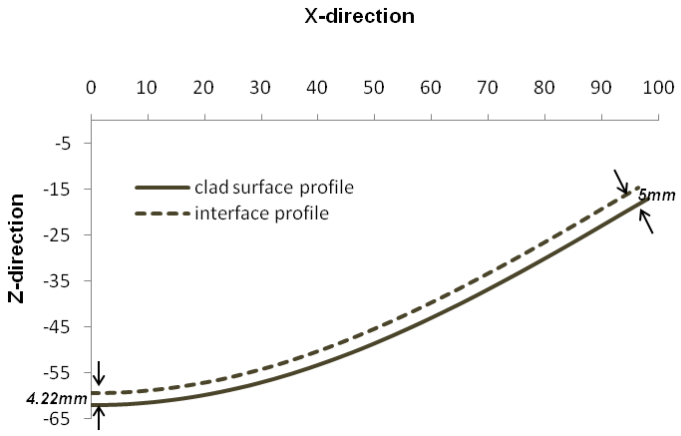

Figure 4.12: The simulation profile of the clad surface and interface for SS316L cladding on C35 substrate

The forging effort increases sharply in the beginning of the forging cycle and becomes stable at the end as shown in the figure 4.13. We can observe a remarkable variation in the forging effort at the end of the forging cycle. This phenomenon may be caused due to high magnitude of remeshing and large forging time step. We may reduce this resonance by avoiding the remeshing and reducing the forging interval.
The temperature distribution during test is shown in figure 4.14, where we can see the temperature drop at the dies contact points and on the surface cladding due to convection heat loss. It can be noted that at the contact points of the die with the workpiece, the temperature drops up to 550°C. The magnitude of the drop is mainly due to thermal exchange coefficient and contact area between the die and work piece. The local aspect of the contact reduces the thermal exchange effect on the simulation results. At the outer surface of the workpiece the small temperature drop of order 10°C is due to convection and radiation heat loss.

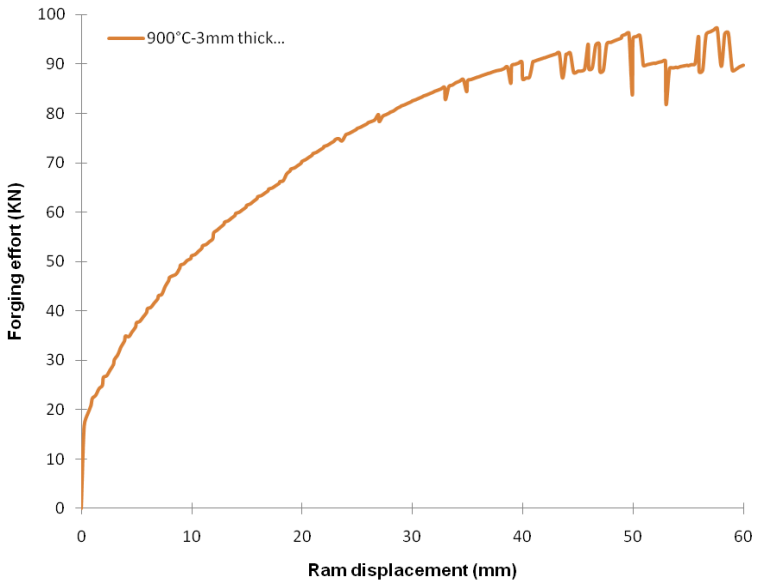

Figure 4.13: The forging effort with the ram displacement during hot bending simulation for SS316L cladding on C35 substrate

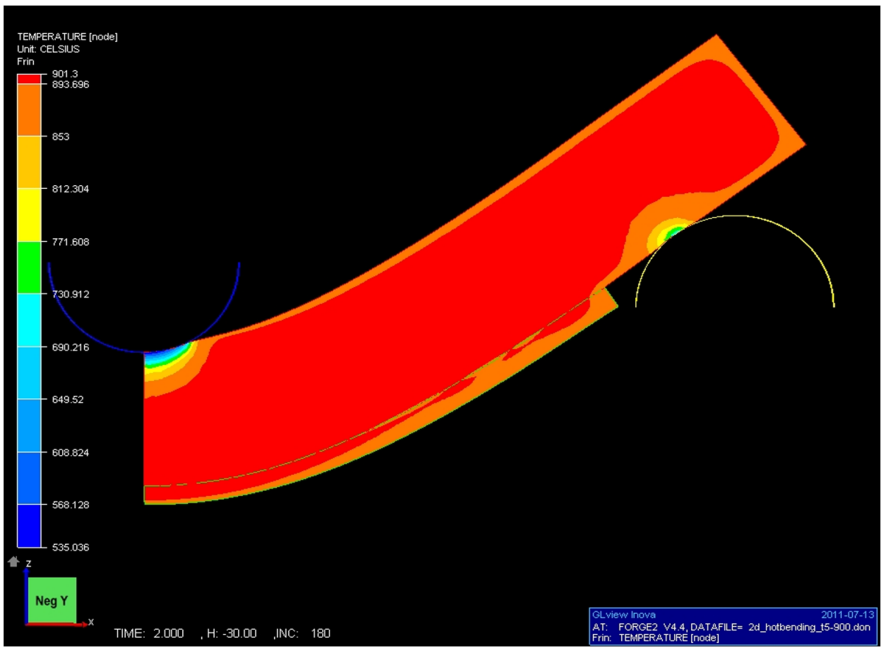

Figure 4.14: Temperature distribution during hot bending simulation for SS316L cladding on C35 substrate

The figure 4.15 indicates the stress distribution along the xx-direction showing the compression on the billet top surface (up to 230 MPa) and tensile stress at the cladding layer surface up to 230 MPa.

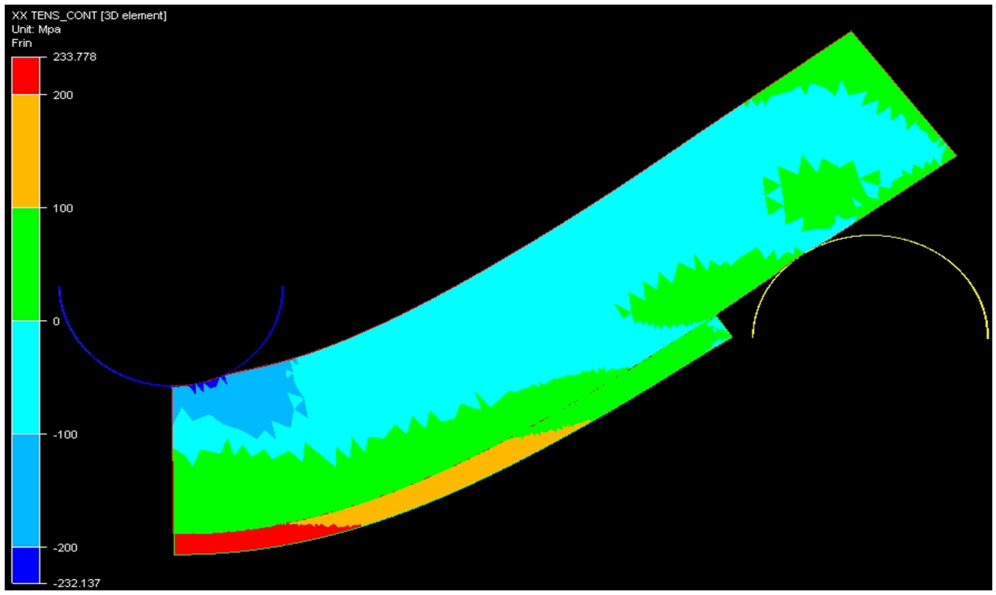

Figure 4.15: Simulation results of the stresses along-xx for SS316L cladding on C35 at 900˚C

The magnified view of the stress distribution near the interface is shown in the figure 4.16. We can see a remarkable variation in the tensile stress across the clad and substrate interface maximum of the order 130 MPa.

The figure 4.17 shows the stress distribution along the yy-direction showing the compression on the billet top surface (up to 134 MPa) and tensile stress (up to 115 MPa) at the cladding surface and are about half the values of the stress in the xx-direction. The cladding layer is in the state of plane tensile stresses which may also be supported by the 2-D hot forging process, which is the condition chosen for all the simulation analysis. The magnified view of the stress distribution near the interface is shown in the figure 4.18. The figure 4.19 shows the stress distribution along the zz-direction showing the compression on

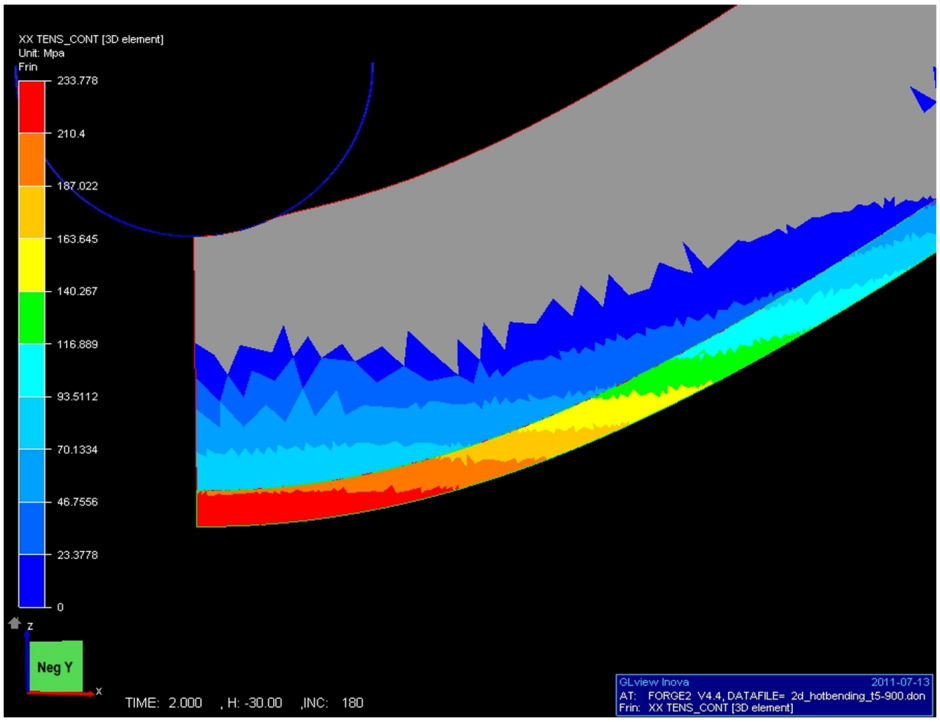

Figure 4.16: Magnified view of the simulation results of the cladding layer showing the stresses along-XX for SS316L cladding on C35 at 900°C

the billet top surface. From the simulation results it is clear that the lowest point at the clad surface is in free condition and the stress σ_{zz} at this point is zero. Here the stress state corresponds to the plane tension. The above simulation results can be written in the matrix form as given under:

$$\sigma = \begin{pmatrix} 230 & 0 & 0 \\ 0 & 115 & 0 \\ 0 & 0 & 0 \end{pmatrix} \tag{4.31}$$

The deviatoric part of the stress is:

$$\sigma^D = \begin{pmatrix} 115 & 0 & 0 \\ 0 & 0 & 0 \\ 0 & 0 & -115 \end{pmatrix} \tag{4.32}$$

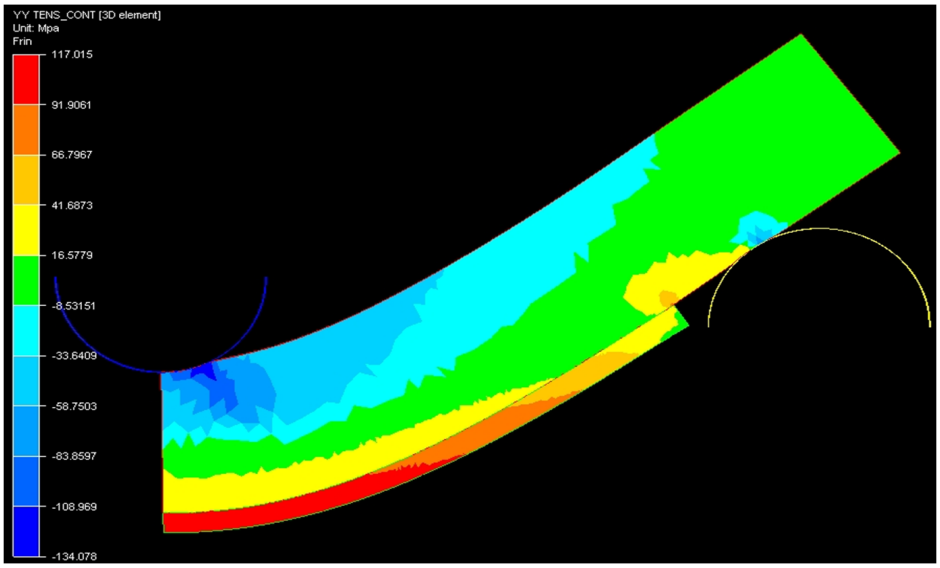

Figure 4.17: Simulation results of the stresses along-yy for SS316L cladding on C35 at 900˚C

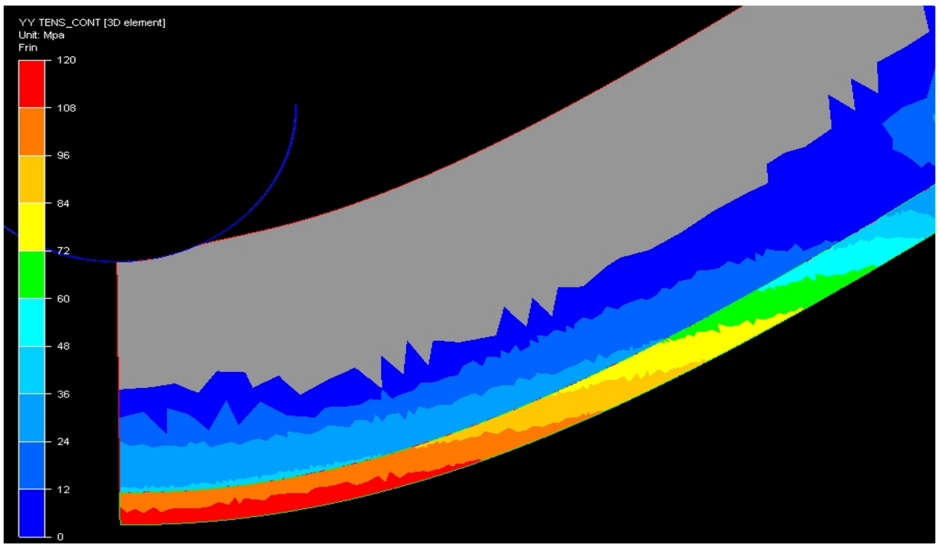

Figure 4.18: Magnified view of the cladded layer stresses along-yy for SS316L cladding on C35 at 900˚C

where σ^D is deviator stress.

$$\varepsilon^p = \begin{pmatrix} \varepsilon_{xx} & 0 & 0 \\ 0 & 0 & 0 \\ 0 & 0 & -\varepsilon_{xx} \end{pmatrix} \tag{4.33}$$

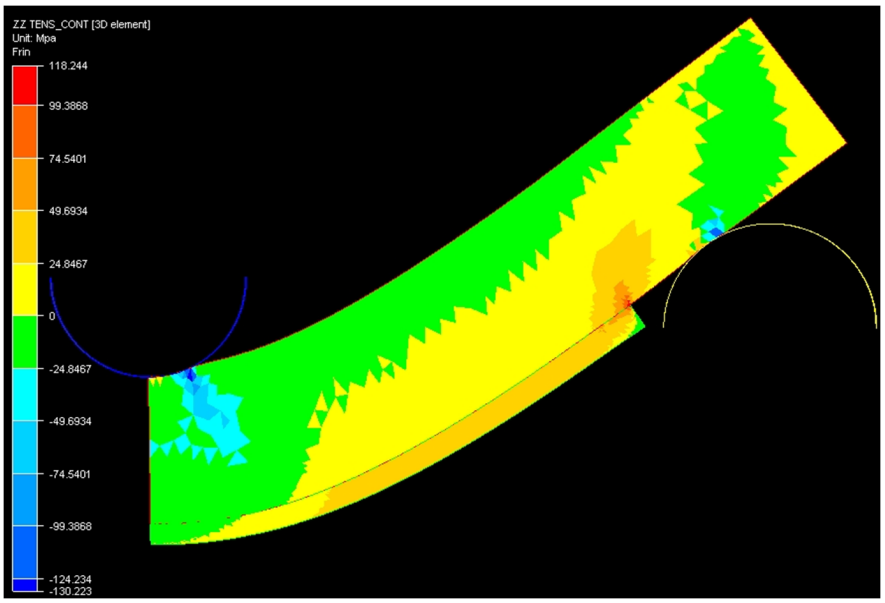

Figure 4.19: The stresses along-zz for SS316L cladding on C35 at 900°C

Overall effect of selected input parameters on simulation results The overall effect of the selected input parameters for the simulation study on the considered out-put parameters is described in this section.

Effect of the cladding thickness The Simulation results of the forging effort at different clad thickness of SS 316L on C35 substrate is shown in the figure 4.20. The forging effort increase with the increase of cladding thickness.

The effect of the cladding thickness on the forging effort is more sensitive as it is far away from the neutral axis of the beam. The effect can be explained by the factor I_{vp} of the equation 4.13. The resonance at the end may be due to one of the reasons of re-meshing and forging interval as described earlier.

The equivalent strain at different clad thickness of SS316L on C35 substrate is shown in the figure 4.21. We can see that the clad thickness do not have a remarkable effect on the equivalent strain in the cladding. This may be due to small variations of the cladding layer as compared to large thickness of the substrate. The neutral axis of the substrate will be shifted toward the cladding material and the equivalent strain on the clad surface will not be so affected.

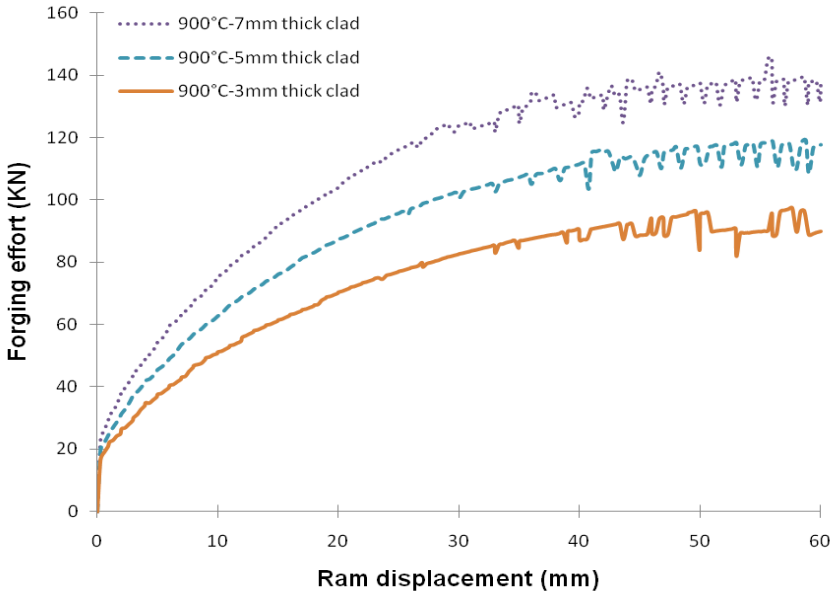

Figure 4.20: Simulation results of the forging effort at different cladding layer thickness of SS316L on C35 substrate at 900˚C

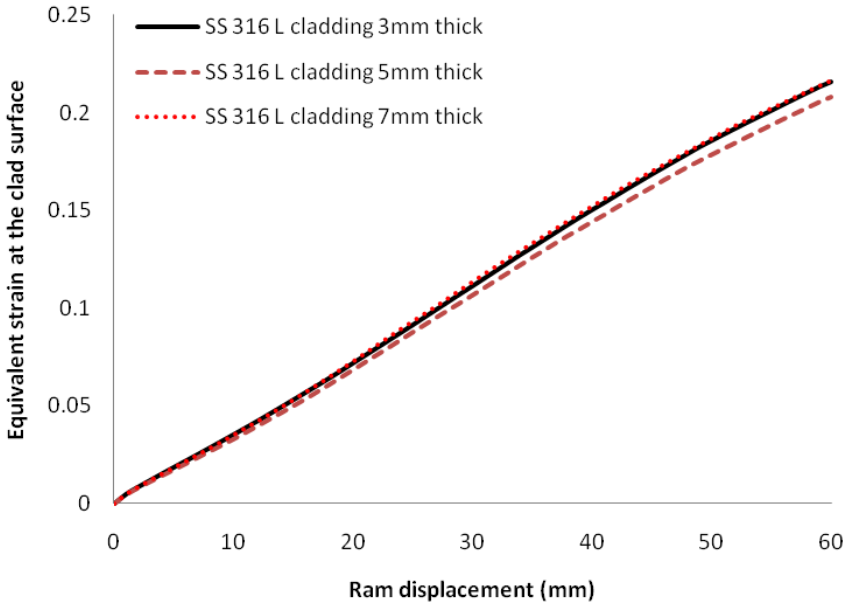

Figure 4.21: Simulation results of the equivalent strain at the clad surface for different cladding thickness for SS 316L on C35 substrate at 900˚C

Effect of the cladding material and temperature The figure 4.22 shows the simulation results of the equivalent strain at the cladding surface for different materials performed at 1050°C.

We can see that the equivalent strain in the cladding layer is the function of

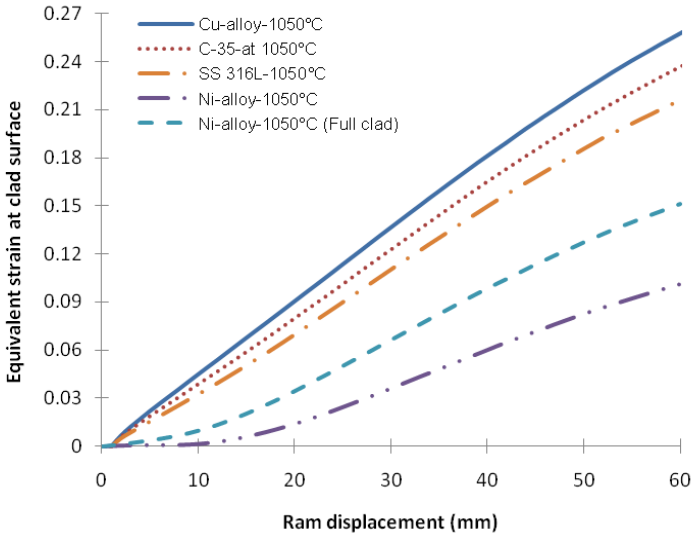

Figure 4.22: Simulation results of the equivalent strain at the cladding surface for different materials performed at 1050°C

the cladded material. For the materials having the behavior laws near to each other (mild steel or stainless steel), there is not a big difference in the equivalent strain rate rather it is largely dependent on the ram displacement. This effect is coherent with the analytical study of the visco-plastic beam deflection. However if we neglect the selected extreme materials (Ni and Cu based alloys), we cannot see a remarkable difference in the equivalent strains. Three different phenomena can explain the difference of equivalent strain.

- Direct effect of the cladded material on the workpiece deformation (As discussed in the analytic analysis)
- Denting effect of the die on the substrate
- Deformation in the uncladded part of the workpiece with weak quadratic moment (only in the elastic limit)

The forging effort and denting effect on the substrate increases with the increase of the hardness of the cladded material for a given ram displacement. The figure 4.23 shows the simulation results of the cladding surface profiles for SS316L and Ni-based alloy cladding on C35 substrate. It can be noted that the denting effect on the substrate for the Ni-based alloy cladding is higher than SS316L cladding on C35 material for a given ram displacement.

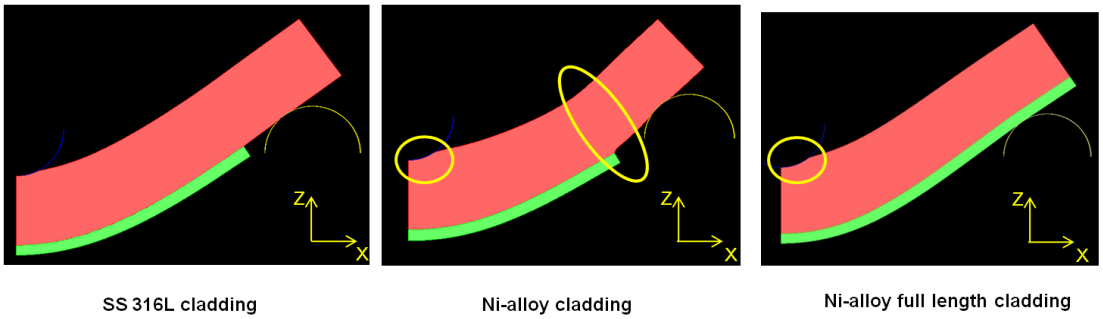

Figure 4.23: The simulation results of the cladding surface profiles for SS316L and Ni based alloy cladding on C35 substrate

Simulation results of the forging effort at different forging temperatures for SS 316L on C35 substrate is given in the figure 4.24.

Simulation results of the forging effort for different cladding materials on C35 substrate is given in the figure 4.25.

The figure 4.26 shows the simulation results of the equivalent strain at cladding surface for SS 316L cladding on C35 substrate at different temperatures. It can be noted that the temperature do not have any remarkable effect on the equivalent strain imposed on the cladding material.

The hot bending simulation was carried out under different tribological and thermal exchange conditions, but these two parameters have not a remarkable influence on the material distribution, cladding profile, equivalent strain in the cladded layer and forging effort due to the local aspect of the contact between the die and workpiece.

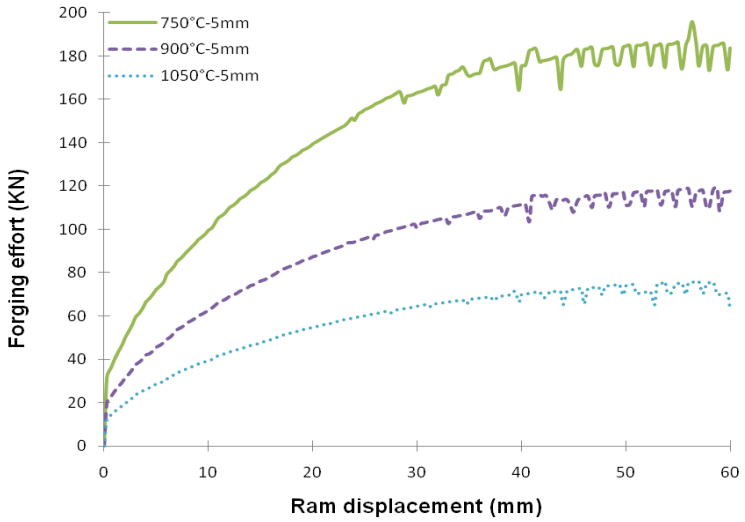

Figure 4.24: Simulation results of the forging effort at different forging temperatures for SS 316L on C35 substrate

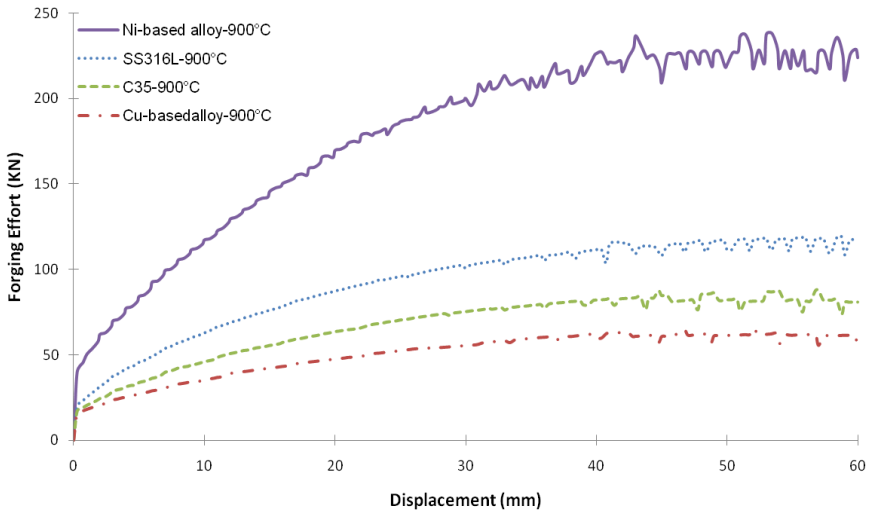

Figure 4.25: Simulation results of the forging effort for different cladding materials on C35 substrate at 900°C

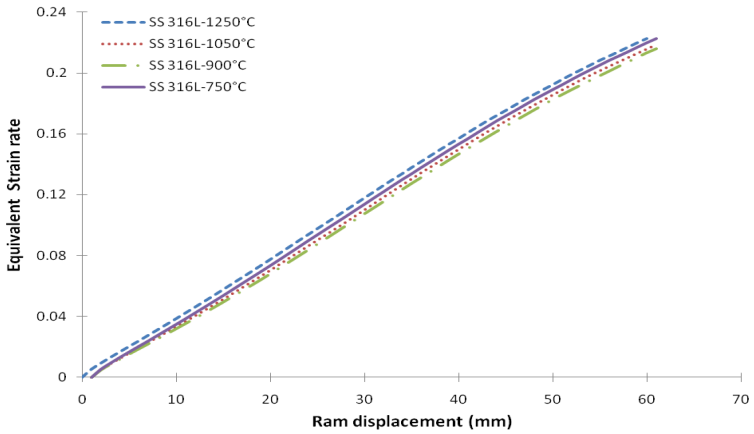

Figure 4.26: Simulation results of the equivalent strain at different temperatures for SS 316L on C35 substrate

Conclusion We may conclude that if reasonable parameters are selected, the hot bending simulation can allow us to guess the equivalent deformation in the clad surface as a function of the ram displacement during the process. The overall deformation profile is not too much dependent on the rheology of the cladded material and other simulation parameters. A less effect of clad thickness on the equivalent strain is observed as the clad thickness is very small compared with the substrate thickness.
The global summary of the hot bending out put results is given in the table 4.2.

++ (Very High sensitivity) + (High sensitivity) +- (Unpredicted Sensitivity) - (Negligible sensitivity)		Sensitivity of the forging parameters		
		Forging Effort	Equivalent Strain	Material distribution
Variation in input hot bending simulation parameters	Material	++	+-	+
	Temperature	++	-	+-
	Cladding Thickness	++	-	+-

Table 4.2: Summary of the hot bending simulation results

Now we will study the experimental results of the hot bending test to validate the characterization of the hot bending test.

4.3.1.3 Hot Bending Experimental Test

The hot bending test is applied for assessing the hot ductility of the cladded layer and substrate material at three different temperatures. The figure 4.27 shows the parameters considered during the hot bending experimental testing.

Different hot bending tests are performed to asses the behavior of SS 316L

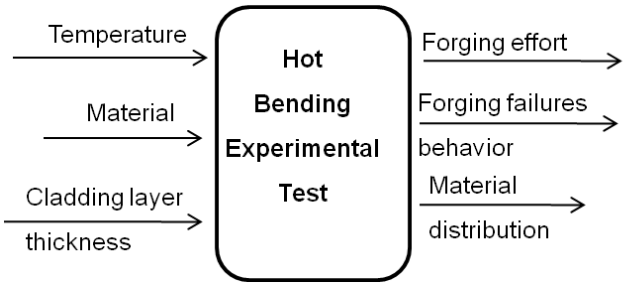

Figure 4.27: In-put and out-put parameters for the hot bending experimental test

cladding on a plate under different hot forging temperatures and cladding dilution rate. The substrate used is low alloy steel S-235 plate of size $300mm \times 150mm \times 30mm$ and its surface was sand blasted to remove oxide scale and dirt before cladding. SS 316 LSi wire of 1.2 mm diameter was used for depositing the clad beads. Chemical composition of the base metal and cladding wire are given in the chapter 1. The plates under test were cladded with an overlap of 40% of total bead width with different dilution rates of 18% and 38% calculated on the basis of the first bead. While we deposit all the beads at an overlapping of 40%, and as discussed in the earlier chapter, (see the Figure 3.42 which shows that the dilution rates of the beads deposited after first bead are lower due to the overlap but fluctuate due the variations in the remelted area of the previous bead). As the single layer cladding is the result of the juxtaposition and partial overlapping of beads which may cause some unevenness in the successive beads. So a "geometrical equilibrium state" is assumed that beyond a certain number of beads, the dilution rate remain constant. For the active part of the cladded

plate under the experimental hot-bending, the global dilution rate is about 2/3 of that of the first bead.

Experimental setup The experimental setup used for the hot bending test is shown in the figure 4.28.

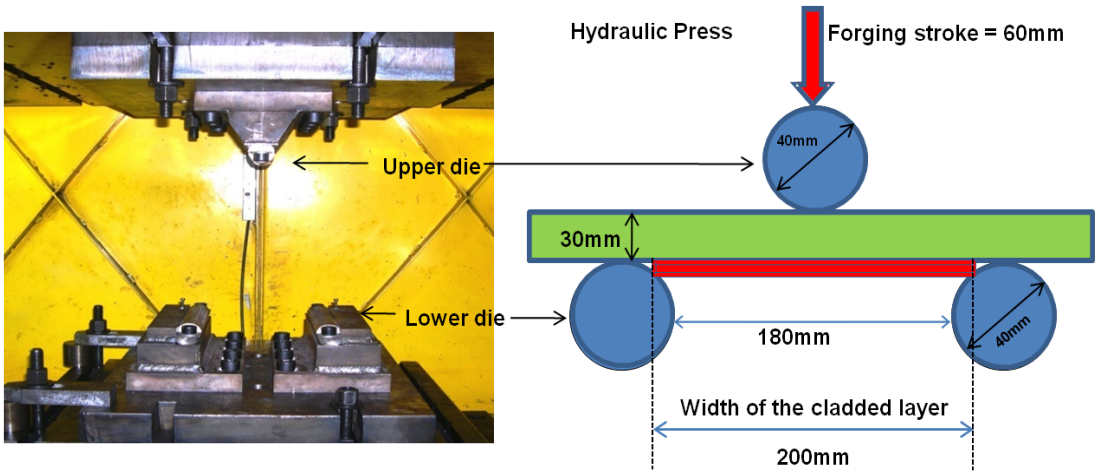

Figure 4.28: Hot bending test apparatus setup

The cladded plate is heated for three different temperatures (750°C, 900°C and 1050°C) under the inert environment of argon flow in the electric oven. The hot bending is carried out along the overlapping direction which may also help to analyze the clad overlapping evolution under hot bending test. The selected input cladding parameters and single bead clad quality parameters are shown in the table 4.3.

Va	Vf	U	Bead width (L)	Reinforcement (r)	Dilution (δ)	wetting angle (θ)
mm/s	m/min	Volts	mm	mm	%	degree
2.5	3.5	24	11.4	3.6	18	61
6.5	6.5	28	12	2.5	38	45

Table 4.3: Cladding input and output parameters selected for hot bending test

Hot Bending Experimental Results The initiation of crack is linked with the hot ductility of the cladding. It may be observed that depending on hot bending temperatures, cracks can be propagated from interface to top cladding surface as shown in the figures 4.29 and 4.30. The results show the hot bending test performed at 750˚C exhibit cracks independent of the cladding layer dilution rates.

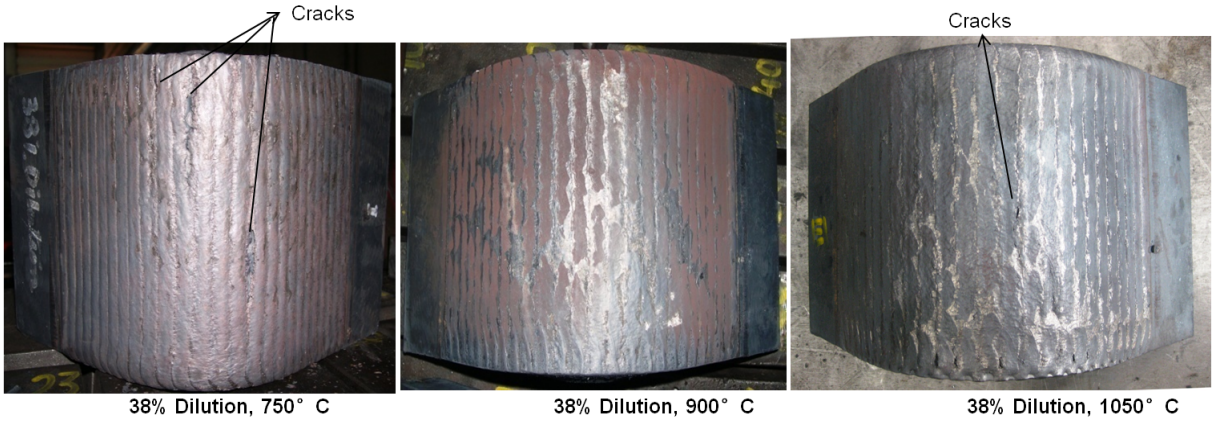

Figure 4.29: Hot bending test results of 38% diluted cladded plate at different temperatures

The summary of the results for the hot bending test is given in the table 4.4. For the test performed at 750˚C, the cladding material may not possess sufficient hot ductility to support the sufficient deformation in the presence of the clad bead adhesion defect and hence the cladded layer under goes the hot cracking. On the contrary, at 950˚C the cladded material has sufficient hot ductility to support the deformation. For the test performed at 1050˚C, the cracks started to occur during the cooling of the work piece and it showed enough hot ductility during the hot bending test. This may be due to different coefficients of the thermal expansions for the substrate and cladded layer that can provoke supplementary deformation, may be due to cooling in the ductility dip range of the cladded material. In all the above cases, the ductility dip is related to the level 2 of forgeability due to lack of penetration defect at the interface which may provoke the cracking.

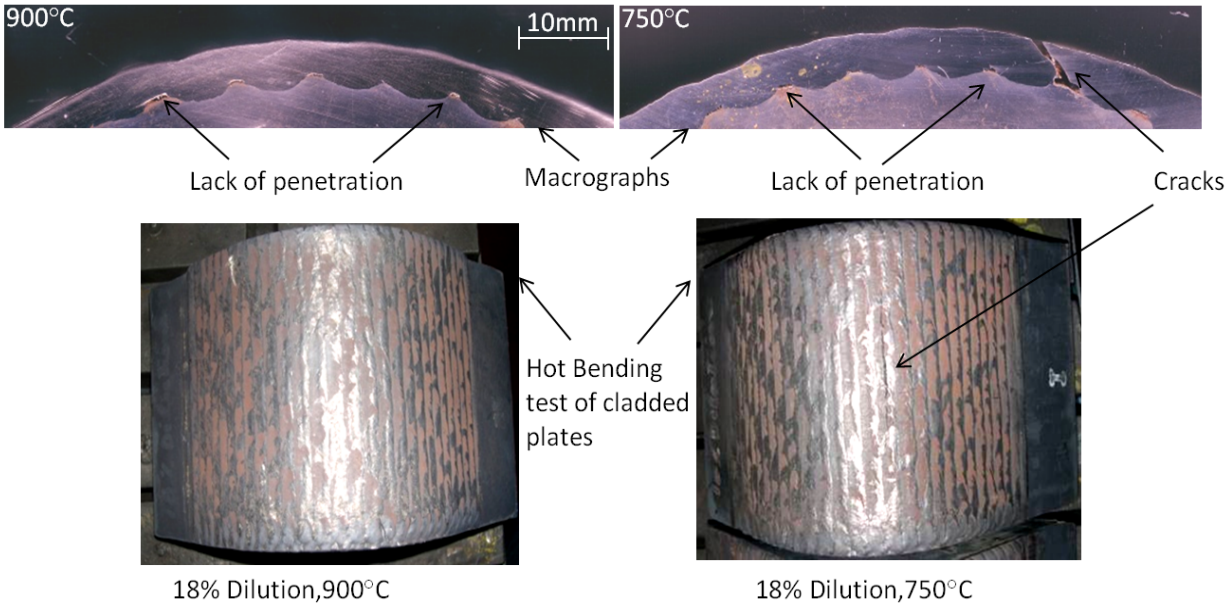

Figure 4.30: Hot bending test results of 18% diluted cladded plate at different temperatures

Hot bending Temperature	Dilution in the 1st Bead	Nominal Energy	Hot cracking	Dilution in the 1st Bead	Nominal Energy	Hot cracking
	%	(KJ /cm)		%	(KJ /cm)	
750°C	18	9.47	yes	38	13.44	yes
900°C	18		No	38		No
1050°C	18		Yes	38		Yes

Table 4.4: Hot bending test results of 18% and 38% diluted cladded plate at different temperatures

To assure the intrinsic ductility of the cladded material, single beads with different dilution rates are deposited and are hot-bended in the perpendicular direction of the beads at different temperatures. It is supposed that the clad beads exhibit an isotropic behavior. All the beads with different dilution rates show sufficient hot ductility and no crack was observed at all the temperatures as shown in the figure 4.31. These results confirm that the cracks occur due to

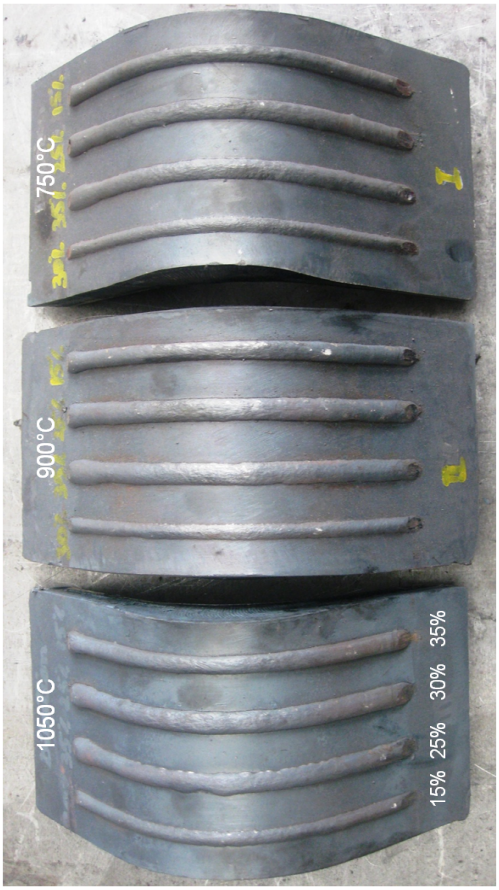

Figure 4.31: Hot bending test results of different dilutions (15%,25%,30%,35%)of single bead cladded plate at different temperatures

lack of ductility around the cladding defects (Level 2 of the ductility) and not only due to the intrinsic ductility of the cladding material. There also exists the effect of the clad bead orientation i,e, the orientation of the ondulation at the substrate/clad interface which may cause some stress concentration points.

The effect of the cladding thickness on the hot bending forging effort is shown in the figure 4.32. The difference in the forging effort from the simulation results may be due to variation in the cladding material due to dilution. The difference in the experimental and simulation forging effort may be as the applied effort is very small as compared to the capacity of the sensors (less sensitive to small forces) in the press used. The difference in the simulation forging effort for the both thickness is of the order of 20 kN, while for the experimental forging effort it increases up to 50 kN. The reason for greater difference in the experimental forging effort may be due to the combined effect of different dilution rate of the two layers and difference in cladding thickness at the same time.

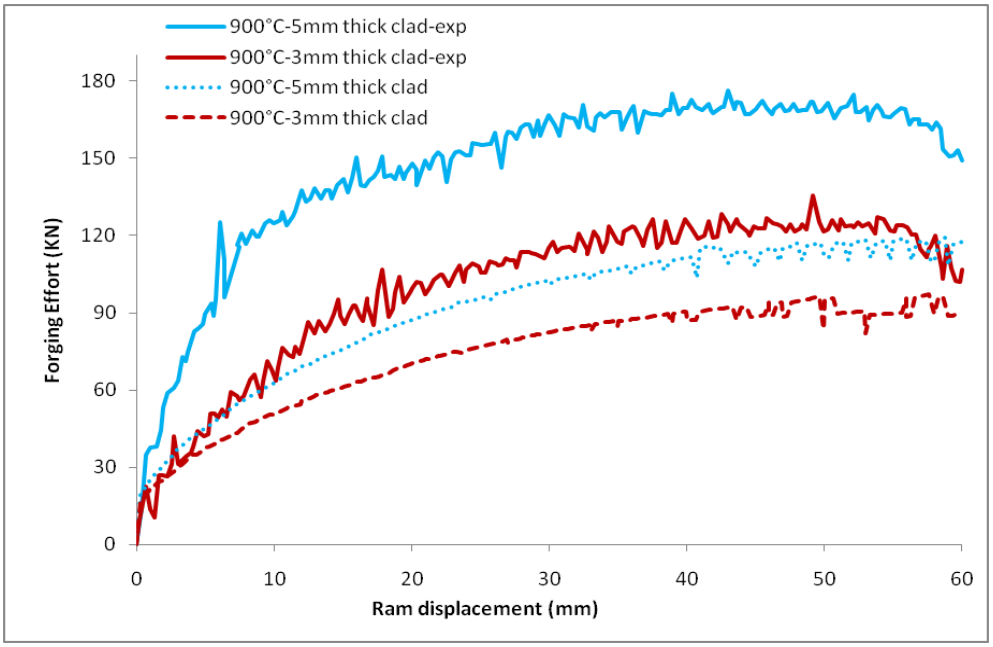

Figure 4.32: Hot bending test results for the forging effort for 18% (5mm thick) and 38% (3mm thick) diluted cladded plate at 900°C

conclusion experimental study From the experimental study we may conclude that the cracks during the hot bending test is not so much dependent on the dilution of the cladded layers. The cracks appeared during the hot bending

when performed at 750°C and during the cooling when performed at 1050°C. If we consider the isotropy in the cladded layer, the above performed test is helpful to determine the hot ductility of the level 1. Any how for the confirmation of the results the hot bending test may be repeated:

- By heating and cooling a cladded plate without hot bending, to observe either the cracks occur or not without hot bending only due to difference in coefficient of expansion and stress concentration due to the clad penetration defects
- By performing the bending test in the direction perpendicular to the beads having already the penetration defect, deposited with torch inclination angle β =0°. This is to avoid the stress concentration effect due to bead penetration ondulation.
- By performing the bending test in the direction parallel to the beads without the penetration defect, deposited with torch inclination angle β =0° to avoid the lack of penetration defect. This test will elaborate the effect of the penetration defect on the cracks initiation.

For further studies, we may proceed with the cooling behavior simulation of the hot bending test.

4.3.1.4 Conclusion related to hot bending test

The hot bending test allows us to estimate the local hot ductility limit of the cladding material for the levels 1 and 2. The hot bending simulation can allow us to guess the equivalent strain in the clad surface as a function of the ram displacement and velocity during the process. The overall deformation profile is not too much dependent on the rheology of the cladded material and other simulation parameters. So the hot bended plate shape is not too much relevant to the level 3 of the forgeability. This level of forgeability may be analyzed by considering the force/displacement curve for cladded and uncladded plates.

However the cracks and ductility dip during the hot bending test may be related to the cooling behavior of the workpiece after the test and difference in the thermal expansion of cladding and substrate material.

4.3.2 The upsetting Test

It is a basic hot ductility test consisting of compressing a series of cylindrical specimens to various levels. The limit for compression without failure by radial or peripheral cracking is considered to be a measure of forgeability. As discussed above, concepts involved in upsetting test are to understand the fundamentals of material flow and initiation of cracks to understand the bi-material forgeability limits.

The experimental setup of the test performed is shown in the figure 4.33.

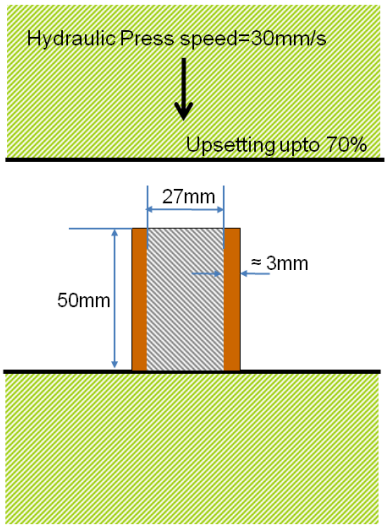

Figure 4.33: The experimental set up for upsetting test

The upsetting test is also studied analytically, numerically and experimentally as for the hot bending test. The aim is to analyze the effect of the test input parameters like friction coefficient, material behavior and temperature.

4.3.2.1 Analytical analysis of the upsetting test

The figure 4.34 shows the input and out put parameters used for the analytical study of the upsetting test. The effect of the variation of all the shown input

parameters on the forging effort is studied.

For the analytical study of the upsetting test, method of slice is applied on a

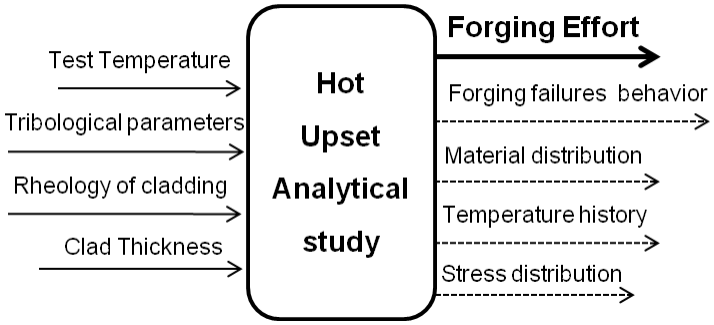

Figure 4.34: The analytical upsetting parameters

cylindrical bar substrate and cladded layer material. The figure 4.35 shows the geometrical and other parameters used for the analytical study of the cladded bar.

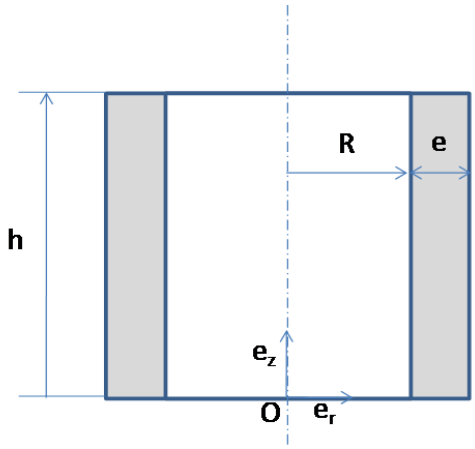

Figure 4.35: Analytical calculation of the upsetting test for a cladded bar/cylinder

The cylindrical symmetry of the problem requires a velocity field in the bar

in the following form:

$$\vec{V}(r,z) = \begin{pmatrix} V_r(r,z) \\ 0 \\ V_z(r,z) \end{pmatrix} \tag{4.34}$$

Considering that the bar remains cylindrical during deformation, the principle of conservation of volume requires the following form for the velocity:

$$\vec{V}(r,z) = \begin{pmatrix} -\frac{r}{2} \\ 0 \\ z \end{pmatrix} \frac{\dot{h}}{h} \tag{4.35}$$

where $\dot{h}$ is upsetting velocity. From the velocity field, we can calculate the strain rate as follow:

$$\dot{\varepsilon}^p = \frac{1}{2}(grad(\vec{v}) + grad(\vec{v})^T) = \begin{pmatrix} -\frac{1}{2} & 0 & 0 \\ 0 & -\frac{1}{2} & 0 \\ 0 & 0 & 1 \end{pmatrix} \frac{\dot{h}}{h} \tag{4.36}$$

Strain rate is uniform throughout the cylinder and depends only on the upsetting velocity and height.

$$\dot{\varepsilon}^p_{eq} = \frac{|\dot{h}|}{h} \tag{4.37}$$

In general, the stress tensor may be given in the following form:

$$\sigma = \begin{pmatrix} \sigma_{rr} & \tau_{r\theta} & \tau_{rz} \\ \tau_{r\theta} & \sigma_{\theta\theta} & \tau_{\theta z} \\ \tau_{rz} & \tau_{z\theta} & \sigma_{zz} \end{pmatrix} \tag{4.38}$$

The stress tensor is reduced to:

$$\sigma_{tensor} = \begin{pmatrix} \sigma_{rr} & 0 & 0 \\ 0 & \sigma_{\theta\theta} & 0 \\ 0 & 0 & \sigma_{zz} \end{pmatrix} \tag{4.39}$$

The deviator stress is given by:

$$\sigma^D = \sigma - \frac{1}{3}tr(\sigma) = \begin{pmatrix} \frac{2}{3}\sigma_{rr} - \frac{1}{3}(\sigma_{\theta\theta} + \sigma_{zz}) & 0 & 0 \\ 0 & \frac{2}{3}\sigma_{rr} - \frac{1}{3}(\sigma_{\theta\theta} + \sigma_{zz}) & 0 \\ 0 & 0 & \frac{2}{3}\sigma_{rr} - \frac{1}{3}(\sigma_{\theta\theta} + \sigma_{rr}) \end{pmatrix}$$

σ^D is parallel to $\dot{\varepsilon}^p$ means that the first two terms on the diagonal are equal. This requires that:

$$\sigma_{rr} = \sigma_{\theta\theta} \tag{4.40}$$

By applying this condition we can get:

$$\sigma^D = \frac{1}{3}(\sigma_{zz} - \sigma_{rr}) \begin{pmatrix} -1 & 0 & 0 \\ 0 & -1 & 0 \\ 0 & 0 & 2 \end{pmatrix} \tag{4.41}$$

It is assumed that the material meets the criterion of Von Mises. The Von Mises equivalent stress must be equal to σ_0, the flow stress in the material.

$$\sigma_{eq} = \sqrt{\frac{3}{2}\sigma^D : \sigma^D} = |\sigma_{rr} - \sigma_{zz}| = \sigma_0 \tag{4.42}$$

So the relation between the two stress components become like that:

$$|\sigma_{rr} - \sigma_{zz}| = \sigma_0 \tag{4.43}$$

The stress tensor is reduced to:

$$\begin{pmatrix} \sigma_{rr} & 0 & 0 \\ 0 & \sigma_{rr} & 0 \\ 0 & 0 & \sigma_{rr} - \sigma_0 \end{pmatrix} \tag{4.44}$$

where,

$$\sigma_{zz} = \sigma_{rr} - \sigma_0 \tag{4.45}$$

This relationship is obtained by considering the free lateral surface of the bar for which σ_{rr}=0 and σ_{zz} is negative. Applying the fundamental principle of applied

Statics for a segment of the bar bounded by:
$r\epsilon[r; r+dr], \theta\epsilon[\theta - \frac{d\theta}{2}; \theta + \frac{d\theta}{2}], z\epsilon[0, h]$
we consider the following equilibrium in the direction $\vec{e_r}$

$$(\sigma_{rr} + d\sigma_{rr})(r+dr).h.d\theta - \sigma_{rr}.r.h.d\theta - 2\sigma_{\theta\theta}h.dr.\sin\frac{d\theta}{2} + 2\tau.dr.d\theta \quad (4.46)$$

where τ is the shear stress exerted by the die on the material in contact with die/material. It opposes the relative motion of the material on the die, τ is negative. We can obtain by developing the relationship of the order 2 and taking into account equality between the radial and ortho radial stresses :

$$d\sigma_{rr} = -2\frac{\tau}{h}dr \quad (4.47)$$

Application for the Coulomb friction case In the case of Coulomb friction, the frictional shear stress is related to the normal pressure of contact by the following relation:

$$\tau = -\mu\sigma_n \quad (4.48)$$

where μ is the friction co-efficient and σ_n is the normal pressure at the die-material contact. In the method of slices, we assume the stress field uniform throughout the slice. The stress σ_{zz} is opposite of the contact pressure.

$$\sigma_{zz} = -\sigma_n \quad (4.49)$$

The equation 4.45 also impose that:

$$d\sigma_{rr} = d\sigma_{zz} \quad (4.50)$$

Finally we get following relation for the components of the stress σ_{zz} which is applicable to both substrate and cladding:

$$\frac{d\sigma_{zz}}{\sigma_{zz}} = -\frac{2\mu}{h}dr \quad (4.51)$$

In the substrate, the solution of the equation 4.51 gives:

$$r\epsilon[0,R]\sigma_{zz} = \lambda_s.exp(-\frac{2\mu_s}{h}r) \tag{4.52}$$

$$r\epsilon[R,R+e]\sigma_{zz} = \lambda_r.exp(-\frac{2\mu_s}{h}r) \tag{4.53}$$

Following are the limiting conditions:

$$\sigma_{rr}(R+e) = 0 \tag{4.54}$$

and

$$\|\sigma_{rr}\|_{r=R} = 0 \tag{4.55}$$

where $\|\sigma_{rr}\|$ is the discontinuity function.
The outer surface of the bar is free, the normal stress at this surface is zero. The continuity conditions also impose that the discontinuity of normal stress across the cladding-substrate interface is zero as well (see the equation 4.55). Considering equation 4.45, we obtain the boundary conditions for σ_{zz} as following:

$$\sigma_{zz}(R+e) = 0 - \sigma_{0r} = -\sigma_{0r} \tag{4.56}$$

$$[\sigma_{zz} + \sigma_0]_{r=R} = 0 \tag{4.57}$$

the last equation becomes:

$$\sigma_{zz}(R^-) + \sigma_{0s} = \sigma_{zz}(R^+) + \sigma_{0r} \tag{4.58}$$

where σ_{0s} and σ_{0r} are the flow stresses in the substrate and cladding layer respectively. $\sigma_{zz}(R^-)$ is the stress at r=R in the substrate and $\sigma_{zz}(R^+)$ is the same stress in the cladding. After applying the boundary conditions the relation can

be written as:

$$\lambda_r = -\sigma_{0r}.\exp(2\frac{\mu_r}{h}(R+e)) \tag{4.59}$$

$$\lambda_s = \{\sigma_{0r}(1-\exp(2\mu_r\frac{e}{h}))-\sigma_{0s}\}\exp(2\frac{\mu_s R}{h}) \tag{4.60}$$

For the forging effort calculation we use the relation:

$$F = \int_0^{R+e} 2\pi r\sigma_{zz}dr \tag{4.61}$$

After an integration by parts on the substrate and the cladding, and assuming that the two friction coefficients are identical, we obtain the following expression for the forging effort:

$$F = \frac{\pi h}{2\mu^2}[h\lambda_s + \exp(\frac{-2\mu R}{h})(\lambda_r-\lambda_s)(h+2\mu R) - \exp(\frac{-2\mu(R+e)}{h}) \lambda_r(h+2\mu(R+e))] \tag{4.62}$$

The expression of "F" shows the geometrical quantities "R" and "e" are functions of the initial height and diameter of the bar, the initial cladding thickness and upsetting height. The principle of conservation of volume gives:

$$R = R_o\sqrt{\frac{h_o}{h}} \tag{4.63}$$

$$e = e_o\sqrt{\frac{h_o}{h}} \tag{4.64}$$

The flow stress of the substrate and the cladding layer can be calculated from the equivalent plastic strain and strain rate. The coefficients defined by relations 4.59 and 4.60 can be calculated from the expression of flow stress calculated by a Norton-Hoff law or Spittel law. This possibility is that the equivalent plastic strain and strain rate are uniform in the cladded workpiece. Equivalent plastic

strain ε_{eq}^{p} is given by the following equation:

$$\varepsilon_{eq}^{p} = ln(\frac{h_o}{h}) = \varepsilon \tag{4.65}$$

The strain rate can be calculated by the equation 4.37. The flow stresses are described by the simplified form of the Spittel law as follow:

$$\sigma_0 = A \exp(m_1) T \epsilon^{m_2} \exp(\frac{m_4}{\epsilon}) \dot{\epsilon}^{m_3} \tag{4.66}$$

This law and the associated coefficients are only valid for given range of temperatures, strain and strain rate data for each material.

Results of the analytical analysis The result obtained for an upsetting of 70%, under different conditions are obtained analytically. The figures 4.36 shows the evolution of the forging effort during 70% upsetting for 3mm thick SS316L cladding on the C35 substrate at 900°C for coefficient of friction, μ =0.3.

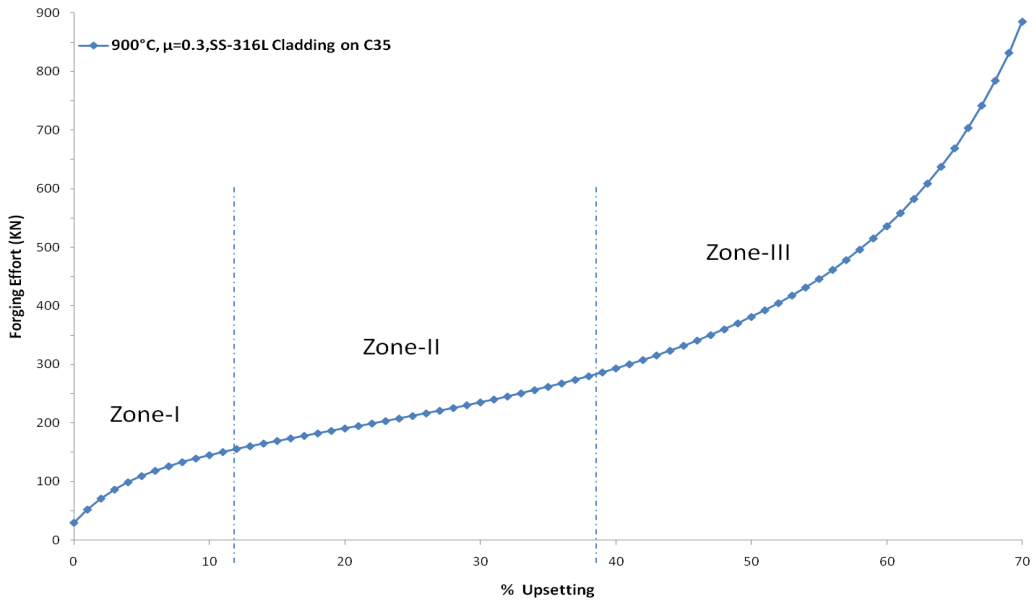

Figure 4.36: The forging effort evolution during 70% upsetting for SS316L cladding on the C35 substrate at temperature 900°C for the analytical study

The above figure shows that the forging effort behavior with the % upsetting can be divided in three zones in general. In the zone I, the forging effort increases sharply (Due to hardening phenomenon found with the law of behavior Spittel) and zone II is a transition between the zone I and zone III and is the point of the inflexion where the force displacement slope is minimum. In zone III there is again a rapid increase in forging effort with the increase of upsetting. This is due to a combination of several factors including the increase of the strain rate as the diameter of the workpiece increases and an accumulation of tangential friction forces.

From the figures 4.37 and 4.38, we can note that temperature and cladding thickness variation show the same behavior and are more sensible for the last two zones of the forging/upsetting curve.

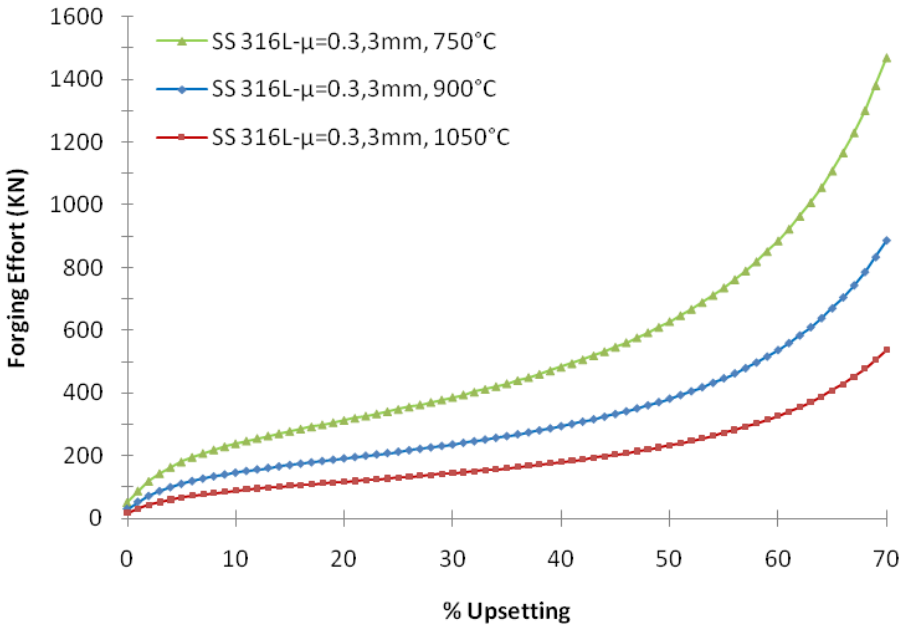

Figure 4.37: The effect of the test temperature on the forging effort of SS316L cladding on the C35 substrate at temperature 900˚C for the analytical upsetting study

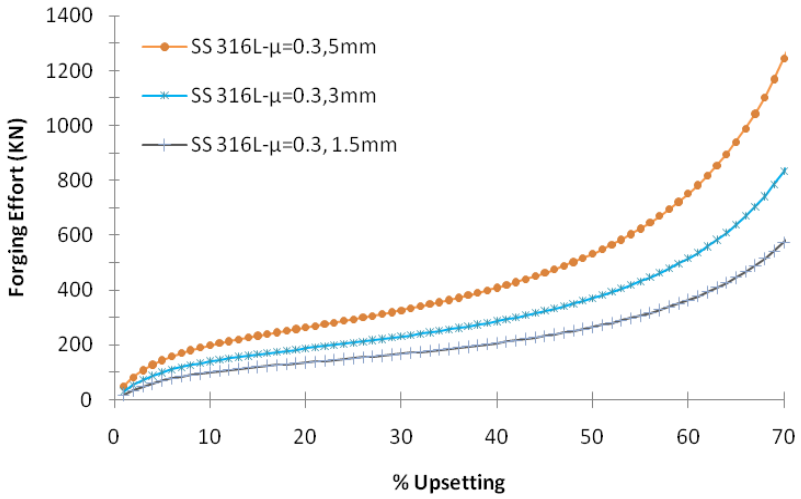

Figure 4.38: The effect of the cladding thickness on the forging effort of SS316L cladding on the C35 substrate at temperature 900°C for the analytical upsetting study

On the other hand, the variation in the die-workpiece friction co-efficient has a remarkable affect on the zone III of the curve as shown in the figure 4.39. The phenomenon explains the friction effect with the increase of bar diameter and % upsetting. By considering the frictionless interface, we get the following relation for the forging effort which shows that the forging effort depends on the material behavior and the cladding thickness:

$$F = \sigma_{os}\Pi R^2 + \sigma_{or}\Pi e(2R + e) \tag{4.67}$$

The variation in temperature and thickness shows a clear effect in the zone I. The temperature affects directly the material behavior while the thickness affects the initial section of the bar. Similarly the change of the material (see figure 4.40) also shows the effect on the three zones of the forging effort/displacement curve.

Analytical test conclusion If we consider the zone III of the forging effort/displacement curve, we may derive a relation between the forging effort and

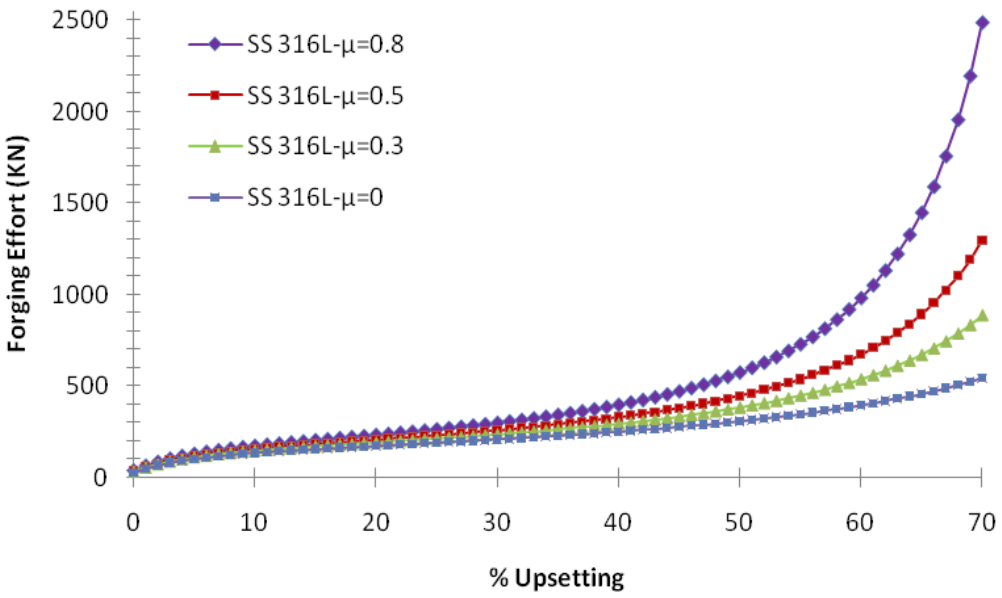

Figure 4.39: The effect of friction coefficient on the forging effort of SS316L cladding on the C35 substrate at temperature 900˚C for the analytical upsetting study

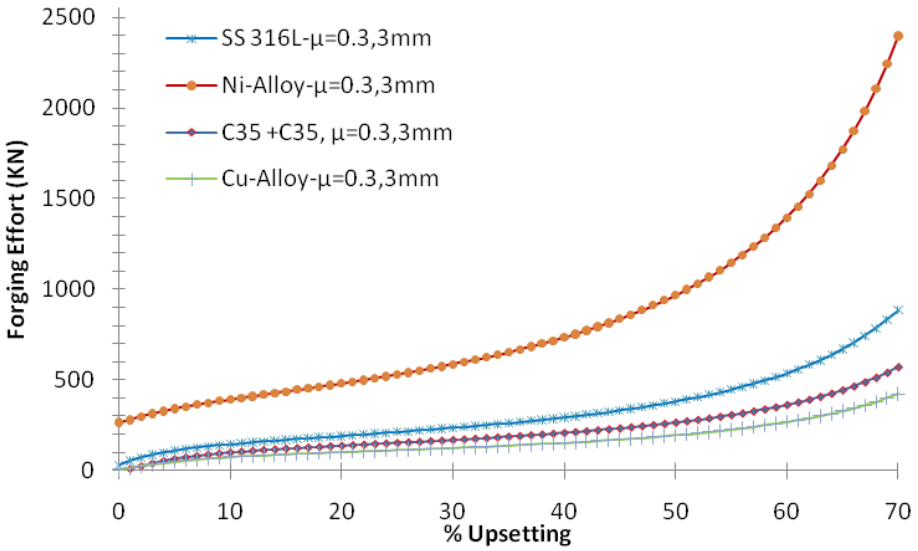

Figure 4.40: The effect of the cladded material on the forging effort on the C35 substrate at temperature 900˚C for the analytical upsetting study

material behavior. The effect of the friction coefficient becomes significant for higher upsetting values. In the next section we will analyze the effect of the main forging parameters on the cladding surface deformation by the simulation upsetting test.

4.3.2.2 The upsetting Simulation Test

For the simulation analysis, the upsetting test for different thermal exchange and tribological conditions at the work piece and the die interface is also performed. The behavior of the cladded work piece subjected to forging effort at several combinations of parameters as shown in the figure 4.41 is under study.

The parameters considered during the upset simulation test include, the die-

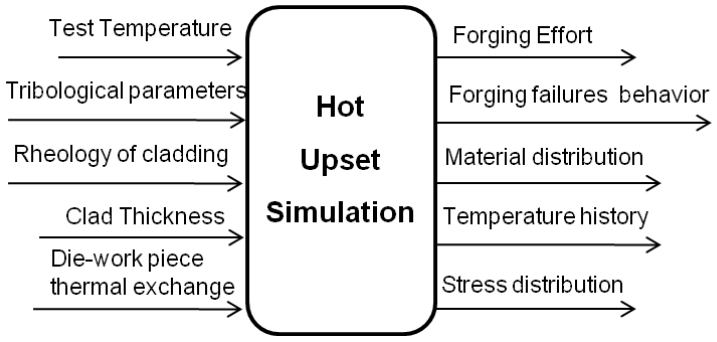

Figure 4.41: In-put and out-put parameters for the simulation of the hot upsetting test

workpiece interface as well as the cladding layer-substrate interface, the rheological behavior of the cladding material and the initial temperature of the cladded workpiece, are shown in the figure 4.42. Other parameters such as the thermal conduction of the cladding material or forging speed are not considered as process variables in this work.

The base metal and cladded layer material are defined from the database of the software describing the rheological and thermal properties of known material grades as discussed already in the hot bending test section. The rheological law used by the software is the Hansel-Spittel law describing an elasto-viscoplastic

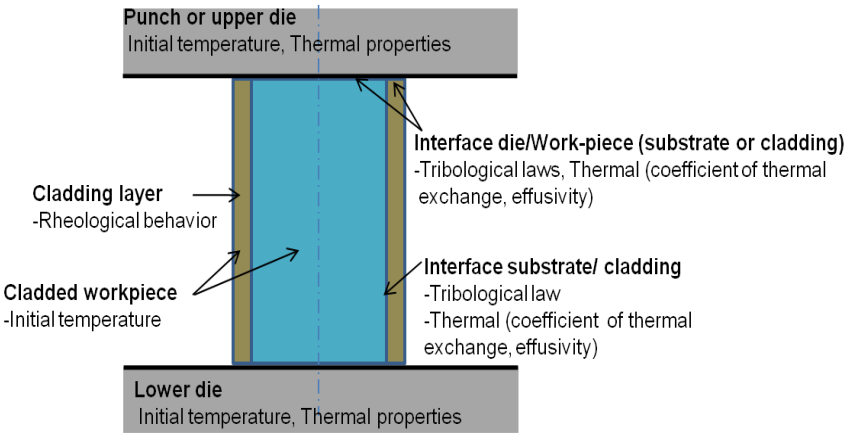

Figure 4.42: Characterization approach for upset test of bi-material cladded hot forged product

thermal behavior and is well suited to represent the hot forming behavior of metals. As already discussed above, in most cases, we use a simplified form of the Hansel-Spittel law as given below:

$$\sigma_f = Ae^{m_1 T}\epsilon^{m_2}e^{\frac{m_4}{\epsilon}}\dot{\epsilon}^{m_3} \tag{4.68}$$

This law and the coefficients are only valid for given range of temperatures, strain and strain rate data for each material. The bilateral sticking criteria is applied at the base metal and cladding layer interface although practically there is weld cladding interface between them. The values of the constants for the materials used are given in the table 4.5.

	A	m_1	m_2	m_3	m_4
C35	1498.8708	-0.00269	-0.12651	0.14542	-0.05957
SS316L	8905.34	-0.00383	0.01246	0.09912	-0.02413
Ni-based alloy	356229.03	-0.00647	0.02892	0.15357	$1.2Xe^{-5}$

Table 4.5: The coefficients of the Hansel-Spittel law for upset simulation test

Hot upsetting simulation Results The result obtained from the upsetting simulation for an upsetting upto 70%, taking reference of the sticking friction between the die-work piece interface are shown in the following section.
The figure 4.43 shows the distribution of equivalent strain for the 70% upsetting of the bar at 900˚C under the sticking friction condition at the die work piece interface for SS316L cladding on C35 substrate.

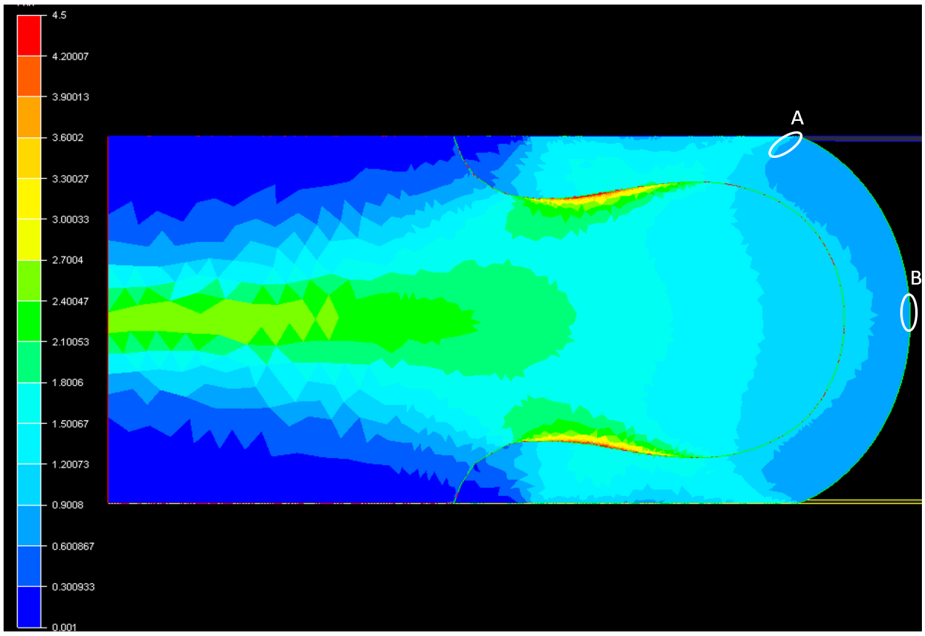

Figure 4.43: Simulation results of the equivalent strain with sticking friction criteria for SS316L cladding on C35 substrate at 900˚C

The figure 4.44 shows a higher equivalent strain at the interface as compared to the clad surface under the sticking friction condition at the die work piece interface for SS316L cladding on C35 substrate at 900˚C.

The Simulation results of the forging effort with sticking friction condition at the die/work-piece interface while deposition of 3 mm thick SS316L cladding on C35 substrate at 900˚C is shown in the figure 4.45. The evolution of the forging effort during 70% upsetting, shows that the forging effort behavior with the %

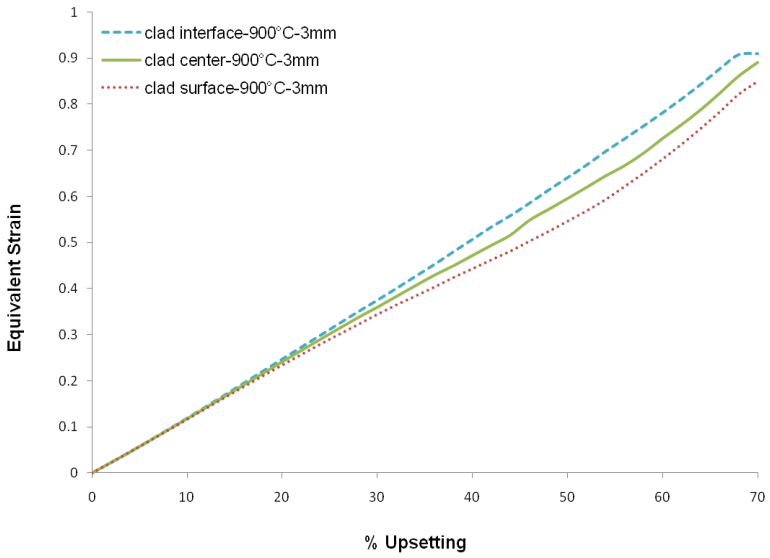

Figure 4.44: Simulation results of the equivalent strain with sticking friction criteria at different positions of the cladded layer of SS316L on C35 substrate at 900°C

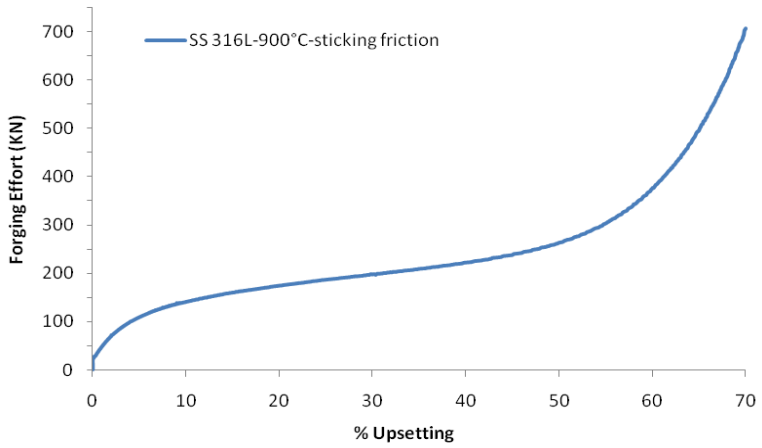

Figure 4.45: Simulation results of the forging effort with sticking friction criteria at the die/work-piece of SS316L cladding on C35 substrate at 900°C at low thermal exchange ($2.10^3 Wm^{-2}k^{-1}$)

upsetting can be divided in three zones in general as described in the analytical analysis zone. For each of these forging effort curves, there are three different behaviors:

1. The first zone, the force increases rapidly. There is a hardening phenomenon found with the law of behavior Spittel.

2. For the transition zone, the force displacement slope is minimum.

3. At the end of the upsetting, the effort increases again rapidly. This is due to a combination of several factors including the cooling of the billet which reduces the ductility of the material, the strain rate increases as the diameter of the workpiece increases as well as an accumulation of tangential friction forces.

The temperature distribution during the test is shown in the figure 4.46, where we can see the temperature drop in the certain upper thickness of the work piece due to convection and radiation heat loss and above all heat conduction in the die.

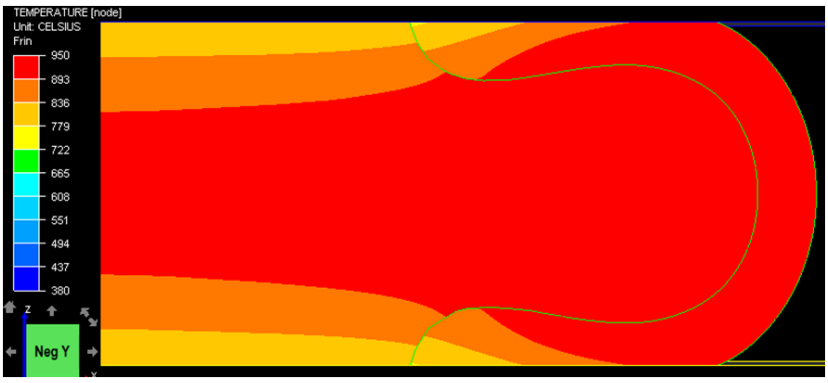

Figure 4.46: Temperature distribution during upsetting simulation for SS 316L cladding on C35 substrate with sticking friction at die/work piece interface performed at 900°C

The figure 4.47 indicates the stress distribution along the xx-direction. The stresses at the top and bottom edges of the work piece approaches upto 400 MPa

while at the clad-substrate interface of the both edges goes upto 160 MPa, when performed with the sticking friction at the die-workpiece interface.

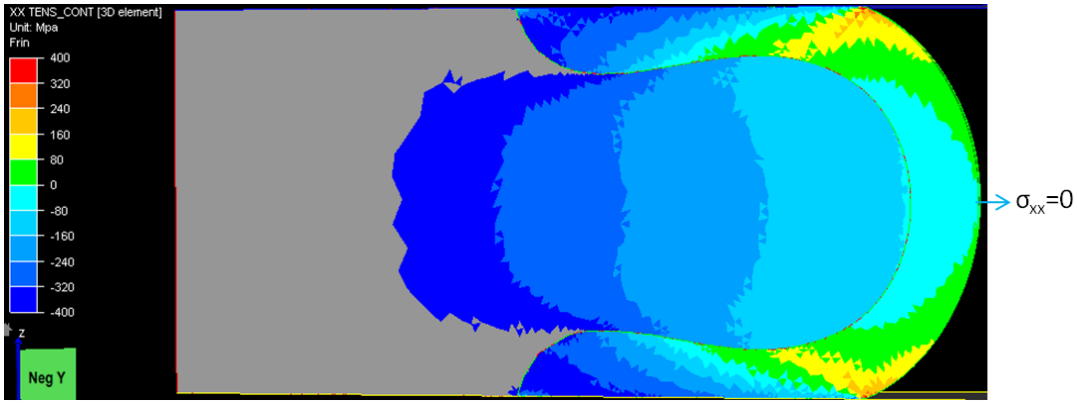

Figure 4.47: Simulation results of the Stresses along-xx for SS316L cladding on C35 at 900˚C with sticking friction conditions at die/work piece interface

The figure 4.48 shows the stress distribution along the yy-direction showing the tensile stresses at the clad top surface (up to 290 MPa). The stress tensor at the point A and B are shown in the following equations at the 70 % of the upsetting. These values correspond to the SS316L cladding on C35 at 900˚C with the sticking friction conditions at die/work piece interface. The figure 4.49 shows the stress distribution along the zz-direction showing the tensile stresses at the clad top surface (up to 215 MPa).

With FORGE 2009 it is possible to estimate the probability of the damage of the workpiece by calculating the Lathan coefficient. The indicator LATANDCN is used to predict rupture phenomena by the following equation 4.69:

$$La = \int_0^{\bar{\varepsilon_f}} \sigma_{max} d\bar{\varepsilon} \tag{4.69}$$

where, $\bar{\varepsilon_f}$ is the effective strain at fracture, σ_{max} is the maximum tensile stress and $\bar{\varepsilon}$ is the effective strain.

While applying the above criteria it is observed that, the simulation shows a higher possibility of longitudinal and orthoradial/ circumferential rupture when

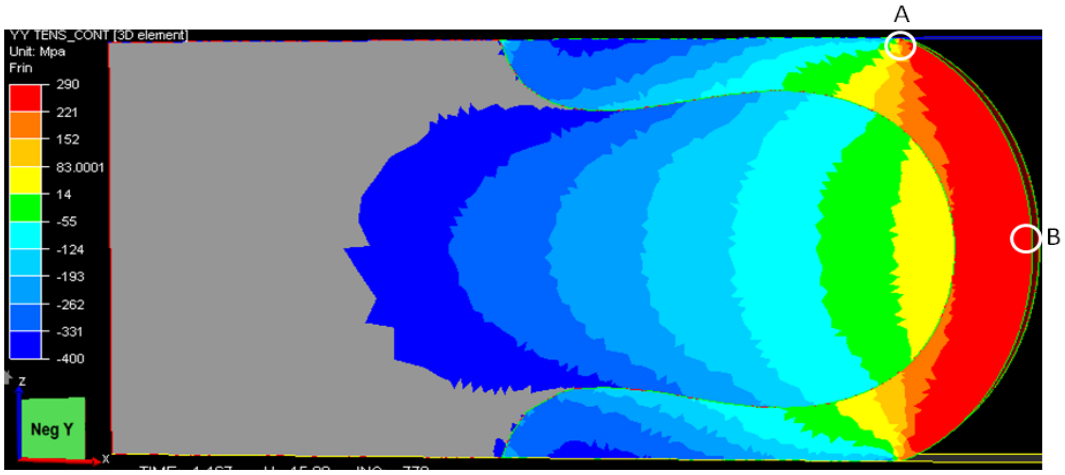

Figure 4.48: Simulation results of the Stresses along-yy for SS316L cladding on C35 at 900˚C with with sticking friction conditions at die/work piece interface

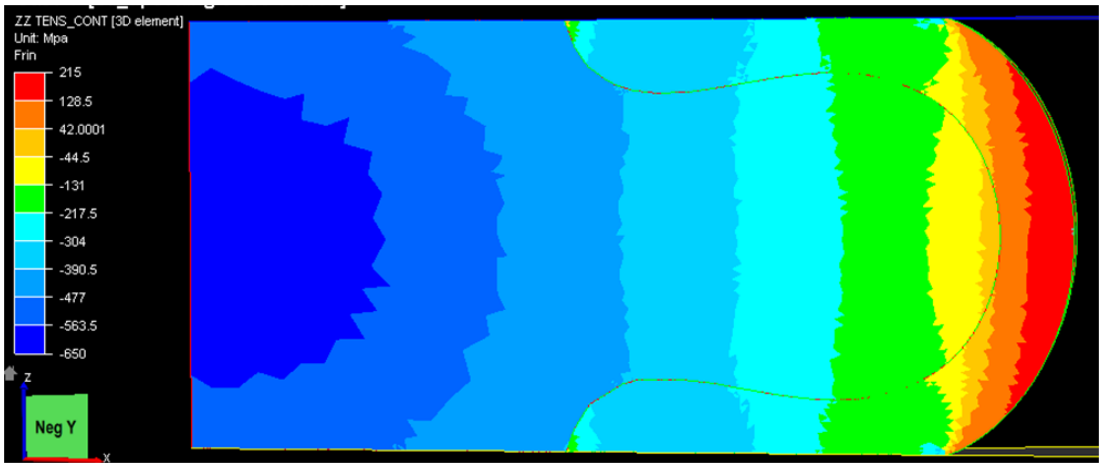

Figure 4.49: Simulation results of the Stresses along-zz for SS316L cladding on C35 at 900˚C with with sticking friction conditions at die/work piece interface

sticking friction is applied at the die/workpiece interface as shown in the figure 4.50. The possibility of cracks in the zone B is common for all materials while in the zone A near the die work piece contact it is due to upsetting of a cladded workpiece.

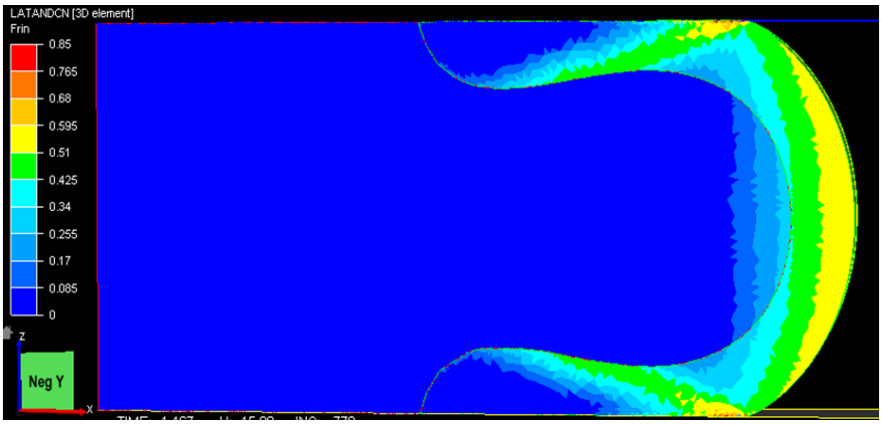

Figure 4.50: The failure criterion of LATANDCN during upsetting simulation for SS316L cladding on C35 substrate with sticking friction conditions at die/work-piece interface at 900˚C

The cladding surface and interface deformation profiles for SS316L cladding on C35 substrate at 900˚C for sticking friction conditions is shown in the figure 4.51.

The substrate takes the form of spur and the cladding layer is distributed on it.

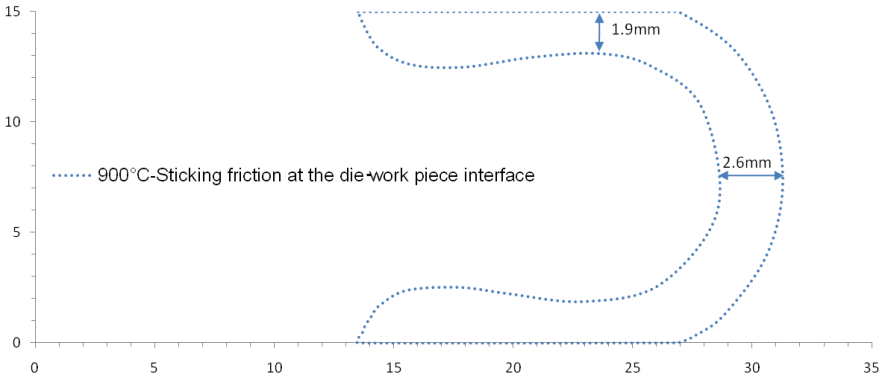

Figure 4.51: The simulation results of the cladding surface and interface deformation profiles for SS316L cladding on C35 substrate at ticking friction conditions performed at 900˚C

The cladding thickness is minimum near the edge of the contact point with the die.

Overall effect of selected input parameters on upsetting simulation results The overall effect of the selected input simulation study parameters on the considered out put parameters is described in this section.

Overall effect of cladding thickness The simulation results of the forging effort at different clad thickness of SS 316L on C35 substrate is shown in the figure 4.52. It is evident that forging effort increases with the increase of cladding thickness. For both cladding thicknesses, the forging effort increases sharply in the beginning and end of the forging cycle and remains stable in the middle. The maximum value of the forging effort with the sticking friction interface for cladding thickness of 3 and 5mm goes upto 1075 and 680 kN respectively.

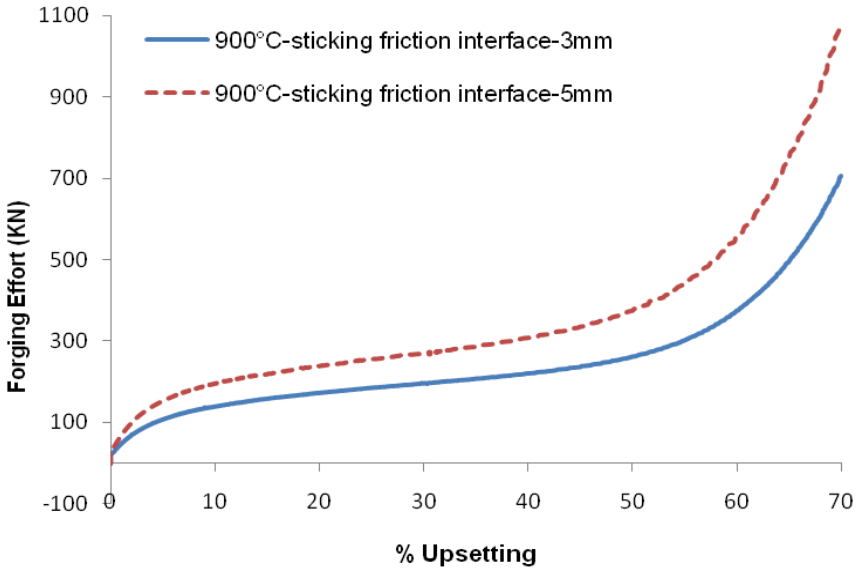

Figure 4.52: Simulation results of the forging effort at different cladding thickness for SS 316L on C35 substrate at 900°C

We can note that cladding thickness variation show the same behavior of forging/upsetting curve as in the analytical study of the cladding thickness variation. The influence on the zone II is apparent by the variation of cladding thickness. Simulation results of the equivalent strain at point B (see the figure 4.48) for different clad thickness at a temperature of 900°C for SS 316L on C35 substrate

is given in the figure 4.53. The equivalent strain at the clad surface gives higher values for higher clad thickness.

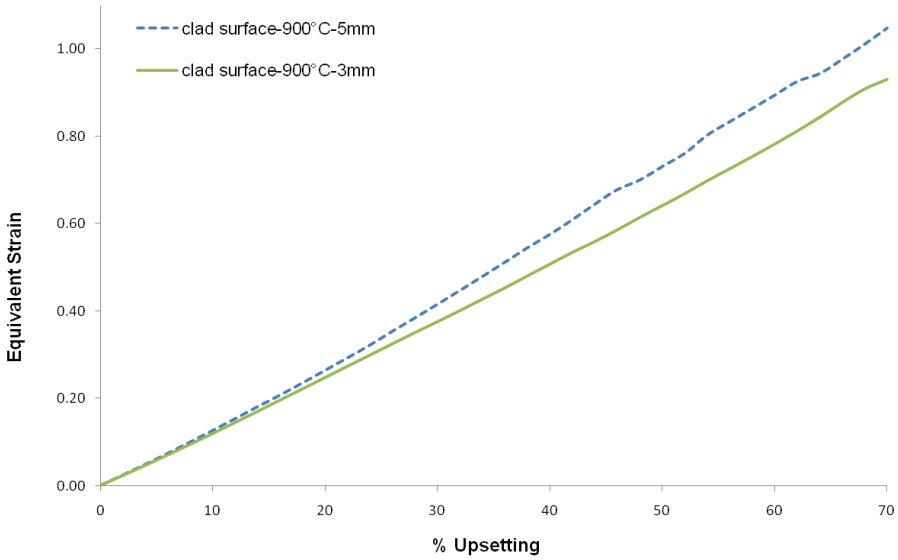

Figure 4.53: Simulation results of the equivalent strain at different cladding thickness for SS 316L on C35 substrate at 900°C

Overall effect of the cladding material The figure 4.54 shows the simulation results of the cladding material distribution for different materials deposition on C35 substrate. For the Ni-based alloy cladding, we can see notches at the clad surface edges. Globally, there is not a big difference in the material distribution behavior during the upsetting test.

The variation in the material behavior shows the effect on the three zones of the forging effort/displacement curve (see the figure 4.55) and is in accordance with the analytical results especially at the start of the upsetting.

Overall effect of Tribological and thermal exchange conditions The figure 4.56 shows that the material distribution is different for different tribological and heat exchange conditions (thermal exchange ($2.10^3 W m^{-2} k^{-1}$) for b,c and d of the figure 4.56) at the die-workpiece interface. The variation of the cladding

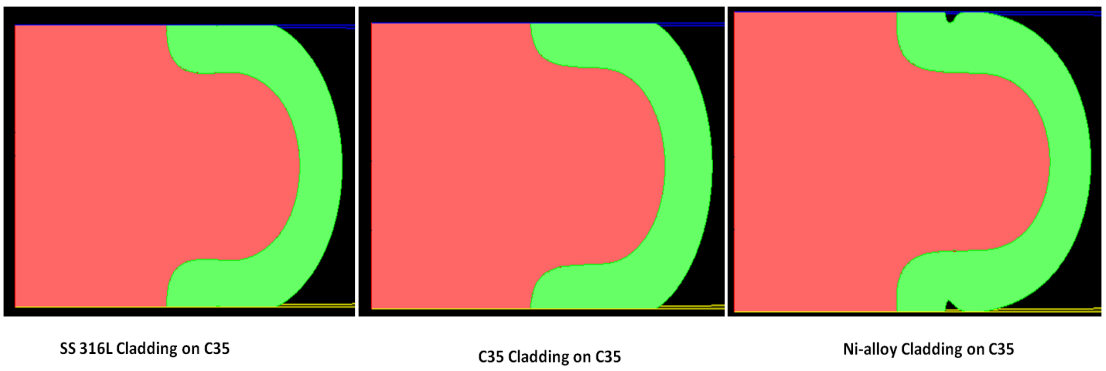

Figure 4.54: The simulation results of the cladding surface profiles for SS316L and Ni based alloy cladding on C35 substrate

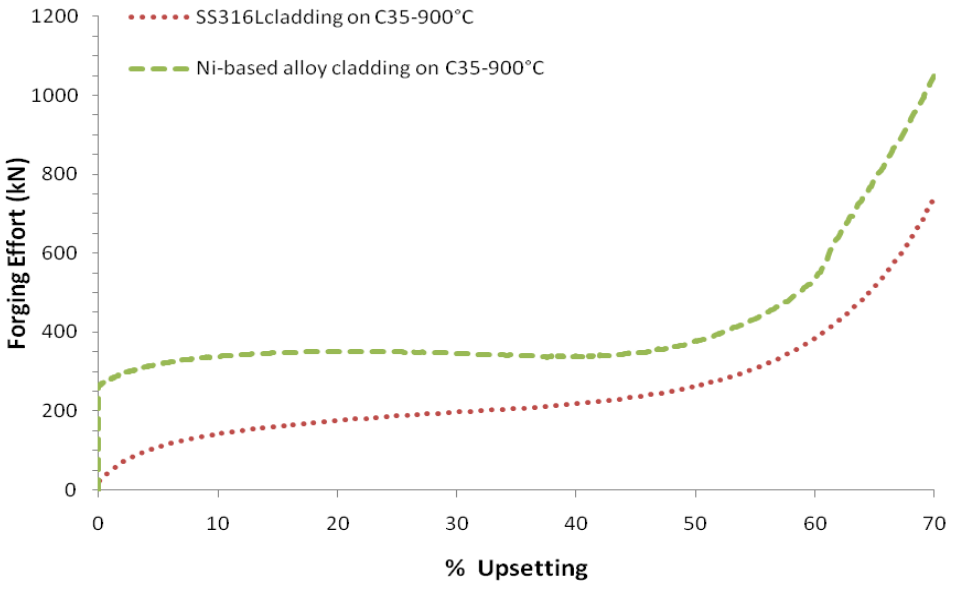

Figure 4.55: The simulation results of effect of the cladding material(SS316L and Ni based alloy) on forging effort performed under sticking friction at 900˚C

layer thickness with the change of the tribological conditions is also shown here. It may be noted that friction effect is not the only factor that provoke the bar-

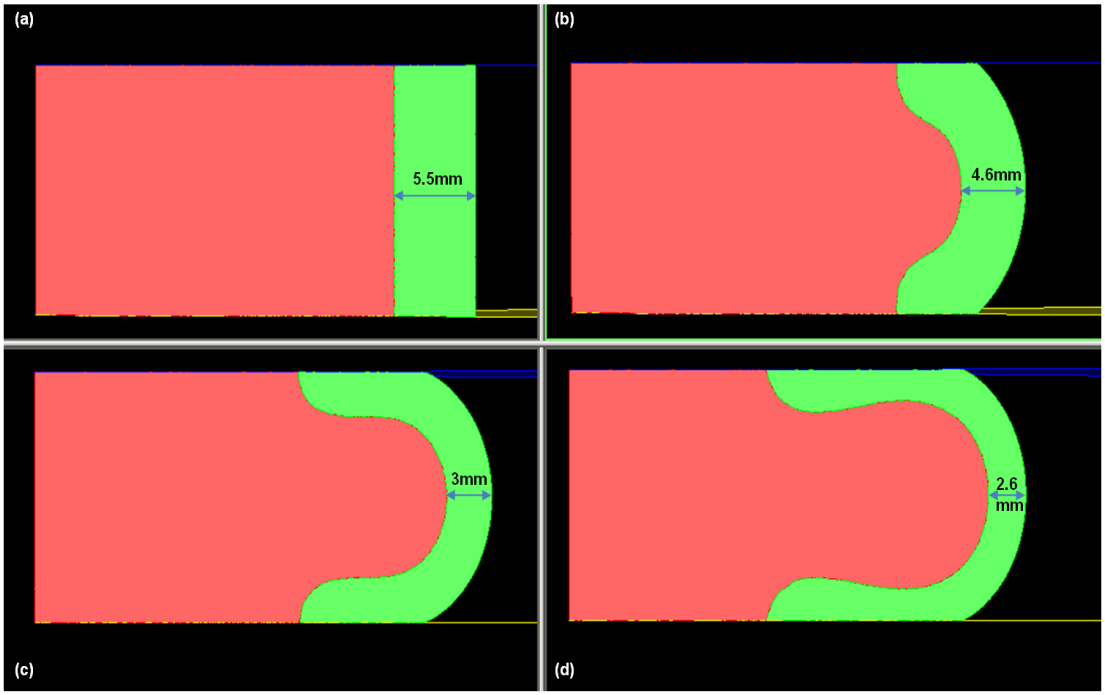

Figure 4.56: Simulation results of the effect of tribological on cladding material distribution for SS316L cladding on C35 substrate(900°C) (a) sliding friction under adiabatic conditions,(b)sliding friction, (c) Die-workpiece interface friction(μ=0.15) and (d) Sticking friction

reling effect during upsetting test but the thermal exchange with the die may also cause this phenomenon by cooling of the workpiece material at the tool workpiece interface. This exchange produces the gradient of the flow stress in the workpiece that behaves like the frictional effect.

The figure 4.57 shows the simulation results of the forging effort at different tribological conditions for SS316L cladding on C35 substrate at 900°C. It can be observed that for an upsetting of 70% , the forging effort for the sticking friction interface approaches upto 700kN and under adiabatic conditions and sliding friction at the die-workpiece interface the forging effort reduces remarkably to 480kN. The decrease of the forging effort in the zone II for the sticking friction

criterion may be due to the decrease in the cladding thickness. We observed that the cladding thickness for the adiabatic condition has increased remarkably at the end of the upsetting.

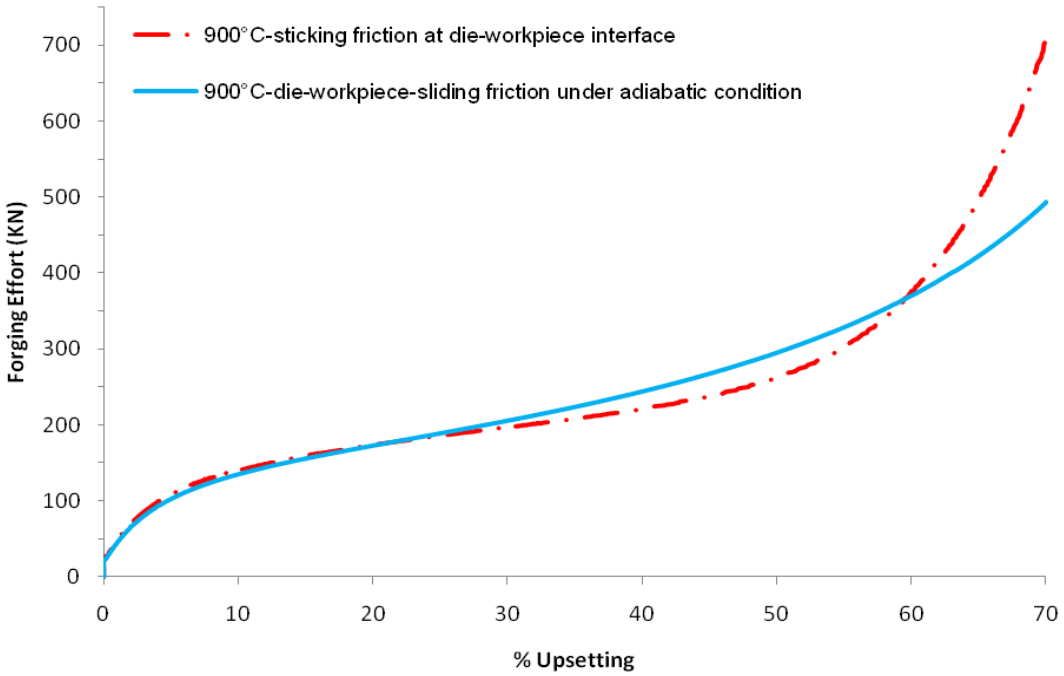

Figure 4.57: Simulation results of the forging effort at different tribological and thermal exchange conditions (for thermal exchange coefficient=$(2.10^3 Wm^{-2}k^{-1})$ and adiabatic) for SS316L cladding on C35 substrate at 900°C

The figure 4.58 shows the effect of high die-workpiece interface thermal exchange on the temperature distribution and the damage probability (The failure criterion of LATANDCN). The surface temperature is dropped up to 100°C and hot ductility and forgeability is remarkably reduced under these conditions. The same type of behavior for the Ni-alloy cladding layer was observed even at the low thermal exchange and upsetting upto 60% as shown in the figure 4.59 due to Ni-alloy rheological high sensitivity to temperature variations.

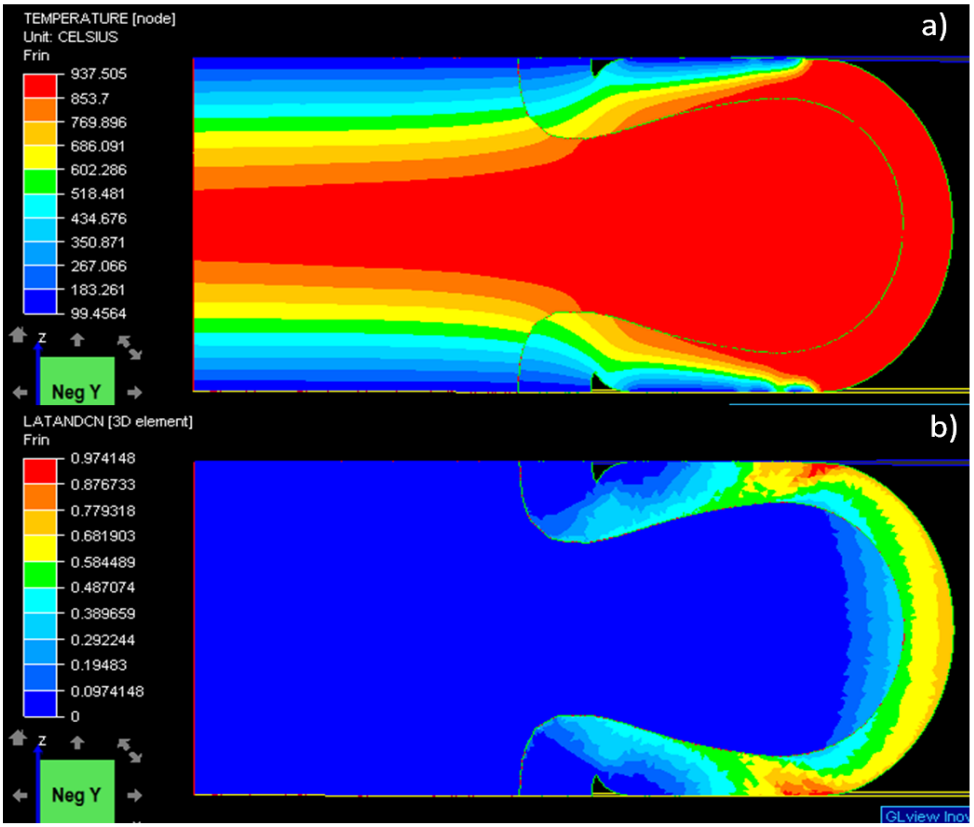

Figure 4.58: The effect of high thermal exchange ($2.10^8 Wm^{-2}k^{-1}$) on the temperature distribution (a) and damage probability (b) for SS316L cladding on C35 substrate at 900°C

Due to high thermal exchange a "skullcap" like temperature drop is observed which may provoke notching phenomenon in the cladded layer. There may be two reasons of this phenomenon:

- There is a strong temperature fall due to high thermal exchange which may cause a decrease in the hot ductility.
- Due to higher sensitivity of the ductility with the temperature, this phenomenon may occur even for moderate temperature fall as in the case of Ni-based alloys cladding.

The figure 4.60 shows the effect of different die-workpiece interface thermal exchange on the forging effort. The forging effort increase with the increases of

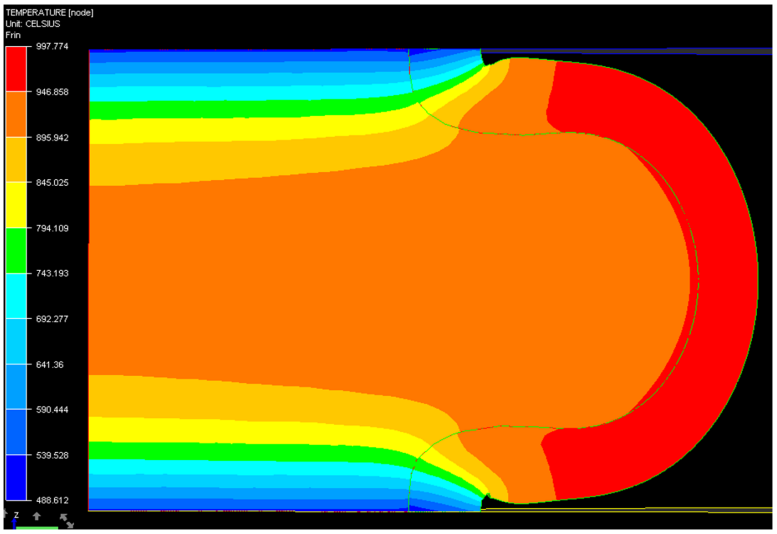

Figure 4.59: The temperature distribution for the Ni-based alloy cladding on C35 substrate at 900˚C

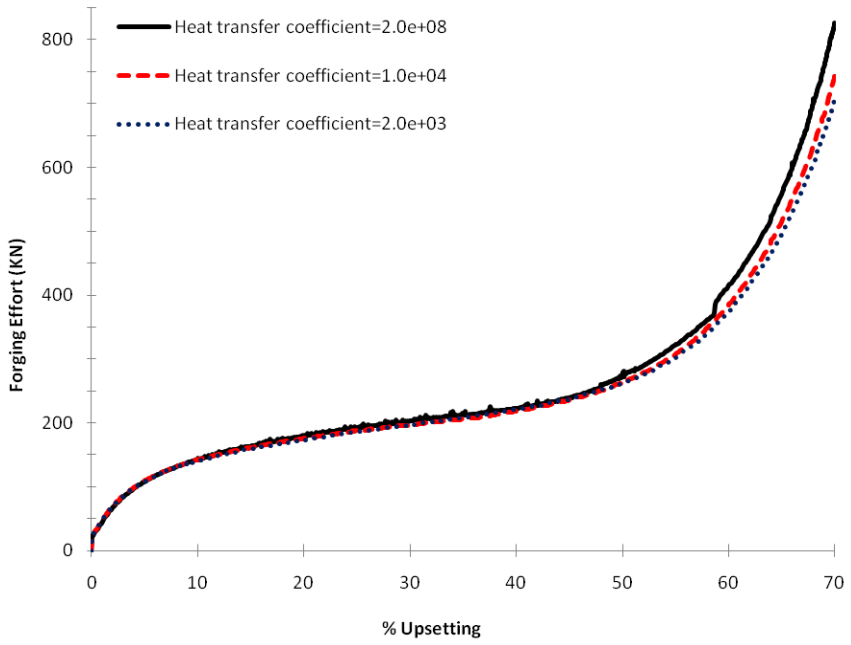

Figure 4.60: Simulation results of the forging effort at different heat exchange conditions for SS316L cladding on C35 substrate at 900˚C for sticking tribological conditions

the thermal exchange between die and workpiece. A little increase in the forging effort may be related to higher friction at lower surface temperature of the workpiece. The effect of the thermal exchange is decreased due to the sticking conditions of the upsetting test.
The effect of tribological conditions on the damage probability (The failure criterion of LATANDCN) is shown in the figure 4.61 at point B. For the adiabatic conditions, the possibility to failure is zero due to compressive stresses.

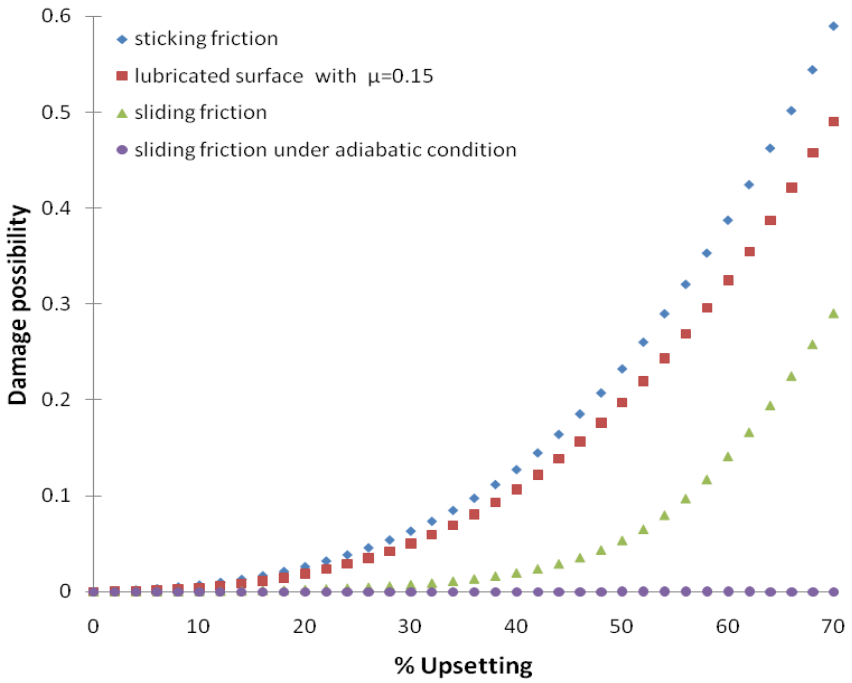

Figure 4.61: Simulation results of the damage behavior at different tribological conditions at point B of the figure (4.43)for SS316L cladding on C35 substrate at 900°C

We can observe that the possibility of the cracks for the sticking friction conditions is maximum.

Overall effect of initial temperature Simulation results of the forging effort at different forging temperatures for SS316L on C35 substrate is given in the

figure 4.62. The forging effort for the SS316 cladding on C35 keeping the interface as sticking friction for 70% of upsetting give the value of 1035, 695 and 450kN for the temperatures of 750˚C, 900˚C and 1050˚C respectively. It is observed that the forging effort decreases with the increase of the forging temperature due to the direct effect on the flow stresses of the material. The material and temperature variations have an important effect on the zone II and zone III of the force /displacement curve.

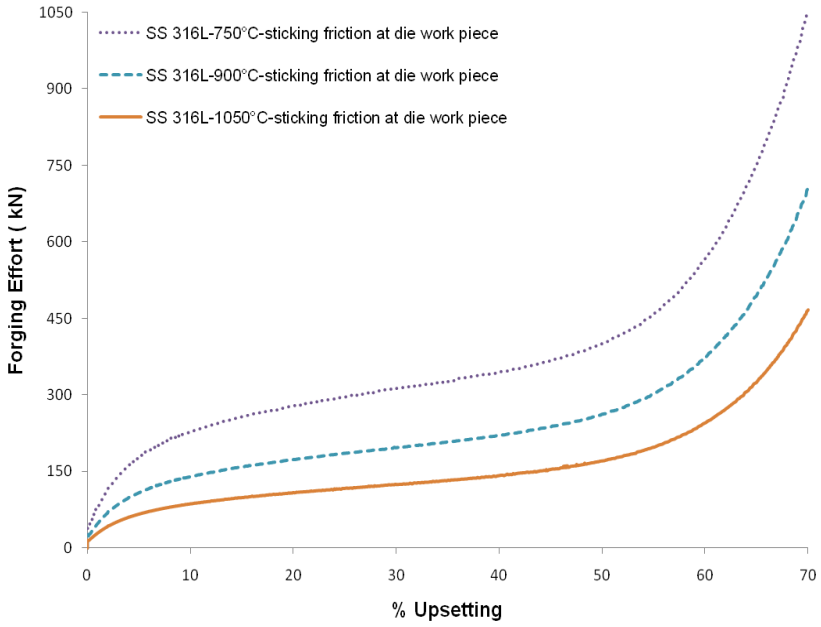

Figure 4.62: Simulation results of the forging effort at different forging temperatures for SS316L on C35 substrate with sticking friction at the tool workpiece interface

Conclusion On contrary to the hot bending test, the solicitation on the cladding are not uniform due to the barreling effect of the workpiece because of combined effect of friction and thermal exchange. The aim is to control the tribological effects of the test by imposing the sticking friction conditions, to fix the strain and strain rate of a given geometry of the workpiece as the function of the upsetting

distance only. Thus it is possible to control solicitations in the cladding with the help of upsetting test parameters directly.

4.3.2.3 Upsetting Experimental Test

The parametric study of the cladded workpiece upset test includes the percent upsetting, test temperature and tribology of workpiece and die interface. The figure 4.63 shows the parameters considered during the upsetting experimental testing.

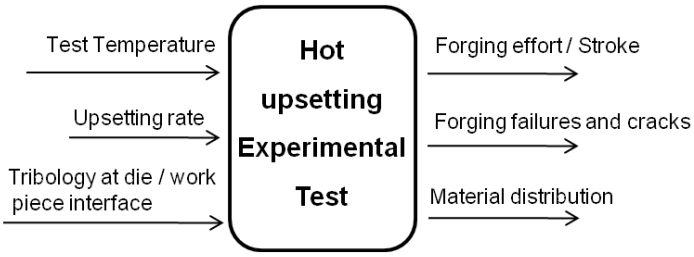

Figure 4.63: In-put and out-put parameters for the hot upsetting experimental test

Principle of the test In the upsetting test, a work piece is upset between two plan dies until a crack appears and depending on the appearance of cracks, the upset rate of the next trial is increased or decreased. The increase or decrease step (the percentage upset) is adjusted with the reference to the total bar height. From the last un cracked test, the upset increment step is reduced to refine the applicable range as shown in the figure 4.65. Cladded samples were obtained by cutting the original bar. So there is a dispersion of the sample length that should be taken into account in calculating the real upset rate. The equipment layout is shown in the figure 4.64 consisting of a modular tool holder and tool. Two types of tools with different tribological behaviors are used for the experimental upset tests as described below:

- Striated die, we avoid slippage at the tool / material interface

- The smooth die with and without lubrication (graphite + water)

The cladded samples are heated in an electric furnace under normal atmosphere while the die was not preheated and smooth die was lubricated by the a brush.

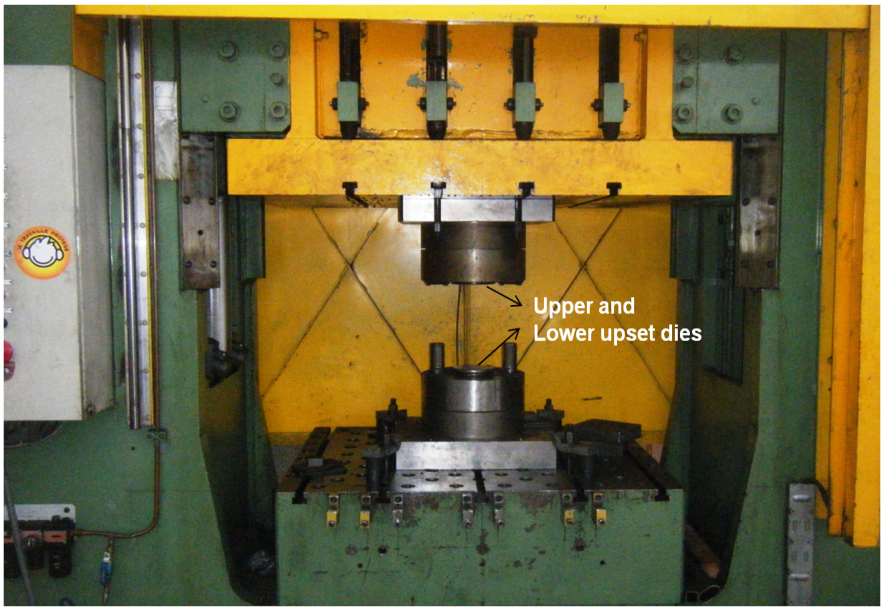

Figure 4.64: Setup for the experimental upsetting test

Materials A bar (C15) of diameter 27 mm is cladded by a stainless steel 316L wire of 1.0 mm diameter for the upset testing by rotating welding platforms with a predefined program. At a constant rotation speed at a specific overlapping distance and torch orientation to favor the arc melt are used. The bar cladding test is carried out on the following welding parameters: wire feed speed = 4.2 m/min, U = 22 V and welding speed = 5.3 mm /s.

Experimental results The output quantities of the parametric study of upsetting of the cladded workpiece are:

- The forging effort as a function of the displacement
- The presence or absence of cracks

- The material distribution

The presence or absence of cracks is determined visually and by die penetrant testing after complete cooling of the workpiece after the test. The appearance of cracks can occur during the upset test or during cooling. After complete cooling, a die penetrant test is performed to reveal the cracks on the workpiece surface.

The materials distribution after forging is observed by the macrographs of the

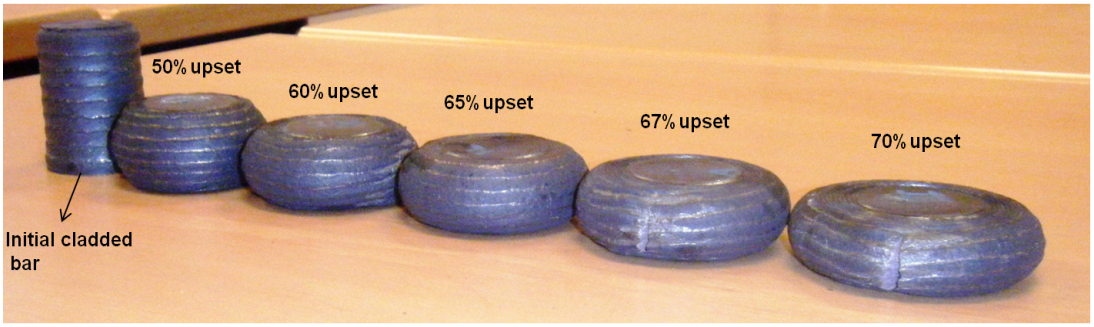

Figure 4.65: Photos of the performed experimental tests heated upto 750°C with the striated die surface

workpiece after cutting and polishing and chemical etching by nital 2% allowing to distinguish the interface between two materials. The macrographs for different % upsetting with striated die surfaces between the die-workpiece interface at a temperature of 750°C are shown in the figure (4.66).

The forging effort and sliding displacement are directly provided by the sensors in the hydraulic press. The forging effort is calculated from the pressure in the main cylinder of the machine. The figure 4.67 shows a comparison of the forging efforts during simulation and experimental at different temperatures. The forging effort increases with the decrease of the temperature both for experimental and simulation tests for a 60% of upsetting. The difference of the experimental and simulation forging effort values is minimum up to 35kN for the 60% upsetting. The deviation between the experimental and simulation results apparently is due to the difference in the slope of the zone II. The simulation was performed with a cladding material SS316L with uniform cladding thickness while for the experimental test the cladding material is diluted and exhibits a wavy morphology.

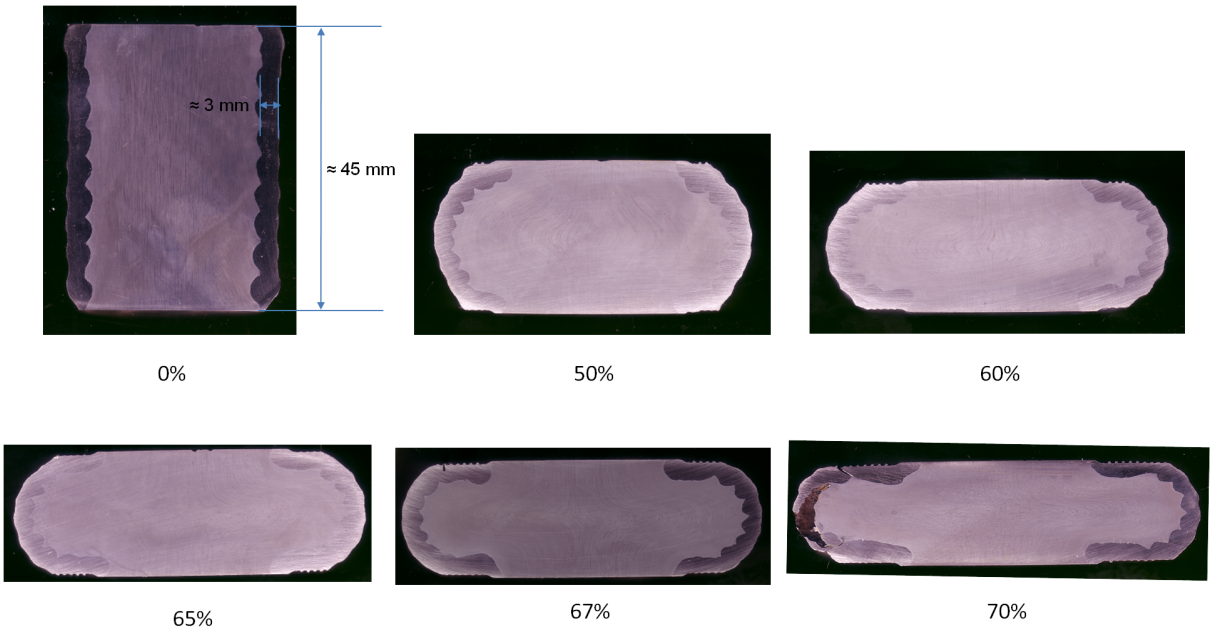

Figure 4.66: The macrographs of the performed series of upset test at 750°C

Both of these parameters have the effect on the behavior of the zoneII in the forging effort/displacement curve.

The experimental forging effort variation for the upsetting test performed at 1050°C under different tribological conditions is shown in the figure 4.68. The forging effort for the striated die surface is maximum and goes up to 425kN for the 60% of upsetting. It decreases to 335kN for smooth die surface with no lubrication and is further reduced to 310kKN when performed with the lubricated surface. This effect is due to the increase of the coefficient of friction between the die-workpiece interface for the striated die and due to increase of thermal exchange due to lubrication.

The failure mechanism for the test performed at 750°C according to the LATANDCN criteria as shown in the equation 4.69, is used to predict rupture phenomena. The experimental results performed at a temperature of 750°C with striated die and simulation results for the compatible parameters are shown in the figures 4.69 and 4.70.

Indeed, the software indicates that the peripheral zone of the work piece is the

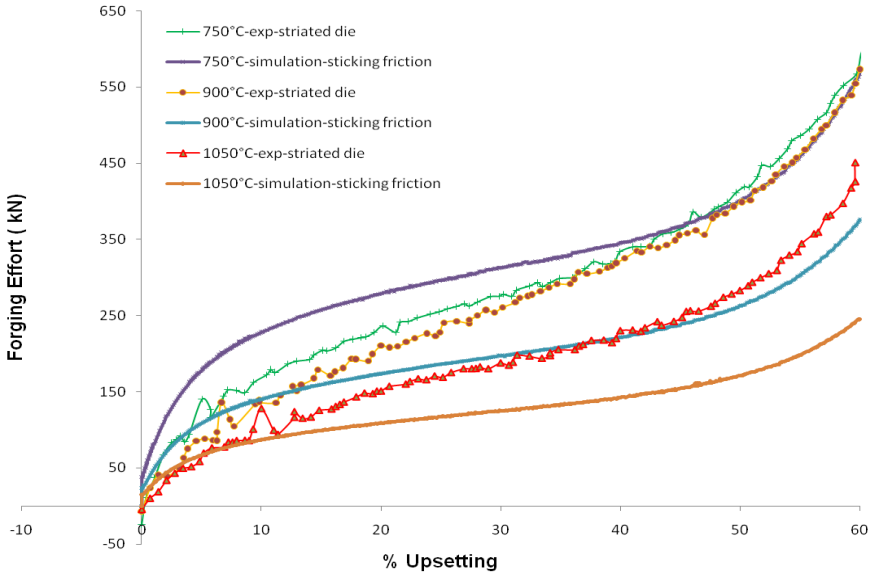

Figure 4.67: Simulation and experimental results of the forging effort for SS316L cladding on C35 at different temperatures

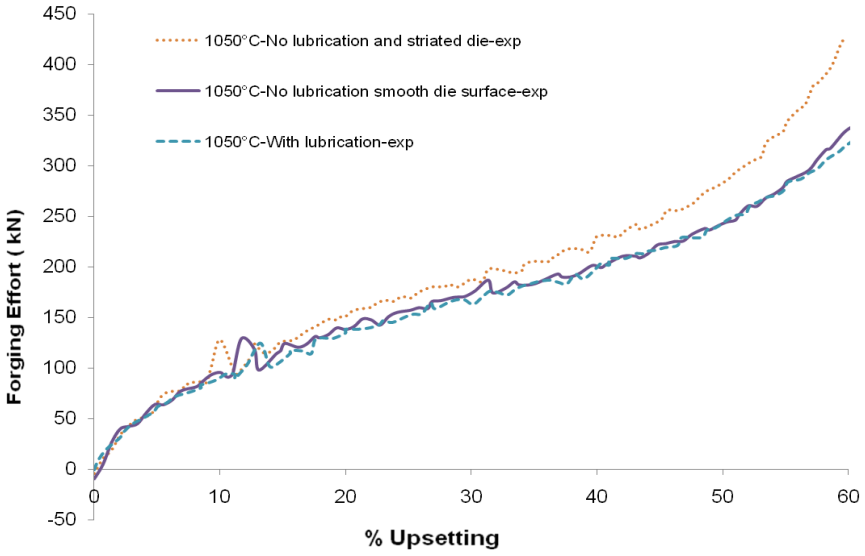

Figure 4.68: The experimental results of the forging effort for SS316L cladding on C35 at 1050˚C under different tribological conditions

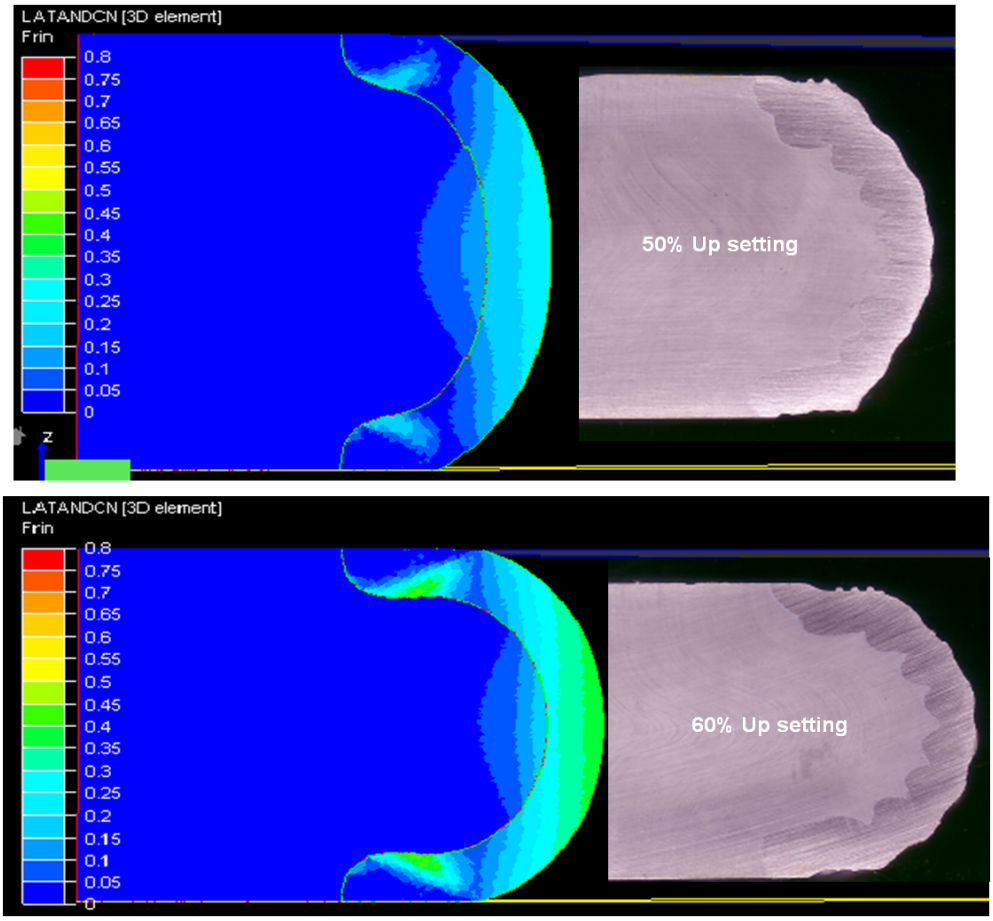

Figure 4.69: Simulation and experimental comparison of failure at 50% and 60% upsetting at 750°C for SS316L cladding on C35

most susceptible to the rupture. For upsetting simulation up to higher values, we observed longitudinal (characteristic of the mono-material upsetting) and circumferential (related to bimaterial upsetting) cracks. It is important to be noted that the ondulation effect at the cladding interface plays a big role in the cracks initiation. On contrary to the simulation results this effect can cause the two types of cracking separately or simultaneously. It was observed that for the longitudinal cracking the cladding thickness was less thick due to the wavy morphology of the cladding layer. This effect may also be explained by considering the reorientation of the stresses due to the wavy behavior of the interface. We can not however quantify the probability of damage or cracks to be sure but, the simulation seems

to agree with experimental results.

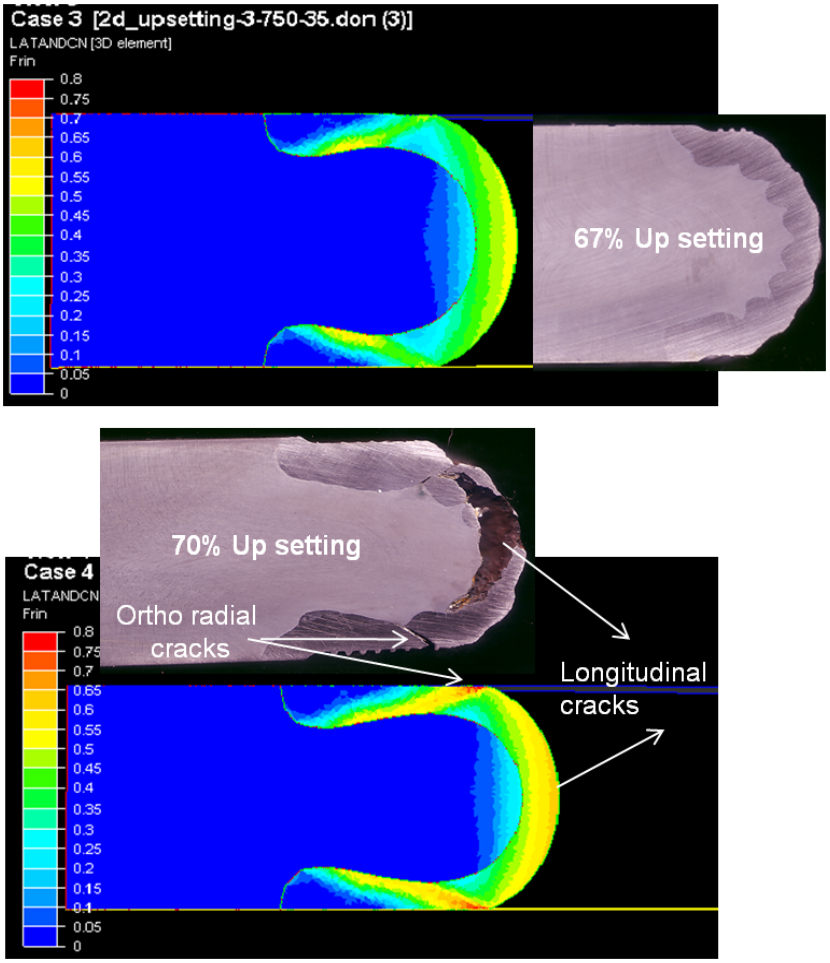

Figure 4.70: Simulation and experimental comparison of failure up to 70% upsetting at 750˚C for SS316L cladding on C35

The table 4.6 shows the effect of temperature and % upsetting on the rupture and cracks occurrence under striated die experimental conditions. It may be observed at upsetting temperature of 750˚C and 900˚C, longitudinal cracks occur more frequently, while at temperate 1050˚C, circumferential cracks are more often. We may comment that at 1050˚C the material posses more ductility as compared at 750˚C and 900˚C and exhibits more upsetting before the occurrence of longitudinal cracking. From a certain value of upsetting probability of the

circumferential cracking increases according to the Lathan criterion. The wavy morphology of the cladding interface plays an important role in the reorientation of the stresses and should be taken into account.

Upsetting Conditions	Cracking occurrence	Upsetting Conditions	Cracking occurrence	Upsetting Conditions	Cracking occurrence
750°C for 50% Upsetting	X	900°C for 60% Upsetting	X	1050°C for 60% Upsetting	X
750°C for 50% Upsetting 60	X	900°C for 63% Upsetting	X	1050°C for 70% Upsetting	Circumferential
750°C for 65% Upsetting	longitudinal	900°C for 67% Upsetting	X	1050°C for 70% Upsetting	Circumferential
750°C for 65% Upsetting	longitudinal	900°C for 65% Upsetting	X	1050°C for 70% Upsetting	Circumferential
750°C for 65% Upsetting	longitudinal	900°C for 65% Upsetting	Longitudinale		
750°C for 67% Upsetting	longitudinal	900°C for 65% Upsetting	Longitudinale		
		900°C for 70% Upsetting	Longitudinale		

Table 4.6: The effect of temperature and % upsetting on the cracks occurrence under striated die experimental for SS316L cladding on C35

Upsetting experimental conclusion During the experimental study of the upsetting test, two main types of the cracking as predicted by the simulation analysis along with three different zones of the forging effort/displacement curve were obtained. When SS316L cladded workpiece on a substrate of C15 go through the upsetting test, the longitudinal cracks are more frequent at temperature of 750°C and 900°C and 1050°C, circumferential cracks are more often. The reorientation of the clad beads cause a wavy morphology at the cladding interface which plays an important role in the solicitation applied.

4.3.2.4 Conclusion related to the upsetting Test

The aim of the test performed is to estimate the forgeability limit of a cladded workpiece. The simulation and experimental analysis performed with a striated

die to control the friction effect (equivalent to sticking friction in the simulation study), showed that we can estimate the forgeability of the cladded workpiece at level 1 and 2. Under the striated die upsetting, the strain occurred in the cladding surface are the function of upsetting distance. On contrary to the hot bending test, two main types of the cracking are observed in the both experimental and simulation analysis along with three different zones of the forging effort/displacement curve. We may observe that both the tests performed up till now, do not give us a clear vision of the cladding material behavior with respect to the complete deformed work piece (Level3). Although we can interpret it by using the forging effort/displacement curve especially the zone II.
The hot bending and upsetting tests are probably not sufficient to characterize the forgeability of bi-materials at all the three levels and it seems to introduce some other test like the Plane strain compression test to estimate its forgeability at level 3.

4.3.3 The Plane strain compression Simulation

The simulation test for plane-strain compression is used to measure flow properties of the cladded workpiece. The effect of the material variation between the substrate and the cladding material on the equivalent strain and forging effort of the workpiece is to carried out by the simulation studies. The simulation strategy was kept same as that of the last two forging tests. Bi-punching simulation test for the compression test is also carried out to estimate the material distribution for different cladding materials as shown in the figure 4.71. We may conclude that this test describe the material distribution profile more remarkably. The cladded layer profile of different materials during the plane compression test at 900°C is given in the figure 4.72 which illustrate clearly the effect of the cladding material on the overall material distribution.

The forgeability of the cladded material at level 3 is visible in the plane strain compression test of the cladded material. The simulation test for plane-strain compression is helpful to guess the flow properties of the cladded workpiece as it describes the material distribution profile and global workpiece forgeability, in a better way compared to the earlier performed tests. However the thermal

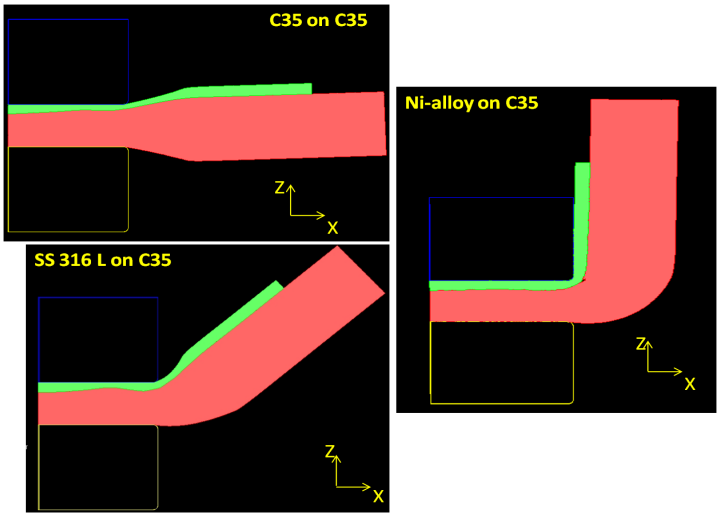

Figure 4.71: Simulation results of different materials cladding on C35 for bi-punch compression test performed at 900°C

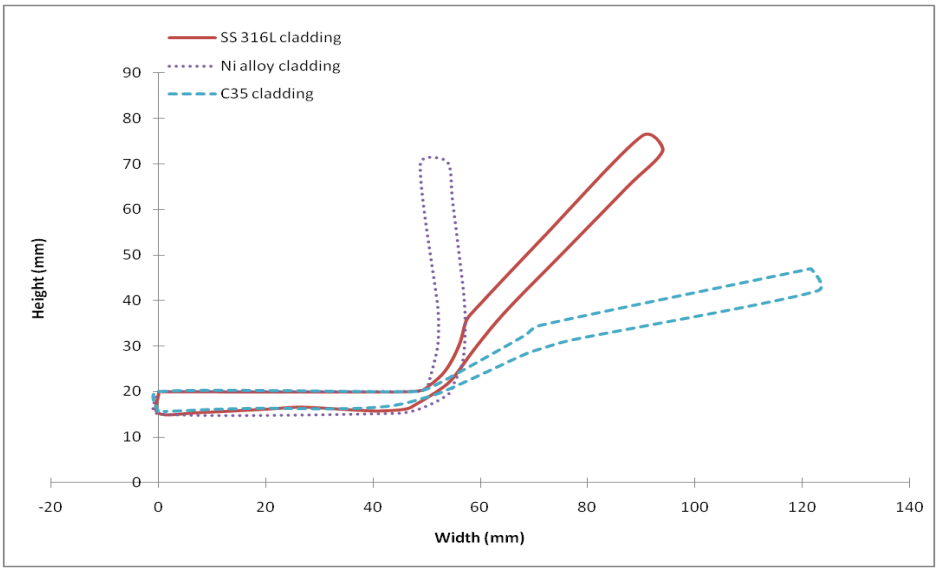

Figure 4.72: Simulation results of the cladded layer profile after the plane compression test for different materials

exchange and tribological conditions may play an important role for the material distribution behavior and should be testted under different condition of thermal exchange and tribology.

4.4 Conclusion

The objective of this chapter is to analyze the ability of a cladded workpiece under hot forging to obtain a desired defect free material distribution and structure. For this purpose a set of hot forging tests is carried out experimentally and numerically to evaluate the feasibility of the proposed idea of cladded bi-material forgeability. As the cladded layer is mixture of the substrate and cladding metal depending on the dilution rate. Due to the difference in rheological properties at different positions of the workpiece, three levels of the hot forging characterization are considered. The hot bending test allows us to estimate the local hot ductility limit of the cladding material for the levels 1 and 2. From the the hot bending simulation test we may guess the equivalent strain in the clad surface as a function of the ram displacement during the process. In case of the upsetting test, the solicitation on the cladding are not uniform due to the barreling effect of the workpiece because of combined effect of friction and thermal exchange are taken into account. The tribological effects of the test are restricted by imposing the sticking friction conditions, to fix the strain and strain rate of a given geometry of the workpiece as the function of the upsetting distance only. The upsetting experiment is performed with a striated die to control the friction effect and under this condition, strain occurred in the cladding surface are the function of upsetting distance. The hot bending and upsetting tests do not provide an ample insight to characterize the forgeability of bi-materials at all the three levels and the plane strain compression simulation test to estimate its forgeability at level 3 was introduced which is helpful to guess the flow properties of the cladded workpiece as it describes the material distribution profile and global workpiece forgeability more remarkably.

Chapter 5

Conclusion And Perspective

The thesis presented is dedicated to forming of the cladded workpieces. The proposed idea of research is based on reversing the classical fabrication sequence of a simple cladded preform by performing the hot forging process after the weld cladding. The expected benefits are structural refinement of fusion welding solidification by hot forging structure. Moreover due to ease of automation of GMAW cladding on simple preforms like plates, discs or cylinders, good control on clad quality parameters (metallurgical and geometric) can be achieved. The proposed concept may have a great technological relevance in manufacturing industry.
The literature review showed that there is a very large number of cladding processes with a variety of materials deposition from polymers, metals to ceramics. The surface geometries and thicknesses are widely dependent on the cladding process. The deposition processes such as PVD can deposit thin films on the complex forms. In contrast, the explosion cladding process can deposit a minimum thickness of sheet metal in the millimeter range only on planes or cylindrical surfaces of large diameters. The weld cladding allows us to deposit metals of superior properties like stainless steels and super alloys on complex metal surfaces. The concern of these processes is often their lack of productivity and reproducibility of the cladding quality. These two disadvantages can be partially solved by automating the weld cladding process.
In the thesis work presented, initially setting up a methodology for controlling the cladding process on simple shapes is performed. This methodology is applied

for the cladding of S235 substrate with a stainless steel 316L by GMAW process by juxtaposition of straight beads. The methodology is based on two approaches:

- The statistical experimental study of a single bead deposition
- The determination of the optimum bead overlapping by using overlapping models

The cladding overlapping calculated from the criterion of "equivalent area" is based on the geometry of the single bead. The input parameters of the method are the characteristics of the cladding layer. These parameters may include the geometry of the clad layer, the metallurgical properties of the clad layer (dilution rate, nominal energy, wire feed speed and initial temperature), the duration of the process (welding speed). The developed methodology is validated by obtaining satisfactory cladding layer in terms of compactness of and the absence of ripples and corrugation. The initial study has also set up the link between the dilution rate, the nominal energy of welding and metallurgical quality of the cladding for a stainless steel on mild steel. The methodology development will be tested also in the case of other cladding types and different materials.
In the second part, the work has focused on the study related to the hot forging behavior of the cladded workpiece. The main difficulty in this study is the unknown behavior of the weld cladded layer. Its composition can be approximated by calculating the dilution rate and its structure is derived from the solidification of welding. The compositions do not correspond to known materials and initial metallurgical structure does not match what is usual in forging. It is therefore necessary to develop tests to characterize the forgeability of the cladded workpieces. For this purpose three forgeability levels/scales were defined:

1. The scale of the cladding: It corresponds to the rheological behavior of the cladding material after cladding including in particular its limit of hot ductility.
2. The scale of including cladding and nearby area of the substrate. This scale takes into account the geometry of the interface between the cladding and the substrate and the cohesion defects.

3. The scale of the cladded workpiece. This part takes into account the ability of multi-material to be shaped to achieve the desired material distribution in the final part.

The classical forgeability tests found in the literature are developed only in the context of mono-material work piece. Their application to the cladded parts is not addressed. In the thesis two possible characterization tests were studied, hot bending and upsetting test. This study was to assess their forgeability of the multi-material in accordance with the above described three levels. Simulations from the analytical model or finite element numerical simulation showed that these two tests to assess the forgeability of the cladded workpiece to the first two levels. In the case of hot bending, the maximum plastic strain in the clad surface can be controlled through the die displacement/stroke. For the same die displacement/stroke, the deformation obtained varies little depending on the material or cladding thickness or the conditions of friction or heat exchange between the die and workpiece. This test is not so sensitive to the material distribution which makes it difficult to assess the scale 3 of forgeability. It is possible to consider the assessment through the hot bending forging effort to the forging stroke by an inverse analysis to trace the behavior of the cladding although it is not validated in the thesis. Experimental tests have shown the important role played by the substrate/cladding interface including its shape and cohesion defects. During hot bending test, the cladding and interface are under plane tension.
The clad bead orientation along with its defects and the undulation of the interface with the substrate plays a major role to determine the cladding ductility. This explains the anisotropy across the cladding and the interface in terms of hot ductility limit and possibly deformation behavior. The experimental results obtained in the case of a S235 steel cladding with a 316L stainless steel have shown the important role of the cooling of the workpiece after the hot forging process. The difference in coefficient of thermal expansion between the cladding and the substrate can cause cracks in the cladding during cooling. Experimental tests were performed for two different thicknesses and dilution. The results in terms of ductility are identical, the tests performed at 750°C show cracks, those conducted at 900°C show no cracks and testing at 1050°C exhibit cracks during

cooling.
In the case of the upsetting test, to control the effect of friction, a die with striated surface is used. By controlling slipping between die and workpiece, we found as in the case of hot bending a good correlation between the cladding deformation and the upsetting displacement, irrespective of the cladding material or thickness . The finite element simulations and experimental tests have shown two possible forms of cracking. The first is commonly encountered during the upsetting of mono material workpiece. The second, however, is a specific form for the cladded workpieces corresponds to a circumferential cracks near or under the die/workpiece contact. Both tests allowed us to show the important role of the interface shape between the substrate and cladding layer. Its ripple, due to the juxtaposition of beads for the layer cladding, gives an "anisotropic" performance on a scale including the cladding thickness and substrate area close to the interface. This aspect is not taken into account in the simulations but can be an objective of the future development.
The problem of evaluation of the ductility on a global scale has not been addressed since the two tests studied were not so favorable in this aspect. The initial simulations of the bi-punching compression test describes the material distribution profile and global workpiece forgeability, in a better way compared to the earlier performed tests. This test if performed like hot bending and upsetting test may estimate in a better way, the overall forgeability of bi-materials. An expected benefit is to forge bi-materials is the improvement of the microstructure of the coating by the hot deformation. This was not addressed in the work presented here. Forgeability tests will also characterize the metallurgical transformations that occur in the cladding and the substrate to qualify and quantify the potential gain.

References

ASM Handbook, c. (1993). *Forming and Forging*, vol. 14, chap. Forging of Carbon and Alloy Steels, 470–477. ASM International. 104

ASM Handbook, I. (2001). *Surface Engineering for Corrosion and Wear Resistance*, chap. 1. ASM International, http://www.asminternational.org. vi, 52, 53, 64

ASM Handbook, I. (2002). *Surface Hardening of Steels*, chap. 11. ASM international, http://www.asminternational.org. 60, 62, 96, 97

AWS (1982). *Welding Handbook*. American Welding Society. 89, 102

Babu, S., Elmer, J., David, S. & Quintana, M. (2002). In situ observations of non-equilibrium austenite formation during weld solidification of an fe-c-al-mn low-alloy steel. In *Mathematical, Physical and Engineering Sciences*, vol. 458, 811–821, The Royal Society. 99

Batchelor, A.W., Lam, L.N. & Chandrasekaran, M. (2002). *Materials Degradation and Its Control by Surface Engineering*. Imperial College Press London. vi, 53, 54, 69, 70

Bhat, D.G. (2007). *Coatings Technology Fundamentals, Testing and processing Techniques*. Taylor and Francis Group. xvii, 58

Blocher, J.M. (1974). Structure/property/process relationships in chemical vapor deposition cvd. *Journal of Vacuum Science and Technology*, **11**, 680–686. vi, 59

Brooks, M. (2008). Advance welding and robotic system, tech Tips,It's All About The Angles. vii, 85

Buchanan, E. (2009). Solidification and microstructural characterisation of iron-chromium based hardfaced coatings deposited by smaw and electric arc spraying. *Surface and Coatings Technology*, **203**, 3638–3646. 63

Cao, X., Jahazi, M., Fournier, J. & Alain, M. (2008). Optimization of bead spacing during laser cladding of ze41a-t5 magnesium alloy castings. *journal of materials processing technology*, **205**, 322–331. 94

Cao, Y., Zhu, S., Liang, X. & Wang, W. (2011). Overlapping model of beads and curve fitting of bead section for rapid manufacturing by robotic mag welding process. *Robotics and Computer-Integrated Manufacturing*, **27**, 641 – 645. 94, 117

Charles, J., Crane, F. & Justin, F. (1989). *Selection and Use of Engineering Materials*. Butterworth and Co. vi, 53, 57

Chiu, K., Cheng, F. & Man, H. (2005). Laser cladding of austenitic stainless steel using niti strips for resisting cavitation erosion. *Materials Science and Engineering: A*, **402**, 126 – 134. 74, 77

Deuis, R., Yellup, J. & Subramanian, C. (1998). Metal-matrix composite coating by pta surfacing. *Composites Science and Technology*, 299–309. 78, 102

Deyev, G. & Deyev, D. (2006). *Surface Phenomena in Fusion Welding Processes*. CRC Press Taylor and Francis Group. 64, 100

D'Oliveira, A., da Silva, P. & Vilar, R. (2002). Microstructural features of consecutive layers of stellite 6 deposited by laser cladding. *Surface and Coatings Technology*, **153**, 203–209. vii, 79, 95

Domblesky, J. & Kraft, F.F. (2007). Metallographic evaluation of welded forging preforms. *Journal of Materials Processing Technology*, **191**, 82 – 86. viii, 111, 112

Domblesky, J., Kraft, F., Druecke, B. & Sims, B. (2006). Welded preforms for forging. *Journal of Materials Processing Technology*, **171**, 141 – 149. 111, 112

Doumanidis, C. & Kwak, Y.M. (2002). Multivariable adaptive control of the bead profile geometry in gas metal arc welding with thermal scanning. *International journal of pressure vessels and piping*, 251–262. 95

Ettaqi, S., Langlois, L. & Bigot, R. (2008). Cobalt-based superalloy layers deposited on x38crmov5 steel base metal by explosion cladding process. *Surface and Coatings Technology*, **202**, 3306 – 3315. vii, 72

Gabriel, D. (2004). *Contribution à l'optimisation des revêtements des moules de fonderie application aux outillages de coulée centrifuge*. Ph.D. thesis, INP. 102

Gebert, A. & Bouaifi, B. (2006). *Modern Surface Technology*, chap. 18. WILEY-VCH Verlag GmbH and Co. 102

Gilles, P., El-Ahmar, W. & Jullien, J.F. (2009). Robustness analyses of numerical simulation of fusion welding net-tg1 application: "single weld-bead-on-plate". *gInternational Journal of Pressure Vessels and Piping*, **86**, 3–12. vii, 73

Harris, T. & Priebe, E. (1993a). *Forming and Forging*, vol. 14, chap. Forging of Stainless Steel, 494–500. ASM International. viii, 109

Harris, T. & Priebe, E. (1993b). *Forming and forging processes*, vol. 14, chap. Forging of Stainless Steel. ASM International. 95, 99, 101

Honma, S. & Yasuda, K. (2004). Study of semi-automatic tig welding. *Welding International*, **18**, 450–455. 75

Howes, T. (2001). Explosive welding, twi knowledge summary. Tech. rep., The welding Institute,UK. xvii, 71

Illiberi, A., Kniknie, B., Van Deelen, J., Steijvers, H., Habets, D., Simons, P., Janssen, A. & Beckers, E. (2011). Industrial high-rate(14nm/s)deposition of low resistive and transparent znox :al films on glass. *Solar Energy Materials and Solar Cells*, 1955–1959. 102

John, C. & Damian, J. (2005). *Welding Metallurgy and Weldability of stainless steels*. John Willey and Sons. viii, 99, 100, 110, 111

Kannan, T. & Murugan, N. (2006). Prediction of ferrite number of duplex stainless steel clad metals using rsm. *The Welding Journal*. 99

Kannan, T. & Yoganandh, J. (2010). Effect of process parameters on clad bead geometry and its shape relationships of stainless steel claddings deposited by gmaw. *Int J Adv Manuf Technology*. 93, 146, 154

Khalid Rafi, H., Janaki Ram, G., Phanikumar, G. & Prasad Rao, K. (2010). Friction surfaced tool steel (h13) coatings on low carbon steel: A study on the effects of process parameters on coating characteristics and integrity. *Surface and Coatings Technology*, **205**, 232 – 242. vi, 70

Khan, I. (2007). *Welding Science and technology*. New Age International Pvt. Ltd. vii, xi, 82, 84, 90, 92, 98, 176

Kim, S.J., Oh, Y.M. & Kim, J.G. (2005). Fe-based hardfacing alloy. *United States Patent Publication*. 97

Klueh, R. & King, J. (1982). Austenitic stainless steel-ferritic steel weld joint failures. *Welding Journal*, 302–311. 100

Krappitz, H. (2006). *Modern Surface Technology*, chap. 16, 239–241. WILEY-VCH Verlag GmbH and Co. vi, 65

Leduey, B., Galand, E., Bauné, E. & Bonnet, C. (May 2007). Improvement of the welder's environment through consumable product development. Tech. rep., Competence: The technical journal of Oerlikon welding and cutting expertise, www.oerlikon-welding.com. vii, 81

Liu, L. & Qi, X. (2009). Effects of copper addition on microstructure and strength of the hybrid laser-tig welded joints between magnesium alloy and mild steel. *Journal of Materials Science*, **44**, 5725–5731. 93

Martin, P.M. (2010). *Deposition Technologies*. Elsevier Inc. 59

Maurice, L., Glenn, E. & Craig, C. (1996). *Fatigue design of aluminum components and structures*. McGraw Hill. 93

Modenesi, P. (1990). *Statistical modeling of narrow gap mas metal arc welding process*. Ph.D. thesis, Cranfield institute of technology. 91

Naidich, Y., Zhuravlev, V., Gab, I., Kostyuk, B., Krasovskyy, V., Adamovskyy, A. & Taranets, N. (2008). Liquid metal wettability and advanced ceramic brazing. *Journal of the European Ceramic Society*, **28**, 717–728. 68

Norrish, J. & Richardson, I. (1988). Back to basics: Metal transfer mechanisms. *Welding and Metal Fabrication*, 17–22. 73

Olson, D. (1985). Prediction of austenitic weld metal microstructure and properties. *Welding Journal*, **64**, 281–295. 100

Palani, P. & Murugan, N. (2006). Sensitivity analysis for process parameters in cladding of stainless steel by flux cored arc welding. *Journal of Manufacturing Processes*, **8**, 90–100. 146, 154

Panjan, P., Cekada, M., Kirn, R. & Sokovic, M. (2004). Improvement of die-casting tools with duplex treatment. *Surface and Coatings Technology*, 561–565. 61

Parker, K. (2011). Cladding with high power diode lasers. 62

Pradeep, G., ramesh, A. & Prasad, B. (2010). A review paper on hardfacing processes and materials. *International Journal of Engineering Science and Technology*, **2**, 6507–6510. 57, 96

Pratihar, S., Turski, M., Edwards, L. & Bouchard, P. (2009). Neutron diffraction residual stress measurements in a 316l stainless steel bead-on-plate weld specimen. *International Journal of Pressure Vessels and Piping*, **86**, 13 – 19. 176

Rajeev, D. & Radovan, K. (2004). Automated torch path planning using polygon subdivision for solid freeform fabrication based on welding. *Journal of Manufacturing Systems*, **23**. viii, 93, 94

Ramirez, A. & Lippold, J. (2004). High temperature behavior of ni-base weld metal: Part i. ductility and microstructural characterization. *Materials Science and Engineering A*, **380**, 259 – 271. 110

Rao, N., Reddy, G. & Nagarjuna, S. (2011). Weld overlay cladding of high strength low alloy steel with austenitic stainless steel-structure and properties. *Materials and Design*, **32**, 2496–2506. vii, 80

Rao, P., Gupta, O., Murty, S. & Koteswara Rao, A. (2009). Effect of process parameters and mathematical model for the prediction of bead geometry in pulsed gma welding. *Int.J of Adv Manufacturing Technology*, **45**, 496–505. 146, 154

SAF manual, A.L.W. (1996). *Guide des produits consommables de soudage pour les procédés Arc,TIG,MIG,Plasma,Arc Submergé et à la flamme*. Air liquid Welding, SAF France. vii, 92

Schwartz, M.M. (1993). *Welding, Brazing and Soldering*, vol. 6. ASM International. 67

Schweitzer, P.A. (2003). *Metallic Materials, Physical, Mechanical and Corrosion Properties*. Marcel Dekker, Inc. 98, 104, 109

Siva, K., Murugan, N. & Logesh, R. (2009). Optimization of weld bead geometry in plasma transferred arc hardfaced austenitic stainless steel plates using genetic algorithm. *The International Journal of Advanced Manufacturing Technology*, **41**, 24–30. 77

Springer, ed. (1992). *A comparison of the properties of coatings produced by laser cladding and conventional methods*, Birmingham,UK. 102

Steward, R., Grossbeck, M., Chin, B., Aglan, H. & Gan, Y. (2000). Furnace brazing type 304 stainless steel to vanadium alloy (v–5cr–5ti). *Journal of Nuclear Materials*, 283–287. vi, 68

Sulzer, M. (March 2009). An introduction to brazing fundamentals, materials, processing. Tech. rep., Sulzer Metco, www.sulzermetco.com. vi, 66, 67

Takadoum, J. (2008). *Materials and Surface Engineering in Tribology*, chap. Materials for Tribology. John Wiley and Sons, Inc. 58, 60

Tillmann, W. & Vogli, E. (2006). *Modern Surface Technology*. WILEY-VCH Verlag GmbH and Co. vi, xvii, 53, 55, 56

Toyserkani, E., Khajepour, A. & Corbin, S. (2005). *Laser Cladding*, chap. 1. CRC Press LLC, http://www.crcpress.com. 57

Tusek, J. & Suban, M. (2000). Experimental research of the effect of hydrogen in argon as a shielding gas in arc welding of high-alloy stainless steel. *International Journal of Hydrogen Energy*, 369–376. vii, 88

Tusek, J. & Suban, M. (2003). High-productivity multiple-wire submerged-arc welding and cladding with metal-powder addition. *Journal of Materials Processing Technology*, **133**, 207 – 213. 74

van Bennekom, A. & Wilke, F. (2003). Comparison between the physical, mechanical and corrosive properties of forged and cast stainless steels. Tech. rep., Krupp Edelstahlprofile. 183

Verlinden, B., Driver, J., Samajdar, I. & Doherty, R.D. (2007). *Thermo-Mechanical Processing of Metallic Materials*, vol. 11, chap. 13, Physical simulation of properties, 349 – 364. Pergamon. viii, 105, 106, 107

Vill, V. (1962). *Friction Welding Of Metals*. American Welding Society. 102

Welding Handbook, A. (1991). *Welding Handbook*. American Welding Society, 8th edn. 70

Weman, K. (2003). *Welding Processes Handbook*. Woodhead Publishing Ltd. vi, 62, 63, 83

Xu, G., Kutsuna, M., Liu, Z. & Yamada, K. (2006). Comparison between diode laser and tig cladding of co-based alloys on the sus403 stainless steel. *Surface and Coatings Technology*, 1138– 1144. vii, 75, 76, 77, 78

Yu, D., Wang, C., Cheng, X. & Zhang, F. (2009). Microstructure and properties of tialsin coatings prepared by hybrid pvd technology. *Thin Solid Films*, 4950–4955. vi, 61

Zhao, L. & Lugscheider, E. (2002). Influence of the spraying processes on the properties of 316l stainless steel coatings. *Surface and Coatings Technology*, **162**, 6–10. 63

Etude de mise en forme de pièces rechargées par forgeage à chaud

RESUME : Le travail de thèse présenté est dédié à la mise en forme des pièces rechargées. L'idée initiale est d'inverser la gamme de fabrication « conventionnelle » consistant à recharger une pièce pré-ébauchée en faisant la mise en forme d'un « lopin » préalablement rechargé. Les avantages escomptés de cette gamme vient dans un premier temps de ce qu'on recharge une forme simple. Ceci devrait faciliter l'automatisation du rechargement et également le amélioration les structures métallurgiques de solidification issues du soudage. Les travaux concernent dans un premier temps la mise en place d'une méthodologie pour la maîtrise de l'opération de rechargement sur des formes simples pour mettre en place le lien entre le taux de dilution, l'énergie nominale de soudage et la qualité métallurgique des revêtements obtenus. Dans un deuxième temps, le travail s'est concentré sur l'étude du comportement en mise en forme des pièces rechargées. La difficulté provient du fait que le comportement du revêtement n'est pas connu. Deux essais de caractérisation ont été étudiés, le pliage à chaud et l'essai d'écrasement. Cette étude a consisté à estimer leur aptitude à évaluer la forgeabilité d'un multi matériaux concernant les trois échelles de forgeabilité: l'échelle du revêtement correspondant au comportement rhéologique du matériau du revêtement incluant sa limite de ductilité à chaud, l'échelle du revêtement incluant le revêtement et la partie proche du substrat et l'échelle de la pièce. Les simulations à partir de modèle analytique ou numérique par éléments finis ainsi que les essais expérimentaux ont permis d'évaluer la forgeabilité du bi-matériau. Les essais expérimentaux de forgeabilité devront également caractériser les transformations métallurgiques se produisant dans le revêtement et le substrat pour qualifier et quantifier le gain potentiel.

Mots clés : Rechargement par soudage, Etude statistique de procédé, Multi matériaux, Forgeabilité de piece rechargée

Forming of the cladded work-pieces by hot forging

ABSTRACT: The thesis presented is dedicated to the forming of the weld cladded work pieces. The proposed idea is based on reversing the classical fabrication layout of simple cladded preforms by performing the hot forging process after the weld cladding. The expected benefits are structural refinement of fusion weld solidification by hot forging structure and the ease of automation of MIG cladding on simple preforms. Initially a methodology is setup for the MIG cladding process on simple shapes which is based on two approaches: the statistical experimental study of a single bead cladding and the determination of the optimum bead overlapping by using two overlapping models to setup the link between dilution rate, nominal energy of welding and metallurgical quality of the stainless steel cladding on mild steel substrate. In a second step, the focus is on the hot forging behavior of the cladded work piece. Keeping in view the following three aspects: the intrinsic forgeability of each material, the forgeability of the structure composed of the cladding and the substrate part near the interface and the ability to control the overall material distribution during the forming process. This work is the result of an initial feasibility study for reversing the classical manufacturing layout and clad a simple shape and get in shape by hot forging which are considered ideal for obtaining complex shapes. The analytical, numerical and experimental trials are carried out to evaluate the forgeability of bi-material. The aim is to assess the forgeability of the multi-material keeping in mind to what extent are we able to find conditions for implementation of the forming that allows us from a rough cladding to get a defect free part with the desired distribution of materials.

Keywords : GMAW cladding, Statistical study of weld cladding process, Multi-materials, Forgeability of cladded work pieces.

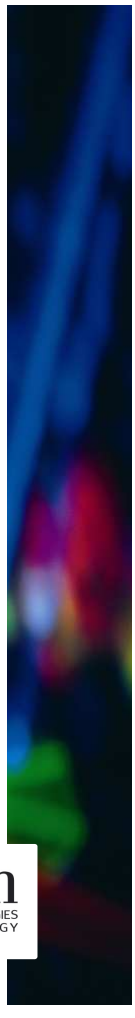

ARTS ET MÉTIERS ParisTech

ParisTech
INSTITUT DES SCIENCES ET TECHNOLOGIES
PARIS INSTITUTE OF TECHNOLOGY